UNIVERSITÉ DU LUXEMBOURG

PhD-FSTM-2021-094
The Faculty of Sciences, Technology and Medicine

# DISSERTATION

Defence held on 19/11/2021 in Esch-sur-Alzette

to obtain the degree of

## DOCTEUR DE L'UNIVERSITÉ DU LUXEMBOURG

## EN *PHYSIQUE*

by

Vasu Prasad PRASADAM
Born on 09 December 1990 in Hyderabad, India

# Functional coatings based on MWCNT-Metal oxide nanocomposite for solar energy harvester application.

## Dissertation defence committee

Dr Naoufal Bahlawane, Dissertation supervisor
*LIST, Luxembourg*

Dr Andreas Michels, Chairman
*Professor, Université du Luxembourg*

Dr Francis Maury, Vice-chairman
*Professor, CIRIMAT, CNRS, Toulouse*

Dr Nathanaelle Schneider, External evaluator
*Professor, PVF, CNRS, Palaiseau*

Dr Dimitra Vernardou, External evaluator
*Professor, Hellenic Mediterranean University*

# *Acknowledgements*

Firstly, I would like to express my deepest gratitude to my PhD supervisor Dr. Naoufal Bahlawane. I feel privileged to have worked under his guidance. Brainstorming sessions with him have taught me how to be a visionary researcher. Deep discussions apart from the scientific topic have helped me grow into a better human being. During PhD journey I experienced what “GURU” means (derived from Sanskrit, meaning a mentor, guide, expert of certain knowledge).

Secondly, I am thankful to Prof. Francis Maury, and Prof Andreas Michels for their insightful advices during the CET meetings and encouraging to continue in research path.

Further. I would like to thank Dr. kamal Baba, Thomas Gaulain and MRT-support staff for their kind technical assistance while troubleshooting the reactors. I am very grateful to Dr. Ali Margot Huerta Flores for introducing hydrogen field and her considerable assistance during the preliminary experiments. I have made few close friends during this journey in the LIST: Kishore, Benjamin, Riyadh, Greg, Deeraj. I appreciate their moral support during the melancholic phase of research.

Finally, I am in great debt to three ladies of my life without them I could not have fulfil my PhD dream. I would like to dedicate my PhD to these great ladies my mom, my aunt, and my partner.

# Abstract

Global energy demand propelled humankind in search of clean and renewable energy sources. Among them, solar energy outstands all the available renewable sources. In this context, concentrated solar thermal technology (CST) and hydrogen storage via solar water splitting feature significant contributions in global power generation. Nevertheless, the major challenge in CST technology is achieving a high solar absorption selectivity with thermal stability above 923 K. Whereas the limited chemical stability and low performance remain significant challenges in solar water splitting technology.

We address these technologies' critical issues through multiwalled carbon nanotubes (MWCNT)-metal oxide hybrid materials. MWCNTs are known for their high solar absorption, thermal and electrical conductivity. While metal oxides such as $VO_2$, Al-doped ZnO are known for their infrared reflecting properties with high transparency in the visible region. $TiO_2$ and ZnO have appropriate band positions for water splitting reactions. Here, combining CNTs and metal oxides at the nanoscale leads to unique properties, not present in individual constituents. We fabricate the MWCNT-metal oxide through the hybrid chemical vapor deposition-atomic layer deposition (CVD-ALD) process. Here the CVD is implemented to grow MWCNTs, while ALD is used to grow conformal metal oxide shells on the 3D porous MWCNT structures.

The MWCNT-$VO_2$ nanostructures performed in this study feature a solar selectivity modulation across the semiconductor-metal transition temperature of $VO_2$, i.e., 67˚C. The thermally induced optical modulation was investigated as a function of the morphology of $VO_2$ phase. The grown $VO_2$ nanoparticles on MWCNT illustrate an enhancement in the spectral emissivity across the SMT temperature. A contrasting optical modulation is displayed by the continuous $VO_2$ layer on MWCNT. Aluminium doped zinc oxide (AZO) layer (4.7 at %) illustrated solar absorbance of 0.96 and thermal emittance of 0.6. The limited thermal stability of the engineered MWCNT-AZO was enhanced by the deposition of a thin $Al_2O_3$ layer at the MWCNT-AZO interface. A core-double shell structure, i.e., CNT-$Al_2O_3$-AZO, withstands thermal treatment at 1000 K for 72 h.

Solar water splitting study on MWCNT-$TiO_2$ and MWCNT-ZnO nanostructures revealed a significant performance improvement relative to the respective oxides. For MWCNT-$TiO_2$ core-shell structure, an enhancement of photocurrent by 400 % was observed relative to planar Si-$TiO_2$. While in MWCNT-ZnO core-shell structure, similar results as CNT-$TiO_2$ is observed but with higher photocurrent density because of better electrical properties of ZnO. We observed an increase of 458 % of the photocurrent density relative to Si-ZnO. The difference in performance between Si-ZnO/$TiO_2$ and MWCNT-ZnO/$TiO_2$ was associated with the diminished electron-hole recombination, efficient electron collection and increased relative surface in the core-shell structure.

# Contents

# 1 INTRODUCTION

Global energy consumption report by US energy information administration projects an increase in the energy consumption by 50% in 2050[1]. Raise in energy consumption is mainly driven by the rise in the global population from 7.8 billion in 2020 to 9.9 billion by 2050[2]. Energy sources such as coal, oil and natural gas are utilized to meet the current global energy demand. However, fossil fuels have limited reserves, consuming them for a long duration can completely deplete the energy resources. It is projected that coal will last for 114 years, natural gas for 53 years and oil for 52 years[3]. Statistical projections can vary in time with global consumption rates and newly found reserves. The fossil fuels scarcity would negatively affect the health care sector, agriculture, pharmaceutical and chemical industries which use 99% fossil fuel as feedstock for their product production[4,5]. There are no economically viable alternative raw materials other than fossil fuels for the cost-effective production of some of the chemical products used in these sectors[6]. For the sake of the above-mentioned critical issues, the consumption of fossil fuels for global energy demand must be reduced. Concurrently, the combustion of fossil fuels leads to the emission of $CO_2$ into the atmosphere, which remains in the atmosphere for longer time, >1000 years, relative to other greenhouse gases. Simulation study for the effect of carbon emission on climate change projects a complete dissolution of the Antarctic ice sheet with 10,000 gigatons of carbon emission into the atmosphere, which would concurrently raise the sea level[7]. Hence, it is recommended to have a global cumulative $CO_2$ emission budget to maintain global surface temperature. Paris climate agreement limits the global $CO_2$ emissions by 600-800 gigatons, so the surface temperature remains less than 2°C above the pre-industrial temperature level[8,9]. However, with the current $CO_2$ emission of 43 gigatons per year, we run out of the carbon budget by 2038[10]. Nevertheless, lower carbon emission per year can give little more time before reaching the end of the limit, as described in figure 1. Alternative renewable energy sources such as solar, wind, hydroelectric, geothermal, and tidal are prominent pathways to meet global energy demand with zero emission[11]. Since the last few years, renewable sources have accounted a considerable share in electricity generation, projected to increase significantly by 2050 to reduce the global required carbon emission. Paris climate policy upsurges electric vehicles in transportation that reduced fossil fuel consumption and carbon emissions.

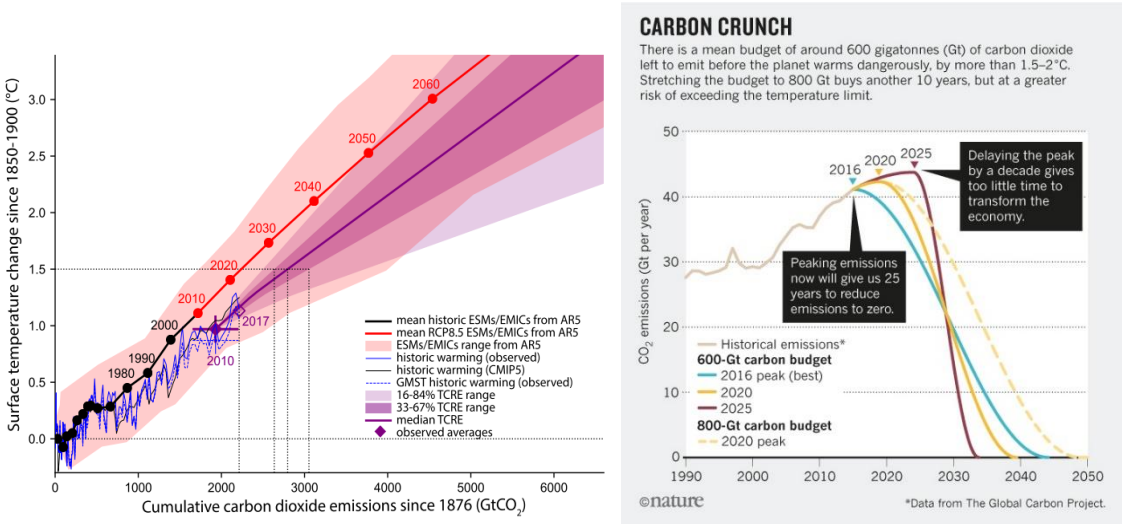


*Figure 1: Left image shows surface temperature projections with respect to the cumulative $CO_2$ emissions in Gt $CO_2$ since 1876. The black line shows the warming calculated by Earth system models based on historical emissions. The red line shows the projected warming based on a business-as-usual scenario taken from Ref[9]. While the right image illustrates the available years before reaching the carbon budget limit. 600 Gt of carbon dioxide budget is left to emit before increasing by 1.5–2°C. Extending the budget to 800 Gt brings a greater risk of exceeding the temperature limit taken from Ref[10].*

Among the available renewable technologies, solar technology provides the most prominent energy resource. Energy received from the sun for 1h accounts for 430 EJ, which exceeds the global energy production in 2011, i.e., 410 EJ[12]. In the last decade, rapid cost reduction in solar energy production from 0.35$/KW-h in 2010 to 0.05 $/KW-h in 2020 is associated with an increased global solar energy contribution to 2.7 EJ. International Energy Agency projects a solar energy contribution of 27% in the global energy production by 2050[13,14]. Solar energy utilization can be categorized into two sections: a) solar capture and conversion technology, b) energy storage.[12]

Two technologies are considered in the capture and conversion of solar energy. Photovoltaics (PV) and concentrated solar thermal (CST) technologies harness solar energy for electricity generation, as shown in figure 3. Photovoltaics directly convert sunlight into electricity by using semiconductor materials. While a concentrated solar thermal system converts sun-heat into electricity via conventional steam power generator[15]. Photovoltaics is a very mature technology with a global installation of 630 GW in 2019[16]. However, PV technology is non-dispatchable with intermittency, leading to the requirement of an external storage system to meet energy demand. In contrast, concentrated solar thermal technology is dispatchable with built-in thermal energy storage capability[17]. In the last decade, numerous CST power plants were installed throughout the world, and intense R&D gave rise to cost-effective advanced materials with high performance, such has Pyromark 2500, black oxide material[18]. Presently electricity generated from CST technology costs around 0.15 $/kW-hr, and an increased production could reduce the price below 0.10 $/kW-hr[19]. As a result, solar thermal power has enormous capability to meet global energy demand. Theoretically, the total global electricity demand can be fulfilled by covering 1% of the Sahara Desert with solar thermal power plants. Thus, solar thermal power systems are expected to play an essential role in future electricity supply and account for 11% of global energy production by 2050.

*Figure 3: Installation of solar power plants: Photovoltaics (left) and Concentrated solar thermal (right)*[15]

Energy storage systems are implemented along with the solar plants to mitigate intermittency issues. These are classified into five major sections for grid application: mechanical, electrical, electrochemical, chemical, and thermal storage[20]. Among them, mechanical storage in the form of potential energy is a widely used technique. Here energy is stored by pumping the water uphill in a reservoir, and when in need, uphill water can drive the turbine to generate electricity. The required large geographical location, slow response and long development time are apparent drawbacks of this approach[21]. Electrochemical storage via batteries is next in line for power grid application. Some batteries have high self-discharge proceeding with short-term energy storage[20,22]. However, extensive large scale energy storage is limited due to high costs, low energy storage density, and limited life cycles[23]. In this context, chemical storage in the form of hydrogen is promising because of the long term storage capability, high efficiency, and minimal environmental effect[24]. Solar power is used in splitting water into $H_2$, $O_2$ through electrolyser. Produced $H_2$ and $O_2$ can be reused for electricity generation through fuel cell technology[25], as shown in figure 4.

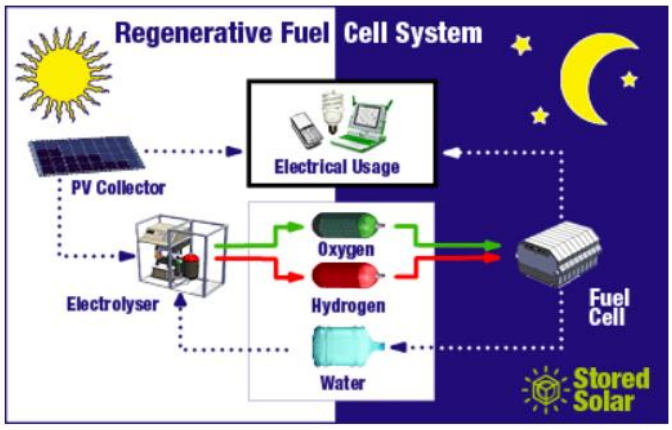


*Figure 4: schematic of regenerative solar fuel cell system*[26] .

Nevertheless, solar thermal systems and chemical storage via solar water splitting technologies have materials-based limitations in achieving high yields. Therefore, new materials are in great need to address the technical challenges related to their performance.

## 1.1 SOLAR THERMAL ENERGY HARVESTING

In the CST system, heat generated by the solar absorbance is transferred via steam to a power generator for electricity production. Currently, four CST technologies are available: Linear Fresnel reflector (LFR), parabolic trough collector (PTC), solar tower collector (STC) and parabolic dish collector (PDC)[27], as shown in figure 5.

*Parabolic trough collector (PTC)* system consists of reflecting mirrors, solar absorber tube and support structures. Reflecting mirrors are in a parabolic shape, concentrating the sunlight on to absorber tube along the focal line of mirrors. A single-axis tracking mechanism is used in the orientation of sunlight throughout the day onto the absorber. *Linear Fresnel reflector (LFR)* system is like PTC, instead uses flat or curved mirrors to concentrate the sunlight onto the long tubular absorber. Here the absorber position is fixed, and individual mirrors are oriented towards the sun using a single-axis tracking mechanism. *Solar tower collector (STC)* system consists of computer-controlled mirrors called heliostat, a central absorber tower. Here all the sunlight is concentrated onto the central tower with the help of two-axis tracking mechanism mirrors. *Finally, a parabolic dish collector (PDC)* consists of a parabolic shaped dish reflector that concentrates the sunlight into a single focal point towards the receiver end. It uses a two-axis tracking mechanism to focus the sunlight throughout the day. Among all these systems, the solar absorber remains the primary component.

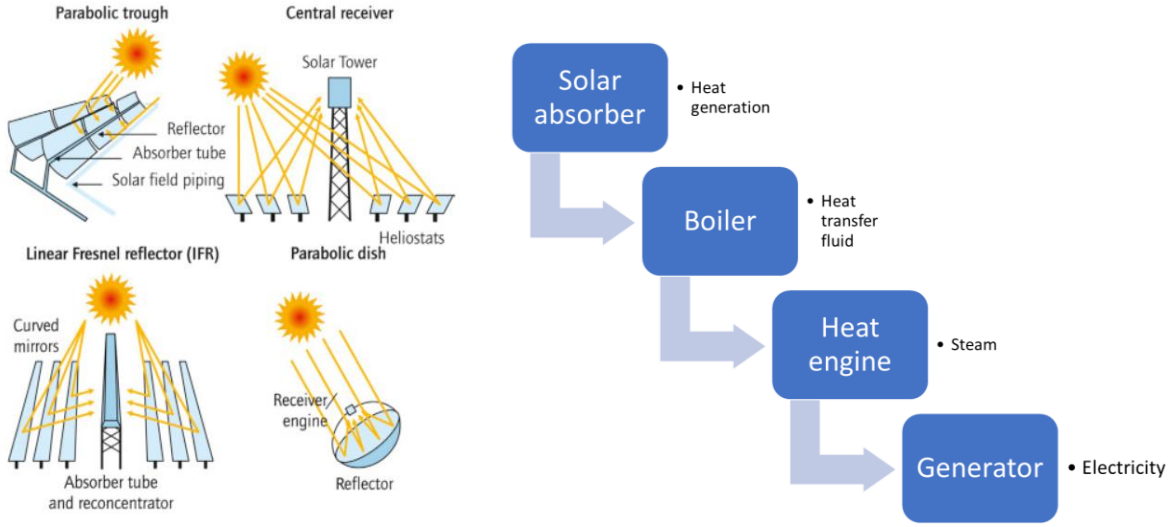


*Figure 5: Schematic of various concentrated solar thermal technologies[28] (left), components of concentrating solar thermal system (right)*

Solar absorbers are central in solar thermal energy harvesting technologies. These materials should have selective solar absorptance characteristics. An Ideal solar selective absorber should exhibit a high absorptance in the solar spectrum region (Am1.5) and low absorptance (emittance) in the mid-far infrared region[29], as shown in figure 6.

According to Kirchoff's law for opaque bodies, the spectral absorptance(α) or thermal emittance (ε) can be given in terms of total hemispherical reflectance (R), as shown in equation 1

$$\alpha\,(\lambda,\theta)\;=\;1-R(\lambda,\theta)\;\text{ or }\epsilon\,(\lambda,T)=1-R(\lambda,T) \qquad \text{Eq1}$$

λ is the wavelength, θ is the angle of incidence, T is the body temperature in kelvin. *Solar absorptance* ($\alpha_s$) is defined as the ratio of solar weighted absorbed radiation to the total solar irradiance given by equation 2.

$$\alpha_s\;=\frac{\int_{0.25\mu m}^{2.5\mu m}[1-R(\lambda,\theta)]\,I_{Am1.5}\,(\lambda)d\lambda}{\int_{0.25\mu m}^{2.5\mu m}I_{Am1.5}\,(\lambda)d\lambda} \qquad \text{Eq2}$$

Where $I_{Am1.5}$ *is the* spectral solar irradiance intensity on the earth surface. From the black body radiation given by equation 3, thermal radiations emitted by any material depend on the body temperature. Therefore, thermal emittance (ϵ) is defined as the ratio of emitted radiation from a hot body to radiation emitted from a black body at that temperature, given by equation 4.

$$BB(\lambda,T)=\frac{C_1}{\lambda^5(e^{C_2/\lambda T}-1)} \qquad \text{Eq3}$$

$$\epsilon\;=\frac{\int_{2.5\mu m}^{25\mu m}[1-R(\lambda,T)]BB(\lambda,T)d\lambda}{\int_{2.5\mu m}^{25\mu m}BB(\lambda,T)d\lambda} \qquad \text{Eq4}$$

$C_1$, $C_2$ are Plank´s constants ($C_1$= 3.74X10$^{-16}$ W m$^2$; $C_2$=1.44X10$^{-2}$ m K), T is the temperature in Kelvin. Thermal emittance is dimensionless; and is unity throughout the spectral range. While it is 0 in the near IR spectral range for an ideal solar selective black coating.

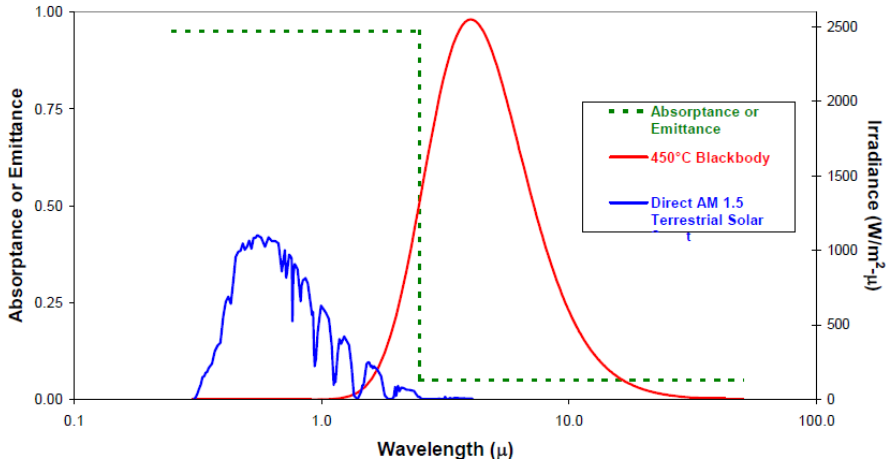


*Figure 6: Spectral characteristics of an ideal selective solar absorber*[29].

Solar to the heat conversion efficiency of the solar absorber is based on factors such as solar absorptance ($\alpha_s$), thermal emittance ($\epsilon$), given in equation 5 under the assumption of no heat loss due to conduction and conviction[30].

$$\eta=\frac{\alpha_s.CF.Q-\epsilon\sigma T^4}{CF.Q} \qquad \text{Eq5}$$

where CF is the solar concentration in a number of Suns, Q is the solar radiative heat flux on absorber *(1000 W/m$^2$), σ is the Stefan-Boltzmann constant (5.67x10$^{-8}$ W/m$^2$ K$^{-4}$),* and T is the

absorber temperature in kelvin. Interaction of light with different materials are illustrated in the ANNEX section.

Selective solar absorption can be achieved by intrinsic characteristics or implementing various structural designs such as semiconductor-metal tandem, multilayer, cermet and surface texturing[31], as shown in figure 7. Among them, cermet design was researched extensively because of its potential high-temperature stability[32]. Temperatures above 923K are required for the next-generation solar thermal harvesters to achieve high efficiency. However, at high temperatures, diffusion, agglomeration, oxidation of the embedded metallic nanoparticles negatively impact the cermet solar absorbance and the thermal emittance[30]. Addition of barrier layers along with non-metallic substrates, and embedded noble metal or bi-metallic particles in the matrix, have reported to improve the thermal stability of solar absorbers. However, still, upon implementing new designs, cermet's have a non-satisfactory performance-thermal stability trade-off.

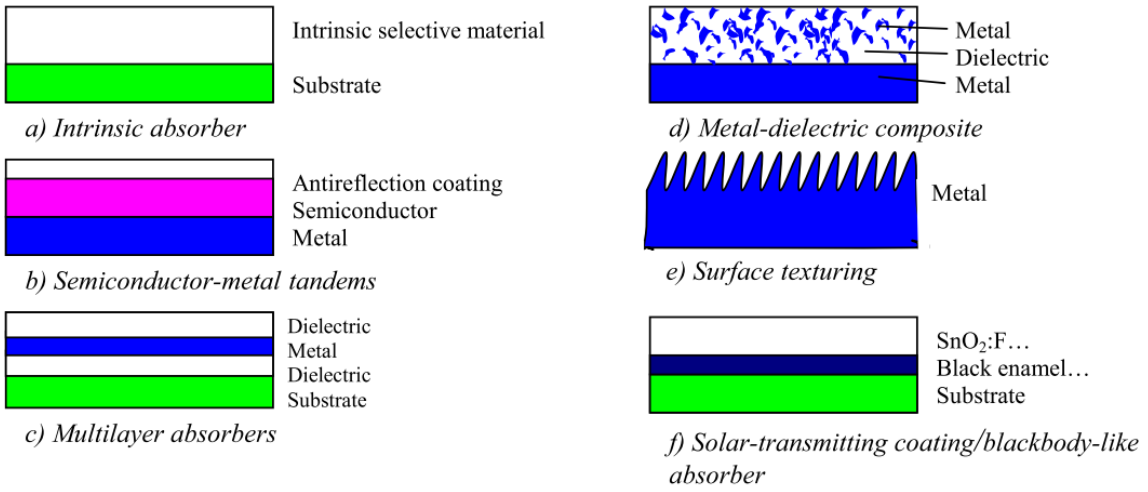


*Figure 7: Schematic designs of different solar selective absorbers[29].*

Carbon-based black paint was developed, showing thermal stability up to 1000K but without any solar selectivity[33]. Later carbon-based tandem solar absorbers were designed to achieve a solar selective absorption[34,35], owing to the metallic nature of the support. However, the last is prone to metal oxide formation leading to a degradation of the performance. Therefore, to counter the thermal stability-solar selectivity trade-off, we consider designs based on MWCNT-metal oxide hybrid materials without relying on the optical properties of the metallic substrate.

## 1.2 CHEMICAL STORAGE VIA SOLAR WATER SPLITTING

Solar water splitting technology can be broadly categorized into photovoltaic coupled with electrolyser (PV-EC) and photo-electrochemical catalysis (PEC)[36], as shown in figure 8. In the

PV-EC system, two mature technologies are coupled to produce $H_2$ fuel. An electrolyser represents a typical electrochemical cell with electrically connected electrodes where the water redox reactions occur. This system is conceptually simple, but tandem photovoltaics are required to get the desired overpotential for water splitting that increases the energy consumption. It is not cost-effective relative to $H_2$ production from fossil fuels[37]. In the PEC system, the photo-absorber material is in direct contact with the electrolyte; photovoltage formed by separation of generated electron-hole pairs drives the redox reactions. This system gives the flexibility to explore earth-abundant catalysts that can reduce the capital investment costs[38].

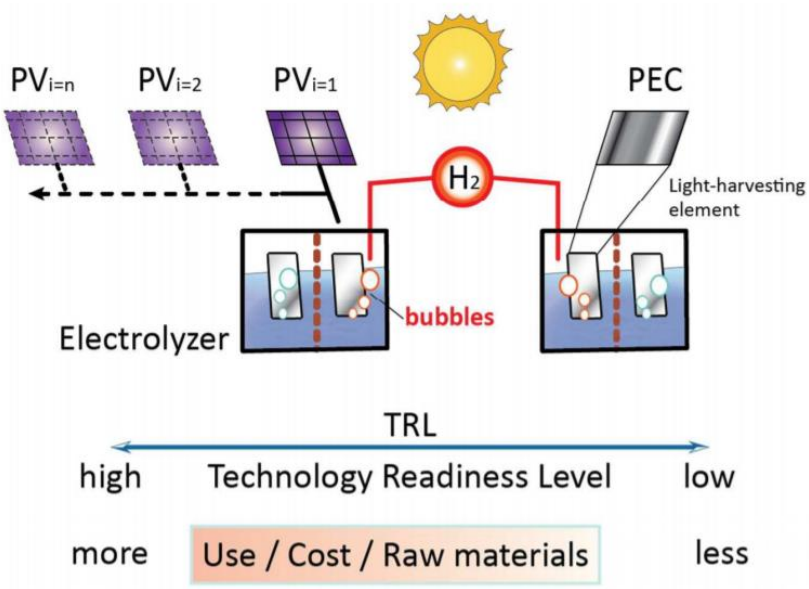


*Figure 8: Schematic representation of PEC and PV–Electrolysis system with their comparison[37].*

Clean hydrogen generation by solar-electrochemical water splitting is an appealing approach. Photo-electrochemical splitting of water utilizes semiconductors as electrode material. The redox reactions are driven by the minority charge carriers of the semiconductor when they reach the surface[39] as illustrated in figure 9. Solar absorption in n-type semiconductors excites electrons to the conduction band, leaving holes in the valence band. This phenomenon generates electron-hole pairs, which are separated by the electric field of the electrode-electrolyte interface. Thus, the holes drift towards the surface, while electrons drift towards the electron collector. In this context, oxygen evolution reaction (OER) occurs at the n-type semiconductor (anode) involving holes. In contrast, the hydrogen evolution reaction (HER) occurs at the p-type semiconductor (cathode) involving electrons. See equations 7 and 6, respectively.

$2H_2O + 2e^- \rightarrow H_2 + 2OH^-$ (HER) Eq 6

$4OH^- \rightarrow O_2 + 2H_2O + 4e^-$ (OER) Eq 7

$OH^-$ + surface site* → HO*+ $e^-$ (intermediate steps of OER)

HO*+ $OH^-$ → O*+ $H_2O$ + $e^-$

$O^* + OH^- \rightarrow HOO^* + e^-$

$HOO^* + OH^- \rightarrow$ surface site* + $O_2 + H_2O + e^-$

The $O_2$ evolution reaction involves 4 electrons along with the formation of O-O double bond. While 2 electrons are involved in the hydrogen evolution reaction. The formation energy of 110 kcal/mol is required for O-O double bond, whereas 104 kcal/mol for H-H bond formation[40]. In principle, due to sluggish kinetics in OER reaction, an overpotential beyond 1.23 $V_{RHE}$ is required for the OER, while the overpotential required for $H_2$ evolution is significantly small[41]. Hence, OER is typically considered as a rate-limiting step in the water-splitting reaction. Therefore, high-performance anode materials are in need. Following are the critical requirements that a photoelectrode should fulfil:

*Strong light absorption:* Light absorption in a material is determined by the optical bandgap. Thermodynamic water splitting equilibrium potential is at 1.23eV, but an overpotential due to kinetic losses is required. Therefore, materials with an optical bandgap of 1.9-3.5eV are suitable[42].

*Better charge carrier separation:* Photogenerated charge carriers must reach the respective electrode-electrolyte interface for a water-splitting reaction. Therefore, efficient charge separation is required. In addition, good electronic properties such as high carrier mobility and large carrier diffusional length are needed. In this context, nanostructured electrodes feature better carrier dynamics with a consequent reduction of the electron-hole recombination[43].

*Fast electrode reactions:* At the electrode-electrolyte interface, charge transfer must be fast without accumulation at the surface, or surface recombination. One of the mitigations is to attach catalyst material at the electrode surface to improve the typically sluggish kinetics [44].

*High chemical stability:* In principle, electrode material should be stable in an aqueous solution for a long duration in both dark, light conditions and under bias application. Semiconductor materials are chemically stable when the material's self-oxidation potential is more negative than water oxidation potential[45]. Other aspects such as non-toxic, highly abundant, and inexpensive, are highly relevant for electrode material.

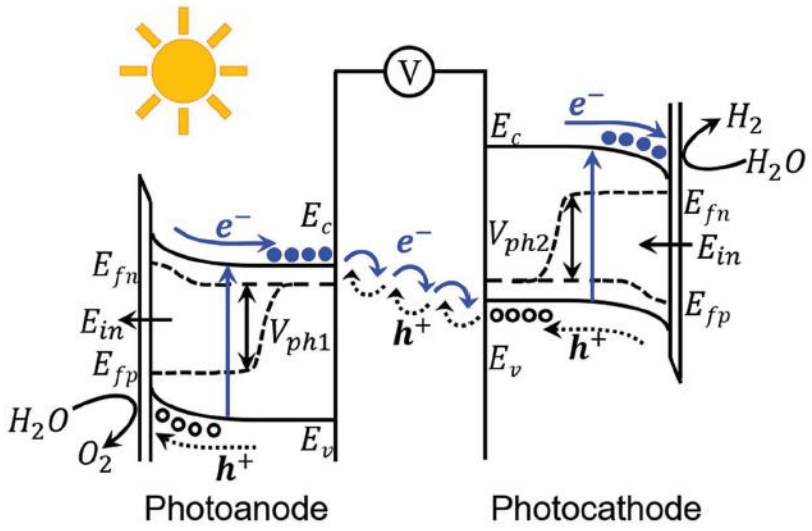


*Figure 9: Schematic illustration of a typical photoelectrochemical cell represented through band energy. Photogenerated majority carriers move to the counter electrode, while the minority carriers drift to electrode-electrolyte interface*[39].

Conventional photovoltaic semiconductors are considered promising materials because they have an appropriate bandgap for the absorption of a broad portion of the solar spectrum. However, these materials have self-oxidation potential positive to water oxidation potential, which indicates the likeliness of material oxidation before the occurrence of water splitting redox reactions, as shown in figure 10. The chemical instability promotes the degradation of solar water splitting efficiency[46].

Most metal oxides marked in the orange box of figure 10 display their self-oxidation potential more negative to the water oxidation potential value. Thus, indicating better chemical stability for metal oxides, which features additional merits such as cost-effectiveness, non-toxicity, and high abundance. In this context, $TiO_2$, ZnO, $WO_3$, $Fe_2O_3$ and $BiVO_4$ have been intensively investigated in PEC water splitting[44]. Nevertheless, metal oxides have poor electrical properties, i.e. low charge carrier mobility, short diffusion length charge carrier[39]. Therefore, reducing their thickness to match the diffusion length scale or nano-structuring is usually used to improve the performance[43]. Further improvement was reported using several approaches such as doping, forming a heterojunction with other semiconductors, and applying a co-catalyst[38].

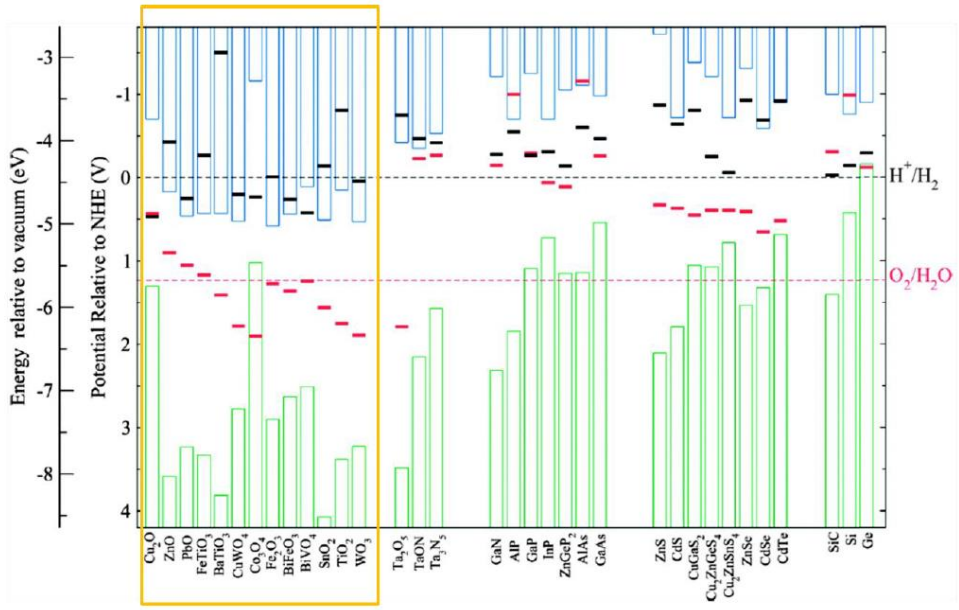


*Figure 10: Red bar indicates self-oxidation potential, black bars represents self-reduction potentials, blue and green boxes shows conduction and valence band potentials respectively for various semiconductors*[45].

CNTs have high electrical conductivity. The addition of CNTs to semiconductors has improved water splitting performance[47]. However, until now, CNT-metal oxide semiconductors are synthesized by sol-gel and hydrothermal processes, both of which are affected by the challenging CNT dispersion in aqueous media as the unmodified CNTs are hydrophobic[48]. The necessary chemical processes for the functionalization are difficult to control, and post-heat treatments are needed to crystallize films. Furthermore, the electronic structure of the CNT-oxide interface is degraded due to the chemical modification of the CNT surface, which limits the PEC water splitting performance[49,50]. Therefore, the core-shell CNT-metal oxide synthesized by the gas phase process is proposed in the present study. This architecture is expected to significantly reduce the electron-hole recombination of the photogenerated charge carriers.

## 1.3 CORE-SHELL APPROACH FOR BOTH TECHNOLOGIES

Synergetic properties of CNT-metal oxide hybrid feature potential application in various technologies such as microelectronics, batteries, sensors, catalysis [51,52,53,54]. In general, MWCNT-metal oxide hybrid fabrication is categorised into ex-situ, in-situ methods[51]. In ex-situ process, synthesized metal oxide nanoparticles are attached to the CNT surface via covalent, non-covalent or electrostatic interactions as shown in figure 11.

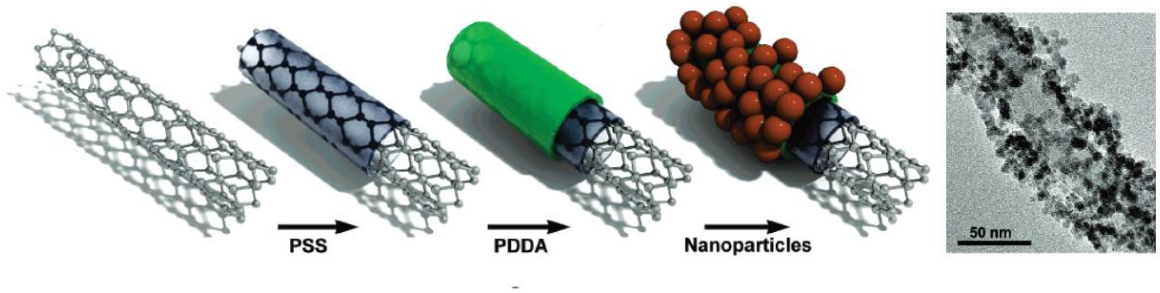


*Figure 11: Schematic illustration of $Fe_2O_3$ nanoparticles deposition on CNT via electrostatic interaction using polyelectrolytes*[55].

Pristine CNTs tend to bundle due to van der Waals forces, feature limited solubility in organic solvents and aqueous solution. Surface functionalization can improve the solubility through formation of new surface group on CNTs, which facilitates hybrid material synthesis. CNTs are functionalized by two methods:

*Non-covalent methods:* Here, functional molecules are adsorbed or wrapped around the CNTs. The delocalized π-electrons of CNTs interact generally with the conjugated compounds via the Van der Waals forces, π–π stacking interactions, hydrogen bonds or electrostatic forces[56]. In general, this process retains the original structure of the CNTs, whereas the properties are adjusted due to weak bonding.

*Covalent methods*: Here the chemical groups are attached to the CNT surface through bonding the π-conjugated skeleton of the CNT. The most common covalent functionalization involves an aggressive treatment in acid, where the carbonyl and carboxyl groups are attached to the CNT surface[57]. However, covalent functionalization comes with detrimental features like structural defects, which disrupts the delocalized electron system in the CNT, consequently degrading the electrical thermal and mechanical properties that affect the material performance[49,58].

For in-situ process, the metal oxide phase is directly grown on the CNT surface. Wet chemical techniques such as electrodeposition[59], sol-gel[53] and hydrothermal[60] are most widely used synthesis methods. In all these techniques, the CNTs surface functionalization is a mandatory sub-step. Through these methods discontinuous metal oxide structures are grown on the CNT surface, as shown in figure 12. Achieving CNT-metal oxide core-shell structures through chemical techniques is limited. Few reports concern the synthesis of a core-shell structure of CNT-$TiO_2$ with functionalization of CNT surfaces through chemical synthesis[61,62]. However, most of the time $TiO_2$ were attached as particles on CNT surface despite of functionalization[63,64,65], raising the question of core-shell synthesis reproducibility via chemical methods. The SWCNTs functionalization via acid treatment was found to alter their electronic structure and lower the electrical conductivity by 3 orders of magnitude[66]. Oxygen or hydrogen plasma treatment of pristine MWCNT has reduced the electrical conductivity from 0.125 to 0.025 Siemen/cm[67].

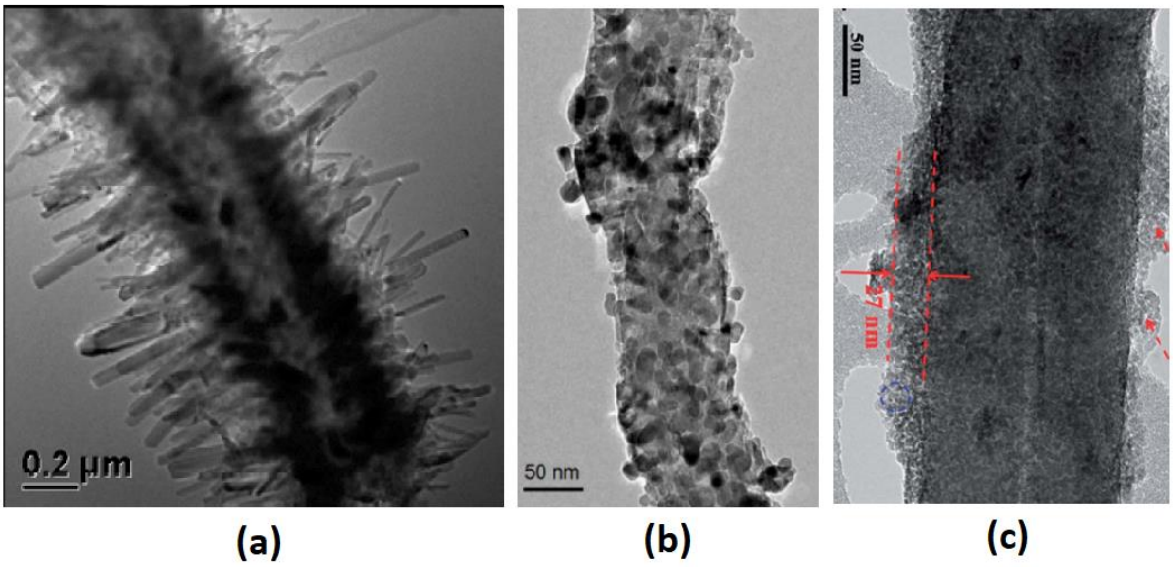


*Figure 12: TEM images of metal oxides growth on CNT through various chemical process; (a) ZnO rods deposited on CNT by hydrothermal[68], (b) $Co_3O_4$ particle on CNT via sol-gel[69], (c) $NiCo_2O_4$ porous layer on CNT via electrodeposition[70].*

Single MWCNT has a high thermal conductivity, 3000 W/m-K at room temperature, which makes them efficient a heat conductor[71]. Nevertheless, this outstanding heat conductivity reduces to 200 W/m-K for MWCNT network because of inter-tube interactions and defect scattering that reduce the phonon mean free path[72]. In general, structural defects created via surface functionalization on CNTs decrease the thermal conductivity further[73,74]. Relative to pristine CNTs, the functionalized CNTs feature both lower electrical (from 640 to 160 Siemen/cm) and thermal conductivity (from 55 to 22 W/m-K) of the CNT-epoxy composite material[75]. An optimized benefit from the electrical and thermal conductivity of CNT would require a firm contact of the individual CNT with the substrate.

The fabrication of CNT-metal oxide device on various substrates through wet chemical technique is a multistep methodology that includes the implementation of additives[76,77]. The required post-deposition treatments can adversely further affect the film-substrate interface, with consequent deterioration of performance. Furthermore, the CNTs are not individually presenting a firm contact with the substrate. Therefore, the thermal and electrical conduction along the CNTs faces several interfaces prior reaching the surface of the substrate. This makes the direct CVD growth of CNTs on the surfaces is inherently advantageous.

Surface functionalization is an inessential step in some gas-phase methods. Physical vapor deposition techniques such as sputtering[78], have been implemented to grow crystalline metal oxide on CNT surfaces. Nonetheless, core-shell structure of CNT-metal oxide is challenging, figure 13, as the sputtering technique is a line-of-sight deposition technique. therefore, the growth of metal oxides on and throughout the length of CNT is not reported so far (cross-section of sample).

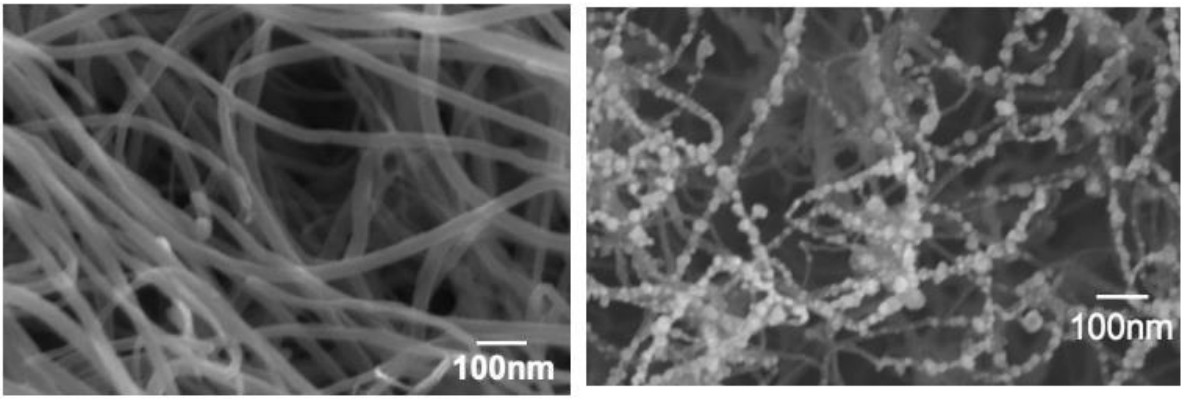


*Figure 13: SEM images of pristine CNT[78] (left) and ZnO nanoparticles deposited on CNT (right).*

Conformal core-shell structures of metal oxide on free standing CNT was reported with the pulsed laser deposition (PLD) technique[79], as shown in figure 14. Nevertheless, conformal coatings on very high aspect ratio 3D MWCNT structures is as challenging as with sputtering for the same reason. Both processes are line-of-sight.

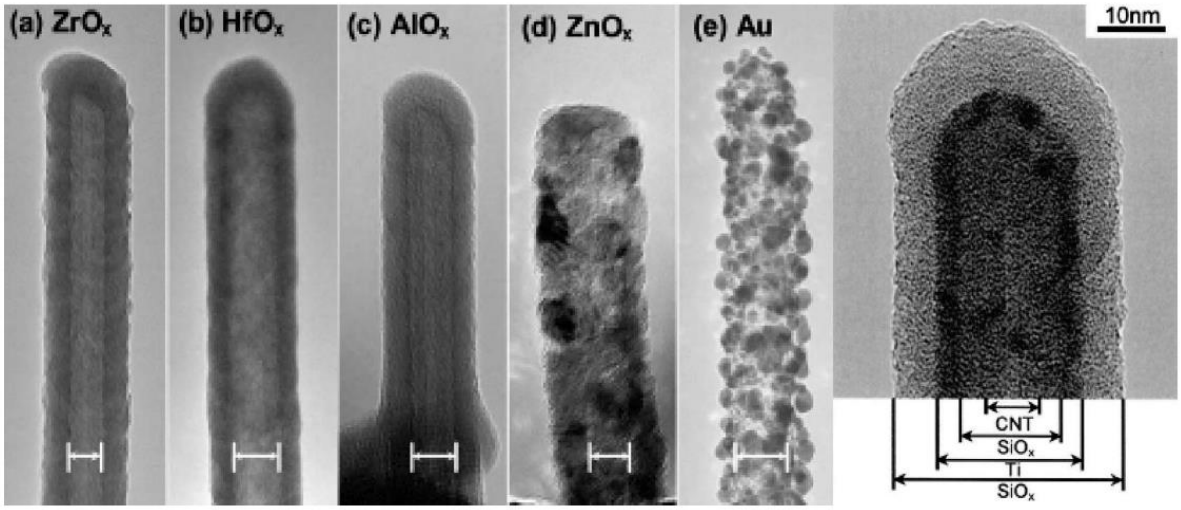


*Figure 14: TEM images of various metal oxides deposited on free standing CNT via PLD technique[79].*

Chemical vapor deposition is a non-line-of-sight process that can enable the growth of oxides on the CNT surface. However, it suffers from non-uniform growth though out the CNT length[80], as shown in figure 15. CNT-metal oxide core-shell structures are highly feasible with Atomic Layer Deposition (ALD), which is a variant of the CVD process, as shown in figure 15. ALD enables a uniform and conformal coatings with precise thickness control on geometrically complex nanostructures because of its self-limiting surface reaction steps[81].

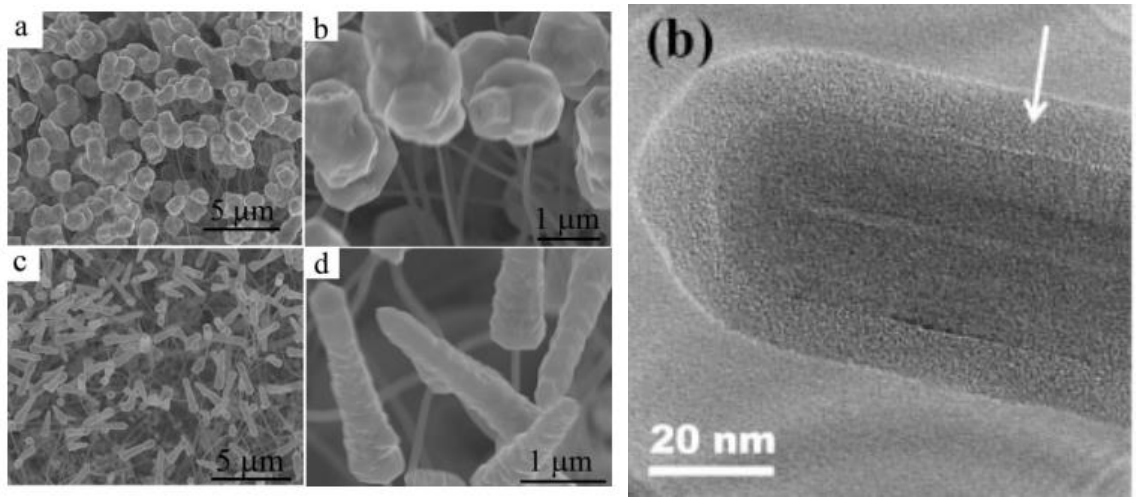


*Figure 15: SEM images of ZnO deposited on CNT via CVD process (left)[80], TEM image of conformal $TiO_2$ on CNT via ALD process (right)[82].*

In this work, we develop CNT-metal oxide hybrid materials through the CVD-ALD process. Here MWCNTs are grown on silicon substrates by CVD followed by metal oxide layer deposition by the ALD process, as illustrated in figure 16. The details of each process will be explained in the next chapter. The hybrid materials CNTs-AZO (AZO: Aluminium doped zinc oxide) and CNT-$VO_2$ oxides are proposed for selective solar absorption, while CNT-ZnO and CNT-$TiO_2$ are proposed for solar water splitting.

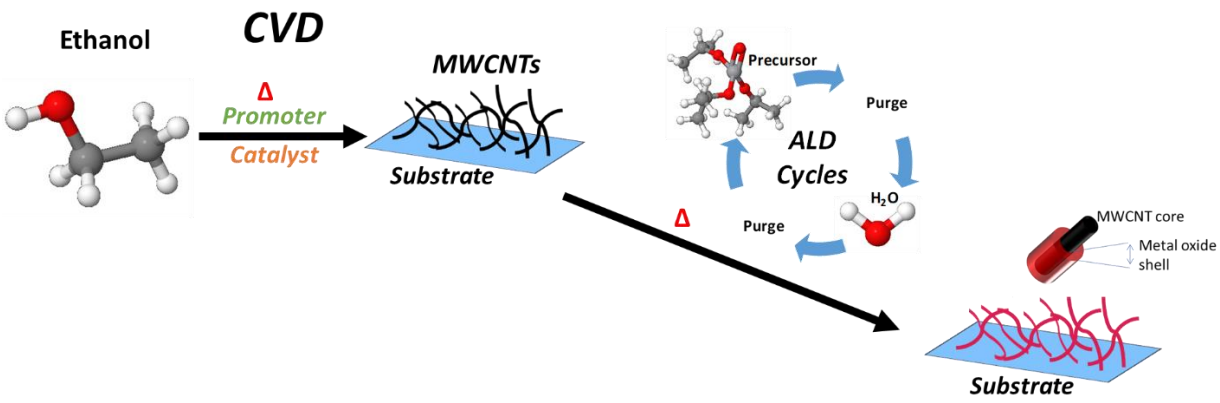


*Figure 16: Schematic representation of hybrid material synthesis by CVD-ALD process.*

### 1.3.1 Solar selective absorber

MWCNTs act like a black body absorber in our design, while degenerate metal oxide semiconductors like Al-doped ZnO or thermally-responsive $VO_2$ act as an infrared reflecting material.

#### 1.3.1.1 *Carbon nanotubes*

S.Lijima first described carbon nanotubes in 1991 as a tubular graphitic structure[83]. Carbon nanotubes (CNTs) are an allotrope of carbon that consist of hexagonal carbon sheets rolled

up in a tube-like structure. CNTs consisting of single graphene sheets are called single-walled carbon nanotubes (SWCNTs), and multi-walled carbon nanotubes (MWCNT) are formed from multilayers of graphene sheets[56], shown in figure 17. SWCNTs have a diameter in the range of 0.4-3nm, and MWCNTs can have a diameter up to 150nm with lengths up to centimetres. Single-walled carbon nanotubes are categorized into three types, i.e. armchair ($n = m$), zigzag ($m = 0$), and chiral ($n \neq m$). Chiral indices $(n, m)$ is given by the orientation of the tube axis to the hexagonal lattice as shown in figure 17.

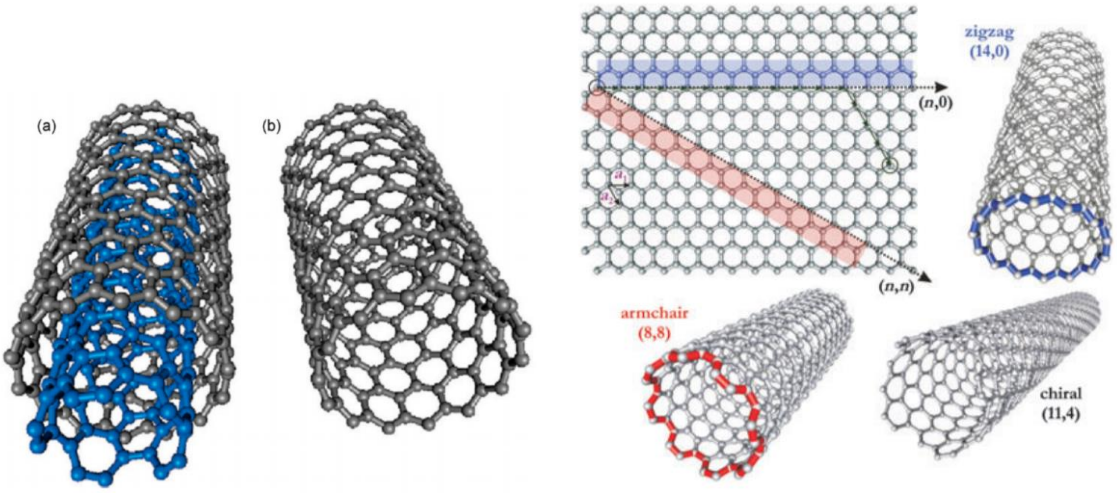


*Figure 17: Structural view of (a) MWCNTs; (b) SWCNTs, taken from reference[56](left); Various chirality's of SWCNTs[84] (right)*

SWCNTs have inter-band and π-plasmon electron transitions from infrared to UV region[85], shown in figure 18. Optical properties of SWCNT depends on the chirality. However, in MWCNTs, optical properties are insensitive to chirality; only π-plasmon electron transitions are present[86]. Optical properties such as transmittance or reflectance depend on the thickness of the MWCNTs. High visible transparency of 90% is observed for very thin MWCNTs (t=50nm) on a transparent substrate. Transparency is further reduced with an increase in MWCNT thickness (t=240nm)[87,88]. In porous vertically aligned MWCNTs with few micrometres length, low reflectance <1% with high solar absorbance is achieved[89,90,91]. Because of their high solar absorbance, MWCNTs are used in straylight space applications[92,93].

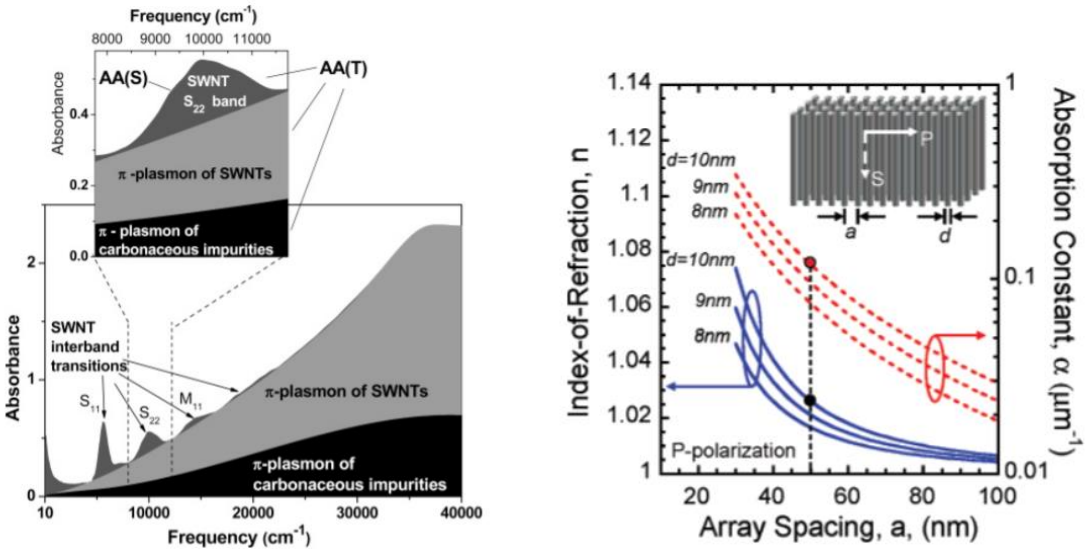


*Figure 18: Schematic illustration of the electronic spectrum of a typical SWNT sample[85] (left); index of refraction and the absorption coefficient as function of MWCNT array spacing[89] (right)*

### 1.3.1.2 ***Metal oxide semiconductors***

Vanadium has multiple oxidation states +2 to +5 and exhibits different crystal structures with different oxygen coordinations[94]. $V_2O_5$ and $VO_2$ phases are studied extensively due to their attractive properties. Outer 3d electrons of vanadium can be localized or in a free state, depending on the electron-electron correlation strength and electron-lattice interactions[95]. Along with layered crystal structure, exciting chemical, physical properties with numerous applications are reported[96].

$VO_2$ phase is of particular interest for our application because of its semiconductor–metal transition near room temperature[97]. This material behaves as a semiconductor at room temperature with a monoclinic crystal structure, while it shows metallic characteristics with a change in crystal structure to tetragonal phase above 67°C. If the phase transition mechanism is due to structural change (Peierls-type) or (Mott-Hubbard type) is not clear. Electrical and optical properties change abruptly at the transition point, as shown in figure 19. $VO_2$ has shown wide application as electrical switches, oscillators, thermal sensors, optical switches, metamaterials, and smart windows[98,99,100].

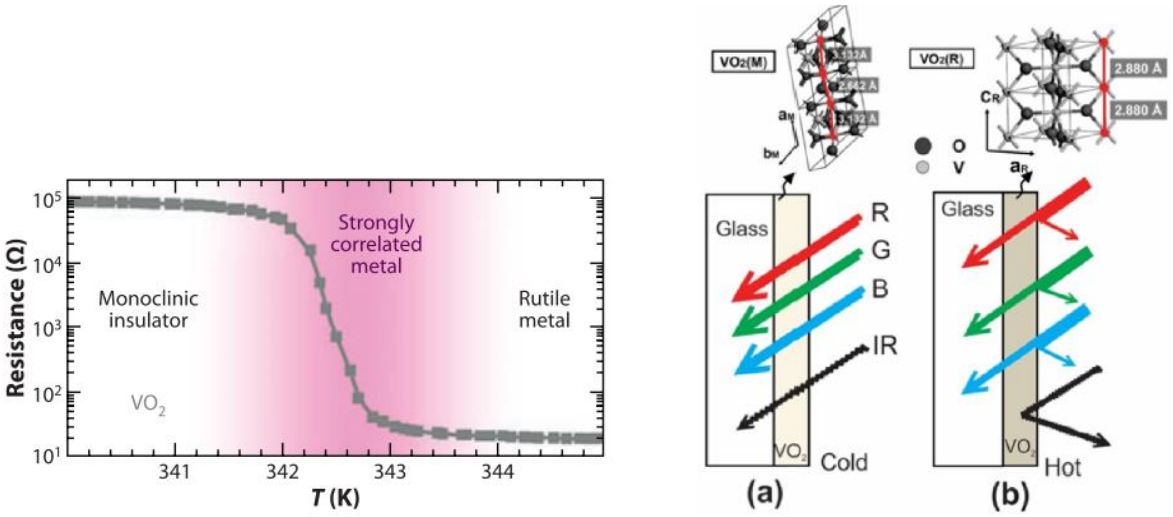


*Figure 19: Electrical resistance as function of temperature[100] (left); (right)-Optical property of $VO_2$ in cold (a), hot state[98] (b)*

ZnO is an n-type semiconductor with a direct bandgap of 3.37eV. The reason behind the intrinsic n-type conductivity is not apparent, yet some studies have pointed it to native defects such as oxygen vacancies and Zn interstitials formed during the synthesis[101]. Later, it is attributed to inevitable hydrogen incorporation into the film during the synthesis[102,103]. High visible transparency combined with a tuneable electrical conductivity enables its use in a wide range of applications, e.g. thin-film transistors (TFTs), buffer layers of solar cells, light-emitting diodes, photodetectors, piezoelectric devices, chemicals, or gases sensors[104,105].

Extrinsic doping with $Al_2O_3$ enhances the conductivity by electron donation from the associated substitutional occupation[106], as shown in below equation.

$$Al_2O_3 \xrightarrow{2ZnO} 2Al_{Zn} + 2O_O^X + 2e^- + \frac{1}{2}O_2 \uparrow$$

With the doping-induced increase in the charge carrier concentration the plasmon frequency shifts to high frequency range (shorter wavelength)[107]. Thus, AZO displays an increased optical reflectance in the infrared region. Furthermore, the bandgap of ZnO increases with Al doping because of an increase in the Fermi level above the original conduction band minimum, also known as the Burstein-Moss shift. Based on these properties, AZO is reported as a promising material for low emittance coatings in the glazing industry[108], as transparent conductors[109].

## 1.3.2 Solar water splitting

MWCNTs act like an electron transport layer in our design, while metal oxide semiconductors like $TiO_2$ or ZnO as photocatalyst materials.

### 1.3.2.1 *Carbon nanotubes*

Electrical conductivity in SWCNTs is determined based on their chiral vector – Metallic: for $[n - m = 3q\ (q = 0,1,2,3 \dots)]$; Semiconductor: for $[n - m = 3q \pm 1\ (q = 0,1,2,3 \dots)]$[110]. SWCNTs have unique electrical properties because of the graphite structure (Sp2) and quantum confinement effect associated with their 1D character and small size. MWCNT consists of several layers of SWCNT with different chirality's, and interaction between the

inner shells complicate the interpretation of conductivity[111]. Four-probe electrical resistivity measurement on MWCNTs with various diameters have demonstrated unique conductivities with both metallic and non-metallic characteristics[112,113]. Individual MWCNT has shown high thermal conductivity of 3000 W/m-K at room temperature and can conduct heat efficiently[71]. While the MWCNT films have reported low thermal conductivity of 200 W/m-K at room temperature due to intertube interactions, defect scattering can reduce phonon mean free path[72]. MWCNTs have ballistic electron conduction, which facilitates the highest current density of $10^9$ A/cm$^2$ relative to copper wire ( $10^6$ A/cm$^2$)[114,115]. Besides, 3D MWCNT porous structures feature enormous surface area, which facilitates applications in supercapacitors[116], ion-battery[117], electrocatalyst[118] and sensors[119] field. CVD grow MWCNTs act as an electron transport network, and the inherent porous structure increases the electrode-electrolyte interface area.

### 1.3.2.2 *Metal-oxide semiconductor*

ZnO nanoparticles are extensively studied for organic pollutants photocatalytic degradation. ZnO features high abundance with nontoxic character[120]. Besides, ZnO nanoparticle facilitates antibacterial activity[121]. ZnO nanostructures feature a favourable band alignment with a more negative conduction band (-0.15 $V_{RHE}$) relative to water reduction potential (0 $V_{RHE}$) and a more positive valence band (3.05 $V_{RHE}$) relative to water oxidation potential (1.23 $V_{RHE}$)[122].

Anatase $TiO_2$ is widely studied due to its interesting properties. $TiO_2$ is nontoxic, biocompatible, has a high dielectric constant, and chemical stability[123]. It is a semiconductor with a bandgap ranging from 3.0 to 3.2 eV. Intrinsic n-type conductivity in $TiO_2$ is attributed to native defects such as oxygen vacancies, titanium interstitials[124]. $TiO_2$ nanomaterials have shown potential applications as anode material in supercapacitors[125], Li-ion batteries[126], photocatalysts[127]. $TiO_2$ has suitable positioning of the conduction and valence band energies to drive Hydrogen evolution (HER) and oxygen evolution reactions (OER)[128].

Nevertheless, ZnO, $TiO_2$ nanostructures suffers from poor electrical conductivity, attachment of CNTs improves the transfer of electrons to the counter electrode as shown in figure 20.

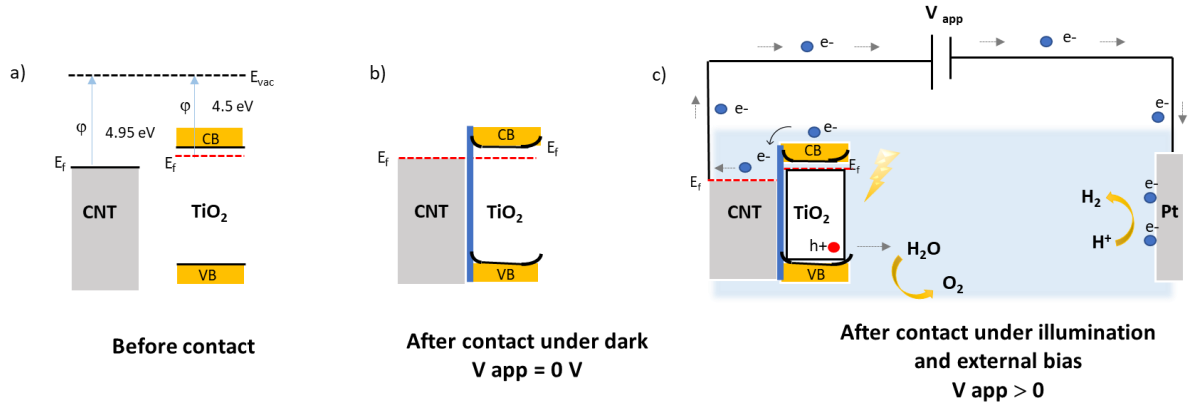


*Figure 20: Illustrative band diagram of MWCNT-$TiO_2$ before (a); after contact at dark equilibrium conditions (b); and under illumination with an external bias (c).*

# 2 EXPERIMENTAL PART

## 2.1 Material Synthesis

### 2.1.1 Chemical Vapor Deposition

#### 2.1.1.1 Fundamentals

*Chemical vapour deposition* is a gas-phase synthesis used to deposit thin films by chemical reactions. CVD is a versatile technique, extensive usage in semiconductor and optoelectronics industries, because of excellent repeatability, controllability, high quality, and cost-effective depositions[129]. Chemical vapour deposition enables the deposition of solid thin films due to the chemical reaction of vapour phase reactant molecules (precursor) with the surface of the substrate. In general, these chemical reactions are initiated by external stimuli such as heat (Thermal-CVD), electromagnetic radiation (Photo-CVD) or plasma (Plasma enhanced-CVD).

In Photo-CVD process, chemical reactions are directly or indirectly driven by light energy. Conventional light sources are arc lamp, $CO_2$ laser, excimer laser, and Nd-YAG laser. Film growth can occur in both atmosphere and low-pressure conditions. In the indirect process, substrate is heated by light absorption, and precursor decomposition on the heated substrate leads to heterogenous chemical reaction. Selective depositions by localised substrate heating can occur through this process[130]. In the direct process, light interaction with precursor promote formation of intermediate radical, which react in the gas phase to produce the final products that diffuse to substrate[131]. Low-temperature depositions are possible from the direct light interaction process. The slow deposition rate is the major limitation for the Photo-CVD process.

In plasma enhanced CVD process, chemical reactions are induced by the electron energy. Application of high-frequency electric field to gaseous species promote plasma formation, consisting of electrons, ions, and electronically excited species. Precursor molecule dissociates into radical species upon impact with the high energy electrons, which induce heterogenous chemical reactions at the substrate. Microwave at 2.4 GHz and radio frequency at 13.5 MHz are most used plasma sources. The temperature of the energetic electrons is equivalent to thousands of kelvins. Thus, films with a high growth rate are formed at low temperatures compared to other CVD variants. Secondary or high vacuum are an essential condition for the film deposition. Nevertheless, contaminated films and ion-bombardment induced substrate deteriorations are major limitations of the PECVD process[132].

Thermally activated CVD, referred as conventional CVD process, is extensively used for deposition of diverse materials. Chemical reactions are initiated by thermal energy in the form of resistance heating or Rf heating. Thermal CVD is limited by substrate material because of the requirement of high temperatures for film deposition. However, with the usage of metal-organic precursors, deposition temperatures are reduced[133]. The film deposition can occur in all three pressure conditions, i.e., atmospheric, secondary vacuum and high vacuum.

In the conventional CVD process, the gas-phase precursor chemically reacts at the heated substrate. The general sequence of events that occur during the CVD process is described in

figure 21. Primarily, gas reactants (blue circles) are transferred into the reactor (step a). The inertial force exerted by substrate on the gas stream yield boundary layer, where the velocity of the gas stream reduces gradually, reaches zero at the substrate. Similar gradient of temperature and concentration is observed in the boundary, which influences the growth kinetics[134]. Gas reactant diffuses through the boundary layer (step b) and is adsorbed onto the substrate (step c). However, there is the possibility of a homogeneous gas-phase reaction (step d) which produces intermediate reactants (green circles) that are absorbed onto the substrate and which the reaction generates by-products (red circles). Adsorbed molecules undergo surface diffusion to form nucleation sites, and subsequent heterogeneous reactions (step e) lead to the nuclei growth to form a film. Lastly, formed by-products and unreacted molecules are desorbed from the substrate and extracted out of the reactor as exhausts (step f)[135].

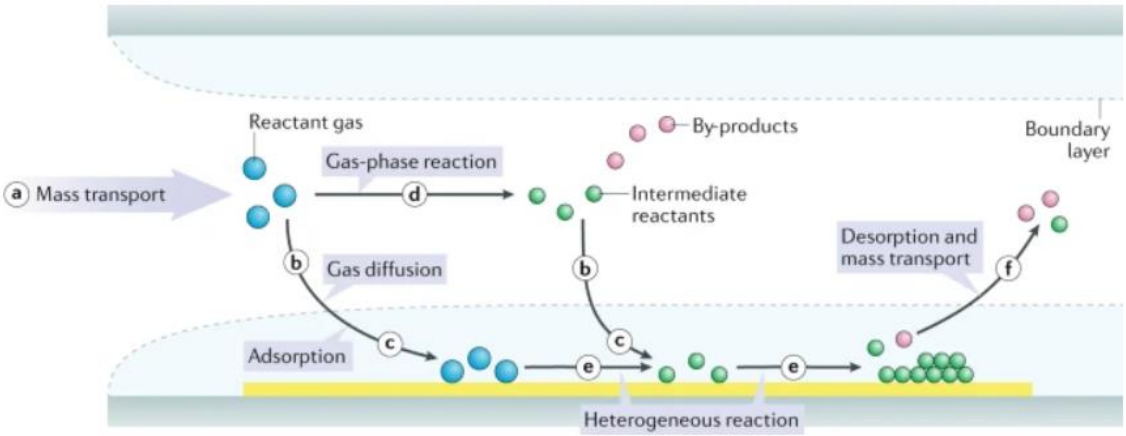


*Figure 21: Schematic of basic steps of a typical CVD process*[135].

Following events might be rate-limiting in the CVD process: Precursor feed rate into the reactor, diffusion of precursor through the boundary layer, and surface reaction rate. Process parameters like temperature and pressure indirectly control these events[136,137].

For instance, at low temperature, the surface reaction kinetics is slow, which follows the Arrhenius equation given in equation 8, as shown in figure 22

$$growth\ rate \propto e^{-\frac{E_a}{RT}} \qquad \text{Eq 8}$$

$E_a$is the activation energy, *R* is the universal gas constant, and *T* is the temperature. So, at low-temperature surface kinetics becomes rate-limiting process. At elevated temperatures, growth rate is reduced due to desorption of the precursors from the deposited surface or its depletion due to parasitic gas-phase reactions. Last lead to formation of unwanted deposition on reactor walls or to particles formation.

At intermediate temperatures, the growth kinetics no longer follows the Arrhenius equation and the weak temperature-dependence growth results from a diffusion-limitation, given in equation 9.

$$growth\ rate\ \propto \frac{D_i\, C_r}{\delta} \sim u^{\frac{1}{2}}\, T^{\frac{3}{2}} \left(\frac{p_r}{P}\right) \qquad \text{Eq 9}$$

$D_i$ is the diffusion coefficient, proportional to the temperature (T) and inversely proportional to the total pressure of the reactor (P). δ is the boundary layer thickness, proportional to u the reactant velocity. $C_r$ is concentration of the reactant, proportional to the partial pressure of the reactant ($p_r$)[138].

The mass transport rate is enhanced by decrease in the total pressure. Boundary layer thickness is reduced with increase in the gas velocity in the bulk, leading to more rapid growth rates. Surface reactions are rate-limiting step in the low-pressure process[139]. However, low-pressure reduces reactant gas partial pressure, which lowers the growth rate because the reaction kinetics depends on the reactant partial pressure[136]. To achieve high growth rate at low pressure process, reactant partial pressure needs to be high, as given in equation 9. However, boundary layer conditions need to be controlled because of viscous gas flow, leading to non-uniform film growth.

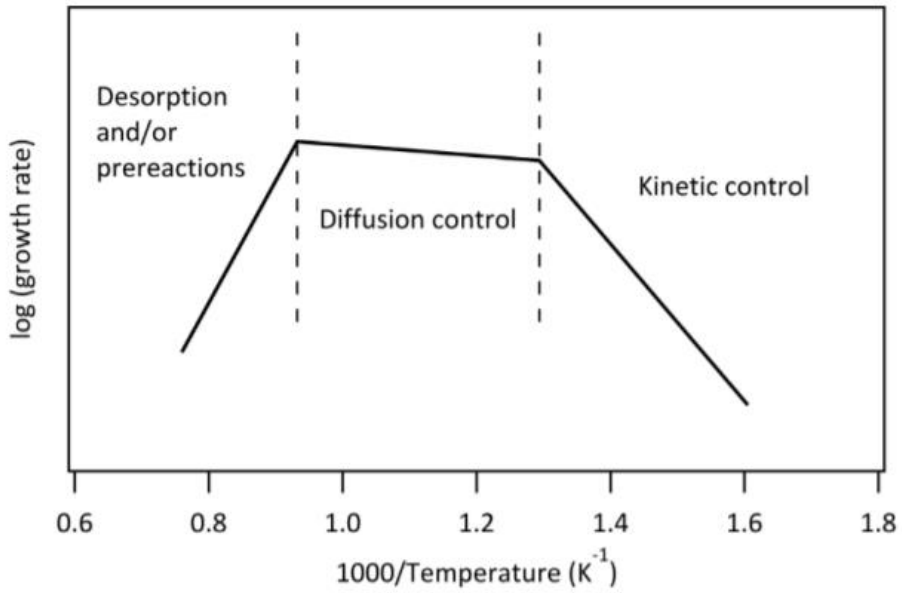


*Figure 22: Plot of the growth rate as a function of growth temperature[137].*

Thin film growth is indicated as successive process that consists of nucleation, coalescence, and thickness. Three modes of growth mechanism can occur in the CVD process[138], as shown in figure 23.

Volmer-Weber mode: Here, adsorbed atom nuclei coalescence into 3D clusters or islands on the substrate. This occurs when the interaction strength between the adsorbed atoms is greater than the interaction between the adsorbed atom and substrate.

Frank–Van Der Merwe Mode: Here, adsorbed atom nuclei coalescence into a homogenous layer on the substrate. This occurs when the interaction strength between the adsorbed atom and substrate surface is strong.

Stransky-Krastanov: It is referred as a mixed-mode, involving both 3D-island and homogenous 2D-layer mechanism. The substrate is initially covered with homogenous 2D-layers grown in Frank–van der Merwe mode, followed with 3D-islands on the surface in the Volmer–Weber growth mode.

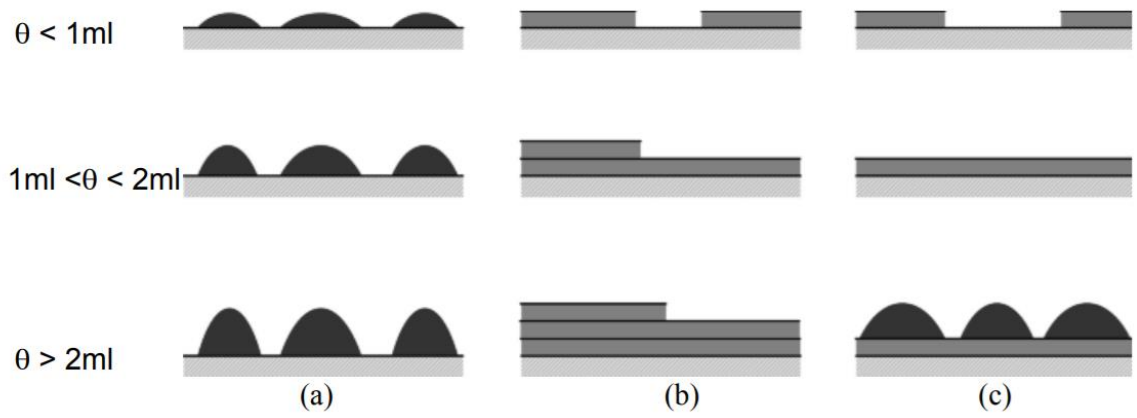


*Figure 23: Three types of growth mode (θ= coverage, ml: monolayer): (a) Volmer-Weber mode, (b) Frank-Van Der Merwe mode and (c) Stransky-Krastanov*[138].

In a CVD process, the operation parameters influence the nucleation and growth modes, which further impact the microstructure and properties of the deposited film[140]. Supersaturation in the CVD reaction system leads to nucleation. Supersaturation is defined as ratio of partial pressure of reactant species in the gaseous phase deviated from equilibrium state to partial pressure of reactant species in the equilibrium state[141]. Blocher established morphological dependence on supersaturation and temperature[142], as shown in figure 24. In general, three types of microstructures can be obtained: Epitaxial single crystal, polycrystalline, and amorphous[137]. Epitaxial growth occurs when lattice parameters of the substrate and the film is matched. For epitaxial growth, high temperature with low saturation promotes surface diffusion of adsorbed precursor to nucleating[132]. The whisker/nanotubes structure is formed with the aid of catalysts at high temperatures and low super saturation conditions. Nucleation occurs at specific sites such as the terrace, ledge and kink on the substrate surface. The polycrystalline film is obtained at intermediate temperature and growth rate. The morphology of crystalline film is formed into columnar and or equiaxed grains. Low temperature, high supersaturation induces the formation of equiaxed grain[136]. In contrast, high temperature favours the columnar grain growth with increases in grain size. Amorphous growth is favoured at low temperatures with a high growth rate. Here the surface diffusion is low relative to adsorbed precursor molecules. At sufficiently high supersaturation with the very low temperature, gas phase molecular collision is enhanced, leading to homogeneous nucleation and growth of powder.

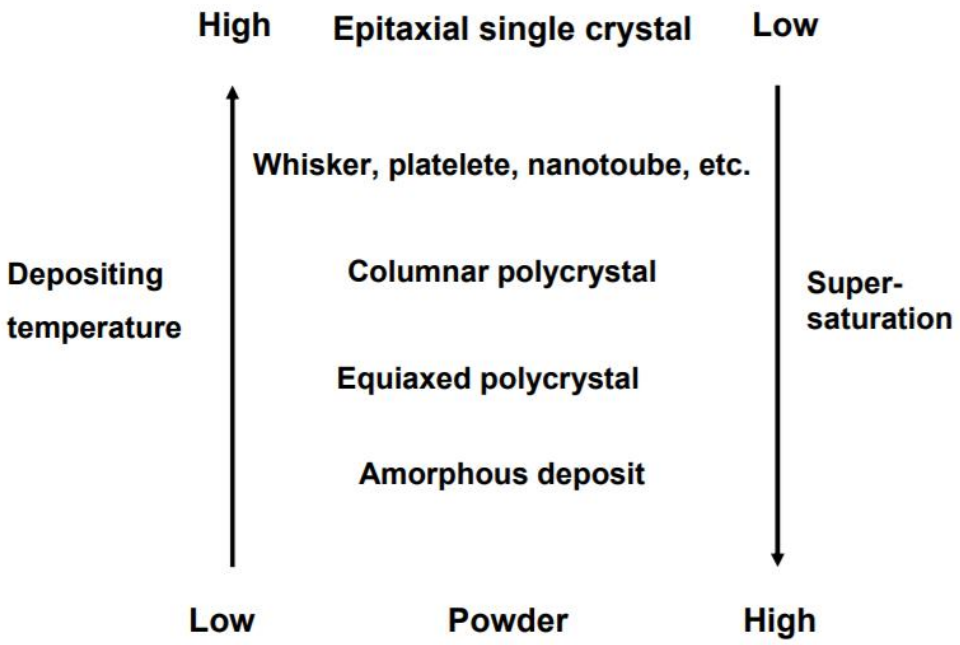


*Figure 24: impact of supersaturation and temperature on the microstructure of CVD films*[142].

#### 2.1.1.2 *Chemical Vapor Deposition of CNT*

Carbon allotropes can be grown on a solid surface by the CVD process through pyrolytic decomposition of hydrocarbons [143]. The synthesis of CNTs is possible from the CVD process through thermal decomposition of hydrocarbons on transition metal catalysts where the nucleation of the CNTs occurs. Metal-catalyst is categorized into two types: supported and unsupported (floating) catalyst.

In the supported catalyst, the metal particles are deposited on the substrate before the hydrocarbon vapor introduction. According to the Young-Laplace relation, for metal particle formation on any substrate, the substrate's surface energy $\gamma_s$ should be smaller than the surface energy of the metal $\gamma_m$. In general, metals have higher surface energy than their oxide counterpart. Hence, we observe de-wetting behaviour leading to the formation of metal particle clusters during the heat treatment process[144]. It was observed that the diameter of CNTs depends on the metal particle morphology[145] and size[146]. However, graphitization was not possible on large metal clusters[147].

In the floating catalyst method, the catalyst is introduced along with the carbon source feedstock. This method avoids the separate heat treatment process required in the supported catalyst approach, promoting a large scale yield of CNT[148].

A growth mechanism of CNT was first proposed by Baker et al., in 1972, based on the hydrocarbon vapor – metal-carbon liquid – crystalline carbon solid (VLS) process[149]. Here carbon source decomposes at the surface of the molten catalyst nanoparticle. Carbon is therefore dissolved in the nanoparticles to form metal carbide. The continuous supply of

carbon beyond the solubility limit promotes the precipitation of tubular carbon structures. Depending on the interaction strength between the catalyst and the substrate, two growth modes can prevail, i.e. catalyst at the tip (weak adherence) and catalyst at the bottom (Strong adherence)[150], as shown in figure 25.

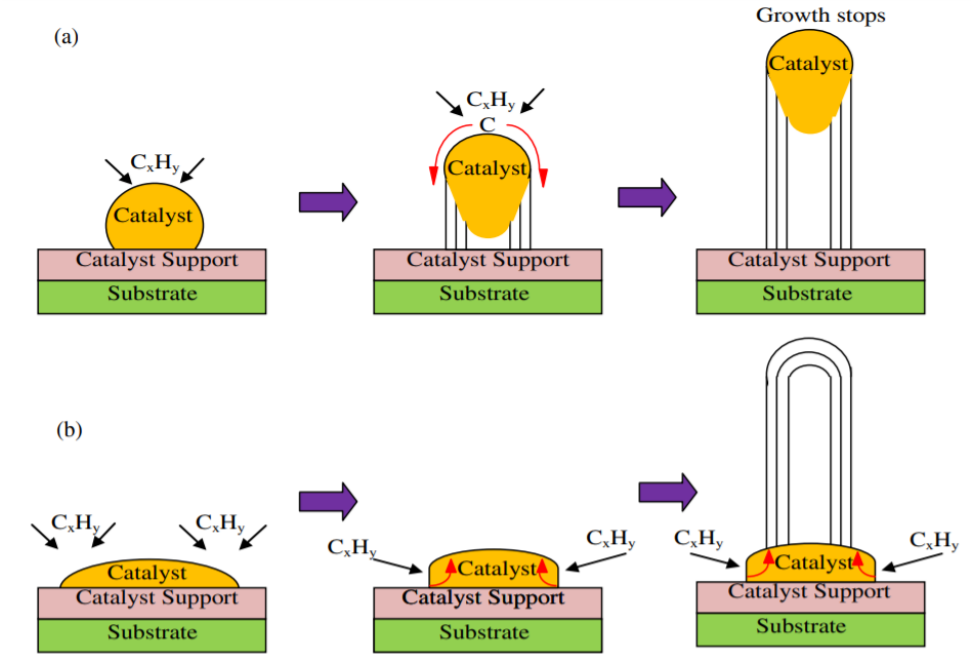


*Figure 25: Schematic of CNT growth mechanism. (a )Tip-growth model and (b) base-growth model*[151].

The catalytic decomposition of hydrocarbons into CNT has also been reported on thermally stable metal-oxide nanoparticles such as alumina[152], zirconia[153]. The VLS growth mechanism accepted for metal catalyst CNT synthesis is not valid for oxide metal free catalysts since carbon dissolution is unlikely. In the vapor-solid-solid growth mechanism, catalyst is in solid phase during the process[154]. It is believed that nanoscale surface protrusions act as nucleating sites for the CNT growth by surface diffusion[155,152,156]. In this scenario, the role of catalyst particles is to provide an active interface where carbon rearrangement can occur. Magrez et al. have proposed a CNT growth mechanism on a non-metallic support surface based on the active Bronsted basic-Lewis acidic sites, where an electron transfer between the support surface and hydrocarbon adsorbate takes place. At Bronsted basic (electron donor) sites, negatively charged carbanion radical condensate are formed and stabilised by the disintegration of attached alkyl groups. The dehydrogenation process promotes the formation of aromatic compounds. Further addition of hydrocarbon leads to a polyaromatic hydrocarbon which can quickly diffuse towards the nanoparticle to integrate into CNT structure, as shown in figure 26. However, at the Lewis primary site (electron acceptor), CNT growth is hindered due to the formation of large complex fragments with a low degree of aromatization[157].

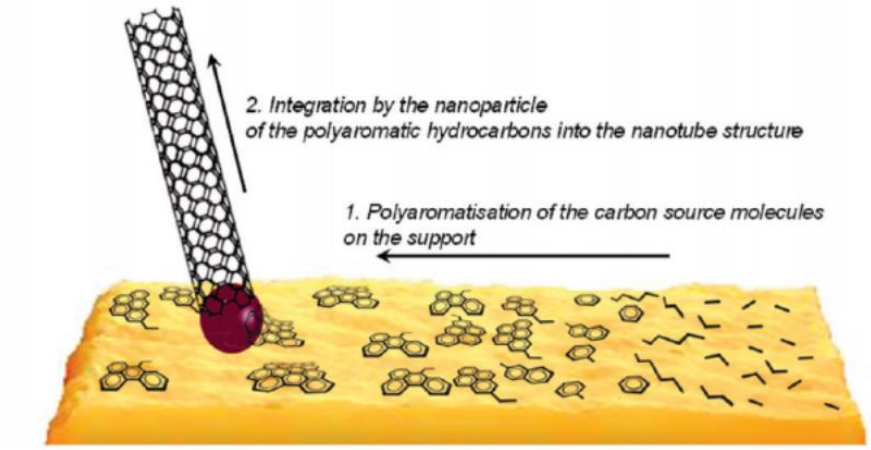


*Figure 26: Scheme describing the growth mechanism of CNTs by CVD based on a two-step process*[157].

**Process used in thesis:** Here, we introduce cobalt acetylacetonate $Co(acac)_2$, magnesium acetylacetonate $Mg(acac)_2$, ethanol mixture as a single feedstock for CNT synthesis, shown in figure 27. $Mg(acac)_2$ is thermally decomposed into MgO particles, and ethanol reduces $Co(acac)_2$ into metallic cobalt catalyst as shown in the below equation. A combination of Co-MgO (catalyst-support) and OH radicals formed upon thermal decomposition ethanol promote the randomly oriented CNT growth. Details of the process are described in the published paper[158].

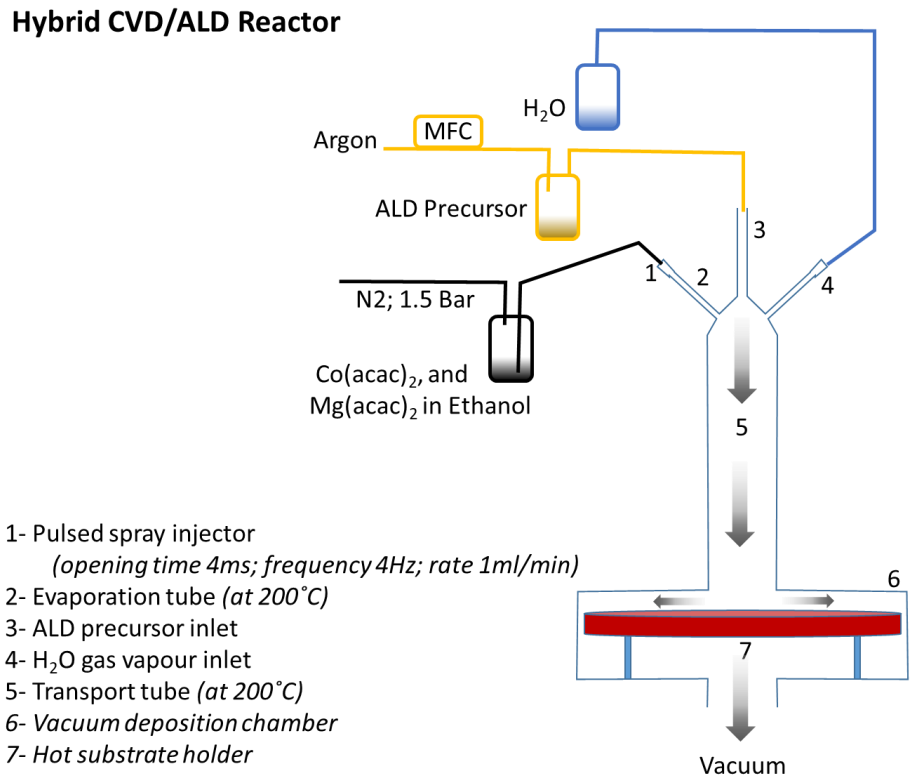


*Figure 27: Schematic of hybrid CVD-ALD reactor used for deposition of MWCNT-metal oxide nanocomposite.*

$$Mg(acac)_2 + Surface \xrightarrow{\Delta} Surface - MgO + volatile\ organics$$

$$Co(acac)_2 + C_2H_5OH + Surface \xrightarrow{\Delta} Surface - Co + CH_3CHO + volatile\ organics$$

$$C_2H_5OH + Surface \xrightarrow{\Delta/Co\ catalyst/MgO\ promoter} Surface - CNT + volatile\ organics$$

## 2.1.2 Atomic layer deposition

### 2.1.2.1 *Fundamentals*

Atomic layer deposition (ALD) is a variant of the CVD process, well established owing to its high conformal depositions on complex substrates and a variety of materials. ALD emerges as an essential processing technique for microelectronics with reduced dimensions[159]. The ALD process is defined as a sequential implementation of self-terminating gas-solid reactions. In principle, it is regarded as a cyclic process because of two self-terminating reactions, as shown in figure 28. In the first half cycle, the self-limiting reaction of the precursor takes place, and the formed by-products and unreacted reactants are evacuated during the purge phase. This is followed by a second self-limiting reaction with the co-reactant and a purge phase. The whole sequence is considered as one ALD cycle, and the thickness of the film is precisely controlled by adjusting the number of applied ALD cycles. As both half-reactions are self-terminating, the surface saturation occurs when all accessible reaction sites have reacted with the reactant molecules[160]. As a result, the film growth is independent of the transport conditions in the deposition reactor. Therefore, ALD is highly suited for complex 3D substrates because of their accurate control of thickness.

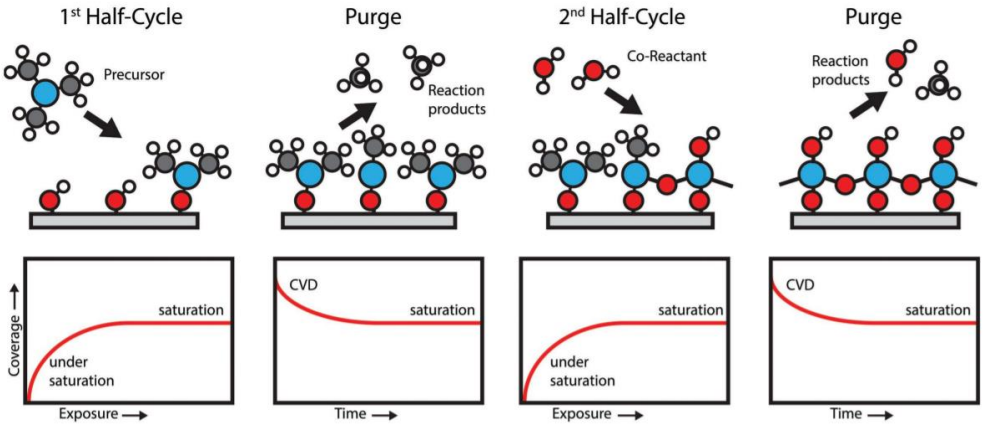


*Figure 28: Schematic of an ALD process cycle, consisting of two half reactions[160].*

The precursor molecule adsorption aspect on the substrate surface describes the adsorption kinetics in the ALD process. Adsorption phenomenon is classified into Physisorption (physical adsorption) and Chemisorption (chemical adsorption)[161]. In physisorption, intermolecular forces, such as van der Waals attraction or hydrogen bonding exists between the precursor molecule and the substrate surface, resulting in multilayer adsorption. While a chemical bond is formed between the precursor and the substrate in the chemisorption process, resulting in monolayer adsorption. Physisorption is a reversible process, while chemisorption may be

reversible or irreversible. Adsorption kinetics can be understood from coverage (Q) of the adsorbent sites as a function of time[162], given by below equation.

$$Q = Q_{eq}(1 - e^{-(K_a p + K_d)t})$$

$K_a$ is adsorption rate constant, $K_d$ is desorption rate constant, p is the partial pressure of reactant, $Q_{eq}$ is the equilibrium coverage, and t is the time. For self-terminating reaction, adsorption should feature irreversible chemisorption characteristics ($K_d$ =0 and $Q_{eq}$ =1). Self-termination saturation is achieved faster with the high partial pressure (p) and adsorption rate constant ($K_a$)[163].

Following chemisorption, mechanisms feature as the main event for self-termination reactions: Ligand exchange, dissociation, association, and oxidation[164,165,163].

**Ligand exchange:** In this mechanism, precursor ligands are removed as volatile products through ligand swapping with the surface group. Basically, exchange mechanism is understood from Bronsted-Lowry (BL) acid-base reactions. Metal organic precursor ligands act as BL basic, and proton abstraction from hydroxyl surface group acts as BL acidic[164]. The best example for this mechanism is the chemisorption of trimethyl aluminium (TMA) onto the hydroxy-terminated surface releases methane as by-product[166], as shown in figure 29.

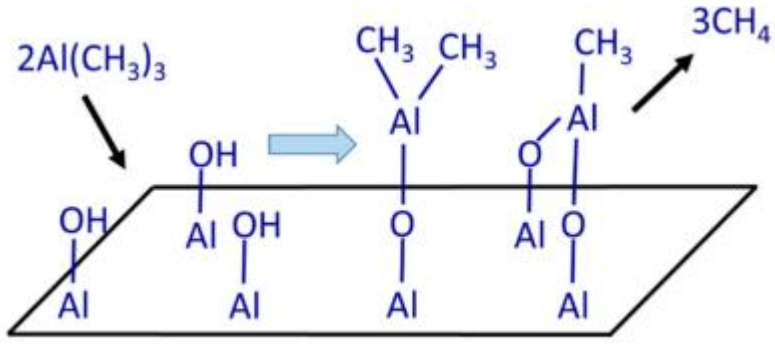


*Figure 29: Illustration of ligand exchange of TMA by proton transfer from hydroxyl surface[166].*

**Dissociative:** In this mechanism, the precursor disintegrates at the substrate or in the gas phase, and all the fragments are chemisorbed on the surface. Classic example is the dissociation of trimethyl aluminium (TMA) precursor on the siloxane bridge, as shown in figure 30. Here Si-O bond is replaced with the Si-C bond from one of the $CH_3$ ligands of $Al(CH_3)_3$. Both the ligand and the precursor are chemisorbed[167]. Dissociative mechanisms are often observed on high surface energy substrates like metals like platinum and ruthenium.

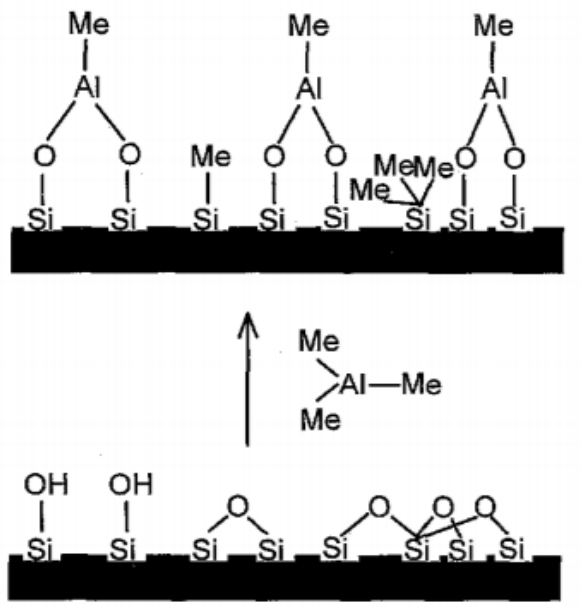


*Figure 30:Illustration of dissociative mechanism of trimethyl aluminium on Siloxane[167].*

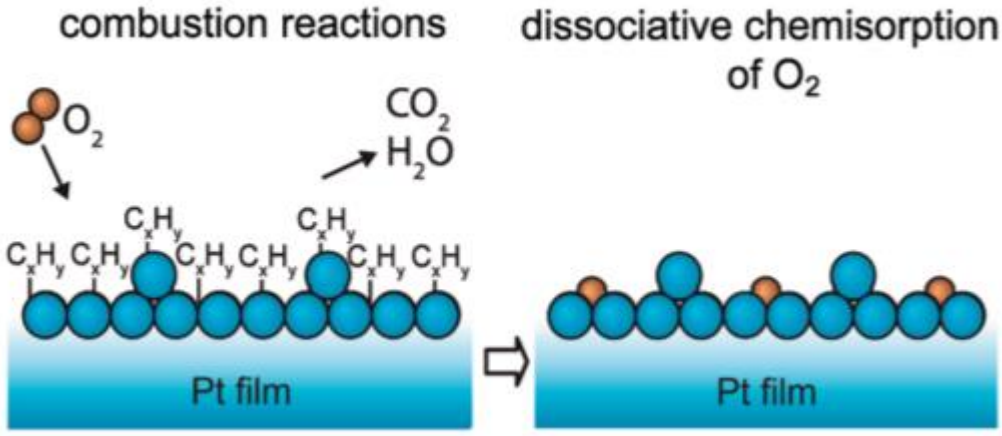


**Associative:** This mechanism is considered as the first step for ligand exchange chemisorption. Here a bond is created between precursor and substrate without breaking their bonds. Bond formation is illustrated as interaction with lone pair of electrons on a Lewis base and an empty orbital of a Lewis acidic species[164]. For example, $Al(CH_3)_3$ has empty Al 3p orbital which is accepts additional electrons. For 3p orbital association, the monomeric TMA is needed, dimer TMA dissociates into monomer at 100-165˚C[168]. Simulations have shown strong interaction with 3p orbital lone pair of electrons and Lewis basic surface hydroxyl or bridged oxygen group[169]. Associated mechanism is followed with ligand exchange process to ensure the chemisorption.

**Oxidation:** In this mechanism, organic ligands are removed from the combustion process through interaction with strong oxidizers such as $O_2$, $O_3$, and $O_2$ plasma. For example, noble metal-organic ligands are removed by combustion phenomena via dissociative chemisorption of $O_2$ into O* (chemisorbed O)[170,171], as shown in figure 31.

*Figure 31: Schematic of organic ligand removal during combustion via dissociative chemisorbed oxygen[170].*

**Saturation:** the surface coverage at saturation depends on the steric hindrance of the ligands and the density of reactive surface sites. Bulky ligands of the precursor shield part of the surface from reacting with precursor molecules and results in a low coverage as shown in figure 32. Because of steric hindrance, growth per cycle is always less than one monolayer.

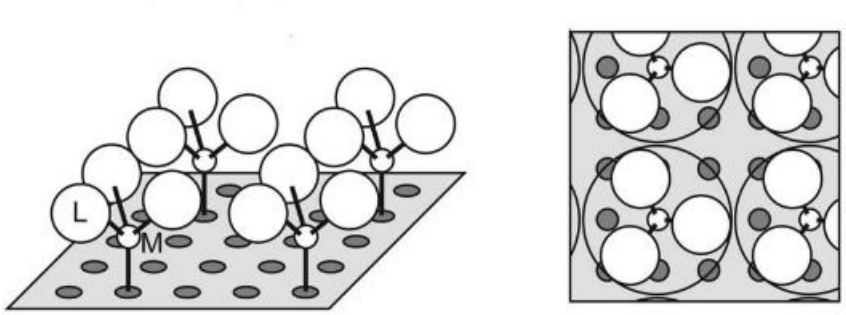


*Figure 32: Schematic illustration of steric hindered, which leads to precursor adsorption on limited sites.*[163]

The amount of material deposited per ALD cycle is referred as the growth per cycle (GPC), which depends on the precursor, substrate, partial pressure, and temperature.

**Partial Pressure:** In principle, ALD is an irreversible chemisorption process. Hence the pressure factor should not influence the growth behaviour. However, few studies have shown that growth rates are enhanced with an increase in the partial pressure of reactants, as shown in figure 33. Here, the authors reported an unsaturated coverage regime, which turns into saturated coverage at higher partial pressure of reactant[172,173,174,175].

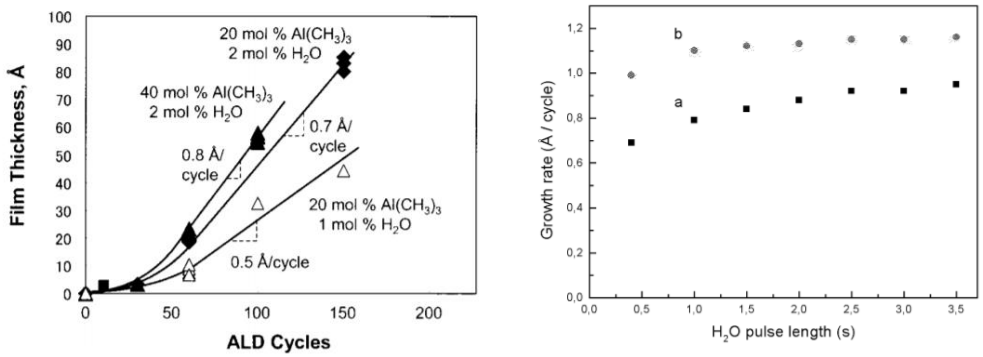


*Figure 33: Effect of ALD growth rate by precursor concentration[173] (left), (right). (a) small (8 x $10^{-6}$ g/s) and (b) large (2 x $10^{-4}$ g/s) water flow rate[175]*

**Temperature:** Substrate temperature has a significant influence on the growth rate, as shown in figure 34. Self-limiting growth occurs between a temperature range referred as the ALD window, where three growth scenarios can be considered. A constant growth rate is observed when the saturation is caused by steric hindrance[176,177], while a decreasing trend is observed when the number of surface reactive sites decreases with the increase in temperature[178,179]. A growth enhancement is observed when thermal activation is needed to overcome an energy barrier across the reaction pathay[180,181]. In the low-temperature region below the ALD window, an increased growth rate is observed with decreasing temperature due to the

precursor multilayer physisorption s. A decreasing growth rate is however more frequent and is associated with insufficient activation energy. While at high temperatures above the ALD window, a high growth rate reveals the decomposition of the precursor (CVD contribution). For thermally stable precursors at high temperatures, a decreased growth rate is due to the reduced residence time of the chemisorbed precursor on the growth surface[182].

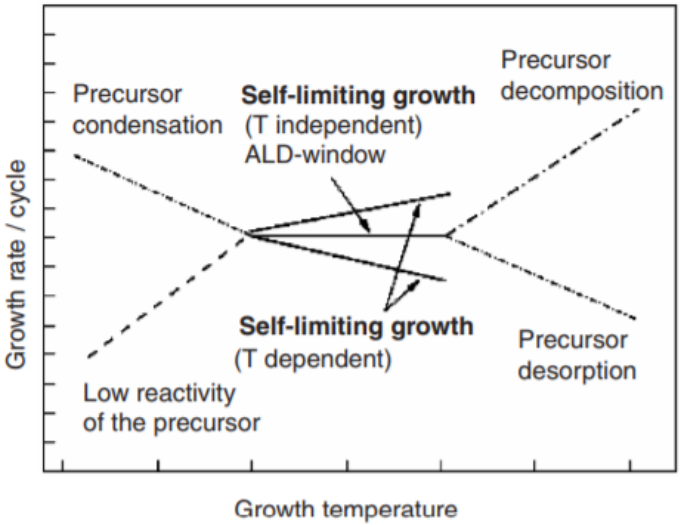


*Figure 34: Growth rate as function of substrate temperature[183].*

**Substrate:** The surface characteristics of the substrate change upon the iteration of ALD cycles, and the GPC might evolve during the process as a consequence. The substrate is increasingly covered by the coating material during the first ALD cycles, which progressively attenuates the effect of the original substrate to reach a constant GPC after a certain number of cycles. Four GPC trends were reported, as shown in figure 35.

a) Steady-state regime: The GPC is constant over the cycles, and this type of linear growth occurs when reactive sites do not change with the number of deposition cycles. It is observed when the steric hindrance of ligands dominates the saturation behaviour.
b) Substrate-enhanced regime: The GPC is high for the initial reaction cycles and gradually decreases to a constant value. This type occurs when the number of reactive sites on the substrate is higher relative to the deposited film.
c) Type-1 substrate-inhibited regime: The GPC is low for the initial cycles and gradually increases to a constant value. A lower number of reactive sites on the substrate compared to the ALD grown material favours this kinetics.
d) Type-2 substrate-inhibited regime: The GPC shows a similar behaviour as Type 1 but reaches a maximum before saturating to a constant value.

There are some reports which assign the GPC category to specific growth models. For instance, Type-2 is assigned to island growth mode[184]. At the same time, other types have displayed diverse growth modes such as layer-by-layer, random and islandic[163]. Improved crystallinity of the ALD films was observed for high ALD temperatures, thick films and

improved purity. Improving the crystallinity of the ALD films might also be addressed via post-deposition treatments.

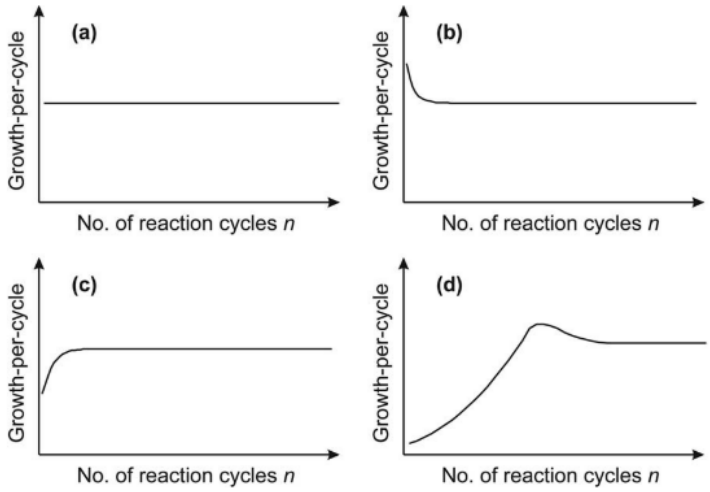


*Figure 35: Various ALD growth types depending on substrate, (a) steady-state, (b) substrate enhanced, (c) substrate inhibited type-1, (d) type-2*[184]*.*

**Precursor:** The precursor plays a crucial role in the ALD process, and essential requirements need to be met:

- *Volatility:* Gases and high vapour pressure liquids are preferred as they are easy to handle and can be delivered with high fluxes. The last favours fast surface reactions.
- *No self-decomposition:* The precursor should feature sufficient thermal stability to enable the self-limiting film growth mechanism.
- *Reactivity:* Fast and complete surface reactions lead to high productivity with high film purity.
- *No etching of the film or the substrate material:* Formed by-products should be inert and volatile, or else growth is prevented.
- *No dissolution into the film or substrate material* else hinders the self-limiting film growth mechanism.

Apart from the essential requirements, some preferred qualities include the price, easy synthesis and handling, non-toxicity and environmental friendliness.

Precursor materials are broadly classified into inorganic (e.g. halides); organometallics (e.g. alkyls and cyclopentadienyls) and metalorganic compounds (e.g. alkoxides, β-diketones, amides, and amidinates) [163,185].

**Halide compounds** such as metal chlorides, fluorides, bromides and iodides were used since the early 1960s as ALD reactants. Halide compounds are inexpensive and categorized as metal-inorganic compounds.

Merits: Halides are highly reactive and thermally stable[186]. Steric hindrance is reduced due to small ligand size. A wide variety of materials such as oxides, nitride, sulphides, etc. are deposited using halides.

Demerits: Most halides are solid; vaporization is a challenging process. Gaseous reaction with hydrogen containing co-reactant results in corrosive by-products such as HF, HCl, HBr, and HI[187].

**Organometallic compounds** such as Alky (metal methyl, ethyl, isopropyl, n-Butyl, and neopentyl) and cyclopentadienyl Cp (methyl-Cp, ethyl-Cp, and isopropyl-Cp) were introduced as ALD reactant since 1980s[163]. They are referred as organometallic compounds because of the direct metal-carbon bond.

Merits: They are highly reactive, resulting in a variety of material deposition such as oxide, nitride, sulphides, etc. Small organic ligands induce the high GPC due to the minimization of steric hindrance[188]. Gaseous reaction by-products are inert volatile substances.

Demerits: Metal compounds are only limited to 12-14 group elements for alkyls and cyclopentadienyls 2, 3, 10 group elements. These compounds decompose at moderate temperature, e.g. $Al(CH_3)_3$ decomposes above 300˚C[189], $ZrCp_2Me_2$ decomposes at 500 °C[190].

**Metal-organic compounds** such as β-diketonate, alkoxide, and alkylamides, were used as ALD reactants since the 1980s. Amidinates were introduced since 2003. Direct metal-carbon bond is absent[185].

Merits: Broad range of elements from group 2-14, except 12 are available as ALD reactants. Wide studied materials such as oxides, nitrides, sulphides, etc. can be deposited[163].

Demerits: Poor thermal stability with decomposition at low temperatures, e.g. $TiOiPr_4$ decomposes at 200˚C[191], $Ti(NMe_2)_4$ decomposes at 150˚C[192] and $Zr(NEtMe)_4$ decomposes at 300˚C[193]. Bulky ligands feature a low growth rate due to the steric hindrance effect. Low vapour pressure results in a challenging evaporation process.

For few decades, many studies have reported the ALD growth for a comprehensive list of metal oxides because of their range of electrical properties extending from insulating, semiconducting, metallic to superconducting [194,195,196].

#### 2.1.2.2 *ALD of vanadium oxide*

Metal precursors such as Vanadium alkoxides ($V^{+5}$), β-diketones ($V^{+4}$), alkyl amides ($V^{+4}$) have been used to grow vanadium oxide films by co-reacting with $H_2O$, $O_3$ or $O_2$ plasma. These films are amorphous in the as-deposited conditions, requiring post-annealing treatments to achieve the desired vanadium oxide phase[98].

In this work, vanadium oxide films are deposited by thermal ALD. Vanadyl (V) tri-isopropoxide (VTOP) was used as the precursor and $H_2O$ for hydrolysis. VTOP and $H_2O$ are introduced into

the reactor chamber sequentially, followed by purging steps, and the ALD cycle is optimised by adjusting the exposures and purge times. The deposition pressure was maintained at ~0.2 mbar, while the deposition temperature was set as an adjustment parameter. During the hydrolysis of VTOP, the isopropoxide ligands are removed through the hydrolysis process. Vanadium oxide ALD half-reactions are shown in the below equations.

$$VO\big(O-(CH-(CH_3)_2)\big)_3 + Surface-OH \xrightarrow{\Delta} Surface-O-VO\big(O-(CH-(CH_3)_2)\big)_2 + HO-(CH-(CH_3)_2)$$

$$Surface-O-VO\big(O-(CH-(CH_3)_2)\big)_2 + 2H_2O \xrightarrow{\Delta} Surface-O-VO(OH)_2 + 2\,HO-(CH-(CH_3)_2)$$

### 2.1.2.3 *ALD of aluminium doped zinc oxide*

In early reports, Zn element, Zinc chloride ($ZnCl_2$) and Zinc acetate ($Zn(CH_3COO)_2$) were used for ZnO deposition using $H_2O$ and $O_2$ co-reactants. However, their usage is limited because of the very low vapor pressure of the precursors, the high deposition temperature, and the resulting corrosive by-products. Metal alkyl precursors like diethyl zinc ($Zn(C_2H_5)_2$) and dimethyl zinc ($Zn(CH_3)_2$) have shown fast reactions with various co-reactants. Diethyl zinc is the most reported precursor for ZnO growth through the ALD process[197,106]. Doping with Trimethyl aluminium ($Al(CH_3)_3$) has resulted in enhanced electrical properties[198].

In this work, diethyl zinc ($Zn(C_2H_5)_2$) and trimethyl aluminium ($Al(CH_3)_3$) highly volatile liquids were used. They feature the vapor pressure of 21 mbar[199] and 15 mbar[200] at room temperature, respectively. Fast surface reactions produce films with low levels of contamination and a high GPC (≈ 0.24 and 0.13 nm/cycle, respectively). *Thermal ALD enables Al-doped ZnO films* via the sequential hydrolysis of diethyl zinc (DEZ) and trimethylaluminum (TMA) precursors. AZO films were made by injecting "m" TMA-$H_2O$ cycle for every "n" DEZ-$H_2O$ cycles. By varying the number of macro cycles "N", thickness of AZO films was controlled. Here one macro-cycle corresponds to "n" DEZ-$H_2O$ cycles and "m" TMA-$H_2O$ cycles as illustrated in figure 36. Through changing "n" and "m", aluminum doping concentration was varied with descriptive annotation shown as AZO N(n:m).

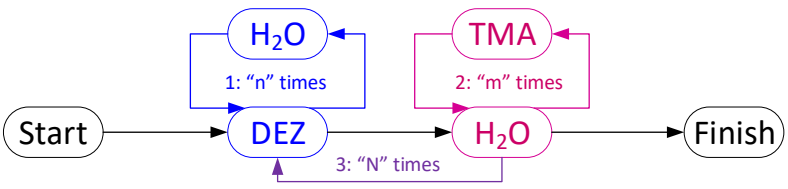


*Figure 36: Scheme of macro cycles for Al doped Zinc oxide.*

During the hydrolysis of DEZ and TMA the alkyl ligands are removed through the hydrolysis process. ALD surface reactions of Al doped ZnO is given in the below equations.

$$Surface-OH + Zn(C_2H_5)_2 \xrightarrow{\Delta} Surface-O-ZnC_2H_5^* + C_2H_6\uparrow$$

$$Surface - O - ZnC_2H_5^* + H_2O \xrightarrow{\Delta} Surface - O - ZnOH^* + C_2H_6 \uparrow$$

$$2ZnOH^* + Al(CH_3)_3 \xrightarrow{\Delta} ZnO - Al - O - Al(CH_3) + 2CH_4 \uparrow$$

$$ZnO - Al - O - Al(CH_3) + H_2O \xrightarrow{\Delta} ZnO - Al_2OOH + CH_4 \uparrow$$

### 2.1.2.4 *ALD of titanium oxide*

Precursors such as halides[201], alkoxide[191], alkylamides[202] have been reported for the ALD growth of $TiO_2$ film. Among them, titanium tetra-isopropoxide (TTIP) reactant has been widely reported for $TiO_2$ deposition[203]. During the hydrolysis of TTIP, isopropoxide ligands are removed through the hydrolysis process[194]. ALD surface reactions of $TiO_2$ growth is given in the below equations.

$$Ti\big(O - (CH - (CH_3)_2)\big)_4 + Surface - OH \xrightarrow{\Delta} Surface - O - Ti\big(O - (CH - (CH_3)_2)\big)_3 + HO - (CH - (CH_3)_2)$$

$$Surface - O - Ti\big(O - (CH - (CH_3)_2)\big)_3 + 3H_2O \xrightarrow{\Delta} Surface - O - Ti(OH)_3 + 3\,HO - (CH - (CH_3)_2)$$

### 2.1.2.5 *ALD on CNTs*

In principle, CNTs have an inert surface with no dangling bonds or surface functional groups. Therefore, film growth by the ALD process is a challenge[204], which can be overcome with the surface functionalization of CNTs[205,206,207]. Pristine CNTs synthesized by the CVD process are prone to defects relative to CNTs of arc discharge method[208]. These defective sites act as nucleating sites for the ALD growth of metal oxides[209,204]. Here chemisorption occurs at defective sites and the nuclei coalescence with an increase in the ALD cycle results in a homogenous layer, as illustrated in figure 37. The ALD growth kinetics is therefore dominated by the defect density at the surface of CNTs[210,50,211].

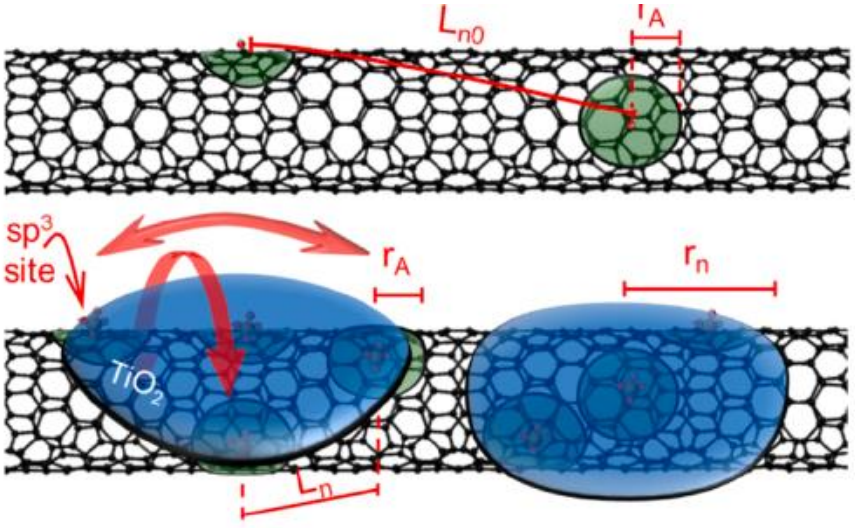


*Figure 37: Scheme illustrating nucleation at defective site (top), radial growth of $TiO_2$ nuclei with increase in ALD cycles[210] (bottom).*

## 2.2 MATERIAL CHARACTERIZATION

Spectroscopy is defined as the interaction of electromagnetic radiations with materials, which features phenomena such as reflection, absorption, transmission, emission, and scattering[212]. Electromagnetic radiations consist of a broad range of wavelengths, interacts uniquely with the materials, as shown in the table. Spectroscopy characterization utilizes the above-mentioned phenomena to understand structure, chemical composition and optical constants of the MWCNT-metal oxide material developed in this thesis.

Table 1: Material characterization techniques using various electromagnetic radiations, taken from reference[212]

| Wavelength region | Wavelength limits | Type of spectroscopy | Usual wavelength range | Types of transitions in chemical systems with similar energies |
|---|---|---|---|---|
| Gamma rays | 0.01-1 Å | Emission | <0.1 Å | Nuclear proton/neutron arrangements |
| X-rays | 0.1-10 nm | Absorption, emission, fluorescence, and diffraction | 0.1-100 Å | Inner-shell electrons |
| Ultraviolet | 10-380 nm | Absorption, emission, and fluorescence | 180-380 nm | Outer-shell electrons in atoms, bonding electrons in molecules |
| Visible | 380-750 nm | Absorption, emission, and fluorescence | 380-750 nm | Same as ultraviolet |
| Infrared | 0.075-1000 µm | Absorption | 0.78-300 µm | Vibrational position of atoms in molecular bonds |
| Microwave | 0.1-100 cm | Absorption<br>Electron spin resonance | 0.75-3.75 mm<br>3 cm | Rotational position in molecules<br>Orientation of unpaired electrons in an applied magnetic field |
| Radio wave | 1-1000 m | Nuclear magnetic resonance | 0.6- 10 m | Orientation of nuclei in an applied magnetic field |

### 2.2.1 Physical and chemical characterization

The thickness of the metal oxide thin film deposited on the silicon substrate was assessed using a multiwavelength ellipsometer *(Film Sense)* with the Cauchy model. Ellipsometry technique measures the change in reflected light polarization from linear to elliptical upon interaction with matter. In a three-phase optical system, as shown in figure 38, the total reflection R is given by the combination of partial reflection coefficient at air-film interface ($r_{01}$), and phase changed reflection at the film-substrate interface($r_{12}$). Ellipsometry

parameters ψ (psi) and Δ (delta) are related to reflected light polarized in parallel ($R_p$) and perpendicular ($R_s$) to the incident plane[213], as shown in the equation.

$$R = \frac{R_p}{R_s} = \tan(\psi)\, e^{i\Delta}$$

$$R_p = \frac{r_{01,p} + r_{12,p}\, e^{-j2\beta}}{1 + r_{01,p}\, r_{12,p}\, e^{-j2\beta}}$$

$$R_s = \frac{r_{01,s} + r_{12,s}\, e^{-j2\beta}}{1 + r_{01,s}\, r_{12,s}\, e^{-j2\beta}}$$

Refractive index and thickness of the film are determined by the phase change (β)[214], given in equation.

$$\beta = \frac{2\,\pi\, d}{\lambda}\sqrt{n_1^2 - n_0^2\, sin^2(\theta)}$$

$$n_1 = \frac{\sqrt{\left(1 - 4sin^2(\theta)\, \tan(\psi)e^{i\Delta} + 2\tan(\psi)e^{i\Delta}\, \tan^2(\psi)e^{i\Delta}\right)}\, n_0 \sin(\theta)}{\cos(\theta)[1 + \tan(\psi)e^{i\Delta}]}$$

d is the thickness of the film, $n_1$, $n_0$ are the refractive index of the film and ambient respectively, λ is the wavelength of the incident beam (633nm), and θ is the angle of incidence (65˚)

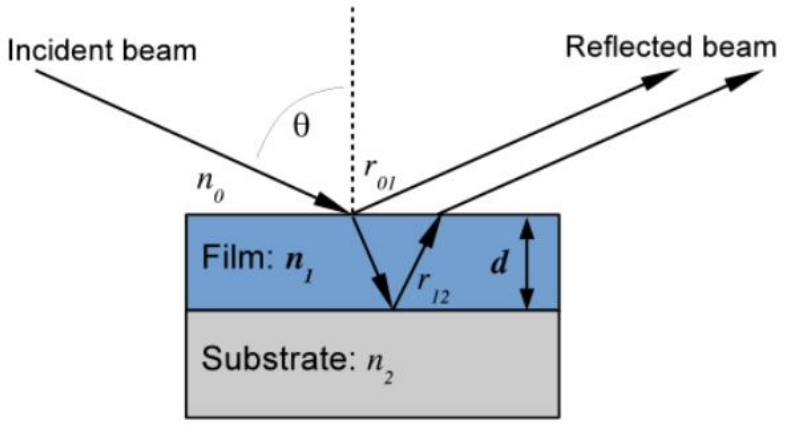


*Figure 38: Schematic of light propagation in three phase optical system[215].*

X-ray diffraction is based on the elastic scattering of the X-rays from the periodically arranged atoms of a crystalline material, as shown in figure 39. From Braggs equation, constructive diffraction occurs when the spacing between the lattice planes matches the wavelength of X-rays[216].

$$n\lambda = 2d \sin\theta$$

Where n is an integer representing the order of diffraction, λ is the wavelength of X-rays, θ is the diffraction angle, and d is lattice spacing. Diffraction pattern as a function of diffraction angle aids in determining the crystal structure of the material. Lattice parameters of the hexagonal ZnO crystal structure are estimated using the relation between lattice spacing and miller indices of diffraction pattern shown in the given equation

$$\frac{1}{d^2} = \frac{4}{3}\left(\frac{h^2+hk+k^2}{a^2}\right) + \frac{l^2}{c^2}$$

Where (a,c) are the lattice parameters of ZnO crystal structure, (h,k,l) are the miller indices of the diffraction pattern, d is lattice spacing. Here Lattice parameter a is calculated using (100) diffraction peak, and c is calculated from (002)[217]. Crystallite size can be estimated using the Debye-Scherrer equation

$$D = \frac{K\lambda}{B\cos\theta}$$

Where D is the crystallite size and K is the Scherrer constant depends on the shape of the crystallite size (for round shape K=0.94), B is diffraction peak broadening, and λ is X-ray wavelength (Cu Kα - 0.154 nm). Diffraction peak broadening is considered due to size, strain, and instrumental effect shown in the given equation.

$$B^2_{total} = B_{size} + B^2_{strain} + B^2_{instrumental}$$

Williamson-Hall plot given in equation considers total broadening to estimate the crystallite size (D) and strain (ε)[218].

$$B_t \cos\theta = \frac{K\lambda}{D} + 4\varepsilon \sin\theta$$

X-ray diffraction *(Bruker D8)*, Cu-Kα X-ray source, was used to identify crystalline phases of metal oxide film, silicon substrate and the grown MWCNT. Data were collected using the grazing incidence at (0.5°), scanning the detector from 0° to 90° with a step size of 0.02°. In grazing incidence-XRD configuration, the beam, Figure 39, has a limited penetration in the material, which enhances the diffraction intensity from the thin-film coating.

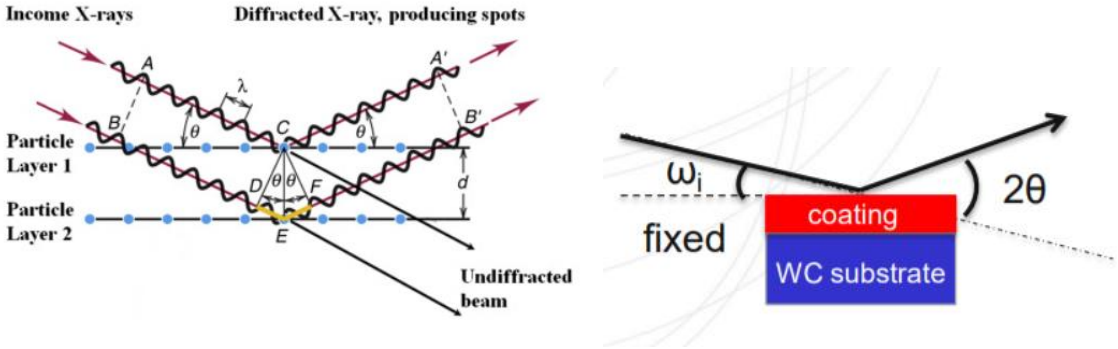


*Figure 39: Schematic of X-ray interaction with periodically arranged lattice atoms[216] (left); GI-XRD measurement (right).*

Raman spectroscopy was performed using an InVia Raman spectrometer (*Renishaw)* with a 532nm, 633nm laser to identify hybrid material phases.

Raman spectroscopy is used to study the rotational and vibrational transitions of molecules. It is based on the inelastic scattering of electromagnetic radiations. When the monochromatic light interacts with molecules, light can be absorbed or scattered. If the photon energy of incident light matches with the electronic transition energy states of the molecules, then the photon is absorbed, and molecules are excited to higher energy levels[219]. When photon energy is not enough to excite to higher electronic transition states, molecules are excited to

virtual vibrational states and de-excited back to ground state. This phenomenon is referred as scattering, shown in figure 40. An elastic scattering, referred as Rayleigh scattering, occurs when no energy is exchanged between the incident photon and molecule. During inelastic scattering the photon energy is exchanged with molecule, i.e., change in frequency of scattered photon from that of the incident photon. In this context, the Stokes Raman effect occurs when the scattered photon frequency is shifted to a lower value relative to incident photon frequency i.e., molecules de-excite from the virtual state to an energy state above the ground states. Anti-Stokes Raman effect occurs when the scattered photon frequency is shifted to higher value relative to incident photon frequency, i.e., molecules de-excite from the virtual state to an energy state which is below the ground states[220]. Stokes-scattering is most observed phenomenon because absorbing materials are in-ground vibrational state at room temperature.

However, Raman spectroscopy analysis is not limited to intramolecular phonon scattering, but also Raman-active lattice scattering, scattering by electronic excitations are detected on thin film semiconductors. The vibrational modes of a thin film reflect the atomic bonding of the material, and the technique has been used as a structure sensitive probe. From Raman spectroscopy of thin films, following properties can be assessed: 1) Long range order - crystalline or amorphous 2) Strain 3) Composition identification 4) Interface structures and thin film reactions 5) Superlattice properties 6) Impurities.

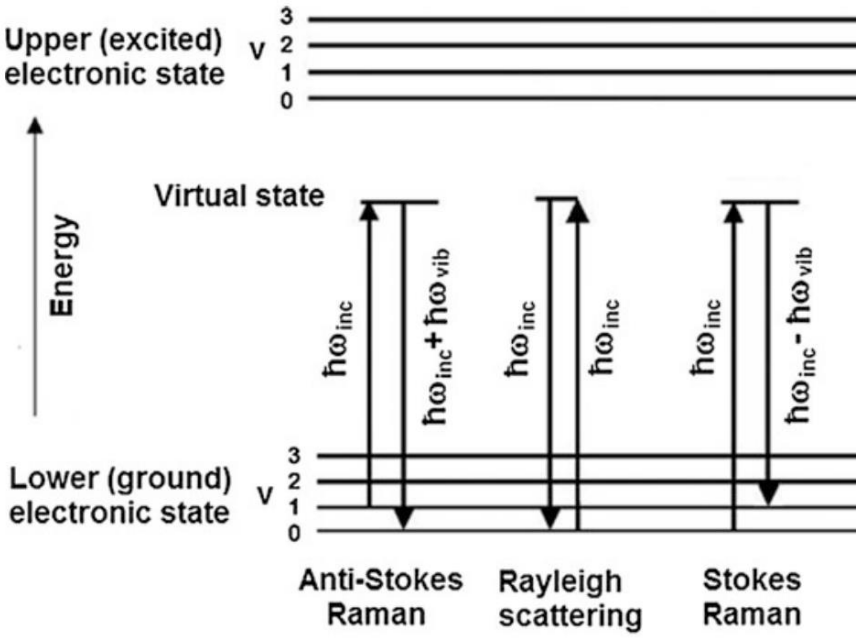


*Figure 40: Energy-level schematic illustrating the states involved in Raman scattering.*

The elemental composition and the chemical states of the elements were studied by x-ray photoelectron spectrometry (XPS) *(Axis Ultra DLD, Kratos Analytical Ltd.)* using monochromatic Al-Kα radiation (E = 1486.6eV), Photoelectron emission take-off angle at 0°with respect to the surface normal.

X-ray photoelectron spectrometry is based on the photoelectric effect[219]. Here, the impingement of x-rays removes the core-electrons of surface atoms, illustrated in figure 41. Ejected electron due to absorption of photon energy ($h\nu$) is referred as photoelectron. Kinetic energy ($E_K$) of the emitted photoelectrons are analysed to estimate the binding energy ($E_B$), as shown in the equation.

$$E_K = h\nu - E_B - \varphi$$

In practice, XPS measurement sample is electrically grounded to the spectrometer, i.e., the fermi levels are aligned. Thus, kinetic energy and work function (φ) are measured from the fermi level of the spectrometer.

$$E_B = h\nu - E_K - \varphi_{sp}$$

The binding energy of core-electrons of different chemical elements is unique and easily distinguishable. Hence, in many cases, core-level photoelectrons are used for elemental analysis, while small shit in binding energy, referred as chemical shift, determines the oxidation state.

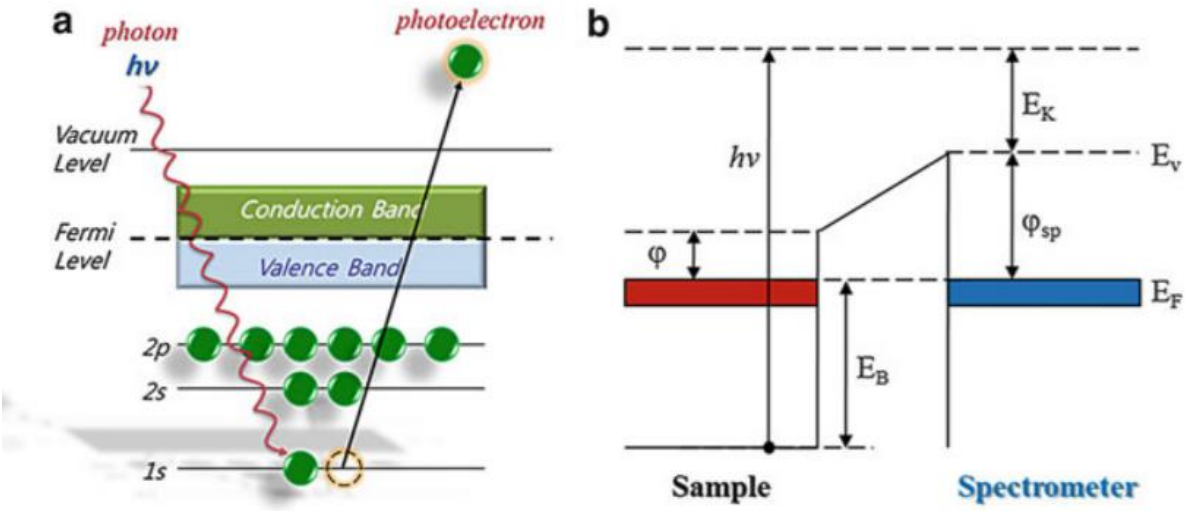


*Figure 41:(a) Schematic of photoelectron emission by the photoelectric effect in a metal. (b) Band energy-level diagram of the sample and the spectrometer[219].*

## 2.2.2 Morphology

Electron microscopy uses a highly energetic focused electron beam to analyse the samples on a very fine scale. When an electron beam hits the sample surface, different signals are produced from certain depth of samples due to various interactions as shown in figure 42. These interactions are realised as both elastic and inelastic scattering. Inelastic scattering is a phenomenon where the electron beam energy is transferred to the sample atoms, resulting in the ejection of electrons from the atoms as secondary electrons. Subsequently, x-rays are emitted when vacancy created by ejected electrons is occupied from the electron of higher orbital energy. In elastic scattering, energy is not exchanged between the electron beam and sample atoms, but the direction of the incident electron beam is changed. Some of the elastically scattered electrons are deflected out of the sample, referred as backscattered

electrons. Each of these interaction signals are collected by the respective detectors for later processing, such as topography, morphology, composition, the orientation of grains, crystallographic information of the sample. Scanning electron microscopy is based on the scattered electrons, while transmission electron microscopy is based on the transmitted electrons[221].

Scanning electron microscopy *(FEI Helios 650)* was used to analyze the microstructure of the films with a working distance of 4-5mm, 2-10V voltage. Standard SEM sample preparation was used. Both top-view and cross-sectional configurations were performed to investigate surface morphology and conformal deposition. Energy dispersive x-ray spectroscopy (EDX) attached to FEI-FIB/SEM system is used for the microscopic analysis of the chemical elements of the sample. MWCNT/metal oxide hybrid materials were characterized using transmission electron microscopy (*S/TEM Themis Z G3, 300kV, Thermo Fisher Scientific)*. Combined EDX (energy dispersive X-ray spectrometer) analysis and high-angle annular dark-field scanning transmission electron microscopy *(HAADF-STEM, 29.5 mrad, probe corrected)* was used for elemental mapping. The TEM sample were prepared by scratching the surface and deposited on lacey carbon grids.

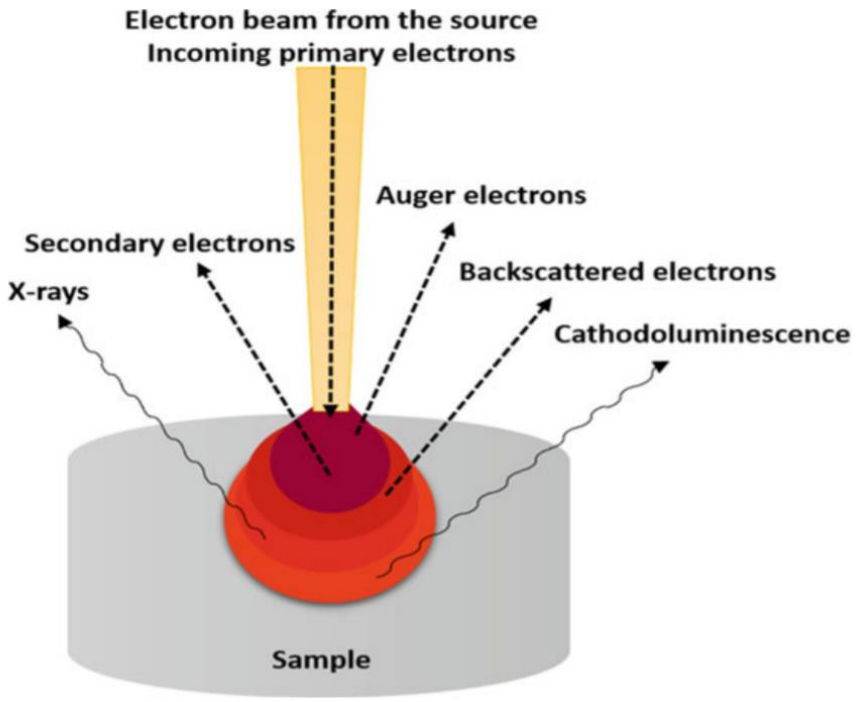


*Figure 42:The interaction of electron beam with specimen and the signal emitted from the sample[221].*

Atomic force microscope is based on interacting forces between the sample and microscopic tip attached to a flexible cantilever. Here the local attractive or repulsive force between the sample and the tip induces bending in the cantilever. Deflected cantilever results in the displacement of the reflected laser beam position on the photodetector, as shown in figure 43. Raster-scanning gives the topography of the sample based on the displacement of the laser beam position. In general, there are three modes of operation, i.e., contact, non-contact, and tapping.

In contact mode, the tip always remains in contact with the sample. As a result, the tip–sample interaction occurs in the repulsive regime. A constant force is used for the feedback loop to maintain the scan height. This mode is limited to hard materials due to possible deformation of the surface during the lateral scan.
In non-contact mode, cantilever is oscillated at its resonant frequency at a smaller amplitude. Here tip is never in direct contact with the sample. During the scanning long range, attractive forces such as Van der Waals and electrostatic forces occur between the tip and sample. As a result, shift of amplitude/phase in the cantilever`s oscillations. Constant amplitude or phase is used in feedback loop to maintain scan height. This mode has poor image resolution.
In tapping mode, cantilever oscillates as in non-contact mode but with larger amplitude, resulting in repeated engagement and disengagement of the tip from the surface. A constant amplitude is used for the feedback loop to maintain the scan height. Due to intermittent characteristics, the lateral force is reduced relative to contact mode. Hence can be used for soft materials with better resolution[222].

The surface topography of the obtained films was studied by atomic force microscopy *(AFM, Bruker Innova)* in tapping mode through etched single crystal silicon probe tip having a radius curvature <10nm. The surface roughness was extracted via the *NanoScope* software.

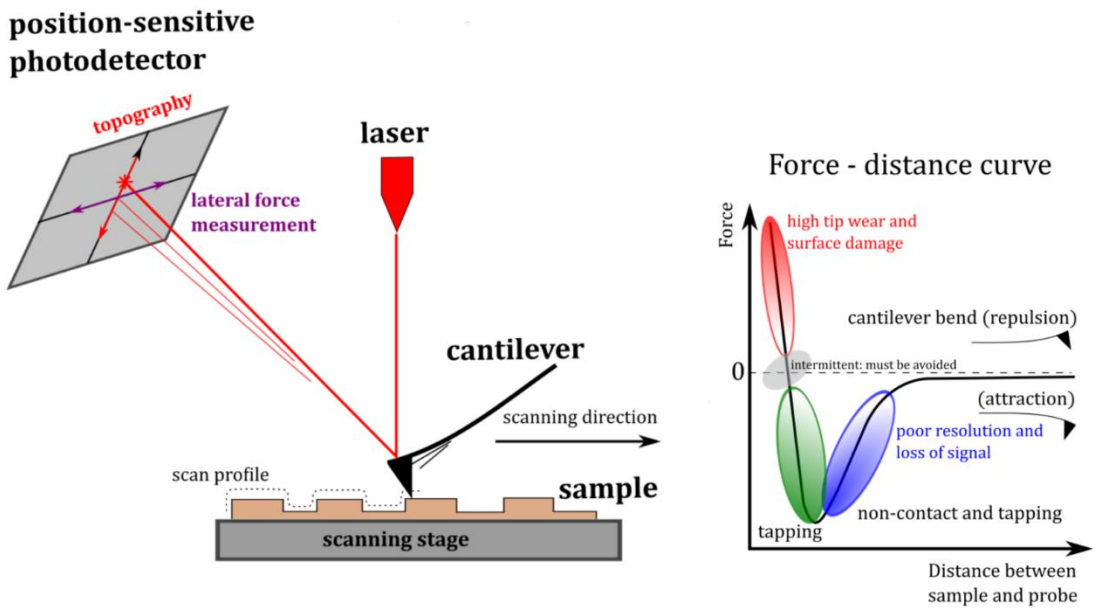


*Figure 43: Schematic of basic AFM set-up (left), force regimes under which each of the three AFM modes operate[223](right).*

### 2.2.3 Solar selective characterization

Sunlight is electromagnetic radiation with spectrum range from partial UV-visible-near infrared region, which has both waves, particle characteristics. When light interacts with matter, basically scattering and absorption phenomena occur depending on the frequency (energy) of the light[224], as shown in figure 44. Absorption is a resonance process where atoms are excited to higher energy states. UV-Visible frequency induces electronic excitations to

higher energy states, and the relaxation process features photon emission. Whereas infrared frequency induces vibrational or rotational excitations of lattice atoms. As-result of absorption, light propagation through the material is attenuated, given by Beer lamberts equation.

$$I = I_O e^{-\alpha d}$$

Where α is the absorption coefficient, and d is the thickness of the material. Scattering is basically represented as a non-resonant process, where the lower photon frequency does not result in higher energy excitations. However, upon photon interaction, atoms are vibrated to the frequency of the incoming photon. Electron clouds present in the atoms oscillate with respect to positive nucleus behaving like a dipole oscillator. So immediately emit the radiation at that frequency. This remission of light is termed as scattering process. In dense material, atoms are arranged periodically, so each atom act as a source of secondary emitted radiations that propagate in a forward direction due to constructive interference. Whereas in the lateral and backward direction, scattered radiations are nullified with destructive interference. Optical properties like reflection, transmission and refraction are a macroscopic manifestation of scattering and interference occurring at atomic level[225].

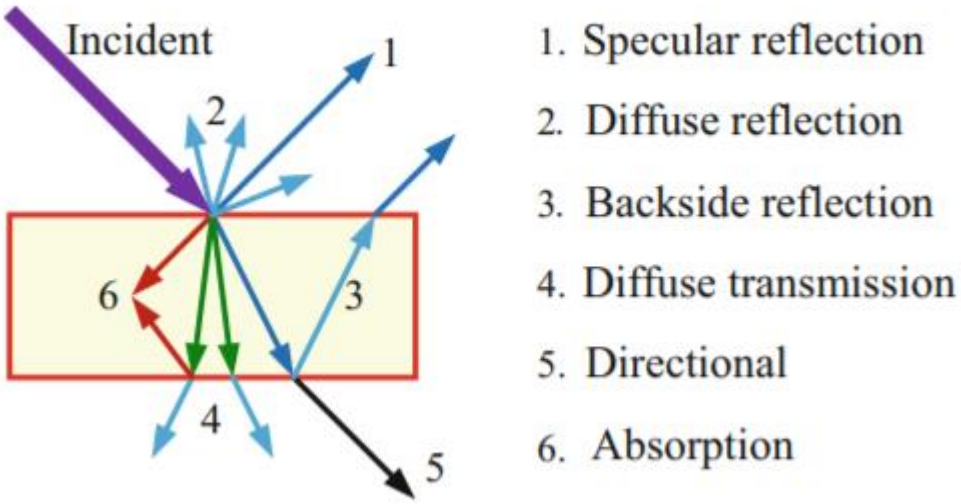


*Figure 44: How light interacts with matter[225].*

Transmission can be understood as scattering in forward direction. Transmission is quantified as the coefficient of transmission or transmittivity (T). It is usually defined as the ratio of the transmitted light fraction ($I_T$) to incident light ($I_O$).

$$T = \frac{I_T}{I_O}$$

However, at the interface, discontinuity occurs, which paves the path for constructive interference of backward scattering. This backward scattering is considered as reflection. Reflection is quantified as the coefficient of reflection or reflectivity (R). It is usually defined as the ratio of the reflected light fraction ($I_R$) to incident light ($I_O$).

$$R = \frac{I_R}{I_O}$$

Light radiated out the sample can have specular or diffusive characteristics, as shown in figure 35. An integrating sphere collects both the specular and diffusive radiations from the sample through internal diffusive reflections[226]. The inner surface of the integrating sphere is coated by strongly scattering, non-absorbing powder. After repeated reflections inside the sphere, all radiation will eventually reach the detector. For total hemispherical transmittance, the sample is placed at the port entrance, while in reflectance measurement sample is placed at the backside of the port, as shown in figure 45.

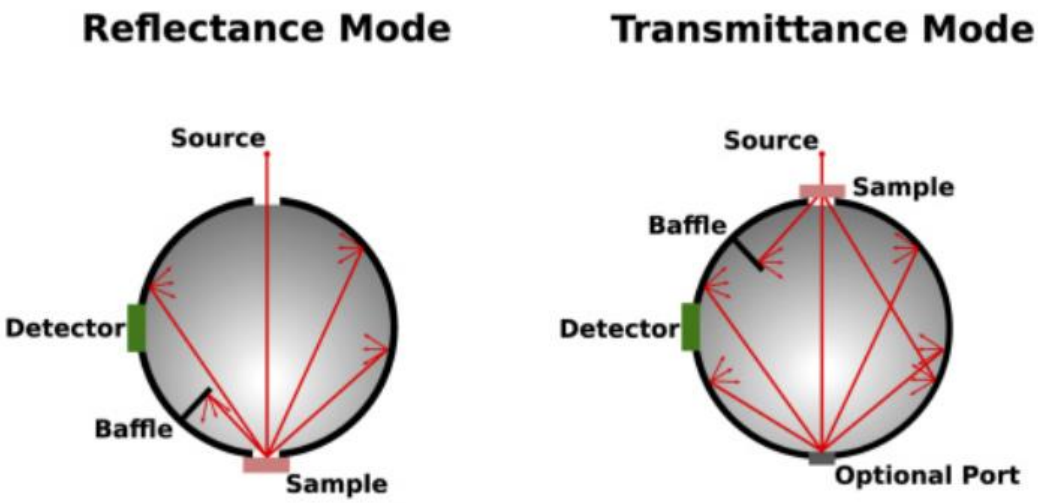


*Figure 45: Illustration of how integrating spheres would be used in optical measurements reflectance (left) and transmittance (right)[226].*

Optical properties were measured using LAMBDA 1050 UV–VIS-NIR spectrophotometer from *Perkin Elmer* and *Bruker* FTIR spectrometer. Details of the process can be seen in below attached published article's[227,228].

### 2.2.4 Solar water splitting characterization

A standard three-electrode setup was used for the photoelectrochemical measurements with the MWCNT-metal oxide as the working electrode, as shown in figure 46. All voltages were measured versus Ag/AgCl reference electrode, and platinum (Pt) was used as the counter electrode. The electrolyte was an aqueous solution of 0.1 M NaOH (pH 12.7). The electrode area, 2 $cm^2$, was front-illuminated using a Xe-lamp at 100mW/$cm^2$. Electrochemical measurements were conducted using an AUTO LAB potentiostat.

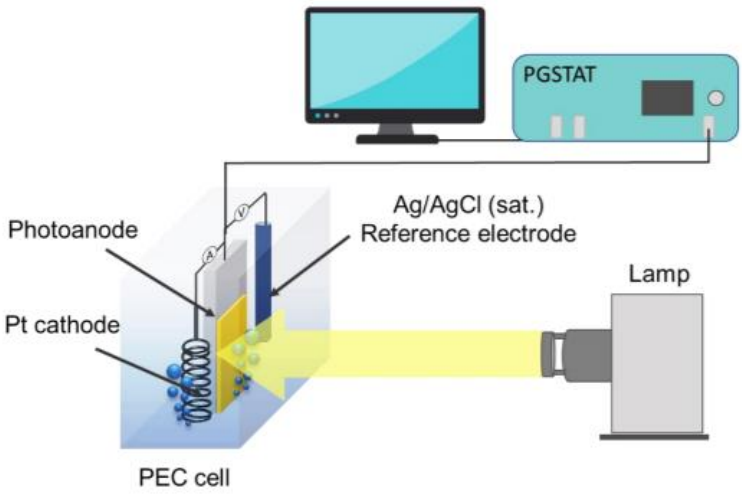


*Figure 46: Schematic of the photoelectrochemical setup*[229].

In CV measurement, the potential of the photoanode is scanned between two potentials at a specific scan rate. As a result, the current obtained from the applied potential is measured by the potentiostat. In general, the current is normalized the geometric area of the electrode, referred to as current density. CV measurements are performed under both light illumination and dark conditions.

Chronoamperometry is performed by applying a constant potential. Sequential illumination of light reveals the steady-state photocurrent from the anode. Chronopotentiometry records open-circuit potential before, during and after illumination of the anode without applying any current. The difference in potential in the dark and under illumination is referred as Photopotential.

Electrochemical impedance spectroscopy (EIS) can distinguish between resistive and capacitive responses of metal oxide electrode interfaces based on the frequency dependence of the observed current. In principle, EIS is an Alternating Current technique where applied potential V(t) is modulated over time with a small amplitude ($|Vo| \sim 5{-}10$ mV) at a controlled frequency (ω) as shown in equation.

$$V(t) = |V_0|\sin(\omega t)$$

Here, ω is an angular frequency defined by ω = 2πf, and f is the frequency in Hz. current measured I(t) is matched in frequency with offset by a phase angle (φ), as given in below equation.

$$I(t) = |I_0|\sin(\omega t + \varphi)$$

Impedance is defined as a resistance at alternating potential and current as given in equation.

$$Z(\omega) = V(t)/I(t)$$

EIS collected data is mostly interpreted through Nyquist spectra, which is a plot of imaginary impedance at Y-axis and real impedance at X-axis, as shown in figure 47. EIS is performed under light illumination and dark conditions. Nyquist plot are fitted to Randle circuit to understand the flow of current across the metal oxide electrode-electrolyte interface. Here faradaic current correlates with the charge transfer resistance ($R_{ct}$) and non-faradaic current to interfacial capacitance ($C_{int}$). EIS provides information regarding the charge transfer and accumulation at metal oxide interface. As a result, mechanistic insights of overall photoanode performance are estimated.

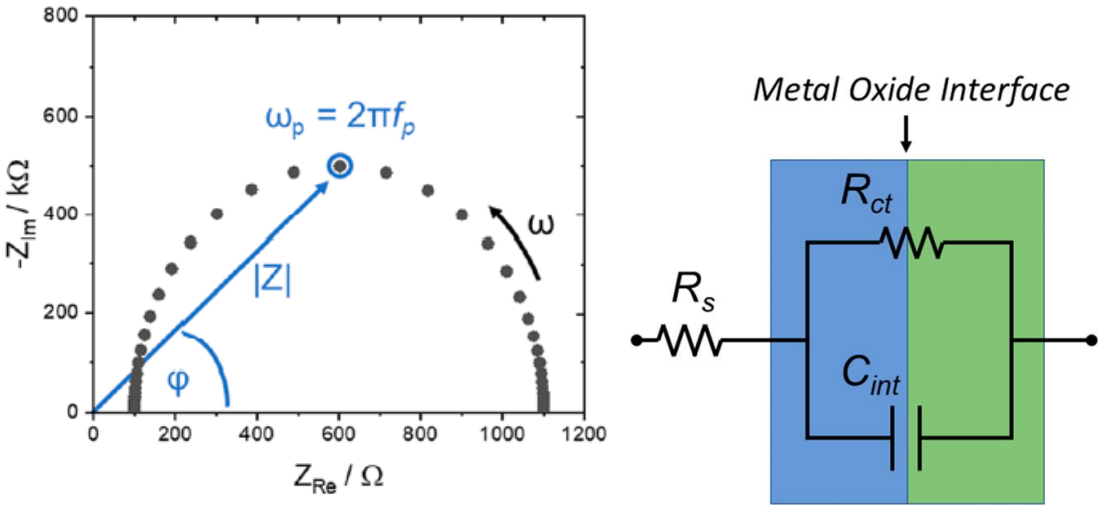


*Figure 47: Basic schematic of Nyquist plot (left) and Randle circuit (right)*[230].

# REFERENCE


1. Kahan A, EIA. EIA projects nearly 50% increase in world energy usage by 2050, led by growth in Asia - Today in Energy - U.S. Energy Information Administration (EIA). *24092019*. 2019;2019:2018-2021. https://www.eia.gov/todayinenergy/detail.php?id=41433. Accessed May 4, 2021.

2. Toshiko kandeda et al. 2020 World Population Data Sheet Shows Older Populations Growing, Total Fertility Rates Declining. *PRB.org*. 2020:2020. https://www.prb.org/2020-world-population-data-sheet/. Accessed May 4, 2021.

3. Ritchie, Hannah; Roser M. Fossil Fuels; Our world in data. *Our world data*. 2018. https://ourworldindata.org/fossil-fuels#when-will-the-world-run-out-of-fossil-fuels. Accessed May 4, 2021.

4. Schwartz BS, Parker CL, Hess J, Frumkin H. Public health and medicine in an age of energy scarcity: The case of petroleum. *Am J Public Health*. 2011;101(9):1560-1567. doi:10.2105/AJPH.2010.205187

5. Green AE, Price-Feeney M, Dorison SH, Pick CJ. Published online ahead of print. *Am J Public Health*. 2020;101(9):1-7. doi:10.2105/AJPH

6. Lee RP. Alternative carbon feedstock for the chemical industry? - Assessing the challenges posed by the human dimension in the carbon transition. *J Clean Prod*. 2019;219:786-796. doi:10.1016/j.jclepro.2019.01.316

7. Winkelmann R, Levermann A, Ridgwell A, Caldeira K. Combustion of available fossil fuel resources sufficient to eliminate the Antarctic Ice Sheet. *Sci Adv*. 2015;1(8).

doi:10.1126/sciadv.1500589

8. Rogelj J, Forster PM, Kriegler E, Smith CJ, Séférian R. Estimating and tracking the remaining carbon budget for stringent climate targets. *Nature*. 2019;571(7765):335-342. doi:10.1038/s41586-019-1368-z

9. SRU German advisory council on the Environment. *Using the CO2 Budget to Meet the Paris Cilmate Targets*.; 2020.

10. Figueres C, Schellnhuber HJ, Whiteman G, Rockström J, Hobley A, Rahmstorf S. Three years to safeguard our climate. *Nature*. 2017;546(7660):593-595. doi:10.1038/546593a

11. Loftus PJ, Cohen AM, Long JCS, Jenkins JD. A critical review of global decarbonization scenarios: What do they tell us about feasibility? *Wiley Interdiscip Rev Clim Chang*. 2015;6(1):93-112. doi:10.1002/wcc.324

12. Lewis NS, Nocera DG. Powering the planet: Chemical challenges in solar energy utilization. *Proc Natl Acad Sci U S A*. 2006;103(43):15729-15735. doi:10.1073/pnas.0603395103

13. Broom D. 5 charts show the rapid fall in costs of renewable energy. 2020. https://energypost.eu/5-charts-show-the-rapid-fall-in-costs-of-renewable-energy/. Accessed May 6, 2021.

14. International Energy Agency. Solar PV – Analysis - IEA. 2020. https://www.iea.org/reports/solar-pv. Published 2020. Accessed May 6, 2021.

15. Lewis NS. Research opportunities to advance solar energy utilization. *Science (80- )*. 2016;351(6271). doi:10.1126/SCIENCE.AAD1920

16. IEA PVPS. Snapshot 2020 - IEA-PVPS. IEA PVPS. https://iea-pvps.org/snapshot-reports/snapshot-2020/. Published 2020. Accessed July 23, 2021.

17. Aprà FM, Smit S, Sterling R, Loureiro T. Overview of the Enablers and Barriers for a Wider Deployment of CSP Tower Technology in Europe. *Clean Technol*. 2021;3(2):377-394. doi:10.3390/cleantechnol3020021

18. Boubault A, Ho CK, Hall A, Lambert TN, Ambrosini A. Durability of solar absorber coatings and their cost-effectiveness. *Sol Energy Mater Sol Cells*. 2017;166(March):176-184. doi:10.1016/j.solmat.2017.03.010

19. Loureiro T, Sterling R, Testani C, et al. Next Generation of Concentrated Solar Power Technologies. *Proceedings*. 2019;20(1):7. doi:10.3390/proceedings2019020007

20. Mahlia TMI, Saktisahdan TJ, Jannifar A, Hasan MH, Matseelar HSC. A review of available methods and development on energy storage; Technology update. *Renew Sustain Energy Rev*. 2014;33:532-545. doi:10.1016/j.rser.2014.01.068

21. Chen H, Cong TN, Yang W, Tan C, Li Y, Ding Y. Progress in electrical energy storage system: A critical review. *Prog Nat Sci*. 2009;19(3):291-312.

doi:10.1016/j.pnsc.2008.07.014

22. Beaudin M, Zareipour H, Schellenberglabe A, Rosehart W. Energy storage for mitigating the variability of renewable electricity sources: An updated review. *Energy Sustain Dev*. 2010;14(4):302-314. doi:10.1016/j.esd.2010.09.007

23. Behabtu HA, Messagie M, Coosemans T, et al. A review of energy storage technologies' application potentials in renewable energy sources grid integration. *Sustain*. 2020;12(24):1-20. doi:10.3390/su122410511

24. Kharel S, Shabani B. Hydrogen as a long-term large-scale energy storage solution to support renewables. *Energies*. 2018;11(10). doi:10.3390/en11102825

25. Yilanci A, Dincer I, Ozturk HK. A review on solar-hydrogen/fuel cell hybrid energy systems for stationary applications. *Prog Energy Combust Sci*. 2009;35(3):231-244. doi:10.1016/j.pecs.2008.07.004

26. Stored Solar : Low Cost PV Driven Electrolysis. https://www.storedsolar.com/electrolysers.html. Accessed July 13, 2021.

27. Barlev D, Vidu R, Stroeve P. Innovation in concentrated solar power. *Sol Energy Mater Sol Cells*. 2011;95(10):2703-2725. doi:10.1016/j.solmat.2011.05.020

28. Deng Z, Zhou J, Miao L, et al. The emergence of solar thermal utilization: solar-driven steam generation. *J Mater Chem A*. 2017;5(17):7691-7709. doi:10.1039/C7TA01361B

29. Kennedy CE. Review of Mid- to High- Temperature Solar Selective Absorber Materials Review of Mid- to High- Temperature Solar Selective Absorber Materials. *Tech Rep Natl Renew Energy Lab*. 2002;NREL/TP-25(July).

30. Xu K, Du M, Hao L, Mi J, Yu Q, Li S. A review of high-temperature selective absorbing coatings for solar thermal applications. *J Mater*. 2020;6(1):167-182. doi:10.1016/j.jmat.2019.12.012

31. Granqvist CG. Solar Energy Materials. *Adv Mater*. 2003;15(21):1789-1803.

32. Cao F, McEnaney K, Chen G, Ren Z. A review of cermet-based spectrally selective solar absorbers. *Energy Environ Sci*. 2014;7(5):1615-1627. doi:10.1039/c3ee43825b

33. Ho CK, Mahoney AR, Ambrosini A, Bencomo M, Hall A, Lambert TN. Characterization of Pyromark 2500 Paint for High-Temperature Solar Receivers. *J Sol Energy Eng*. 2014;136(1):2014-2017. doi:10.1115/1.4024031

34. Selvakumar N, Krupanidhi SB, Barshilia HC. Carbon nanotube-based tandem absorber with tunable spectral selectivity: Transition from near-perfect blackbody absorber to solar selective absorber. *Adv Mater*. 2014;26(16):2552-2557. doi:10.1002/adma.201305070

35. Abendroth T, Althues H, Mäder G, Härtel P, Kaskel S, Beyer E. Selective absorption of Carbon Nanotube thin films for solar energy applications. *Sol Energy Mater Sol Cells*. 2015;143:553-556. doi:10.1016/j.solmat.2015.07.044

36. McKone JR, Lewis NS, Gray HB. Will solar-driven water-splitting devices see the light of day? *Chem Mater*. 2014;26(1):407-414. doi:10.1021/cm4021518

37. Ardo S, Fernandez Rivas D, Modestino MA, et al. Pathways to electrochemical solar-hydrogen technologies. *Energy Environ Sci*. 2018;11(10):2768-2783. doi:10.1039/c7ee03639f

38. Yang W, Prabhakar RR, Tan J, Tilley SD, Moon J. Strategies for enhancing the photocurrent, photovoltage, and stability of photoelectrodes for photoelectrochemical water splitting. *Chem Soc Rev*. 2019;48(19):4979-5015. doi:10.1039/c8cs00997j

39. Yao T, An X, Han H, Chen JQ, Li C. Photoelectrocatalytic Materials for Solar Water Splitting. *Adv Energy Mater*. 2018;8(21):1-36. doi:10.1002/aenm.201800210

40. Blanksby SJ, Ellison GB. Bond dissociation energies of organic molecules. *Acc Chem Res*. 2003;36(4):255-263. doi:10.1021/ar020230d

41. Haschke S, Mader M, Schlicht S, et al. Direct oxygen isotope effect identifies the rate-determining step of electrocatalytic OER at an oxidic surface. *Nat Commun*. 2018;9(1). doi:10.1038/s41467-018-07031-1

42. Chen HM, Chen CK, Liu RS, Zhang L, Zhang J, Wilkinson DP. Nano-architecture and material designs for water splitting photoelectrodes. *Chem Soc Rev*. 2012;41(17):5654-5671. doi:10.1039/c2cs35019j

43. Baxter JB, Richter C, Schmuttenmaer CA. Ultrafast carrier dynamics in nanostructures for solar fuels. *Annu Rev Phys Chem*. 2014;65(December 2013):423-447. doi:10.1146/annurev-physchem-040513-103742

44. Ros C, Andreu T, Morante JR. Photoelectrochemical water splitting: a road from stable metal oxides to protected thin film solar cells. *J Mater Chem A*. 2020;8(21):10625-10669. doi:10.1039/d0ta02755c

45. Chen S, Wang LW. Thermodynamic oxidation and reduction potentials of photocatalytic semiconductors in aqueous solution. *Chem Mater*. 2012;24(18):3659-3666. doi:10.1021/cm302533s

46. Li J, Wu N. Semiconductor-based photocatalysts and photoelectrochemical cells for solar fuel generation: A review. *Catal Sci Technol*. 2015;5(3):1360-1384. doi:10.1039/c4cy00974f

47. Peng T, Zeng P, Ke D, Liu X, Zhang X. Hydrothermal preparation of multiwalled carbon nanotubes (MWCNTs)/CdS nanocomposite and its efficient photocatalytic hydrogen production under visible light irradiation. *Energy and Fuels*. 2011;25(5):2203-2210. doi:10.1021/ef200369z

48. Rai S, Ikram A, Sahai S, Dass S, Shrivastav R, Satsangi VR. CNT based photoelectrodes for PEC generation of hydrogen: A review. *Int J Hydrogen Energy*. 2017;42(7):3994-4006. doi:10.1016/j.ijhydene.2016.10.024

49. Sulong AB, Muhamad N, Sahari J, Ramli R, Deros BM, Park J. Electrical conductivity behaviour of chemical functionalized MWCNTs epoxy nanocomposites. *Eur J Sci Res*. 2009;29(1):13-21.

50. Carlos Guerra, Yucheng Zhang, Meng Li, Vipin Chawla, Rolf Erni, Johann Michler, Hyung Gyu Park and IU. Morphology and Crystallinity Control of Ultrathin TiO2 Layers Deposited on Carbon Nanotubes by Temperature-Step Atomic Layer Deposition. *Nanoscale*. 2015;7(24):10622-10633. doi:10.1039/C5NR02106E

51. Eder D. Carbon Nanotube-Inorganic Hybrids. *Chem Rev*. 2010;110(3):1348-1385. doi:10.1021/cr800433k

52. Zhang W De, Xu B, Jiang LC. Functional hybrid materials based on carbon nanotubes and metal oxides. *J Mater Chem*. 2010;20(31):6383-6391. doi:10.1039/b926341a

53. Aksel S, Eder D. Catalytic effect of metal oxides on the oxidation resistance in carbon nanotube-inorganic hybrids. *J Mater Chem*. 2010;20(41):9149-9154. doi:10.1039/c0jm01129k

54. Mallakpour S, Khadem E. Carbon nanotube–metal oxide nanocomposites: Fabrication, properties and applications. *Chem Eng J*. 2016;302:344-367. doi:10.1016/j.cej.2016.05.038

55. Correa-Duarte MA, Grzelczak M, Salgueiriño-Maceira V, et al. Alignment of carbon nanotubes under low magnetic fields through attachment of magnetic nanoparticles. *J Phys Chem B*. 2005;109(41):19060-19063. doi:10.1021/jp0544890

56. Backes C, Hirsch A. Noncovalent Functionalization of Carbon Nanotubes. *Chem Nanocarbons*. 2010;42(8):1-48. doi:10.1002/9780470660188.ch1

57. Klein KL, Melechko A V., McKnight TE, et al. Surface characterization and functionalization of carbon nanofibers. *J Appl Phys*. 2008;103(6). doi:10.1063/1.2840049

58. Fabian Buffa, Gustavo A. Abraham, Brian P. Grady DR. Effect of nanotube functionalization on the properties of single-walled carbon nanotube/polyurethane composites. *J Polym Sci Part B Polym Phys*. 2007;45:490-501. doi:10.1002/polb.21069

59. Lee CY, Tsai HM, Chuang HJ, Li SY, Lin P, Tseng TY. Characteristics and Electrochemical Performance of Supercapacitors with Manganese Oxide-Carbon Nanotube Nanocomposite Electrodes. *J Electrochem Soc*. 2005;152(4):A716. doi:10.1149/1.1870793

60. Long H, Guo C, Wei G, Jiang L, Yu Y. Facile synthesis of various carbon nanotube/metal oxide nanocomposites with high quality. *Vacuum*. 2019;166(May):147-150. doi:10.1016/j.vacuum.2019.05.002

61. Li Z, Gao B, Chen GZ, Mokaya R, Sotiropoulos S, Li Puma G. Carbon nanotube/titanium dioxide (CNT/TiO2) core-shell nanocomposites with tailored shell thickness, CNT content and photocatalytic/photoelectrocatalytic properties. *Appl Catal B Environ*.

2011;110:50-57. doi:10.1016/j.apcatb.2011.08.023

62. Németh Z, Dieker C, Kukovecz Á, et al. Preparation of homogeneous titania coating on the surface of MWNT. *Compos Sci Technol*. 2011;71(2):87-94. doi:10.1016/j.compscitech.2010.10.017

63. Rajasekar K, Thennarasu S, Rajesh R, Abirami R, Balkis Ameen K, Ramasubbu A. Preparation of mesoporous TiO2/CNT nanocomposites by synthesis of mesoporous titania via EISA and their photocatalytic degradation under visible light irradiation. *Solid State Sci*. 2013;26:45-52. doi:10.1016/j.solidstatesciences.2013.09.003

64. Sampaio MJ, Marques RRN, Tavares PB, Faria JL, Silva AMT, Silva CG. Tailoring the properties of immobilized titanium dioxide/carbon nanotube composites for photocatalytic water treatment. *J Environ Chem Eng*. 2013;1(4):945-953. doi:10.1016/j.jece.2013.08.014

65. Silva CG, Sampaio MJ, Marques RRN, et al. Photocatalytic production of hydrogen from methanol and saccharides using carbon nanotube-TiO2 catalysts. *Appl Catal B Environ*. 2015;178:82-90. doi:10.1016/j.apcatb.2014.10.032

66. Kovtyukhova NI, Mallouk TE, Pan L, Dickey EC. Individual single-walled nanotubes and hydrogels made by oxidative exfoliation of carbon nanotube ropes. *J Am Chem Soc*. 2003;125(32):9761-9769. doi:10.1021/ja0344516

67. Lee S, Peng JW. Effect of plasma treatment on electrical conductivity and Raman spectra of carbon nanotubes. *J Phys Chem Solids*. 2011;72(9):1101-1103. doi:10.1016/j.jpcs.2011.06.012

68. Zhang W De. Growth of ZnO nanowires on modified well-aligned carbon nanotube arrays. *Nanotechnology*. 2006;17(4):1036-1040. doi:10.1088/0957-4484/17/4/032

69. Long H, Guo C, Wei G, Jiang L, Yu Y. Facile synthesis of various carbon nanotube/metal oxide nanocomposites with high quality. *Vacuum*. 2019;166(March):147-150. doi:10.1016/j.vacuum.2019.05.002

70. Liu WW, Lu C, Liang K, Tay BK. A three dimensional vertically aligned multiwall carbon nanotube/NiCo 2O4 core/shell structure for novel high-performance supercapacitors. *J Mater Chem A*. 2014;2(14):5100-5107. doi:10.1039/c4ta00107a

71. Kim P, Shi L, Majumdar A, McEuen PL. Thermal transport measurements of individual multiwalled nanotubes. *Phys Rev Lett*. 2001;87(21):215502-1-215502-215504. doi:10.1103/PhysRevLett.87.215502

72. Yang DJ, Zhang Q, Chen G, et al. Thermal conductivity of multiwalled carbon nanotubes. *Phys Rev B - Condens Matter Mater Phys*. 2002;66(16):1-6. doi:10.1103/PhysRevB.66.165440

73. Kumanek B, Janas D. Thermal conductivity of carbon nanotube networks: a review. *J Mater Sci*. 2019;54(10):7397-7427. doi:10.1007/s10853-019-03368-0

74. Boroushak SH, Ansari R, Ajori S. Molecular dynamics simulations of the thermal

conductivity of cross-linked functionalized single- and double-walled carbon nanotubes with polyethylene chains. *Diam Relat Mater*. 2018;86(April):173-178. doi:10.1016/j.diamond.2018.04.023

75. Park JG, Cheng Q, Lu J, et al. Thermal conductivity of MWCNT/epoxy composites: The effects of length, alignment and functionalization. *Carbon N Y*. 2012;50(6):2083-2090. doi:10.1016/j.carbon.2011.12.046

76. Bryntesen SN, Strømman AH, Tolstorebrov I, Shearing PR, Lamb JJ, Stokke Burheim O. Opportunities for the state-of-the-art production of lib electrodes—a review. *Energies*. 2021;14(5). doi:10.3390/en14051406

77. Jayababu N, Jo S, Kim Y, Kim D. Preparation of NiO decorated CNT/ZnO core-shell hybrid nanocomposites with the aid of ultrasonication for enhancing the performance of hybrid supercapacitors. *Ultrason Sonochem*. 2021;71:105374. doi:10.1016/j.ultsonch.2020.105374

78. Zhu Y, Elim HI, Foo YL, et al. Multiwalled carbon nanotubes beaded with ZnO nanoparticles for ultrafast nonlinear optical switching. *Adv Mater*. 2006;18(5):587-592. doi:10.1002/adma.200501918

79. Ikuno T, Yasuda T, Honda SI, et al. Coating carbon nanotubes with inorganic materials by pulsed laser deposition. *J Appl Phys*. 2005;98(11). doi:10.1063/1.2035891

80. Liu J, Li X, Dai L. Water-assisted growth of aligned carbon nanotube-ZnO heterojunction arrays. *Adv Mater*. 2006;18(13):1740-1744. doi:10.1002/adma.200502346

81. Knez M, Nielsch K, Niinistö L. Synthesis and surface engineering of complex nanostructures by atomic layer deposition. *Adv Mater*. 2007;19(21):3425-3438. doi:10.1002/adma.200700079

82. Gomathi A, Vivekchand SRC, Govindaraj A, Rao CNR. Chemically bonded ceramic oxide coatings on carbon nanotubes and inorganic nanowires. *Adv Mater*. 2005;17(22):2757-2761. doi:10.1002/adma.200500539

83. Lijima S. Helical microtubules of graphitic carbon. *Nature*. 1991;354:56-58.

84. Balasubramanian K, Burghard M. Chemically functionalized carbon nanotubes. *Small*. 2005;1(2):180-192. doi:10.1002/smll.200400118

85. Itkis ME, Perea DE, Jung R, Niyogi S, Haddon RC. Comparison of analytical techniques for purity evaluation of single-walled carbon nanotubes. *J Am Chem Soc*. 2005;127(10):3439-3448. doi:10.1021/ja043061w

86. Lin M, Shyu F. Optical properties of well-aligned multiwalled carbon nanotube bundles. *Phys Rev B - Condens Matter Mater Phys*. 2000;61(20):14114-14118. doi:10.1103/PhysRevB.61.14114

87. Wu Z, Chen Z, Du X, et al. Transparent, conductive carbon nanotube films. *Science (80- )*. 2004;305(5688):1273-1276. doi:10.1126/science.1101243

88. Li J, Hu L, Wang L, Zhou Y, Grüner G, Marks TJ. Organic light-emitting diodes having carbon nanotube anodes. *Nano Lett*. 2006;6(11):2472-2477. doi:10.1021/nl061616a

89. Yang ZP, Ci L, Bur JA, Lin SY, Ajayan PM. Experimental observation of an extremely dark material made by a low-density nanotube array. *Nano Lett*. 2008;8(2):446-451. doi:10.1021/nl072369t

90. Wang XJ, Wang LP, Adewuyi OS, Cola BA, Zhang ZM. Highly specular carbon nanotube absorbers. *Appl Phys Lett*. 2010;97(16):1-4. doi:10.1063/1.3502597

91. Yang ZP, Hsieh ML, Bur JA, et al. Experimental observation of extremely weak optical scattering from an interlocking carbon nanotube array. *Appl Opt*. 2011;50(13):1850-1855. doi:10.1364/AO.50.001850

92. Lehman J, Yung C, Tomlin N, Conklin D, Stephens M. Carbon nanotube-based black coatings. *Appl Phys Rev*. 2018;5(1). doi:10.1063/1.5009190

93. Hagopian JG, Getty SA, Quijada M, et al. Multiwalled carbon nanotubes for stray light suppression in space flight instruments. In: *Carbon Nanotubes, Graphene, and Associated Devices III*. Vol 7761. ; 2010:77610F. doi:10.1117/12.864386

94. Surnev S, Ramsey MG, Netzer FP. Vanadium oxide surface studies. *Prog Surf Sci*. 2003;73(4-8):117-165. doi:10.1016/j.progsurf.2003.09.001

95. B GJ. Anomalous properties of the vanadium oxides. *Annu Rev Mater Sci*. 1971;1(101-138). doi:10.1146/annurev.ms.01.080171.000533

96. Bahlawane BN, Lenoble D. Vanadium Oxide Compounds : Structure , Properties , and Growth from the Gas Phase. 2014:299-311. doi:10.1002/cvde.201400057

97. Lopez R, Haynes TE, Boatner LA, Feldman LC, Haglund RF. Size effects in the structural phase transition of VO2 nanoparticles. *Phys Rev B - Condens Matter Mater Phys*. 2002;65(22):2241131-2241135. doi:10.1103/PhysRevB.65.224113

98. Prasadam VP, Bahlawane N, Mattelaer F, et al. Atomic layer deposition of vanadium oxides: process and application review. *Mater Today Chem*. 2019;12:396-423. doi:10.1016/j.mtchem.2019.03.004

99. Prasadam VP, Dey B, Bulou S, Schenk T, Bahlawane N. Study of VO 2 thin film synthesis by atomic layer deposition. *Mater Today Chem*. 2019;12:332-342. doi:10.1016/j.mtchem.2019.03.005

100. Yang Z, Ko C, Ramanathan S. Oxide Electronics Utilizing Ultrafast Metal-Insulator Transitions. *Annu Rev Mater Res*. 2011;41(1):337-367. doi:10.1146/annurev-matsci-062910-100347

101. Janotti A, Van De Walle CG. Fundamentals of zinc oxide as a semiconductor. *Reports Prog Phys*. 2009;72(12). doi:10.1088/0034-4885/72/12/126501

102. Janotti A, Van De Walle CG. New insights into the role of native point defects in ZnO. *J Cryst Growth*. 2006;287(1):58-65. doi:10.1016/j.jcrysgro.2005.10.043

103. Van De Walle CG. Defect analysis and engineering in ZnO. *Phys B Condens Matter*. 2001;308-310:899-903. doi:10.1016/S0921-4526(01)00830-4

104. Karpina VA, Lazorenko VI, Lashkarev C V., et al. Zinc oxide - Analogue of GaN with new perspective possibilities. *Cryst Res Technol*. 2004;39(11):980-992. doi:10.1002/crat.200310283

105. Coleman VA, Jagadish C. Basic Properties and Applications of ZnO. In: *Zinc Oxide Bulk, Thin Films and Nanostructures*. Elsevier Science Ltd; 2006:1-20. doi:10.1016/B978-008044722-3/50001-4

106. Gao Z, Banerjee P. Review Article: Atomic layer deposition of doped ZnO films. *J Vac Sci Technol A*. 2019;37(5):050802. doi:10.1116/1.5112777

107. Law S, Liu R, Wasserman D. Doped semiconductors with band-edge plasma frequencies. *J Vac Sci Technol B, Nanotechnol Microelectron Mater Process Meas Phenom*. 2014;32(5):052601. doi:10.1116/1.4891170

108. Anderson AL, Chen S, Romero L, Top I, Binions R. Thin films for advanced glazing applications. *Buildings*. 2016;6(3). doi:10.3390/buildings6030037

109. Oh B-Y, Han J-W, Seo D-S, et al. Characteristics of Al-Doped ZnO Films Grown by Atomic Layer Deposition for Silicon Nanowire Photovoltaic Device. *J Nanosci Nanotechnol*. 2012;12(7):5330-5335. doi:10.1166/jnn.2012.6255

110. Dresselhaus MS, Avouris P. Introduction to Carbon Materials Research. In: *Carbon Nanotubes*. Springer Berlin Heidelberg; 2007:1-9. doi:10.1007/3-540-39947-X_1

111. Ajayan PM. Nanotubes from Carbon. *Chem Rev*. 1999;99(7):1787-1799. doi:10.1021/cr970102g

112. Ebbesen TW, Lezec HJ, Hiura H, Bennett JW, Ghaemi HF, Thio T. Electrical conductivity of individual carbon nanotubes. *Nature*. 1996;382(6586):54-56. doi:10.1038/382054a0

113. Langer L, Bayot V, Grivei E, et al. Quantum Transport in a Multiwalled Carbon Nanotube. *Phys Rev Lett*. 1996;76(3):479-482. doi:10.1103/PhysRevLett.76.479

114. Frank S, Poncharal P, Wang ZL, De Heer WA. Carbon nanotube quantum resistors. *Science (80- )*. 1998;280(5370):1744-1746. doi:10.1126/science.280.5370.1744

115. Wei BQ, Vajtai R, Ajayan PM. Reliability and current carrying capacity of carbon nanotubes. *Appl Phys Lett*. 2001;79(8):1172-1174. doi:10.1063/1.1396632

116. Li J, Cheng X, Shashurin A, Keidar M. Review of Electrochemical Capacitors Based on Carbon Nanotubes and Graphene. *Graphene*. 2012;01(01):1-13. doi:10.4236/graphene.2012.11001

117. Zhang Q, Huang JQ, Qian WZ, Zhang YY, Wei F. The road for nanomaterials industry: A review of carbon nanotube production, post-treatment, and bulk applications for composites and energy storage. *Small*. 2013;9(8):1237-1265.

doi:10.1002/smll.201203252

118. Pal S, Sahoo M, Veettil VT, et al. Covalently Connected Carbon Nanotubes as Electrocatalysts for Hydrogen Evolution Reaction through Band Engineering. *ACS Catal*. 2017;7(4):2676-2684. doi:10.1021/acscatal.7b00032

119. Valentini L, Armentano I, Kenny JM, Cantalini C, Lozzi L, Santucci S. Sensors for sub-ppm NO2 gas detection based on carbon nanotube thin films. *Appl Phys Lett*. 2003;82(6):961-963. doi:10.1063/1.1545166

120. Kumar SG, Rao KSRK. Zinc oxide based photocatalysis: Tailoring surface-bulk structure and related interfacial charge carrier dynamics for better environmental applications. *RSC Adv*. 2015;5(5):3306-3351. doi:10.1039/c4ra13299h

121. Qi K, Cheng B, Yu J, Ho W. Review on the improvement of the photocatalytic and antibacterial activities of ZnO. *J Alloys Compd*. 2017;727:792-820. doi:10.1016/j.jallcom.2017.08.142

122. Shaikh AF, Arbuj SS, Tamboli MS, Naik SD, Rane SB, Kale BB. ZnSe/ZnO Nano-Heterostructures for Enhanced Solar Light Hydrogen Generation. *ChemistrySelect*. 2017;2(28):9174-9180. doi:10.1002/slct.201701618

123. Parrino F, Pomilla FR, Camera-Roda G, Loddo V, Palmisano L. Properties of titanium dioxide. In: *Titanium Dioxide ($Tio_2$) and Its Applications*. INC; 2021:13-66. doi:10.1016/b978-0-12-819960-2.00001-8

124. Ardakani HK. Electrical and optical properties of in situ “hydrogen-reduced” titanium dioxide thin films deposited by pulsed excimer laser ablation. *Thin Solid Films*. 1994;248(2):234-239. doi:10.1016/0040-6090(94)90017-5

125. Lou S, Zhao Y, Wang J, Yin G, Du C, Sun X. Ti-Based Oxide Anode Materials for Advanced Electrochemical Energy Storage: Lithium/Sodium Ion Batteries and Hybrid Pseudocapacitors. *Small*. 2019;15(52):1-44. doi:10.1002/smll.201904740

126. Zheng M, Tang H, Li L, et al. Hierarchically Nanostructured Transition Metal Oxides for Lithium-Ion Batteries. *Adv Sci*. 2018;5(3). doi:10.1002/advs.201700592

127. Kment S, Riboni F, Pausova S, et al. Photoanodes based on TiO2 and α-Fe2O3 for solar water splitting-superior role of 1D nanoarchitectures and of combined heterostructures. *Chem Soc Rev*. 2017;46(12):3716-3769. doi:10.1039/c6cs00015k

128. Chen X, Mao SS. Titanium dioxide nanomaterials: Synthesis, properties, modifications and applications. *Chem Rev*. 2007;107(7):2891-2959. doi:10.1021/cr0500535

129. Creighton JR, Ho P. *Introduction to Chemical Vapor Deposition (CVD)*.; 2001. www.asminternational.org. Accessed July 14, 2021.

130. Deutsch RMO and TF. Laser-Induced Chemistry. *Science (80- )*. 1985;227(4688):709-714. doi:10.1126/science.227.4688.709

131. Pola J, Parsons JP, Taylor R. Deposition of germanium by laser-induced photolysis of

organogermanes in the liquid phase. *J Mater Chem*. 1992;2(12):1289-1292. doi:10.1039/jm9920201289

132. Choy KL. Chemical vapour deposition of coatings. *Prog Mater Sci*. 2003;48(2):57-170. doi:10.1016/S0079-6425(01)00009-3

133. Stringfellow GB. Fundamental Aspects of MOVPE. In: *Metalorganic Vapor Phase Epitaxy (MOVPE)*. Wiley Online Library; 2019:19-69. doi:10.1002/9781119313021.ch2

134. Fauzi FB, Ismail E, Syed Abu Bakar SN, et al. The role of gas-phase dynamics in interfacial phenomena during few-layer graphene growth through atmospheric pressure chemical vapour deposition. *Phys Chem Chem Phys*. 2020;22(6):3481-3489. doi:10.1039/c9cp05346h

135. Sun L, Yuan G, Gao L, et al. Chemical vapour deposition. *Nat Rev Methods Prim 1*. 2021;1(1):1-20. doi:10.1038/s43586-020-00005-y

136. Pierson HO. Fundamentals of Chemical Vapor Deposition. In: *Handbook of Chemical Vapor Deposition (CVD)*. William Andrew Publishing; 1999:36-67. doi:10.1016/B978-081551432-9.50005-X

137. Jones AC, Hitchman ML. Chapter 1:Overview of Chemical Vapour Deposition. In: *Chemical Vapour Deposition*. ; 2008:1-36. doi:10.1039/9781847558794-00001

138. Yan X-T, Xu Y. *Chemical Vapour Deposition An Integrated Engineering Design for Advanced Materials*. Springer; 2010.

139. Hitchman ML, Kane J, Widmer AE. Polysilicon growth kinetics in a low pressure chemical vapour deposition reactor. *Thin Solid Films*. 1979;59(2):231-247. doi:10.1016/0040-6090(79)90296-7

140. Bryant WA. The fundamentals of chemical vapour deposition. *J Mater Sci*. 1977;12(7):1285-1306. doi:10.1007/BF00540843

141. Hwang NM, Yoon DY. Thermodynamic approach to the chemical vapor deposition process. *J Cryst Growth*. 1994;143(1-2):103-109. doi:10.1016/0022-0248(94)90372-7

142. Blocher JM. Structure/Property/Process Relationships in Chemical Vapor Deposition Cvd. *J Vac Sci Technol*. 1974;11(4):680-686. doi:10.1116/1.1312735

143. Manawi YM, Ihsanullah, Samara A, Al-Ansari T, Atieh MA. A review of carbon nanomaterials' synthesis via the chemical vapor deposition (CVD) method. *Materials (Basel)*. 2018;11(5). doi:10.3390/ma11050822

144. Kim D, Giermann AL, Thompson C V. Solid-state dewetting of patterned thin films. *Appl Phys Lett*. 2009;95(25):1-36. doi:10.1063/1.3268477

145. Choi YC, Shin YM, Lim SC, et al. Effect of surface morphology of Ni thin film on the growth of aligned carbon nanotubes by microwave plasma-enhanced chemical vapor deposition. *J Appl Phys*. 2000;88(8):4898-4903. doi:10.1063/1.1314614

146. Chhowalla M, Teo KBK, Ducati C, et al. Growth process conditions of vertically aligned

carbon nanotubes using plasma enhanced chemical vapor deposition. *J Appl Phys*. 2001;90(10):5308-5317. doi:10.1063/1.1410322

147. Wei YY, Eres G, Merkulov VI, Lowndes DH. Effect of catalyst film thickness on carbon nanotube growth by selective area chemical vapor deposition. *Appl Phys Lett*. 2001;78(10):1394-1396. doi:10.1063/1.1354658

148. Liu BC, Lee TJ, Lee SH, Park CY, Lee CJ. Large-scale synthesis of high-purity well-aligned carbon nanotubes using pyrolysis of iron(II) phthalocyanine and acetylene. *Chem Phys Lett*. 2003;377(1-2):55-59. doi:10.1016/S0009-2614(03)01092-3

149. Baker RTK, Barber MA, Harris PS, Feates FS, Waite RJ. Nucleation and growth of carbon deposits from the nickel catalyzed decomposition of acetylene. *J Catal*. 1972;26(1):51-62. doi:10.1016/0021-9517(72)90032-2

150. Baker RTK. Catalytic Growth. *Carbon N Y*. 1989;27(3):315-323.

151. Azam MA, Manaf NSA, Talib E, Bistamam MSA. Aligned carbon nanotube from catalytic chemical vapor deposition technique for energy storage device: A review. *Ionics (Kiel)*. 2013;19(11):1455-1476. doi:10.1007/s11581-013-0979-x

152. Liu H, Takagi D, Ohno H, Chiashi S, Chokan T, Homma Y. Growth of single-walled carbon nanotubes from ceramic particles by alcohol chemical vapor deposition. *Appl Phys Express*. 2008;1(1):1-4. doi:10.1143/APEX.1.014001

153. Iii SAS, Baumann TF, Bayer BC, et al. Zr catalyst-carbon-J. am. chem. soc.pdf. 2009;(3):12144-12154. doi:10.1016/j.carbon.2008.10.047.(29)

154. Persson AI, Larsson MW, Stenström S, Ohlsson BJ, Samuelson L, Wallenberg LR. Solid-phase diffusion mechanism for GaAs nanowire growth. *Nat Mater*. 2004;3(10):677-681. doi:10.1038/nmat1220

155. Takagi D, Hibino H, Suzuki S, Kobayashi Y. 200_14a.Carbon Nanotube Growth from.pdf. 2007;2:1-4.

156. Noda S, Hasegawa K, Sugime H, et al. Millimeter-thick single-walled carbon nanotube forests: Hidden role of catalyst support. *Japanese J Appl Physics, Part 2 Lett*. 2007;46(17-19):0-3. doi:10.1143/JJAP.46.L399

157. Magrez A, Smajda R, Seo JW, et al. Striking influence of the catalyst support and its acid-base properties: New insight into the growth mechanism of carbon nanotubes. *ACS Nano*. 2011;5(5):3428-3437. doi:10.1021/nn200012z

158. Prasadam VP, Ramirez F V., Papakonstantinou I, Parkin IP, Bahlawane N. Thermoresponsive Black VO2-Carbon Nanotube Composite Coatings for Solar Energy Harvesting. *ACS Appl Nano Mater*. 2020;3(9):8848-8857. doi:10.1021/acsanm.0c01630

159. Johnson RW, Hultqvist A, Bent SF. A brief review of atomic layer deposition: from fundamentals to applications. *Mater Today*. 2014;17(5):236-246. doi:10.1016/J.MATTOD.2014.04.026

160. Vervuurt RHJ, Kessels WMME, Bol AA. Atomic Layer Deposition for Graphene Device Integration. *Adv Mater Interfaces*. 2017;4(18):1-19. doi:10.1002/admi.201700232

161. Puurunen RL. Growth Per Cycle in Atomic Layer Deposition: A Theoretical Model. *Chem Vap Depos*. 2003;9(5):249-257. doi:10.1002/cvde.200306265

162. Muneshwar T, Cadien K. Surface reaction kinetics in atomic layer deposition: An analytical model and experiments. *J Appl Phys*. 2018;124(9). doi:10.1063/1.5044456

163. Puurunen RL. Surface chemistry of atomic layer deposition: A case study for the trimethylaluminum/water process. *J Appl Phys*. 2005;97(12). doi:10.1063/1.1940727

164. Richey NE, De Paula C, Bent SF. Understanding chemical and physical mechanisms in atomic layer deposition. *J Chem Phys*. 2020;152(4). doi:10.1063/1.5133390

165. Barry ST, Teplyakov A V., Zaera F. The Chemistry of Inorganic Precursors during the Chemical Deposition of Films on Solid Surfaces. *Acc Chem Res*. 2018;51(3):800-809. doi:10.1021/acs.accounts.8b00012

166. Dillon AC, Ott AW, Way JD, George SM. Surface chemistry of Al2O3 deposition using Al(CH3)3 and H2O in a binary reaction sequence. *Surf Sci*. 1995;322(1-3):230-242. doi:10.1016/0039-6028(95)90033-0

167. Lakomaa EL, Root A, Suntola T. Surface reactions in Al 2 O 3 growth from trimethylaluminium and water by atomic layer epitaxy. *Appl Surf Sci*. 1996;107(100):107-115. doi:10.1016/S0169-4332(96)00513-2

168. Laubengayer AW, Gilliam WF. The Alkyls of the Third Group Elements. I. Vapor Phase Studies of the Alkyls of Aluminum, Gallium and Indium. *J Am Chem Soc*. 1941;63(2):477-479. doi:10.1021/ja01847a031

169. Elliott SD, Greer JC. Simulating the atomic layer deposition of alumina from first principles. *J Mater Chem*. 2004;14(21):3246-3250. doi:10.1039/b405776g

170. MacKus AJM, Leick N, Baker L, Kessels WMM. Catalytic combustion and dehydrogenation reactions during atomic layer deposition of platinum. *Chem Mater*. 2012;24(10):1752-1761. doi:10.1021/cm203812v

171. Singh JA, Thissen NFW, Kim WH, et al. Area-Selective Atomic Layer Deposition of Metal Oxides on Noble Metals through Catalytic Oxygen Activation. *Chem Mater*. 2018;30(3):663-670. doi:10.1021/acs.chemmater.7b03818

172. M.Y. Li, Y.Y. Chang, H.C. Wu, C.S. Huang, J.C. Chen JLL and SMC. Effect of Process Pressure on Atomic Layer Deposition of Al2O3. *ECS Trans*. 2007;3(19):107-117.

173. Kuse R, Kundu M, Yasuda T, Miyata N, Toriumi A. Effect of precursor concentration in atomic layer deposition of Al 2O3. *J Appl Phys*. 2003;94(10):6411-6416. doi:10.1063/1.1618918

174. Poodt P, Mameli A, Schulpen J, Kessels WMM (Erwin), Roozeboom F. Effect of reactor pressure on the conformal coating inside porous substrates by atomic layer

deposition. *J Vac Sci Technol A Vacuum, Surfaces, Film*. 2017;35(2):021502. doi:10.1116/1.4973350

175. Matero R, Rahtu A, Ritala M, Leskelä M, Sajavaara T. Effect of water dose on the atomic layer deposition rate of oxide thin films. *Thin Solid Films*. 2000;368(1):1-7. doi:10.1016/S0040-6090(00)00890-7

176. Putkonen M, Sajavaara T, Johansson LS, Niinistö L. Low-temperature ALE deposition of Y2O3 thin films from β-diketonate precursors. *Chem Vap Depos*. 2001;7(1):44-50. doi:10.1002/1521-3862(200101)7:1<44::AID-CVDE44>3.0.CO;2-Q

177. Puurunen RL. Growth per cycle in atomic layer deposition: Real application examples of a theoretical model. *Chem Vap Depos*. 2003;9(6):327-332. doi:10.1002/cvde.200306266

178. Puurunen RL. Correlation between the growth-per-cycle and the surface hydroxyl group concentration in the atomic layer deposition of aluminum oxide from trimethylaluminum and water. *Appl Surf Sci*. 2005;245(1-4):6-10. doi:10.1016/j.apsusc.2004.10.003

179. Ott AW, Klaus JW, Johnson JM, George SM. "Al2O3 thin film growth on Si (100) using binary reaction sequence chemistry." *Thin Solid Films*. 2009;517(20):5950. doi:10.1016/j.tsf.2009.01.027

180. Aarik J, Aidla A, Kiisler AA, Uustare T, Sammelselg V. Effect of crystal structure on optical properties of TiO2 films grown by atomic layer deposition. *Thin Solid Films*. 1997;305(1-2):270-273. doi:10.1016/S0040-6090(97)00135-1

181. Becker JS, Suh S, Wang S, Gordon RG. Highly conformal thin films of tungsten nitride prepared by atomic layer deposition from a novel precursor. *Chem Mater*. 2003;15(15):2969-2976. doi:10.1021/cm021772s

182. Suntola T. Surface chemistry of materials deposition at atomic layer level. *Appl Surf Sci*. 1996;100-101:391-398. doi:10.1016/0169-4332(96)00306-6

183. Ritala M, Niinistö J. Chapter 4:Atomic Layer Deposition. In: *Chemical Vapour Deposition*. ; 2008:158-206. doi:10.1039/9781847558794-00158

184. Puurunen RL, Vandervorst W. Island growth as a growth mode in atomic layer deposition: A phenomenological model. *J Appl Phys*. 2004;96(12):7686-7695. doi:10.1063/1.1810193

185. Miikkulainen V, Leskelä M, Ritala M, Puurunen RL. Crystallinity of inorganic films grown by atomic layer deposition: Overview and general trends. *J Appl Phys*. 2013;113(2). doi:10.1063/1.4757907

186. Aarik J, Aidla A, Mändar H, Uustare T, Kukli K, Schuisky M. Phase transformations in hafnium dioxide thin films grown by atomic layer deposition at high temperatures. *Appl Surf Sci*. 2001;173(1-2):15-21. doi:10.1016/S0169-4332(00)00859-X

187. Kai-Erik Elers, Mikko Ritala, Markku Leskeli ER'. NbCl, as a precursor in atomic layer

epitaxy Kai-Erik. *Appl Surf Sci*. 1994;82-83:468-474. doi:10.1016/0169-4332(94)90260-7

188. Ylilammi M. Monolayer thickness in atomic layer deposition. *Thin Solid Films*. 1996;279(1-2):124-130. doi:10.1016/0040-6090(95)08159-3

189. Puurunen RL, Lindblad M, Rootc A, Krausea AOI. Successive reactions of gaseous trimethylaluminium and ammonia on porous alumina. *Phys Chem Chem Phys*. 2001;3(6):1093-1102. doi:10.1039/b007249o

190. Putkonen M, Niinistö J, Kukli K, et al. ZrO2 thin films grown on silicon substrates by atomic layer deposition with Cp2Zr(CH3)2 and water as precursors. *Chem Vap Depos*. 2003;9(4):207-212. doi:10.1002/cvde.200306254

191. Johnson AM, Stair PC. Alternative low-pressure surface chemistry of titanium tetraisopropoxide on oxidized molybdenum. *J Phys Chem C*. 2014;118(50):29361-29369. doi:10.1021/jp505653u

192. Elam JW, Schuisky M, Ferguson JD, George SM. Surface chemistry and film growth during TiN atomic layer deposition using TDMAT and NH3. *Thin Solid Films*. 2003;436(2):145-156. doi:10.1016/S0040-6090(03)00533-9

193. Lee B, Choi KJ, Hande A, et al. A novel thermally-stable zirconium amidinate ALD precursor for ZrO2 thin films. *Microelectron Eng*. 2009;86(3):272-276. doi:10.1016/j.mee.2008.03.020

194. Ponraj JS, Attolini G, Bosi M. Review on atomic layer deposition and applications of oxide thin films. *Crit Rev Solid State Mater Sci*. 2013;38(3):203-233. doi:10.1080/10408436.2012.736886

195. Blanquart T, Niinistö J, Ritala M, Leskelä M. Atomic layer deposition of groups 4 and 5 transition metal oxide thin films: Focus on heteroleptic precursors. *Chem Vap Depos*. 2014;20(7-9):189-208. doi:10.1002/cvde.201400055

196. Sheng J, Lee J-H, Choi W-H, Hong T, Kim M, Park J-S. Review Article: Atomic layer deposition for oxide semiconductor thin film transistors: Advances in research and development. *J Vac Sci Technol A*. 2018;36(6):060801. doi:10.1116/1.5047237

197. Tynell T, Karppinen M. Atomic layer deposition of ZnO: A review. *Semicond Sci Technol*. 2014;29(4). doi:10.1088/0268-1242/29/4/043001

198. Na JS, Peng Q, Scarel G, Parsons GN. Role of gas doping sequence in surface reactions and dopant incorporation during atomic layer deposition of Al-Doped ZnO. *Chem Mater*. 2009;21(23):5585-5593. doi:10.1021/cm901404p

199. Hu J, Gordon RG. Textured aluminum-doped zinc oxide thin films from atmospheric pressure chemical-vapor deposition. *J Appl Phys*. 1992;71(2):880-890. doi:10.1063/1.351309

200. Wind RA, George SM. Quartz crystal microbalance studies of Al2O3 atomic layer deposition using trimethylaluminum and water at 125 °C. *J Phys Chem A*.

2010;114(3):1281-1289. doi:10.1021/jp9049268

201. Matero R, Rahtu A, Ritala M. In situ quadrupole mass spectrometry and quartz crystal microbalance studies on the atomic layer deposition of titanium dioxide from titanium tetrachloride and water. *Chem Mater*. 2001;13(12):4506-4511. doi:10.1021/cm011046+

202. Lim GT, Kim DH. Characteristics of TiOx films prepared by chemical vapor deposition using tetrakis-dimethyl-amido-titanium and water. *Thin Solid Films*. 2006;498(1-2):254-258. doi:10.1016/j.tsf.2005.07.121

203. Niemelä JP, Marin G, Karppinen M. Titanium dioxide thin films by atomic layer deposition: A review. *Semicond Sci Technol*. 2007;2:1-2. doi:10.1007/s10482-008-9238-y

204. Marichy C, Pinna N. Carbon-nanostructures coated/decorated by atomic layer deposition: Growth and applications. *Coord Chem Rev*. 2013;257(23-24):3232-3253. doi:10.1016/j.ccr.2013.08.007

205. Willinger MG, Neri G, Rauwel E, Bonavita A, Micali G, Pinna N. Vanadium oxide sensing layer grown on carbon nanotubes by a new atomic layer deposition process. *Nano Lett*. 2008;8(12):4201-4204. doi:10.1021/nl801785b

206. Marichy C, Donato N, Latino M, et al. Gas sensing properties and p-type response of ALD TiO2coated carbon nanotubes. *Nanotechnology*. 2015;26(2):24004. doi:10.1088/0957-4484/26/2/024004

207. Szilágyi IM, Bakos LP, Nóra J, et al. Photocatalytic and Gas Sensitive Multiwalled Carbon Prepared by Atomic Layer Deposition. *Nanomaterials*. 2020;10:252.

208. Zhang Y, Utke I, Michler J, Ilari G, Rossell MD, Erni R. Growth and characterization of CNT-TiO2 heterostructures. *Beilstein J Nanotechnol*. 2014;5(1):946-955. doi:10.3762/bjnano.5.108

209. Marichy C, Tessonnier JP, Ferro MC, et al. Labeling and monitoring the distribution of anchoring sites on functionalized CNTs by atomic layer deposition. *J Mater Chem*. 2012;22(15):7323-7330. doi:10.1039/c2jm00088a

210. Guerra-Nuñez C, Putz B, Savu R, et al. The nucleation, radial growth, and bonding of TiO2 deposited via atomic layer deposition on single-walled carbon nanotubes. *Appl Surf Sci*. 2021;555(December 2019). doi:10.1016/j.apsusc.2021.149662

211. Zhang Y, Guerra-Nuñez C, Li M, et al. High Conformity and Large Domain Monocrystalline Anatase on Multiwall Carbon Nanotube Core-Shell Nanostructure: Synthesis, Structure, and Interface. *Chem Mater*. 2016;28(10):3488-3496. doi:10.1021/acs.chemmater.6b01209

212. Nielsen SS. Basic Principles of Spectroscopy. *Instr Man Food Anal Second Ed*. 1998:89-90. doi:10.1007/978-1-4615-5439-4_25

213. Hajduk B, Bednarski H, Trzebicka B. Temperature-Dependent Spectroscopic

Ellipsometry of Thin Polymer Films. *J Phys Chem B*. 2020;124(16):3229-3251. doi:10.1021/acs.jpcb.9b11863

214. Fujiwara H. *Spectroscopic Ellipsometry: Principles and Applications*. John Wiley and Sons; 2007. doi:10.1002/9780470060193

215. Ellipsometry Technology Information - Film Sense Ellipsometer. https://film-sense.com/ellipsometry-technology/#ellipsometry. Accessed August 3, 2021.

216. Bashir S, Liu J. Characterization of Nanomaterials. In: *Advanced Nanomaterials and Their Applications in Renewable Energy, Elsiver*. Elsiver; 2015:117-180,. doi:10.1016/B978-0-12-801528-5.00003-8

217. Dasgupta NP, Neubert S, Lee W, Trejo O, Lee JR, Prinz FB. Atomic layer deposition of Al-doped ZnO films: Effect of grain orientation on conductivity. *Chem Mater*. 2010;22(16):4769-4775. doi:10.1021/cm101227h

218. Ameh ES. A review of basic crystallography and x-ray diffraction applications. *Int J Adv Manuf Technol*. 2019;105(7-8):3289-3302. doi:10.1007/s00170-019-04508-1

219. Dietzek B, Cialla D, Schmitt M, Popp J. *Introduction to the Fundamentals of Raman Spectroscopy*. Vol 66. Springer International Publishing; 2018. doi:10.1007/978-3-319-75380-5_3

220. Prochazka M. Basics of Raman Scattering (RS) Spectroscopy. In: *Surface-Enhanced Raman Spectroscopy*. Springer; 2015:7-19. doi:10.1007/978-3-319-23992-7_2

221. Akhtar K, Khan SA, Khan SB, Asiri AM. *Scanning Electron Microscopy: Principle and Applications in Nanomaterials Characterization*.; 2018. doi:10.1007/978-3-319-92955-2_4

222. Johnson D, Hilal N, Bowen WR. *Basic Principles of Atomic Force Microscopy*. Elsevier Ltd; 2009. doi:10.1016/B978-1-85617-517-3.00001-8

223. AFM scanning. https://www.maxiv.lu.se/accelerators-beamlines/support-labs-microscopy/atomic-force-microscopy/afm-scanning-modes/. Accessed August 5, 2021.

224. Eugene Hecht. *Optics 4th Edition*. Pearson; 2002. https://www.pearson.com/us/higher-education/product/Hecht-Optics-4th-Edition/9780805385663.html. Accessed June 16, 2021.

225. Zhang Y-J. *Handbook of Image Engineering*.; 2021. doi:10.1007/978-981-15-5873-3

226. Cook PD, Bixler JN, Thomas RJ, Early EA. Prediction of tissue optical properties using the Monte Carlo modeling of photon transport in turbid media and integrating spheres. *OSA Contin*. 2020;3(6):1456. doi:10.1364/osac.377805

227. Prasadam VP, Ramirez F V., Papakonstantinou I, Parkin IP, Bahlawane N. Thermoresponsive Black VO 2 –Carbon Nanotube Composite Coatings for Solar Energy Harvesting. *ACS Appl Nano Mater*. 2020;3(9):8848-8857.

doi:10.1021/acsanm.0c01630

228. Prasadam VP, Gautier N, Bahlawane N. CNT nanoengineering for thermally stable selective solar absorption. *Mater Today Commun*. 2021;28:102552. doi:10.1016/j.mtcomm.2021.102552

229. Cárdenas Morcoso D. Advanced semiconductors for photo-electrocatalytic solar fuel production. July 2020. doi:10.6035/14104.2020.679916

230. Bredar ARC, Chown AL, Burton AR, Farnum BH. Electrochemical Impedance Spectroscopy of Metal Oxide Electrodes for Energy Applications. *ACS Appl Energy Mater*. 2020;3(1):66-98. doi:10.1021/acsaem.9b01965

# 3 RESULTS AND DISCUSSION

## 3.1 SOLAR SELECTIVE ABSORPTION APPLICATION

The demand for solar absorbers with operating temperatures above 900 K, was satisfied using carbon-based materials. However, this material has a poor solar absorption selectivity. Tandem structures including carbon nanotubes and metallic surface feature an enhanced solar absorption selectivity but diminishes the thermal stability. To address the solar-selectivity and thermal stability trade-off, the MWCNT-Metal oxide architectures were investigated using the hybrid CVD-ALD process. In this context, two different infrared reflecting layers, i.e. vanadium dioxide and aluminium doped zinc oxide were considered to induce solar selectivity in the MWCNT without relying on the metallic substrate.

In Chapter 3.1.1., we review the ALD process for vanadium oxides along with the vast range of potential applications. The development of an ALD process for vanadium dioxide is addressed in the chapter 3.1.2. Solar-selectivity characterization of fabricated MWCNT-Vanadium dioxide is addressed in chapter 3.1.3. The thermal stability and solar selectivity trade-off of ALD optimized Aluminium doped Zinc oxide-MWCNT hybrid material is illustrated in chapter 3.1.4.


1. V.P. Prasadam, N. Bahlawane, F. Mattelaer, G. Rampelberg, C. Detavernier, L. Fang, Y. Jiang, K. Martens, I.P. Parkin, I. Papakonstantinou, “Atomic layer deposition of vanadium oxides: process and application review”, Materials Today Chemistry, Volume 12, 396-423, 2019.
2. V.P. Prasadam, B. Dey, S. Bulou, T. Schenk, N. Bahlawane, “Study of $VO_2$ thin film synthesis by atomic layer deposition”, Materials Today Chemistry, Volume 12, 332-342, 2019.
3. Prasadam, Vasu Prasad and Ramirez, Francisco V. and Papakonstantinou, Ioannis and Parkin, Ivan P. and Bahlawane, Naoufal, “Thermoresponsive Black $VO_2$–Carbon Nanotube Composite Coatings for Solar Energy Harvesting”, ACS Applied Nano Materials Volume 3, 8848-8857, 2020.
4. Vasu Prasad Prasadam, Nicolas Gautier, Naoufal Bahlawane, “CNT nanoengineering for thermally stable selective solar absorption”, Materials Today Communications, Volume 28, 102552, 2021.

### 3.1.1 Literature review of ALD of vanadium oxide and its application.

Vanadium oxides promotes interesting 'd' orbital electrons that behave as localized or free electrons due to the crystal field splitting. Vanadium features various oxidation states, i.e., +5, +4, +3, +2. Thus, it can co-ordinate to oxygen in different polyhedral structures. Polyhedral coordination and electron-electron interactions promote wide properties of vanadium oxide, consequently, feature applications in varied fields.

In this review, we addressed the available metal organic vanadium precursors and reported ALD process for the growth of amorphous $VO_x$ and discusses thermal treatments required to convert amorphous $VO_x$ into crystalline phases. We focus on applications where ALD has already been found or we believe will find wide usage in the near term. This includes energy storage applications, electronic devices, and smart windows.

Following metal-organic precursors were extensively reported in the growth of vanadium oxide film through the ALD process. Among them VTOP and TEMAV precursors are most intensely studied because of viable reactivity with different co-reactants and high vapour pressure.

| Precursor | | Vapour pressure | Reactivity | | | Thermolysis threshold |
|---|---|---|---|---|---|---|
| | | | $H_2O$ | $O_3$ | $O_2$-Plasma | |
| $V^{3+}$ | $V(^iPrMeAMD)_3$ | 6.6 Pa @ 70°C | × | ✓ | - | - |
| $V^{+4}$ | $V(NMe_2)_4$ (TDMAV) | 133 Pa @ 64°C | ✓ | ✓ | ✓ | 120°C |
| | $V(NEtMe)_4$ (TEMAV) | 13 Pa @ 25°C<br>24 Pa @ 45°C<br>57 Pa @ 82°C | ✓ | ✓ | ✓ | >175°C |
| | $VO(acac)_2$ | 0.21 Pa @ 96°C | × | ✓ | - | 180°C |
| | $VO(tmhd)_2$ | 0.24 Pa @ 96°C | × | × | ✓ | 160°C |
| $V^{+5}$ | $VO(O^iPr)_3$ (VTOP) | 6 Pa @ 25°C<br>39 Pa @45°C<br>268 Pa @ 82°C | ✓ | ✓ | ✓ | 100°C |

VTOP: vanadium oxy-tri-isopropoxide; TDMAV: tetrakis dimethylaminovanadium; TEMAV: Tetrakis ethylmethyl amino vanadium. $VO(acac)_2$): Vanadyl acetylacetonate; $VO(tmhd)_2$: Vanadyl tetramethyl heptadionate

Materials Today Chemistry 12 (2019) 396–423

Contents lists available at ScienceDirect

Materials Today Chemistry

journal homepage: www.journals.elsevier.com/materials-today-chemistry/

# Atomic layer deposition of vanadium oxides: process and application review

V.P. Prasadam [a], N. Bahlawane [a], F. Mattelaer [b], G. Rampelberg [b], C. Detavernier [b], L. Fang [c], Y. Jiang [c], K. Martens [d], I.P. Parkin [e, f], I. Papakonstantinou [g, *]

[a] Material Research and Technology Department, Luxembourg Institute of Science and Technology, 41, Rue Du Brill, Belvaux, L-4422, Luxembourg
[b] Department of Solid State Sciences, Ghent University, Krijgslaan 281, Ghent, S1, 9000 Gent, Belgium
[c] Key Laboratory of Novel Materials for Information Technology of Zhejiang Province, School of Materials Science and Engineering, Zhejiang University, State Key Laboratory of Silicon Materials, Hangzhou, 310027, China
[d] IMEC, Kapeldreef 75, 3001 Leuven, Belgium
[e] Materials chemistry research centre, Department of Chemistry, UCL, 20 Gordon Street, London, WC1H OAK UK
[f] Faculty of Mathematical and Physical Sciences, University College London, Gower Street, London, WC1E 6BT, UK
[g] Photonic Innovations Lab, Department of Electronic and Electrical Engineering, University College London, Torrington Place, London, WC1E 7JE, UK

ARTICLE INFO

*Article history:*
Received 16 January 2019
Received in revised form
15 March 2019
Accepted 15 March 2019

*Keywords:*
Postdeposition annealing
Energy storage
Lithium ion batteries
Supercapacitors
Smart windows

ABSTRACT

Atomic layer deposition (ALD) is a method of choice for the growth of highly conformal thin films with accurately controlled thickness on planar and nanostructured surfaces. These advantages make it pivotal for emerging nanotechnology applications. This review sheds light on the current developments on the ALD of vanadium oxide, which, with proper postdeposition treatment yields a variety of functional and smart oxide phases. The application of vanadium oxide coatings in electrochemical energy storage, microelectronics and smart windows are emphasized.



## 1. Introduction

With 0.019% in the earth crust, vanadium can be considered a highly abundant element [1]. The strong electron–electron interactions in several vanadium oxide phases resulting from the localized character of partially occupied 'd' orbitals provide these materials with remarkable properties for numerous technological applications [2]. Vanadium shows multiple oxidation states ranging from −3 to +5 and exhibits crystalline structures with different oxygen coordinations, for example, octahedral, pentagonal bipyramids, square pyramids and tetrahedral sharing corners, edges or faces [3]. In these compounds, vanadium features either single or mixed oxidation states. The Magneli $V_nO_{2n-1}$ and Wadsley series $V_nO_{2n+1}$are examples of compounds with mixed oxidation states. The physicochemical properties of the different phases vary substantially with the oxidation state of vanadium cations [4].

The strongly correlated and the layered vanadium oxide phases feature interesting chemical and physical properties, making them valuable building blocks for the design of functional and smart devices. Vanadium oxides find applications in microelectronics [5,6], energy storage devices [1,7], smart windows [8–10] and catalysis [11]. Ternary vanadium oxides with $AVO_3$ perovskite, for example, $SrVO_3$ and $CaVO_3$, do not feature strong metal-insulator (MIT) behaviour [6,11]; nevertheless, they exhibit interestingly high transparency and electrical conductivity with a plasmon energy superior to 1.33eV. These properties make them promising transparent conducting oxides [12]. Rare-earth vanadate such as $LaVO_3$, however, features a Mott-insulator gap of 1.1eV, which makes them appealing as solar absorbers [13].

Several review articles on the state of the art regarding the synthesis of vanadium oxides address the physical vapour deposition, chemical vapour deposition and liquid-phase synthesis

* Corresponding author.
*E-mail addresses:* naoufal.bahlawane@list.lu (N. Bahlawane), christophe.detavernier@ugent.be (C. Detavernier), yzjiang@zju.edu.cn (Y. Jiang), Koen.Martens@imec.be (K. Martens), i.p.parkin@ucl.ac.uk (I.P. Parkin), i.papakonstantinou@ucl.ac.uk (I. Papakonstantinou).

https://doi.org/10.1016/j.mtchem.2019.03.004

[14–16]; in this review, we focus, instead, on atomic layer deposition (ALD), a process which has not been reviewed so far. First introduced in the 1960s, this technique is currently receiving an ever-growing attention as a method of choice for the growth of conformal coatings on nanostructures with high aspect ratios. The sequential and self-terminating character of the ALD enables an exclusive surface reaction between the precursor and the reactant, while excluding the precursor thermolysis. A detailed history of the ALD technique was recently reported [17,18]. The self-termination of the sequential reactions is particularly appealing for the deposition on nanopowder and nanostructured surfaces. This article is organised as following: Section 2 reviews the available precursors and developed ALD chemistries for the growth of amorphous $VO_x$; whereas section 3 discusses the (non-trivial) annealing conditions required to convert $VO_x$ into crystalline phases. The last three sections focus on applications where ALD has already found or we believe will find wide usage in the near term. In particular, section 4 focuses on energy storage applications, section 5 focuses on electronic devices, particularly ones utilizing electronic means to control the metal to insulator transition in $VO_2$ and, finally, section 6 reviews the application of ALD grown $VO_2$ in smart windows.

## 2. Atomic layer deposition of $VO_x$

Controlling the ALD process of vanadium oxide is an efficient mean to secure conformal coatings and achieve high control over the thickness on the nanometre scale. The ALD process is cyclic, involving the chemisorption of the precursor until surface saturation, and then its reaction with the reactants ($H_2O$, $NH_3$, $O_3$) to form the desired coating. Efficient purging between the sequential exposures is mandatory to confine the chemical reactions during the growth sequences. The self-limitation of the sequential ALD surface reactions is, therefore, a prerequisite. Extending the subsequent surface exposure to the reactants should not influence the growth rate per cycle when this condition is satisfied, and an increase of the growth rate per cycle when extending the surface exposure to the precursor is an evidence of its thermolysis reaction, which is considered as a parasitic side reaction in the ALD process. A second characteristic of a controlled ALD process is the presence of a temperature window, within which saturation occurs. This temperature window is often limited by the volatility of the precursor on one side and its thermolysis on the other [19–21]. Third, the self-limiting nature of the ALD half-cycles implies that coatings can be conformal on high–aspect ratio structures. Indeed, ALD is nearly unmatched in high–aspect ratio coverage, which has been essential for the development of microelectronics over the last decade [22]. In the following sections, we report on ALD chemistries of vanadium oxides.

### 2.1. β-diketonate compounds

#### 2.1.1. Vanadyl acetylacetonate

Vanadyl acetylacetonate, [$VO(C_5H_7O_2)_2$], is a blue-green solid compound in which the vanadium cation is in the +4 oxidation state. The four oxygen atoms of the 'acetylacetonate' ligands (acac) form a square pyramid, whereas the vanadyl oxygen occupies the apex position. The two acac skeletons of the same molecule are not coplanar and form an angle of 15.7° with each other. The overall coordination geometry is displayed in the inset of Fig. 1 [23]. $VO(acac)_2$ features a molecular-type structure with temperature-sensitive intermolecular Van der Waals interaction [24]. The thermogravimetric analysis (TGA), Fig. 1, reveals a weight loss above 150°C with no residue under vacuum (0.7 mbar) indicating its complete sublimation [25]. At atmospheric pressure, the TGA exhibits a weight loss above 250°C, resulting in partial decomposition with a residue of 20 w% [24]. A vapour pressure of 0.21 Pa was reported at 96°C for this compound, which sublimes as a monomer [25].

Although the $VO(acac)_2$ synthesis was reported in 1957 [26], the first ALD results using this precursor were reported by Keranen et al., [27]. In this study, the precursor was maintained at 170°C to generate sufficient vapour pressure, and the implementation of a carrier gas was necessary. The ligand removal was performed in a subsequent step via an annealing in air at 350 °C for 6 h. Upon interaction with the deposition surface, the vanadium content reached nearly the theoretical monolayer of vanadate with 2.3 $VO_x$/$nm^2$. As the objective of this study was to adjust the surface acidity, no systematic study confirming the self-limited ALD half-cycles was reported.

The deposition of $VO_x$ starting from [$VO(acac)_2$] and molecular oxygen was reported by Dagur et al., [28] at a substrate temperature of 400–475°C, resulting in crystalline $VO_2$. Although the ALD cycles were optimized at 4s and 1s of exposure to $VO(acac)_2$ and oxygen, respectively, no evidence of self-saturating ALD half-cycles was provided. The growth rate was nevertheless measured at 0.24 nm/cycle, which is nearly equal to one monolayer of $VO_2$ structure. As the reported TGA analyses show, Fig. 1 [24,25,29], significant thermolysis of the precursor occurs above 180°C. Therefore, the study reported with VO(acac)2 [28] is performed at an excessively high temperature and using molecular oxygen which is a non-reactive ALD reactant. This work can, therefore, be described as a pulsed chemical vapour deposition (CVD).

The available literature with the commercially available [$VO(acac)_2$] shows its limited pertinence as an ALD precursor. Although high temperatures are needed for the evaporation (170°C), its thermolysis occurs already at 180°C, which leaves a very narrow processing window for ALD growth. The only reported systematic

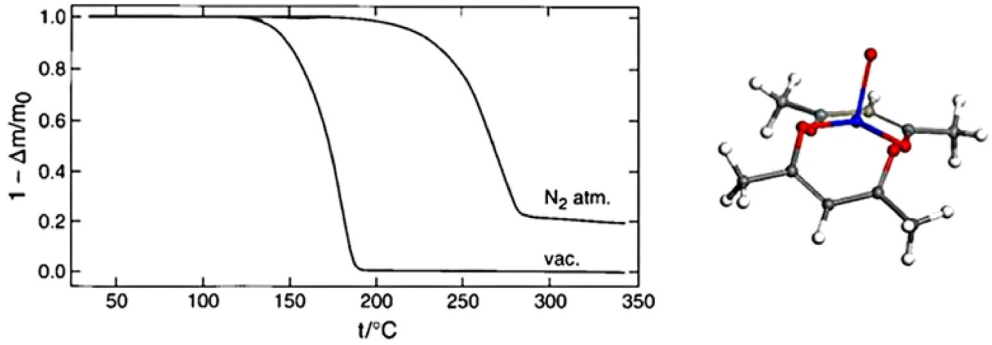


**Fig. 1.** Thermogravimetric analysis of $VO(acac)_2$ performed at 2°C/min [24]. Reproduced with permission from John Wiley and Sons. The inset corresponds to the molecular structure: V: blue; O: Red; C: Grey, H: white.

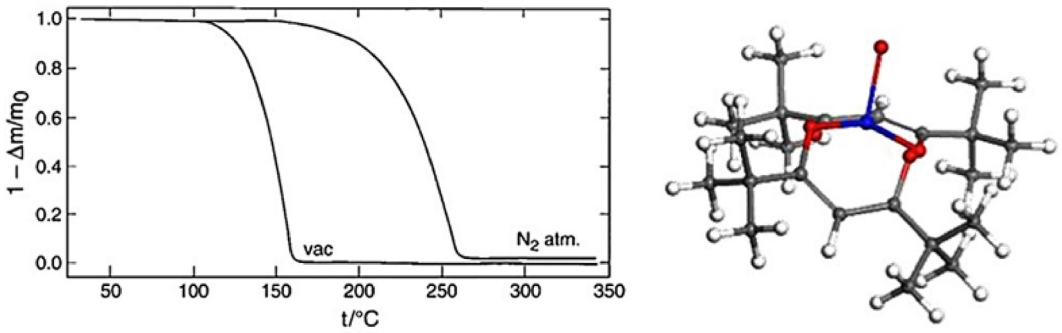


**Fig. 2.** Thermogravimetric analysis of $VO(tmhd)_2$ at 2°C/min [24]. Reproduced with permission from John Wiley and Sons. The inset represents the molecular structure: V: blue; O: Red; C: Grey, H: white.

study with this precursor was performed at temperature far exceeding the thermal decomposition, where the CVD process dominates the growth.

### 2.1.2. Vanadyl tetramethyl heptadionate

Vanadyl bis(2,2,6,6-tetramethyl-3,5,- heptadionate $[VO(tmhd)_2]$/ $[VO(C_{11}H_{19}O_2)_2]$ is a solid compound in which the vanadium cation is in the +4 oxidation state. The skeleton structure is similar to that of vanadyl acetylacetonate except that the change from methyl to *tert*-butyl group on the ketonate ring. The overall coordination geometry is displayed in the inset of Fig. 2 [23]. $[VO(tmhd)_2]$ features a molecular-type structure with temperature-sensitive Van der Waals intermolecular interaction from 105 to 295 K [24]. The TGA, Fig. 2, reveals a weight loss starting at 110°C with no residue under vacuum (0.7 mbar) [24]. At atmospheric pressure, the TGA exhibits a weight loss starting at 160°C and results in a 5 w% residue, indicating the occurrence of a partial decomposition [24]. Relative to $VO(acac)_2$,$VO(tmhd)_2$ features a significantly lower fraction of decomposition, which is in line with a higher thermal stability. A vapour pressure of 0.27 Pa was measured for this compound at 96°C, which vaporises as a monomer [25].

Ostreng et al., [30,31] have implemented the reaction of $[VO(tmhd)_2]$ with ozone ($O_3$) for the ALD of $VO_x$. The precursor was sublimed at 125°C under a flow of inert carrier gas. Self-limited reactions were reported at 186°C, using exposure times above 2 and 3s for $[VO(tmhd)_2]$ and $O_3$, respectively. The growth rate per cycle was far below a monolayer and is temperature-dependent within the 162–235°C window range and featured a value of 0.02–0.09 nm/cycles. Furthermore, evidence of parasitic CVD contribution was observed above 200°C [30,31].

As the ALD growth requires on one side an efficient vaporization of the precursor and on the other side its self-limited reaction on the surface, an operating ALD window within the 125–160°C range might be expected based on the reported TGA results. The excessively low deposition rate per cycle below 160°C is probably the reason why the 125–160°C temperature window was not given attention.

Although the precursor contains a $V^{4+}$ cation, the reported ALD processes implement ozone, which results in its further oxidation to form amorphous or crystalline $V_2O_5$ films depending on the temperature. The low reactivity of $[VO(tmhd)_2]$ has probably hindered the investigation of its hydrolysis reaction in the ALD process. Beyond its low vapour pressure and low reactivity, $[VO(tmhd)_2]$ is not commercially available, which considerably limits its suitability for the ALD of vanadium oxide thin films.

### 2.1.3. Statement regarding β-diketonate compounds

The available literature on the ALD of vanadium oxide starting from β-diketonate compounds is very limited, and the reported growth processes are systematically performed at temperatures exceeding the thermolysis threshold of the vanadium precursor, which is certainly related to their low reactivity.

The volatility and thermal stability of vanadyl β-deketonate compounds have been compared, see Fig. 3 [25]. Based on the weight-loss threshold temperature, the performed TGA in argon ambience reveals a volatility that evolves in the order: $[VO(hfa)_2] \gg [VO(tmhd)_2] > [VO(acac)_2]$. Furthermore, the thermal stability, assessed by the residual mass, shows an equivalent performance for $[VO(hfa)_2]$ and $[VO(tmhd)_2]$; both are more stable than $[VO(acac)_2]$. Among the discussed compounds, $VO(hfa)_2$ appears as the most promising beta-diketonate for the ALD of $VO_x$; however, no study was reported so far with this compound. The low reactivity of β-diketonates in general would be a significant drawback with this family of precursors.

## 2.2. Alkoxide compounds

Vanadium oxy-tri-isopropoxide (VTOP) $[VO(OC_3H_7)_3]$ is a liquid compound at room temperature with vanadium in the +5

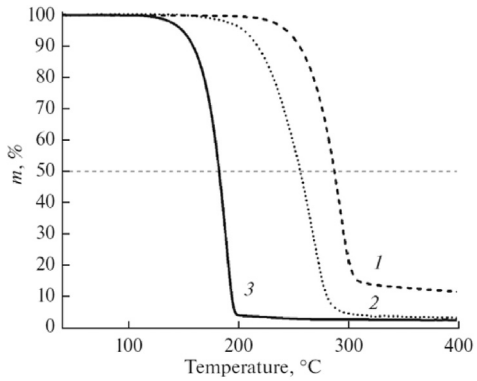


| Compounds | T (°C) | Vapour pressure/Pa | $\Delta_s H°(298K)$ kJ/mol |
|---|---|---|---|
| $VO(acac)_2$ | 96 | 0.21 | 132±4 |
| $VO(tmhd)_2$ | 96 | 0.27 | 126±11 |
| | 57 | 0.0047 | |
| $VO(hfa)_2$ | 57 | 0.18 | 119±10 |

**Fig. 3.** Thermogravimetric analysis of (1) $[VO(acac)_2]$, (2) $[VO(tmhd)_2]$ and (3) $[VO(hfac)_2]$ at 10°C/min. hfac: hexafuoro acetylacetonate [25]. Reproduced with permission from Springer Nature. The table summarizes the vapour pressures and evaporation enthalpies of these compounds.

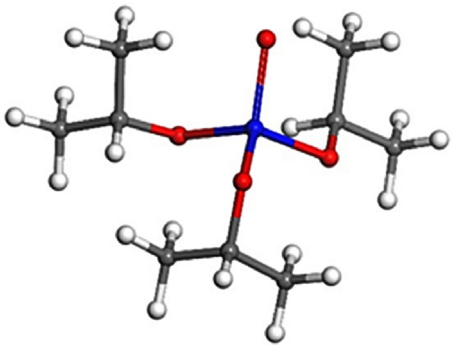

**Fig. 4.** Molecular structure of VTOP. (V: blue; O: Red; C: Grey, H: white). VTOP, vanadium oxy-tri-isopropoxide.

oxidation state. The molecule features a trigonal pyramidal structure with vanadyl oxygen at the apex and alkoxide groups at the edges (Fig. 4). The precursor possesses a vapour pressure of 6 Pa at room temperature [32], 39 Pa at 45°C [33] and 268 Pa at 82°C [34]. According to the previous work [35,36], the vanadium oxy-tri-alkoxide is reported to be monomeric in pentane solution. The formation of oligomers in vanadium oxy-tri-alkoxide compounds depends on the temperature, solvent, concentration and size of the alkyl groups. Compounds with smaller alkyl groups, for example, vanadium oxy tri methoxide, dimerize, whereas the compound with iso-butoxide groups remains as a monomer. As the tri-iso-propoxide compound is bulky, the stabilisation of the monomer form is most likely. This precursor was widely used for the synthesis of vanadium pentoxide, but no TGA investigation has been reported so far.

Vanadium pentoxide films were grown by ALD from the reaction of VTOP precursor with $H_2O$ [33], $O_2$ plasma [37] or $O_3$ [38].

Badot et al. [33] have reported on the hydrolysis reaction of VTOP, and the obtained films were extensively investigated for electrochemical energy storage [39–44]. The evaporation of VTOP was performed either at room temperature [33] or at 40–45°C using an inert carrier gas [37,38]. A temperature-independent growth rate was observed in the 50–100°C window with a rate of 0.017–0.02 nm/cycle [33]. Significantly higher growth per cycle was noticed above this temperature range [33,37,45]. The observed slow reaction of water with the adsorbed VTOP was attributed to the bulky iso-propoxide ligands that hinder access to the vanadium–oxygen bond [37]. The observed precursor thermolysis at 150–190°C is kinetically limited and enables still a high conformality of the coating [33]. It is worth mentioning that even at 190°C, the growth rate was still below one monolayer of vanadium oxide per cycle. As-deposited films were amorphous with vanadium in the +5 oxidation state [33].

Musschoot et al. [37] have reported on the plasma-enhanced (PE-ALD) and thermal ALD for the growth of vanadium pentoxide with VTOP precursor using either $H_2O$ or $O_2$. Constant growth rate was observed between 50 and 100°C with the typical self-saturating half-cycle reactions. PE-ALD with either water or oxygen has given a constant growth rate of 0.07 nm/cycle, which is significantly high relative to the thermal ALD with water [37]. Films obtained with PE-ALD exhibited, however, a higher carbon contamination using water plasma, 22% versus 6.5% with the thermal ALD using water. However, when oxygen plasma is used, no carbon was reported in the as-deposited films [37]. This indicates that the oxygen plasma burns carbon species generating volatile products, resulting in pure films.

Chen et al. [38] have implemented the reaction of $O_3$ with VTOP and reported an ALD window with a constant rate of 0.027 nm/cycle at 170–185°C. Nevertheless, the investigated very short exposure times marginalize the CVD contribution. The as-deposited films under these conditions were pure-phase, crystalline $V_2O_5$ with an enhanced (001) orientation. The growth kinetics was noticed to be slow below 170°C, which was attributed to the insufficient energy to activate the reaction of $O_3$ with surface ligands. Higher deposition rates were attributed to the precursor thermolysis [38].

Other studies, Table 1, were devoted to the ALD of vanadium oxide starting from VTOP, but no systematic demonstrations of the self-limitation of the sequential ALD reactions were reported. A clear disagreement regarding the thermolysis temperature threshold of VTOP is worth mentioning. Extending the exposure time of the surface to VTOP was observed to yield an increasing growth rate even at 100°C [46]. Although an increase of the growth per cycle can be attributed to the presence of residual water vapour in the reactor or to the slow kinetics, the VTOP thermolysis is very likely affecting a significant part of reported experiments above 100 °C in Table 1. Nevertheless, the typically used short exposure times to VTOP marginalizes this effect.

Consequently, the VTOP thermolysis is very likely affecting all experiments performed above 100°C in Table 1. Therefore, only few studies were performed under thermolysis-free ALD process. In general, VTOP has been evaporated at RT-45°C, which defines an appealing ALD processing window at 45–100°C. It is worth noting that other equivalent alkoxide compounds are commercially available such as: vanadium(V) oxytrietoxide and vanadium(V) oxytripropoxide. Although, these compounds feature comparable physicochemical properties, their thermolysis behaviour and reactivity with water vapour might exhibit significant contrast. Unfortunately, these compounds were not investigated as ALD precursors so far [46–57].

**Table 1**
Summary of the ALD parameters used for the growth of $VO_x$ starting from VTOP precursor.

| Oxidant | Process | Carrier gas | Evaporation Temp. (°C) | Deposition Temp. (°C) | Exposure time (s) VTOP/Oxidant | Rate (Å/cycle) | Ref |
|---|---|---|---|---|---|---|---|
| $O_3$ | Thermal | $N_2$ | 45 | 170–195 | 0.5/2 | 0.27–0.81 | [38,47,48] |
| $H_2O$ | Thermal | $N_2$ | 45 | 50–140 | 0.1/1.2 | 0.17 | [33,39,41–44] |
| | | | | 70–130 | 0.5/2 | 0.3 | [49,50] |
| | | | | 125–175 | 2.6/0.2 | 0.2–0.3 | [51,52] |
| | | | | 180 | 20/20 | – | [53] |
| | | | 40 | 135 | 2/5 | 0.3 | [45] |
| | | Ar | | 50–200 | 2/5 | 0.2 | [37] |
| | | – | | 110–150 | 0.5/2 | 0.37 | [54] |
| | | | – | 150 | 120/120 | 0.8–1 | [55,56] |
| | Plasma | Ar | 40 | – | 2/5 | 0.7 | [37] |
| $O_2$ | | | | | | | |
| | | $N_2$ | 45 | 180 | 20/60 | – | [57] |

VTOP, vanadium oxy-tri-isopropoxide; ALD, Atomic layer deposition.

### 2.3. Alkylamide compounds

Vanadium (IV) amide complexes are volatile, reactive, produce non-corrosive by-products, and leave marginal impurities in the films [58]. Alkylamide compounds with higher molecular weight decompose at higher temperatures due to the steric hindrance [59,60]. Ethylamide compound have, for example, higher thermal stability relative to methylamide counterpart but features a lower vapour pressure. Vanadium dialkyamides [$V(NRR')_4$], (R, R' = methyl or ethyl or both) are monomeric in nature [61,62].

#### 2.3.1. Tetrakis ethylmethyl amino vanadium

Tetrakis ethylmethyl amino vanadium (TEMAV) is a green liquid at room temperature and is commercially available. The reported TGA measurement of the precursor, Fig. 5, shows a clear temperature window between evaporation and decomposition, where the ALD process can be optimized. The thermal decomposition of the precursor takes place above 175°C, whereas it is significantly volatile under vacuum below 100°C [63]. The vapour pressure of this compound is reported as a function of temperature in the form of the Clausius–Clapeyron equation log (P/torr) = 6.59–2640/(T/K) in the range of 343–383 K [64]. The implementation of TEMAV requires heating the precursor source at 65–70°C and the use of an inert carrier gas [63,65–67].

The TEMAV precursor was implemented with $H_2O$, $O_3$ and $O_2$-plasma as reactants for the synthesis of vanadium oxide [65–67]. Authors reported a thermal decomposition above 175°C, whereas the self-limited ALD reactions were observed up to 150°C. TEMAV quickly saturates the surface after 2s of exposure, while 5s is required with ozone for the removal of the ligands at 150°C enabling a growth rate of 0.07 nm/cycle [67]. The vanadium oxidation state (+4) was retained in the as-deposited amorphous films using $H_2O$ or $O_3$ as reactants [65]. In the case of plasma $O_2$ as the oxidant, polycrystalline $V_2O_5$ was formed upon deposition, and vanadium has, therefore, a +5 oxidation state.

Blanquart et al. [63] reported a constant growth rate with growth per cycle (GPC) of 0.04nm/cycle within the 100–175°C temperature range using the reaction of TEMAV with $O_3$. Similar behaviour with a GPC of 0.08nm/cycle was observed using the reaction of TEMAV with $H_2O$ at 125–200 °C. The resulting films were amorphous and featured a +4, +5 mixed oxidation state for vanadium. The authors have demonstrated a conformal coating on textured surfaces with a 60:1 aspect ratio [63].

The supply of precursors in ALD can be performed using the direct liquid injection approach by diluting the precursor in an inert solvent. The precursor dose is then introduced into a flash vaporiser before reaching the growth chamber. Premkumar et al. have used this process for the ALD of vanadium oxide using the reaction of TEMAV with $H_2O$ and $O_3$ as reactants [68–70]. TEMAV in these reports was diluted to a concentration of 0.2 M in octane. Authors noticed the thermal decomposition of the precursor already at 100 °C [68] in the absence of any reactants. As a result, no self-limited reactions can take place at ≤100 °C, and the deposition rate per cycle increases with the extension of the exposure time to the precursor. The obtained films were amorphous, and vanadium features a mixed +4 and + 5 oxidation state [69].

A summary of the reported studies with TEMAV is displayed in Table 2. The highly dispersed growth rate, 0.45-1Å/cycle, is quite remarkable. It is also worth noting that 150 °C is a common temperature for ALD in all reports regardless of the type of energy input and reactive gas.

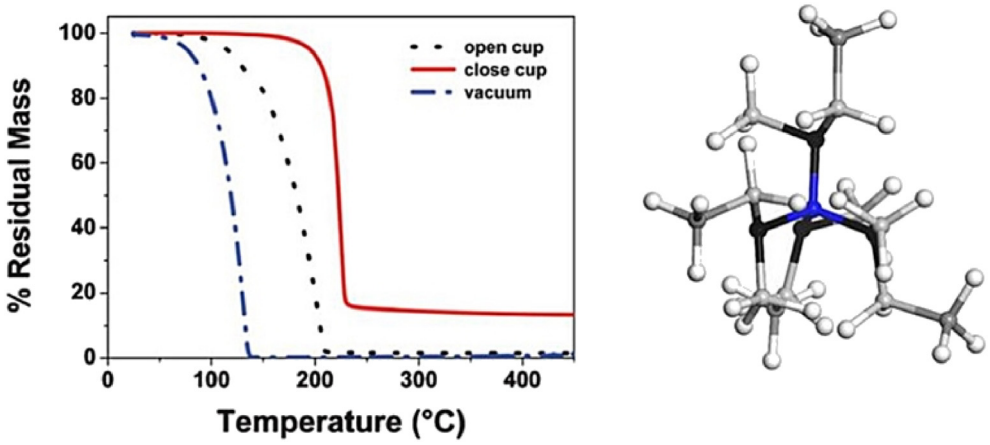


**Fig. 5.** Thermogravimetric analysis of TEMAV [63]. Reproduced with permission from the Royal Society of Chemistry. The inset corresponds to the structure of the compound: V: blue; N: Black; C: Grey, H: white. TEMAV, Tetrakis ethylmethyl amino vanadium.

**Table 2**
Summary of the ALD parameters used for the growth of $VO_x$ starting from TEMAV precursor.

| Oxidant | Process | Carrier gas | Evaporation Temp. (°C) | Deposition Temp. (°C) | Exposure time (s) TEMAV/oxidant | Rate (Å/cycle) | Ref |
|---|---|---|---|---|---|---|---|
| $O_3$ | Thermal | $N_2$ | 70 | 150 | 5/5 | 0.7–1 | [65–67] |
| | | | 65 | 100–175 | 1.2/1 | 0.45 | [63] |
| | | Ar | – | 100–150 | 5-10/10-5 | 1–0.4 | [68,70] |
| | | – | 105–115 | 150 | 0.03–0.015/0.05–0.045 | 0.77–0.9 | [71–74] |
| $H_2O$ | Thermal | $N_2$ | 70 | 150 | 5/5 | 0.67 | [65–67] |
| | | | 65 | 125–200 | 1.2/1 | 0.8 | [63] |
| | | | – | 125–150 | 0.05/0.015 | – | [75,76] |
| | | Ar | – | 150 | 5/10 | 0.5 | [69] |
| | Plasma | | 60 | 150 | 12/0.2 | 0.2 | [77] |

TEMAV, Tetrakis ethylmethyl amino vanadium.

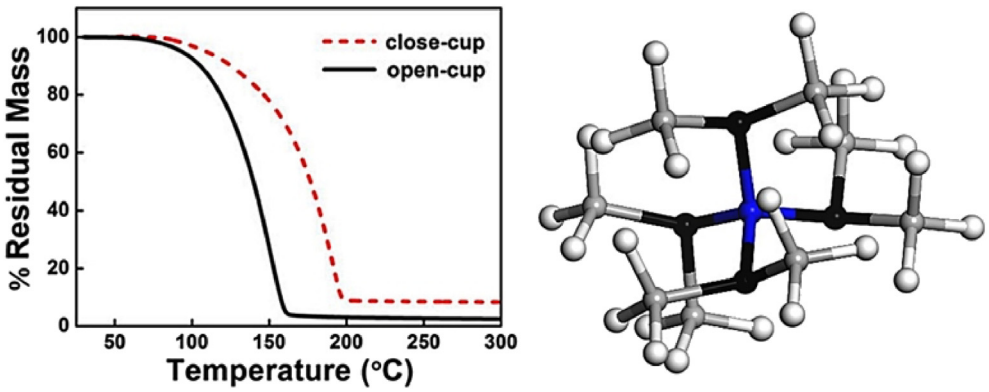


**Fig. 6.** Thermogravimetric analysis of TDMAV [78]. Reproduced with permission from Cambridge University Press. The inset corresponds to the molecule structure: V: blue; N: Black; C: Grey, H: white. TDMAV, tetrakis dimethylaminovanadium.

### 2.3.2. Tetrakis dimethylaminovanadium

Tetrakis dimethylaminovanadium (TDMAV) is a solid compound at room temperature. The TGA analysis, Fig. 6, shows a significantly low sublimation temperature, which confirms high volatility [78]. The TGA analysis features, however, a residue with open and closed cups, which is a clear indication of the partial decomposition of the precursor in both cases. The vapour pressure of the compound was 133 Pa at 64 °C, which is significantly high relative to TEMAV that needs to be heated at 107 °C to reaches this value. The compound exhibits a monomeric structure in the gas phase [61,62].

Wang et al., [78,79] have reported the thermal ALD of vanadium oxide by implementing the reaction of TDMAV with $H_2O$ or $O_3$. Authors reported that the volatility of the precursor is high enough to allow sublimation at room temperature. A temperature-independent growth rate was observed at temperatures between 50 and 120 °C. Below 120 °C, a growth rate of 0.045 nm/cycle was measured with $O_3$, which is significantly high relative to 0.03 nm/cycle obtained with $H_2O$. A significant thermolysis of the precursor was noticed above 120 °C. Authors have demonstrated self-limited surface reactions with TDMAV and $H_2O$ at 50 °C. Increasing the temperature was, however, favourable for the attainment of pure films. Amorphous films with mixed +4 and + 5 oxidation states of vanadium were obtained. Vanadium oxide films obtained with $H_2O$ as a reactant had less carbon and nitrogen contamination than films made using $O_3$ oxidant [78,79].

Lv et al., [80] implemented the reaction of TDMAV with $H_2O$ in thermal ALD. The precursor was evaporated at 60 °C and carried into the reactor using Ar flow. Temperature-independent growth was reported at 150–200 °C, with a strong thermolysis contribution above 200 °C. Authors reported self-limed reactions at 150 °C. Amorphous films grew at the rate of 0.094 nm/cycle, and vanadium retained the oxidation state of the precursor (+4).

Although the implementation of TDMAV for the ALD of $VO_x$ was only addressed in a limited number of articles, a clear controversy can be highlighted as far as the thermolysis threshold, and temperature-independent growth rate region are concerned. The precursor features a sufficient volatility at room temperature, and a high reactivity with water vapour as films could be grown at 50 °C.

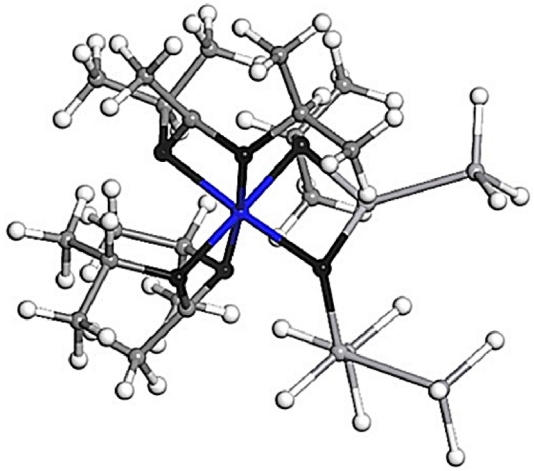

**Fig. 7.** [V(iPr-MeAMD)$_3$]) molecular structure: V: blue; N: Black; C: Grey, H: white.

### 2.3.3. Vanadium amidinates

Vanadium tris-diisopropylacetamidinate [(V(iPr-MeAMD)$_3$)] Fig. 7 is a red-brown solid compound with a vapour pressure of 6.6 Pa at 70 °C [81]. Owing to the chelating effect, the precursor is thermally stable relative to the other nitrogen coordinated alkylamide compounds. The molecule features a distorted geometry from octahedral towards trigonal prismatic. The precursor features a monomeric structure in the gas phase because of the bulky ligand and higher coordination to vanadium (III), which presents a distorted octahedral geometry [82].

M. Weimer et al. [83,84] have implemented the [(V(iPr-MeAMD)$_3$)] compound with different reactants for the growth of vanadium oxide thin films. The precursor was vaporized at 190 °C, and a temperature-independent growth was observed at 0.16 nm/cycle below 225 °C with $O_3$. Using $H_2O_2$ reactant, however, the temperature-independent growth was extended to 150–250 °C with a significantly lower rate 0.04nm/cycle. All reaction steps were confirmed to be self-limited at 200 °C. Amorphous $V_2O_5$ films were deposited with $O_3$ and $H_2O$, $O_2$ oxidants, whereas films grew neither with $H_2O$, $O_2$ nor $H_2$. Authors reported about the synergy effect between reactants and reported the growth of amorphous $VO_2$ films with $H_2$ dosing after the oxidation with $H_2O_2$. However, no self-limiting reactions were obtained.

## 2.4. Statements regarding the ALD of $VO_x$

This section summarizes the reported studies on the ALD of vanadium oxide starting from various precursors. It is surprising to see the limited number of investigated precursors despite the immense interest towards vanadium materials and their growth by ALD. A considerable number of commercially available potential vanadium precursors remain unexplored. Surprisingly striking variations between different sources were observed regarding the thermolysis threshold and the ALD window. The values stated in Table 3 refer to the lowest reported thermolysis threshold. An

**Table 3**
Summary of the main characteristics of the investigated precursors for the growth of vanadium oxide with ALD.

| Precursor | | Vapour pressure | Reactivity | | | Thermolysis threshold |
|---|---|---|---|---|---|---|
| | | | $H_2O$ | $O_3$ | $O_2$-Plasma | |
| $V^{3+}$ | $V(^{i}Pr\text{-}Me\ AMD)_3$ | 6.6 Pa @ 70 °C | X | √ | – | – |
| $V^{4+}$ | $V(N\ Me_2)_4$(TDMAV) | 133 Pa @ 64 °C | √ | √ | √ | 120 °C |
| | $V(N\ Et\ Me)_4$(TEMAV) | 13 Pa @ 25 °C<br>24 Pa @ 45 °C<br>57 Pa @ 82 °C | √ | √ | √ | >175 °C |
| | $VO(acac)_2$ | 0.21 Pa @ 96 °C | X | √ | – | 180 °C |
| | $VO(tmhd)_2$ | 0.24 Pa @ 96 °C | X | X | √ | 160 °C |
| $V^{5+}$ | $VO(O^{i}Pr)_3$ (VTOP) | 6 Pa @ 25 °C<br>39 Pa @45 °C<br>268 Pa @ 82 °C | √ | √ | √ | 100 °C |

VTOP, vanadium oxy-tri-isopropoxide; ALD, Atomic layer deposition; TDMAV, tetrakis dimethylaminovanadium; TEMAV, Tetrakis ethylmethyl amino vanadium.

increased growth per cycle when extending the exposure time to the vanadium precursor might be the signature of a parasitic thermolysis contribution. Among the investigated precursors, three featured a convenient reactivity with the conventionally used reactants for the growth of oxides by thermal ALD. These three precursors were also the ones exhibiting the highest vapour pressures: TDMAV; TEMAV and VTOP. If vaporized at room temperature, these precursors should enable a conveniently wide ALD processing window up to the thermolysis threshold. TDMAV can be distinguished among the three valuable precursors by its higher thermolysis temperature, which makes it particularly appealing for ALD processes with water vapour as reactant. In fact, using water as reactant at low temperatures implies the use of excessively long purge times, which makes the process slower. VTOP is the most investigated precursor so far, which is likely related to its convenient handling in air and the low toxicity of the reaction products.

## 3. Posttreatment of ALD-grown vanadium oxides

The as-deposited $VO_x$ do not always feature the desired characteristics. The art of posttreatment in $VO_x$ is far more challenging, as implied by the richness of the V-O phase diagram. This section addresses the relevance between the oxidation state of vanadium in the as-deposited film and the posttreatment parameters: temperature, pressure and partial pressure of the oxidant, or reducer. We summarize the literature and highlight some new alternatives and unexplored or underexplored areas.

ALD-grown vanadium oxides already come in a wide range, that is, from amorphous to crystalline and with vanadium in various oxidation states, as extensively discussed in section 2. However, the degree of crystallinity often plays a large role in the device characteristics. For example, amorphous $V_2O_5$ thin films, powders and aerogels have been reported to store lithium more efficiently and with higher capacities compared to their crystalline counterpart [85–87]. As another example, the same vanadium IV oxidation state in a different crystal lattice form, that is, $VO_2$ (M1/R) compared to $VO_2$(A) or $VO_2$(B) can either exhibit thermochromic properties in the former case, whereas no thermochromic behaviour is observed in either of the latter lattices [88]. Often, the degree of crystallinity can be controlled in process, as described in section 2.1.2 for ALD using [$VO(tmhd)_2$] and $O_2$ (amorphous 162–196 °C, crystalline $V_2O_5$ 196–235 °C) [31] or using TEMAV and $O_2$ plasma as highlighted in section 2.3.1, which produces amorphous films below 100 °C but crystalline $V_2O_5$ at higher temperatures [37,65,67,87,89].

Besides the crystal structure, the vanadium oxidation state also plays a major role in device characteristics. The vanadium oxidation state can often be tuned in process by choosing precursors with an appropriate vanadium oxidation state. As highlighted in section 2, three oxidation states of vanadium are presently found in literature (Table 3). If this is not sufficient, the oxidation state can be raised by utilizing an oxidizing ALD reactant such as oxygen plasma and ozone or lowered by utilizing a reducing ALD reactant such as hydrogen or ammonia plasma. Furthermore, deposition temperature also plays a role, as demonstrated by for example the TEMAV/ozone process, where the density of the grown films varied from ~0.3 mol/cm$^3$ to more than 0.4 mol/cm$^3$ from 100 to 175 °C, respectively [90].

Despite this large degree of in-process control already found in the ALD processes reported, there is a limitation in the films grown. In general, all reported films are either amorphous or crystalline $VO_2$ or $V_2O_5$. When the phase diagram derived by Wriedt [91] in Fig. 8 is observed, five principal single-valent vanadium oxides exist V, VO, $V_2O_3$, $VO_2$ and $V_2O_5$, with vanadium in the 0, +2, +3, +4 and + 5 oxidation state, respectively. Besides that, two families of mixed-valence vanadium oxides do exist: the Magnéli and Wadsley series, which can be written as $V_nO_{2n-1}$(n = 4–9) and $V_nO_{2n+1}$(n = 3,4,6) [14,91,92]. The wide range of stable oxidation states and polymorphic forms, each with their own physicochemical properties and application range, indicates that the crystallinity and phase control exhibited in process during ALD is insufficient, and often a careful postdeposition treatment is necessary to obtain the required crystal phase. The complexity of the V-O phase diagram, ranging from the primary stable oxides as $VO_2$ and $V_2O_5$ to metastable states such as $VO_2$(B), makes the annealing very sensitive to all environmental parameters. In the following section, we will discuss the influence of ambient, temperature, substrate and deposited film.

### 3.1. Processing parameters

#### 3.1.1. Influence of temperature and ambience

*3.1.1.1. Role of temperature.* The influence of temperature on the crystallisation of the ALD-made vanadium oxide thin films cannot be understood only by simply reading the phase diagram in Fig. 8. This would assume that the oxygen content in the film remains constant, which is not the case, as shown in many examples hereafter. Oxygen content in the film after the thermal treatment is largely influenced by the ambient, substrate, nature of the films as well as temperature. Furthermore, the annealing is not simply a function of temperature, but a function of the total thermal budget. A higher thermal budget is reached either by increasing the exposure temperature or the exposure time. This was for example demonstrated by Tangirala et al. [75], which showed that the crystallisation of a TEMAV + $H_2O$-grown film could be attained by a 30 min annealing at 450 °C under a controlled $N_2/O_2$atmosphere, while 5 min were not enough. Similarly, Lv et al. found that

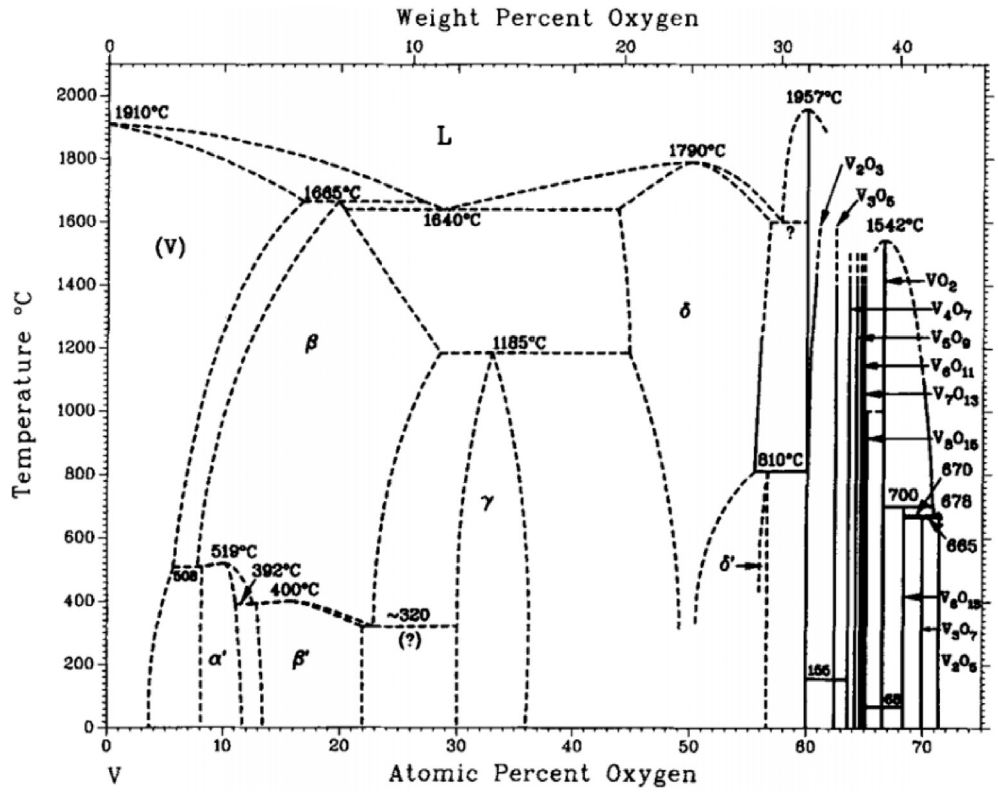


**Fig. 8.** Assessed V-O phase diagram (Condensed System, 0.1 MPa). Reprinted by permission from Springer Nature: Springer, Bulletin of alloy phase diagrams [91], Copyright 1989.

annealing-induced crystallisation of a TDMAV + $H_2O$-grown film, although already displaying some crystallinity even after 30 min of annealing at 450 °C in Ar ambient, takes a long time for crystal growth to completely occur as shown in Fig. 9. Nanocrystalline films were formed after 30-min of annealing, whereas fully crystallised films are obtained after 100 min [80]. In general, it can be stated that raising the temperature induces crystallisation and can raise the oxidation state, provided sufficient partial pressure of oxygen is available.

*3.1.1.2. Oxidizing atmosphere.* Mattelaer et al. separated the concepts of thermodynamic-phase formation and kinetic-phase formation by applying *in-situ* X-ray diffractometer (XRD) to observe the phase formation of TEMAV-grown films dynamically in a range of oxygen partial pressures (3.7, 7.4, 14.8, 29.6 and 48.1 Pa and ambient air), as shown in Fig. 10. The summary of this dataset, also shown in Fig. 10, should not be interpreted as a thermodynamic phase diagram, because the process is not isothermal. The phase formation diagrams display the kinetic path the films go through while being heated at 0.25°/s in the ambient under study. From these results, the trend in temperature confirms that higher temperatures favour crystallisation and eventually a change of oxidation state depending on the oxygen partial pressure. Phases emerge in oxidative ambient in order of increasing oxidation state: $VO_2$–$V_6O_{13}$–$V_4O_9$–$V_3O_7$–$V_2O_5$with respective to the average oxidation states for the V of 4–4.33–4.5–4.67–5 [65,87].

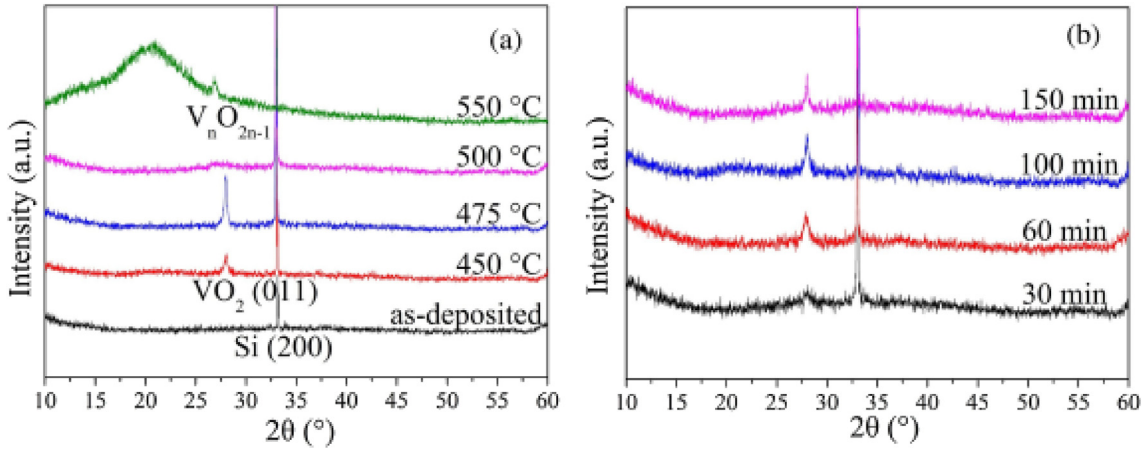


**Fig. 9.** XRD patterns of (a) $VO_2$/Si deposited using TDMAV and water at 200 °C after 100 min annealing in Ar or (b) different duration at 450 °C, Reprinted from Ref. [80], Copyright 2017, with permission from Elsevier. TDMAV, tetrakis dimethylaminovanadium.

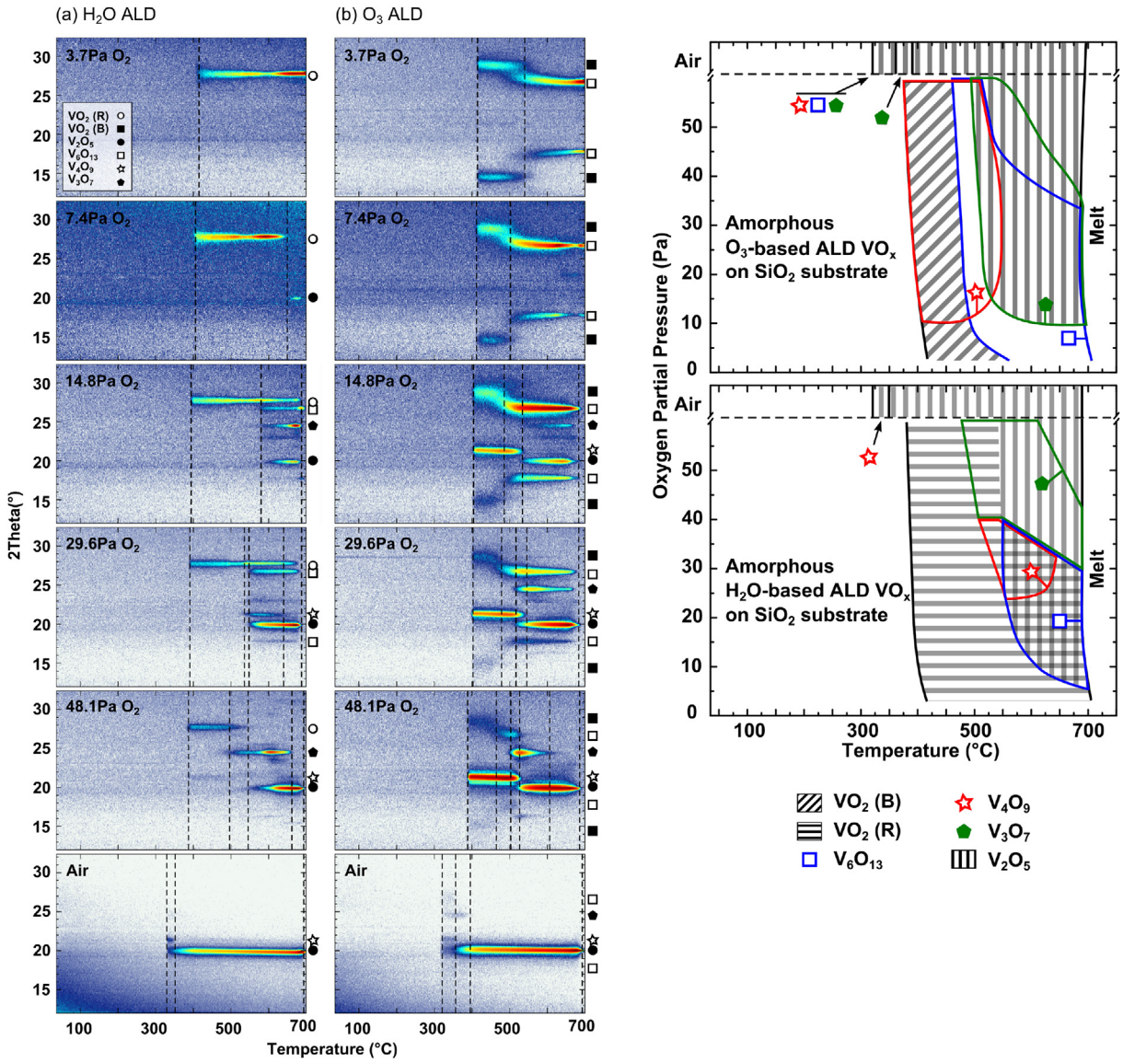


**Fig. 10.** Phase formation diagrams resulting from the in-situ XRD monitoring. The legend displayed with the figure provides an explanation for the reader to identify which phases are formed at which temperature and oxygen partial pressure. For example, in ambient air for the $H_2O$/TEMAV-based films, the film is initially amorphous (blank fill), then first crystallizes into a mixture of $V_2O_5$ (vertical stripe fill) and $V_4O_9$ (star symbol) and finally crystallizes completely to $V_2O_5$ (vertical stripe fill) and melt (indicated on the figure). If a region is marked by a coloured contour, this corresponds to the colour of the symbols found in the legend. (left) In-situ XRD on TEMAV-grown ALD films with (a) $H_2O$ or (b) $O_3$as a reactant, at various oxygen partial pressures while annealing at 0.25°/second. (right) Phase formation diagrams resulting from the *in-situ* XRD monitoring. Reproduced from Refs. [65,87], with permission from the Royal Society of Chemistry. ALD, atomic layer deposition; TEMAV, Tetrakis ethylmethyl amino vanadium.

Besides varying oxygen partial pressure at atmospheric pressure, Tangirala et al. also examined annealing at lower pressure. They found that TEMAV + $H_2O$-grown amorphous $VO_2$ film crystallised only at well-defined conditions, that is, 425 °C or 450 °C with a flow containing 1.22% or 1% $O_2$, respectively, under atmospheric pressure conditions. However, in mild vacuum conditions (~$10^{-2}$ Torr), the oxygen component in the flow could be much higher, and crystallisation to $VO_2$ was also achieved at 500 °C in a 100% $O_2$ flow [75]. This opens up another parameter in phase space, which is only marginally explored, the influence of the pressure on the oxidation/crystallisation.

Finally, Rambelberg et al. [93] showed that combining a well-defined partial pressure of an oxidizing gas (such as $O_2$) to an otherwise reducing ambient (such as $H_2$) resulted in a higher degree of control over the phase formation. This indicates that further research in the direction of bifunctional ambient could also be interesting.

*3.1.1.3. Reducing atmosphere.* Most art on postdeposition annealing of ALD vanadium oxide films deals with controlling the oxygen concentration between 0% (inert atmosphere such as He, $N_2$ or Ar) and 100% (pure $O_2$) and investigates the effect of this ambient on the crystallisation and oxidation/reduction behaviour of the ALD-made $VO_x$ films. In general, the crystallisation of films into a low−oxidation state oxide as $VO_2$(B) or $VO_2$(M) is much more challenging than forming crystalline $V_2O_5$, as this is the high-temperature stable phase: traces of oxygen in the ambient will readily cause oxidation of crystalline $VO_2$ to higher oxidation states, as shown in Fig. 10. However, besides controlling the oxygen concentration, the introduction of a reducing ambient can facilitate the formation of low-valence vanadium oxide films. Song et al. investigated the crystallisation behaviour of VTOP + $H_2O$-grown films in air and in forming gas ambient (95% $N_2$+ 5% $H_2$, FGA). Fig. 11 shows the results of 1 h isothermal annealing at 300, 400 or 500 °C. While $V_2O_5$ was readily formed already at 300 °C in air, monoclinic $VO_2$

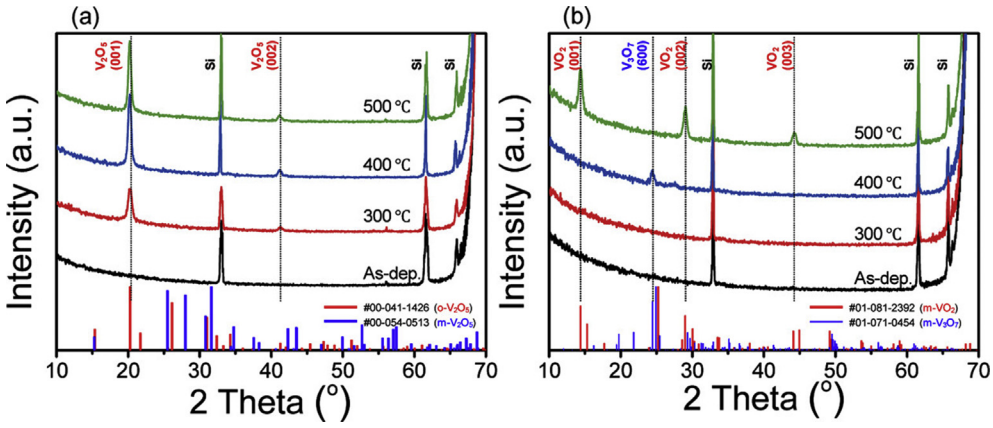


**Fig. 11.** XRD patterns of the as-deposited and postdeposition annealed $VO_x$ thin films at 300, 400 and 500 °C for 1 h in (a) air and (b) forming gas. Reprinted from [45]. Copyright 2017 American Chemical Society.

was formed at 500 °C via monoclinic $V_3O_7$ at 400 °C [45]. However, the obtained crystalline $VO_2$(M) features nanoparticles morphology rather than continuous films.

The presence of oxygen during crystallisation is a critical factor to maintain a continuous $VO_x$ film [66,69,78]. This implies that, if an enhanced surface area is required, as for catalysis or energy storage, annealing in oxygen-free ambient can be the optimal pathway. Very few researches have been performed using reducing ambient, which is potentially interesting to control the oxidation state further and form oxides below $VO_2$ or metallic vanadium nanoparticles.

### 3.1.2. Influence of deposited film

Several precursors have been used for the deposition of vanadium oxides by ALD, as extensively discussed in section 2. Generally, they can be divided into three classes according to their vanadium oxidation state as summarised in Table 3: +III vanadium precursors such as V($^i$Pr-Me AMD)$_3$; +IV vanadium precursors such as [VO(tmhd)$_2$,VO(acac)$_2$], V(N Me$_2$)$_4$ (TDMAV) and TEMAV and +V vanadium precursors such as VTOP and $VOCl_3$. According to pure ligand exchange reaction chemistry, this also determines the oxygen content into the deposited films, for example, TEMAV + $H_2O$ ALD leads to $VO_2$ films [37,89], and VTOP + $H_2O$ leads to $V_2O_5$ films [94]. However, the oxidative ($O_2$ plasma, $H_2O$ plasma, ozone) or reductive (acetic acid) ALD chemistry used alters the vanadium oxidation state in the films compared to that in the precursors, rendering different oxygen contents and often inducing crystallisation. The oxygen content (or vanadium oxidation state) in the deposited film will have a direct influence on the crystallisation and initial oxidation/reduction stages during postdeposition annealing of these films. Peter et al. [69], and later Mattelaer et al. [65], found that the deposition of films using TEMAV yielded almost identical amorphous $VO_2$ films using either water or ozone as a reactant, except for the density, which was significantly higher for the water-grown films than for the ozone-grown films and strongly influenced by the deposition temperature and $O_3$ exposure time. Rampelberg et al. linked those density differences to the different crystalline states of $VO_2$, that is, higher-density $VO_2$(M1) or lower-density $VO_2$(B) [90]. As shown in Fig. 10, at low oxygen partial pressure, this indeed resulted in the crystallisation of $VO_2$(M1) or $VO_2$(B) from the water- or ozone-grown films, respectively. Similarly, Peter et at linked the density of the as-deposited films to either close to $VO_2$ or $V_2O_5$, resulting in much smoother $VO_2$ films using optimized conditions at 1.6Pa $O_2$ [69].

Furthermore, as not all ALD chemistry is able to deposit a 'clean' vanadium oxide film, impurities such as carbon or hydrogen can often be incorporated into the films. Musschoot et al. showed that this carbon content in the films can delay the crystallisation of amorphous ALD vanadium oxides. They examined VTOP as an ALD vanadium source with thermal and PE-ALD. While water plasma enhanced the growth rate compared with thermal ALD, the carbon content was higher. Both films were amorphous as deposited, but crystallisation was delayed. The water-grown film crystallised between 400 and 450 °C to $V_3O_7$, and further oxidised to $V_2O_5$ between 450 and 500 °C, while the higher C-content PE-ALD grown film only crystallised at 500 °C to $V_2O_5$ [37,89].

### 3.1.3. Influence of substrate

The crystallisation and oxidation/reduction behaviour is sensitive to the oxygen content in the films (section 3.1.2) and to the oxygen partial pressure after annealing (section 3.1.1). Both parameters retain particular attention during the design of the post-deposition annealing process. However, the effect of the substrate on which the films are deposited is often overlooked. An easily oxidizable substrate, such as copper or titanium nitride, can scavenge oxygen from the vanadium oxide film; some substrates can donate oxygen to the films and act as an oxygen source, whereas a third class of substrates can be classified as oxygen-indifferent, such as Pt films which neither donate nor scavenge oxygen from the ALD films during anneal. Permkumar et al. studied the crystallisation behaviour of $VO_2$ from amorphous ALD $VO_x$ films grown from TEMAV + $O_3$at 150 °C. It was observed that $VO_2$ could be crystallised at 500 °C in oxygen partial pressures up to 11Pa $O_2$ on a 1 nm $SiO_2$ on Si substrate. In contrast, further oxidation to mixed-phase $VO_2/V_3O_7$was observed already at ≥6Pa $O_2$ on 90 nm $SiO_2$, indicating an oxygen loss from the amorphous film through the thin $SiO_2$ layer into the silicon substrate, which was prevented using a thicker $SiO_2$ barrier [68].

In the same way, the difference between $SiO_2$, TiN or Pt/TiN substrates was examined by Mattelaer et al. The phase formation diagrams on the $SiO_2$ substrates in Fig. 10 can be compared with those in Fig. 12, where the same annealing conditions were applied on TiN or TiN capped with Pt. Besides the larger number of phases that are formed on $SiO_2$ substrate, the oxidation of the vanadium oxide films to higher oxides was delayed on both TiN and Pt/TiN substrates. This was related to oxygen scavenging by TiN in both cases, demonstrating a clear influence of substrate [65].

Permkumar et al. [68] studied the crystallisation behaviour of $VO_2$ from amorphous ALD VOx films grown from TEMAV + O3 at

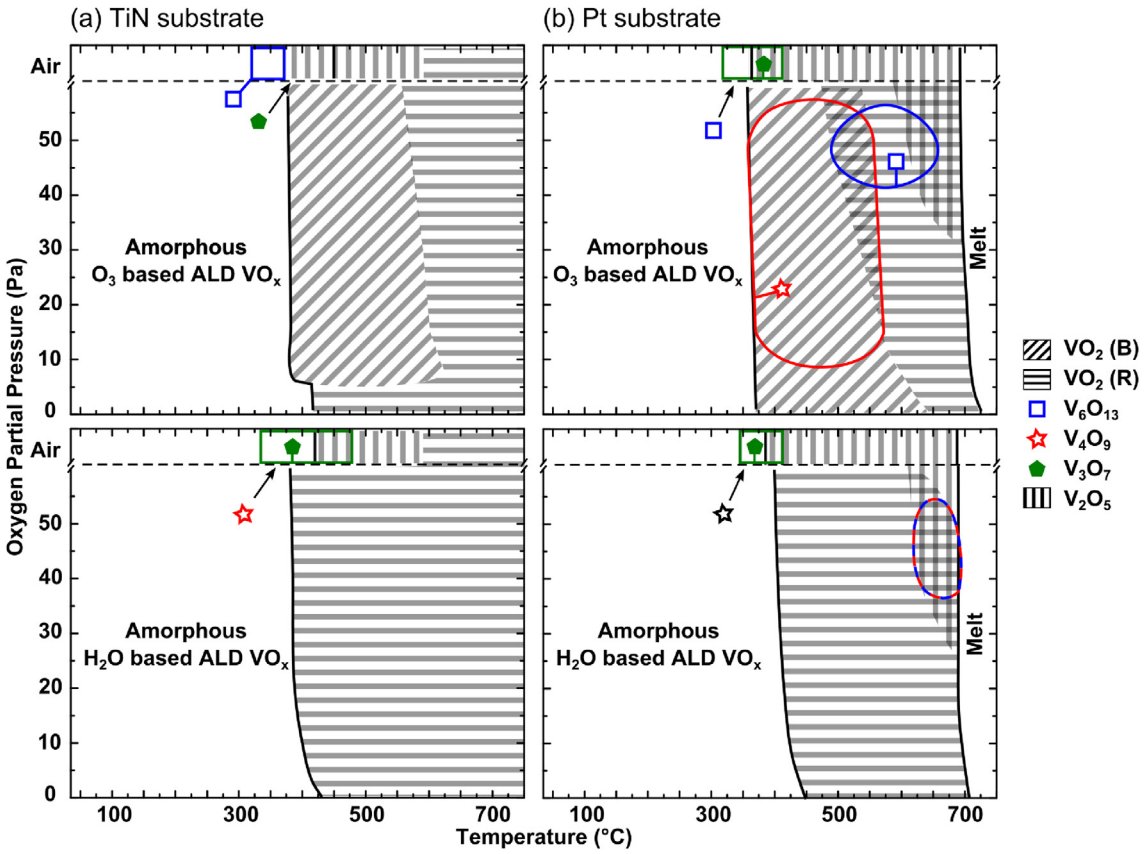


**Fig. 12.** Phase formation diagrams of the $VO_x$ crystal states ($2 < x < 2.5$) on TiN substrates (left) and on Pt/TiN substrates (right), at 0.25 °/s for He ambients with oxygen partial pressure of 3.7, 7.4, 14.8, 29.6 and 48.1 Pa, and in ambient air. The absence of the melt-line on the left figure is related to the presence of rutile $TiO_2$ from the substrate, complicating the analysis of the $VO_2$(R) phase on the TiN substrate at high temperatures. An explanation regarding the interpretation of these figures can be found in the caption of Fig. 10. Reproduced from Ref. [65] with permission from the Royal Society of Chemistry. ALD, atomic layer deposition.

150 °C. It was observed that while a mixed-phase $VO_2/V_3O_7$ was observed already at oxygen partial pressures starting from 6 Pa $O_2$ on 90 nm $SiO_2$, pure $VO_2$ could be crystallised at 500 °C in oxygen partial pressures up to 11Pa $O_2$ on a 1 nm $SiO_2$ on Si substrate. The origin of this different stabilisation behaviour on these two substrates with a similar surface chemistry (both $SiO_2$) can only be related to the underlying substrate. In the case of the thick $SiO_2$ layer, the substrate is saturated with oxygen, so no oxygen scavenging from the ambient can occur, resulting in oxidation of the vanadium oxide films at lower oxygen partial pressures. In the case of the thinner $SiO_2$ substrate layer, oxygen scavenging from the ambient can occur to partially oxidize the underlying Si substrate, resulting in a delayed oxidation of the grown vanadium oxide films.

### 3.2. Influence of postdeposition annealing on the surface morphology

#### 3.2.1. Thickness and temperature

As highlighted in the previous section, an excellent control over the crystallinity and oxidation state of vanadium oxide films can be achieved by postdeposition annealing of ALD-made films. However, besides crystallinity, film and surface morphology also play a paramount role in device characteristics, as well be shown in the following sections on applications of ALD $VO_x$ films in energy storage (section 4), microelectronics (section 5) and thermochromic glazing (section 6). For example, electrical devices, such as the electrochromic films discussed in section 6, can only be operated if they are continuous, while for catalysis, the enhanced surface area is beneficial. Rampelberg et al. investigated the morphology evolution upon the conversion to $VO_2$(M1) and revealed a significant sensitivity to the annealing step, as shown in Fig. 13. Although the crystallisation behaviour was thickness insensitive (~450 °C in 1Pa $O_2$), lowering the film thickness or further increasing the thermal budget resulted in faster agglomeration of the films to form isolated particles, and films below 11 nm fell outside the processing window to obtain a closed $VO_2$(M1) film [66].

#### 3.2.2. Surface and ambience

Peter et al. further showed that, besides film thickness and temperature, the presence of oxygen in the annealing ambient, and the nature of the substrate, also played a role in agglomeration of films, more specifically of $VO_2$ films. They suggested that post-deposition annealing, especially in the case when a valence change is necessary to obtain stoichiometric $VO_2$, is typically accompanied by rough morphology and agglomeration on dielectric substrates [69]. These were attributed to dewetting of the dielectric surfaces by the metallic $VO_2$ and are strongly enhanced by the volume change during the heat treatment [69]. A systematic coarsening of vanadium oxide was reported on fused silica substrates upon annealing in pure $N_2$ [78]. When very similar films were annealed by Lv et al. [80] in inert ambient (pure Ar in their case), film cracking was observed but no agglomeration was seen, indicating a better adhesion to the Si surface compared to the fused silica. The interplay between the presence of oxygen in the ambient and the nature of the substrate (adhesion, surface chemistry, lattice matching, thermal expansion coefficient matching) is not yet completely understood and requires further research. Fig. 14.

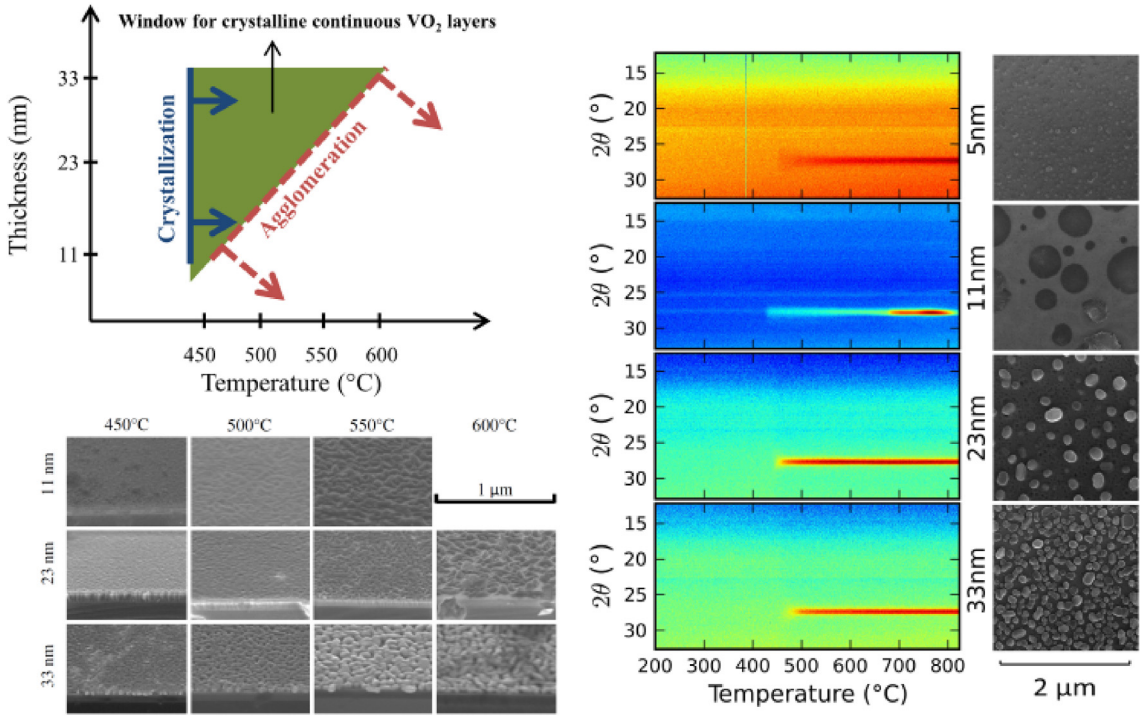


**Fig. 13.** (top left) Process window for the crystallisation of amorphous vanadium oxide films grown from TEMAV and $O_3$ and annealed in a 1Pa $O_2$ ambient, illustrating the effect of thickness and temperature on the morphology. (bottom left) SEM images of 11, 23 and 23 nm films after isothermal anneal for 30 min in 1Pa $O_2$ at 450, 500, 550 or 600 °C, (right) in-situ XRD demonstrating the independence of thickness on the crystallisation temperature under the same conditions (same precursors, reactant and an annealing ambient of 1Pa $O_2$) Reprinted from Ref. [66], Copyright 2014, with permission from Elsevier. TEMAV, Tetrakis ethylmethyl amino vanadium;

## 4. Applications of vanadium oxides in energy storage

The global energy scarcity and environment deterioration have compelled an intensive exploration of sustainable and clean energy storage. Rechargeable batteries and supercapacitors are considered as the most favourable options among various energy storage technologies. Herein, the choice of electrode materials is of vital importance for the electrochemical performance. Typically, materials of interest are found among those with an open crystal structure and a relatively low density. The vanadium oxides in the Wadsley series, that is, $VO_2$, $V_6O_{13}$, $V_4O_9$, $V_3O_7$ and $V_2O_5$, are known as the layered vanadium oxides and have attracted a continuous and fervent attention as promising electrode materials for next-generation advanced electrochemical energy storage owing to their high specific capacity, abundant resource and low cost [95–97]. Therefore, many synthesis methods for vanadium oxides electrode have been shown to exhibit excellent electrochemical performance, including wet-chemical approaches [98,99], CVD [100] and ALD [30,50,65,87,94,101,102]. ALD is a powerful vapour phase deposition technique which can accurately control film thickness, conformity, morphology and composition because of its cyclic and self-limiting character. Consequently, vanadium oxides prepared by ALD as electrodes have delivered superior properties for energy storage.

### 4.1. Lithium-ion batteries

Among various energy storage technologies, lithium-ion batteries (LIBs) are one of the most attractive rechargeable batteries because of their high energy density, long cycling life, no to little memory effect and reduced environmental impact [103–107]. The layered vanadium oxides allow the insertion of ions, which makes them high-capacity cathode materials for LIBs as shown in Fig. 15

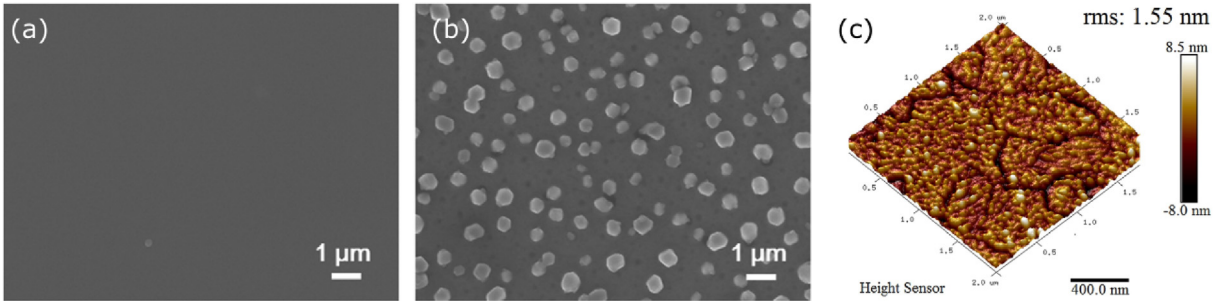


**Fig. 14.** SEM top-view images comparatively showing the accompanying morphological change of a TDMAV + $H_2O$-grown $VO_x$ film (a) before and (b) after the annealing process in pure $N_2$ at 600 °C on fused silica substrates, reproduced with permission from [78]. (c) AFM image of a TDMAV + $H_2O$-grown $VO_x$ film on n-type silicon after anneal at 425 °C in Ar, Reprinted from Ref. [80], Copyright 2017, with permission from Elsevier. TDMAV, tetrakis dimethylaminovanadium; SEM, scanning electron microscopy.

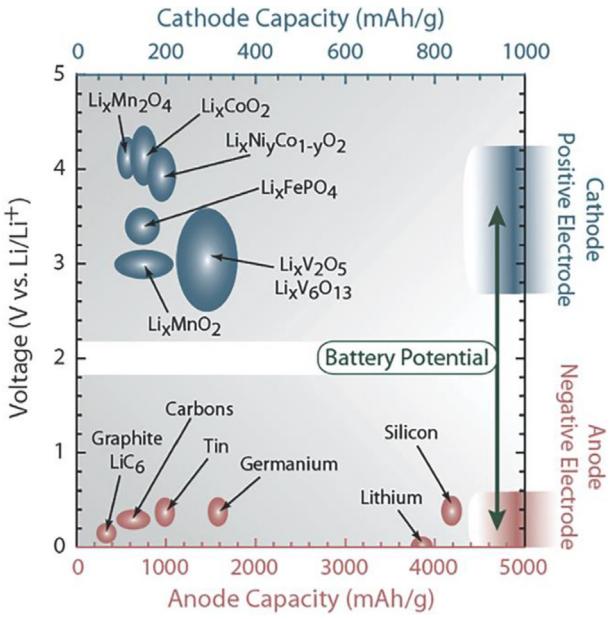


**Fig. 15.** Diagram illustrating the lithium-ion capacity and electrochemical reduction potentials of conventional anode and cathode materials [108].

[108]. The conformal nature of ALD allows the construction of very thin electrodes on highly structured 3D electrodes, such as multi-wall carbon nanotubes ((MW-)CNTs) and silicon etch–based structures as pillars or trenches. This enables a very fast charging thanks to the reduced diffusion length in thin film and a considerable capacity attributed to the area enhancement factor of the substrate compared to the footprint area [87], ultimately allowing the integration into 3D all-solid-state thin-film batteries [109]. On the other hand, the excellent phase control and high quality of the films allows for the study of ALD vanadium oxides as 'model system' electrodes.

Despite the phase-richness of vanadium oxides, most research was concentrated on the lithium-ion insertion into $V_2O_5$ [86]. Theoretically, the specific capacity of $V_2O_5$ can reach 147 mA h $g^{-1}$ with 1 Li-ion inserted per $V_2O_5$ unit, 294 mA h $g^{-1}$with 2 Li ions inserted per $V_2O_5$ and 440 mA h $g^{-1}$with 3 Li-ions inserted per $V_2O_5$, that is, full lithiation to $Li_3V_2O_5$.

The theoretical capacity of the complete lithiation of $V_2O_5$ is much greater than the typically commercialized materials such as $LiMn_2O_4$ (148 mA h $g^{-1}$) [110], $LiFePO_4$(170 mA h $g^{-1}$) [111] and $LiCoO_2$(274 mA h $g^{-1)}$ [112], as shown in Fig. 15. When one lithium per unit cell is stored (charging to $LiV_2O_5$), the original lattice structure is maintained, causing $V_2O_5$ to be extremely reversible (over 1000 cycles without capacity loss [30,113] and to display an excellent kinetics thanks to the high electronic conductivity in this range [114]. However, charging beyond 1 lithium per $V_2O_5$ unit cell is accompanied by irreversible lattice changes from up-up-down-down alternations of $VO_4$-pyramids to up-down-up-down alternations [115]. This structure transformation, along with lowered conductivity and poor structural stability (solubility of $V^{3+}$ and $V^{4+}$ species), leads to inferior electrochemical performance [116–118].

Constructing nanostructures for $V_2O_5$ by ALD is one of the most attractive strategies to overcome these drawbacks and thus further optimize its property in LIBs [30,50,53,56,57,94]. For example, Østreng et al. deposited nanostructured cathodes of $V_2O_5$ with different thicknesses, particle sizes and morphologies using ALD. A cathode layer of 10 nm (500 ALD-cycles) delivered a superior electrochemical performance relative to other cathodes thicknesses. This sample delivered a high specific capacity of 118 mA h $g^{-1}$at 1C within the potential window of 2.75–3.8 V. It even handled discharge rates of up to 960 C and showed stable capacity up to 650 cycles with a modest capacity fading that remained within 80% of the original capacity after 1530 cycles and endured up to 4000 cycles without failure at 120 C. This remarkable performance is because of good contact with the current collector and the electrolyte, along with small particle size [30]. Chen et al. reported a detailed study of ALD $V_2O_5$ as a high capacity cathode material, using VTOP precursor (see section 2.2 for details of ALD process) and comparing two oxidants, $O_3$ and $H_2O$. $O_3$-based films were crystalline and exhibited an improved electrochemical performance, compared with $H_2O$-grown film, which was amorphous. This crystalline film showed a high capacity of 127 mA h $g^{-1}$for 1Li/$V_2O_5$, 283 mA h $g^{-1}$ for 2Li/$V_2O_5$ and 389 mA h $g^{-1}$ for 3Li/$V_2O_5$ at 1C [50]. In addition, the hybridization of $V_2O_5$ with other materials such as carbon, carbon nanotubes (CNTs), and $TiO_2$ has also proven to be extremely effective for enhancing the electrochemical performance [53,56,94,119]. Chen et al. successfully fabricated multi-wall carbon nanotube (MWCNT)/$V_2O_5$ sponges for LIBs cathode by ALD as shown in Fig. 16. This cathode delivered a high initial area capacity of 1.284 mA h $cm^{-2}$ for 3 Li transfer (4.0–1.5 V), although cyclability was poor. In the 4.0–2.1 V range for 2Li/$V_2O_5$, the initial

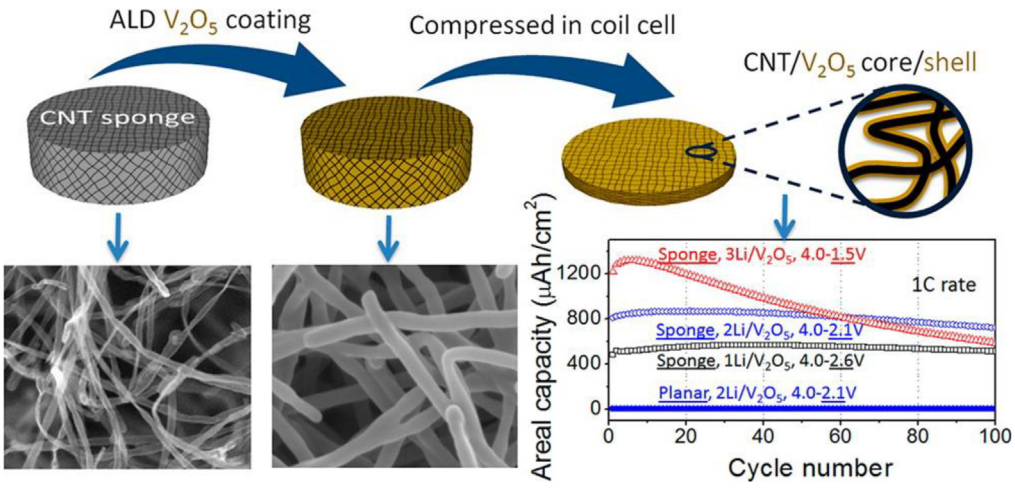


**Fig. 16.** The synthesis schematic and electrochemical performance of $V_2O_5$-coated MWCNT sponge [94]. ALD, atomic layer deposition; MWCNT, multiwall carbon nanotube.

area capacity was 0.818 mA h $cm^{-2}$ at 1 C and the cycling stability was largely improved. Furthermore, the capacity of 0.155 mA h $cm^{-2}$ was maintained with 50 C rate, giving an outstanding rate property. The excellent electrochemical performance of this hybrid cathode can be ascribed to its unique nanostructure. The sponge structure exhibited a high surface area, allowing for a high amount of active material loading, whereas the MWCNTs offer fast electrons transport channels. Furthermore, the thin uniform layer of $V_2O_5$ (<16 nm) enables fast (de)/lithiation of the active material. Finally, the high porosity of the sponge provides an easy access of electrolyte to the active storage material [94].

However, the cycling stability of two lithium ions into $V_2O_5$ is still not perfect, as the lower oxidation state vanadium can still dissolve in the liquid electrolyte. Kurttepeli et al. constructed a heterogeneous $TiO_2/V_2O_5$/MWCNT structure to tackle this issue, as shown in Fig. 17. Here, it was shown that the core-shell-shell structure still enabled all the excellent properties found by Chen et al., but the addition of a lithium-conductive protective coatings prevented V-dissolution and further stabilized the electrode, as shown in Fig. 17 [119].

Despite the main focus on $V_2O_5$, ALD also allows the study of model system electrodes. On the one hand, the excellent phase control shown in the previous sections on ALD films also allows the study of all other vanadium oxides in the Wadsley series as potential electrodes. Mattelaer et al. [87] found that all phases, that is, $VO_2$(B) up to $V_2O_5$, were able to store lithium. $VO_2$(B) was found to exhibit good cyclability along with storage of one lithium into $VO_2$, whereas $V_4O_9$ exhibited the highest initial capacity (1380 mAh/$cm^3$). Their rate performance is summarised in Fig. 18.

Besides crystalline phases, the low-temperature nature of ALD also allows the study of amorphous vanadium oxides. Le Van et al. synthesized amorphous ~200 nm $VO_x$ films using ALD, resulting in good cyclability and much higher capacity than the crystalline counterparts (455 mAh/g) [43]. Similarly, Mattelaer et al. were able to obtain amorphous $VO_2$ and $V_2O_5$ by tuning the process conditions using the TEMAV precursor (refer to sections 2.3.1 and 3.1 for more details). As can be seen in Fig. 18, very high capacities up to 1.4 Ah/$cm^3$ were found for amorphous $VO_2$ (~20 nm), alongside excellent capacity retention at high rates (80% at 100C), related to both higher lithium diffusion coefficients compared to their crystalline counterparts and the thin-film nature of the electrodes [87].

### 4.2. Supercapacitors

In addition to LIBs, supercapacitors are also promising for energy storage because they are able to deliver high power density which is also important for practical applications [120]. Therefore, vanadium oxides used for supercapacitors have also been explored because of the broad range of their oxidation states and low cost [47,51,52,121]. Surprisingly, the aforementioned unique hybrid nanoarchitecture composed of vanadium oxides and MWNTs prepared by ALD also showed excellent performance when used

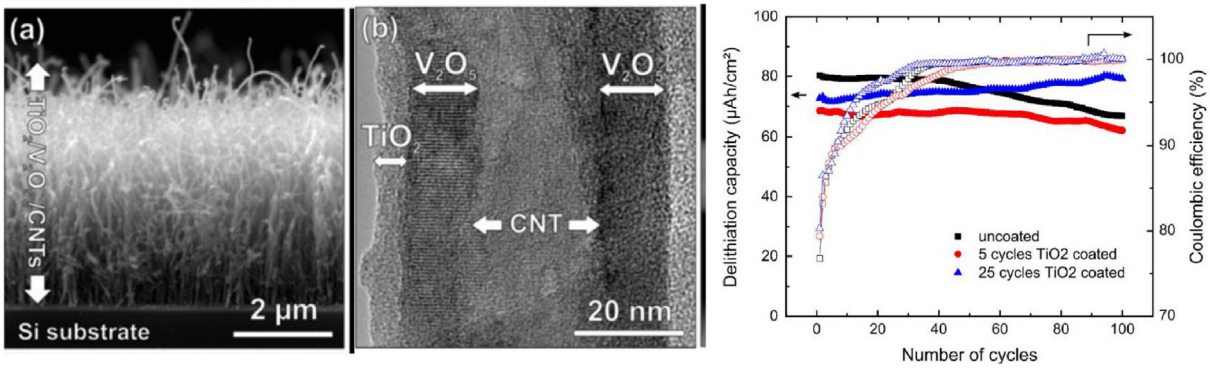


**Fig. 17.** Cross-section SEM image (left) and HRTEM image (middle) of 25 ALD cycles $TiO_2$-coated $V_2O_5$/CNTs. (right) Cyclability testing of uncoated $V_2O_5$/CNTs and of 5 and 25 ALD cycles $TiO_2$ on $V_2O_5$/CNTs samples at a current corresponding to 2C between 2.0 and 4.0 V vs Li+/Li. Reprinted with permission from Ref. [119]. Copyright 2017 American Chemical Society. CNT, carbon nanotube; ALD, atomic layer deposition; HRTEM, high-resolution transmission electron microscopy.

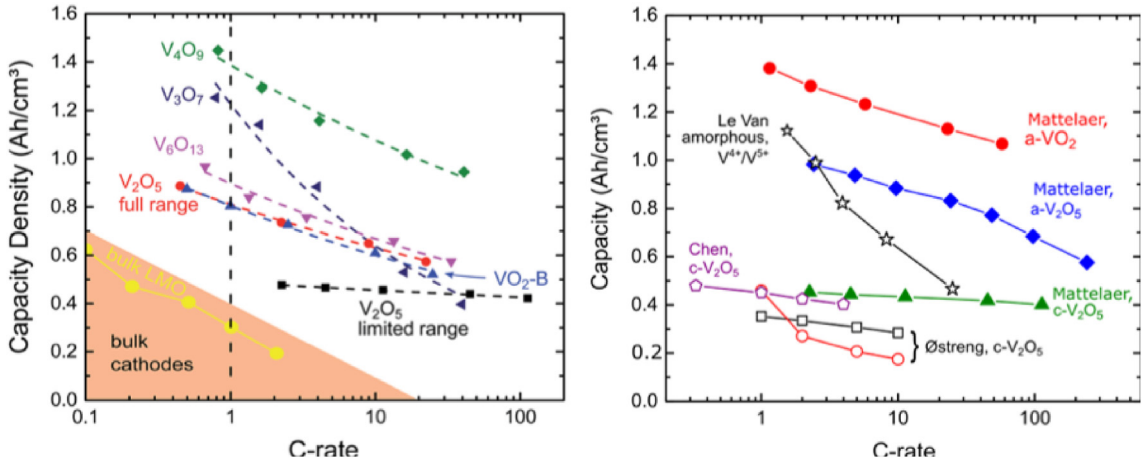


**Fig. 18.** (left) Comparison of the performance of various ALD-derived crystalline vanadium oxides (Published by The Royal Society of Chemistry) and (right) benchmarking of amorphous to crystalline vanadium oxides [30,43,65,87]. ALD, atomic layer deposition.

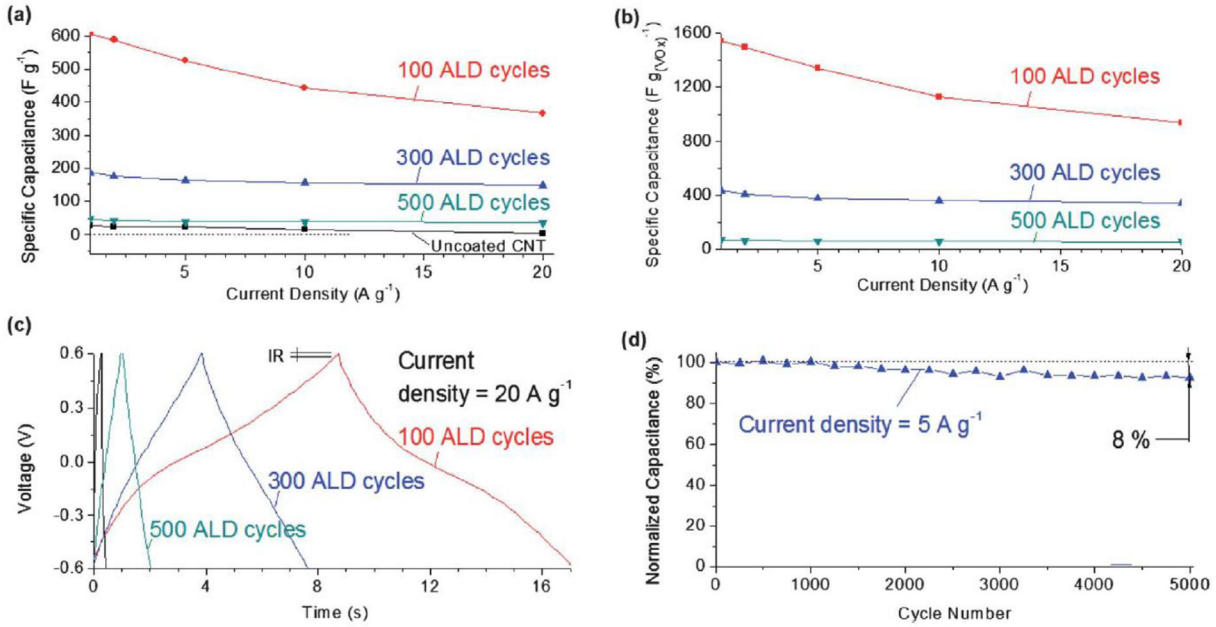


**Fig. 19.** Changes in the specific capacitance of the produced electrode samples for: (a) composite electrode and (b) contribution of $VO_x$ coating as a function of current density. (c) Charge-discharge profiles of the produced electrodes at the current density of 20 A/g. (d) A typical capacitance retention of $VO_x$ coating as a function of charge-discharge cycle numbers [121]. ALD, atomic layer deposition.

as supercapacitor electrode, see Fig. 19. A very high capacitance of up to 1550 F $g^{-1}$ was achieved at the current density of 1 A $g^{-1}$. Such high capacitance values are unprecedented for supercapacitor electrodes measured in a symmetrical two-electrode configuration in aqueous electrolytes. Its capacitance can reach up to above 1550 F $g^{-1}$even at a current density as high as 20 A $g^{-1}$. Furthermore, it also showed an excellent cycling performance. The capacitance loss was only 8% at a current density of 5 A $g^{-1}$ after 5000 cycles. This striking performance of such hybrid nanomaterial makes it an ideal candidate as electrode material for supercapacitors in real applications [121]. Hybrid nanostructures resulting from the incorporation of vanadium oxides with carbon or other conductive materials have also been used as electrode materials for supercapacitors with enhanced performance [47,51].

Interestingly, Daubert et al. found an intrinsic limit to the potential improvements of carbon-based supercapacitive performance. Owing to the excellent conformality of ALD, pore sealing can occur in nanoporous carbon electrodes. They found that, using VTOP as a precursor, pores with diameters below 13 Å, that is, close to the precursor diameter (9.6 Å) are closed during deposition as shown in Fig. 20. Counterintuitively, they found much larger increases in coated macroscopic carbon black or activated carbon, compared with microscopic carbon-based electrodes, as this pore-sealing fraction was much smaller [52].

## 5. Electronic phase control of $VO_2$

To allow either electronic or photonic applications, electronic phase control of $VO_2$ is key. By controlling the phase of $VO_2$ to be either the metal or insulator, one can switch electronic current or voltage signals for nanoelectronics applications or modulate electromagnetic waves, in photonics applications. A memory function arises if both phases, or memory states, can be maintained for a sufficiently long time at the same device operating conditions (input signals, temperature and other). Now, how can $VO_2$ be

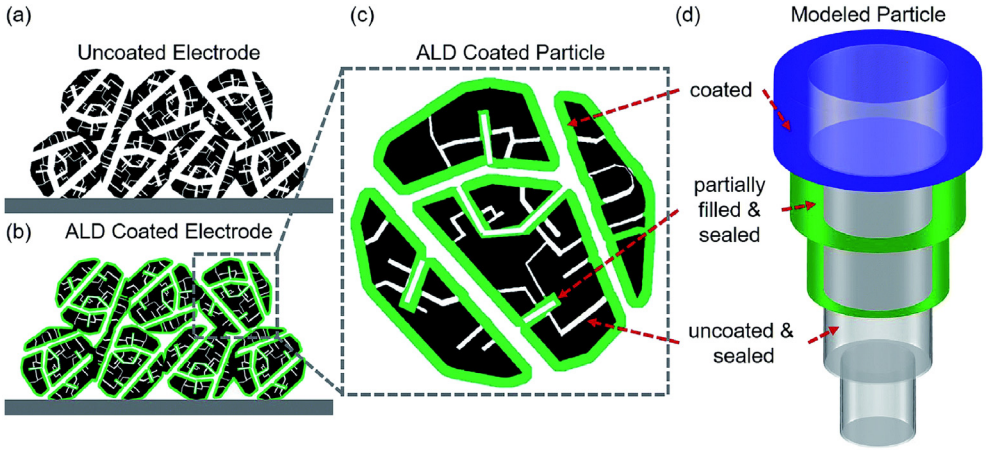


**Fig. 20.** (a–c) Illustration of pore sealing that can occur by deposition of a pseudocapacitive material using ALD, and (d) a model used to study this pore sealing, based on a series of narrowing tubes. Reprinted from Ref. [52]. ALD, atomic layer deposition.

switched between its phases electronically? We will treat the current understanding of the electronic switching of $VO_2$'s phase. This allows the deduction of challenges and opportunities for ALD $VO_2$ thin films for electronics and photonics.

In recent years, ALD has become a prominent technique for the deposition of dielectric [122] and metallic thin-films for nano-electronic applications [123–125]. The self-limiting surface reactions of ALD enable a precise control over film thickness and stoichiometry which are essential for the nanoscale thin films used in nano-electronics. In addition, the high conformality allows deposition onto three-dimensional (3D) structures, as increasingly required for advanced nanoelectronic applications. ALD of $VO_2$ presents a manufacturing friendly technique for potential $VO_2$ applications.

The direct way to switch $VO_2$ is to heat or cool it across its MIT electrically by means of Joule heating either by a nearby heater element by running a current through the $VO_2$ itself or by the Peltier effect. In section 5.1, the switching of $VO_2$ 2-terminal devices is discussed. In such devices, a current is run through $VO_2$ itself. The switching mechanism of such devices has been a subject of recent discussion in literature. The use of ALD $VO_2$ films, which have become available very recently and which are suitable for manufacturing of nanosized and 3D devices, has been reported in such device research.

Heating, however, requires a significant amount of power, which is an impediment for some contemporary applications. Low power is very important, for example, in highly mobile Internet of things applications. Researchers have explored alternative switching mechanisms and have attempted to switch $VO_2$ at constant temperature, looking for a so-called field-induced MIT in field effect transistor (FET) devices, which can be considered a holy grail in the field. In the second section, an overview is given of this $VO_2$ FET research. In 3-terminal FET devices, a channel current runs through $VO_2$between source and drain terminals. This channel current is controlled by a third, gate terminal. Most of this research has a fundamental character and has not been done with techniques suitable for manufacturing such as ALD; however, the ALD deposition of dielectric thin films has played a key role in this work and has allowed the fabrication of $VO_2$ FETs with high-quality gate dielectrics.

### 5.1. Switching of $VO_2$ 2-terminal devices

Two-terminal thin film $VO_2$ devices show an abrupt decrease of resistance when the current or voltage applied exceeds a threshold value. Investigations of few-micron–sized thin film $VO_2$ two terminal devices have widely reported that the observed steep decrease of resistance at a critical current or voltage is related to a field-induced metal–insulator transition [126–133]. However, recent work [134–141] has found the switching to be induced by Joule heating rather than directly by the applied electric field.

The fabrication of $VO_2$ coplanar two terminal devices (20–100 $\mu$m length) by Duchene et al., [142] allowed measurements of the pretransition region and the transition parameters of the current-voltage (I-V) characteristic. It is proposed that when a voltage is applied between the electrodes, the internal temperature rises and the device switches to the 'on' state. Threshold voltage and current were investigated versus ambient temperature. Below about 10 °C, switching was proposed to be a pure thermistor effect; above this point, application of voltage was proposed to cause the device temperature to rise to the phase transition temperature, when the conductivity increased sharply. The I-V characteristics in the pretransition region and the I-V thermal transition phenomena were explained by means of a theoretical model.

Zimmers et al., [135] used fluorescence spectra of rare-earth–doped micron sized particles as local temperature sensors on $VO_2$ two terminal devices (10, 20 $\mu$m length). As the insulator-metal transition was induced by a dc voltage or dc current, the local temperature reached the transition temperature indicating that Joule heating played a predominant role.

Freeman et al., [137] examined the structural evolution of tensile-strained vanadium dioxide thin-film devices ($6 \times 9.4\ \mu m^2$) across the electrically driven insulator-to-metal transition by nanoscale hard X-ray diffraction. A metallic filament with rutile (R) structure was found to be the dominant conduction pathway for an electrically driven transition, while the majority of the channel area remained in the monoclinic M1 phase. The filament dimensions were estimated using simultaneous electrical probing and nanoscale X-ray diffraction.

Nanoscale $VO_2$ two terminal devices were fabricated with different electrode separations down to 100 nm and the dc switching voltage and current dependence on device size and temperature were studied [140]. The nanoscale devices allowed the evaluation of $VO_2$ as an electronic switching material at a relevant scale for future nanoelectronics applications. Reducing the electrode separation to the $VO_2$ grain size is used as an approach to limit the occurrence of inhomogeneous (filamentary) and cascaded switching, because the current will traverse less or no grain boundaries between the electrodes. This allows us to study the transition in devices more closely approximating intrinsic single-crystal behaviour. Studying the origins of geometrically uniform switching which is expected to show the most straightforward behaviour and is most relevant for nanoscale devices. The observations of the geometrical and temperature dependence, and hysteresis of switching were found to be consistent with a Joule heating mechanism governing the switching. The power at which a device switched decreased linearly with increasing temperature, characteristic for a Joule-heating induced transition. Pulsed measurements showed a switching time to the high resistance state of the order of one hundred nanoseconds, consistent with heat dissipation time. Despite the Joule heating mechanism which was expected to induce device degradation, devices can be switched for more than 1000 cycles.

The work by Tadjer et al., [141] reported on two terminal switching devices making use of an ALD deposited vanadium oxide layer. Amorphous vanadium oxide ($VO_2$) films were crystallised with an *ex situ* annealing at 660–670 °C for 1–2 h under a low oxygen pressure ($10^{-4}$ to $10^{-5}$ Torr). Under these conditions, the crystalline $VO_2$ phase was maintained, whereas formation of the $V_2O_5$ phase was suppressed. Electrical transition from the insulator to the metallic phase was observed in the 37–60 °C range, with an $R_{OFF}/R_{ON}$ ratio of up to about 750. The lateral electric field applied across two terminal device structures induced a reversible phase change. Both the width and slope of the field induced MIT I-V hysteresis were dependent upon the $VO_2$ crystalline quality.

The power needed for reaching a MIT decreased linearly with temperature, confirming Joule heating was the predominant switching mechanism for that sample. However, this was not the case for partially crystallised $VO_2$ film and a soft (non-abrupt) transition profile was measurable even near room temperature in the 1.8–2.5 V range. The behaviour in this 'soft-MIT' region was attributed to the fact that the thermal conductivity of $VO_2$ is also phase dependent and could change by as much as 60% over the course of the MIT, ultimately leading to a non-abrupt field switching profile as the critical temperature is approached during measurement.

### 5.2. The transverse field-induced metal-insulator transition and the transverse field effect in $VO_2$ field effect transistor devices

A question which has instigated both fundamental and applied research is whether $VO_2$ could possess an electrostatic field–induced metal-insulator transition—or not. More specifically, the switching of a strongly correlated material such as $VO_2$ between a

metallic and an insulating phase by means of applying an electric field transverse to the material's interface with a gate electrode evokes the possibility of a switch device outperforming the present metal oxide semiconductor field effect transistor (MOSFET). Such a device is also referred to as Mott transistor or an MIT FET. The MOSFET is the dominant switching device in contemporary nanoelectronics and relies on the modulation of the surface conductivity of a semiconductor by a transverse field applied with a gate electrode. A metallic on-state in an MIT FET would allow a much lower on-resistance and a significantly higher transistor drive current.

It is important to rule out electrochemically and thermally driven effects (e.g. Joule heating) before ascribing certain encountered characteristics to MIT induced by electrostatic charging as in the aforementioned hypothetical MIT FET. In some work in literature, Joule heating has not been satisfactorily ruled out for transitions occurring at a certain drain-source bias or for gate voltage dependence of such a transition. Electrochemically induced phase transitions are typically induced at significantly longer time scales than electronic effects. Electrochemically switched devices (e.g. resistive random access memory (RAM)) tend to have lower cyclability, the amount of repeated switching possible before device failure occurs. However, electrochemical switching might enable memory applications. It is crucial as well is to work with high quality and well-characterized $VO_2$ films, to assure that the intended phase is obtained while also assuring a well-insulating gate insulator on top or below the $VO_2$ film. At present, MIT or Mott FET behaviour not induced by Joule heating or electrochemical effects has not been rigorously proven to exist in correlated oxide FETs. For $VO_2$, the basic understanding of the field effect, the change in surface conductance with an applied transverse electric field is of fundamental and applied interest as well, and is not yet fully understood.

A study carried out by Ruzmetov et al [143] emphasized that the quality of the gate dielectric layer and its interface with $VO_2$ were critical factors for detecting the field effect in 3-terminal $VO_2$ devices. For this reason, the authors explored a number of ways of synthesizing the gate dielectric within the device: e-beam evaporation of $SiO_2$ and $Al_2O_3$, RF sputtering of $SiO_2$ and $Si_3N_4$, and ALD of $HfO_2$ and $Al_2O_3$. It was found for the gate-on-top-type devices with non-ALD dielectric that, while the high quality of $VO_2$ can be preserved, the devices suffered from large leakage through the gate dielectric. These devices showed gate voltage modulation of drain current which was history dependent and of which the resistance continued to increase for some time (~10min) even after the gate voltage was removed.

However, it was found that the devices with the gate below the $VO_2$ film offered better quality of the gate dielectric layer as opposed to the gate-on-top devices. For the better quality bottom gate devices, a highly uniform 25 nm thick $Al_2O_3$ insulating layer was deposited by ALD on top of n-Si conducting substrate which served as a base for 60–150 nm $VO_2$ growth by means of RF sputtering from a $V_2O_5$target. The ALD-grown gate insulator/$VO_2$ interfaces exhibited reproducible electrical response to applied gate voltages, with no time dependence or persistence beyond removal of the gate voltage. At T = 60 °C applying gate voltages of 0.5 V led to a systematic, reversible and low drop in the channel resistance of about −0.26%(see Fig. 21).

Ji et al., [144] attempted to modulate the $VO_2$ MIT in single-crystal $VO_2$ nanowires via electrochemical gating using an ionic liquid. Individual single-crystal $VO_2$ nanobeam grown by vapour phase transport was used with a width and thickness of a few 100 nm. To attain high charge densities by applying a static electric field, a nanowire electric double-layer transistor (EDLT, see Fig. 22) was used involving an organic ionic liquid diethylmethyl(2-methoxyethyl)ammonium bis(trifluoromethylsulfonyl)imide

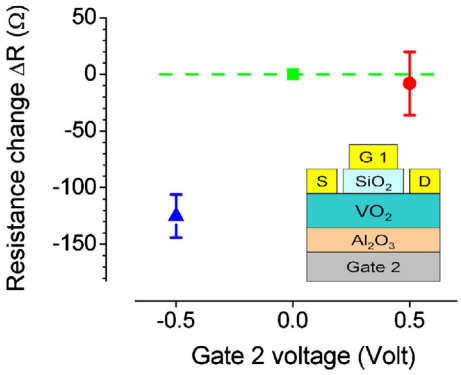


**Fig. 21.** The gate voltage modulation of source-drain resistance of the $VO_2$ channel as observed by Ruzmetov et al. The inset shows the device diagram. Reprinted from Ref. [143] with the permission of AIP publishing.

(DEME-TFSI) as a gate electrode. Stray water contamination in the ionic liquid was found to lead to large, slow, hysteretic conductance responses to changes in the gate potential applied by means of the ionic liquid. It was suggested that these changes were the result of electrochemical doping via hydrogen. In the absence of this chemical effect, gate response was found to be minimal. The authors suggested that significant field-effect modulation of the MIT is not possible, along the crystallographic directions of the reported nanowires.

Using an ionic liquid as an electrolytic gating medium, induced surface charge densities of ~$10^{14}$/$cm^2$ at the liquid–$VO_2$ interface are expected. The absence of any detectable gating effect in the insulating state was found to be surprising. Certainly some gate response would be expected for a conventional semiconductor with a band gap of ~0.5 eV. Surface states were asserted to be a possible impediment, but Ji et al. noted that surface states had not been a problem for field effect modulation in a number of oxide systems.

Nakano et al. [145] reported that semiconducting $VO_2$ can be rendered metallic by applying a strong electric field transverse to the $VO_2$ interface with an ionic liquid (DEME-TFSI) in an EDLT device. In these devices, no gate dielectric was present and $VO_2$ was in direct contact with the ionic liquid. These field-effect transistors consisted of $VO_2$(001) epitaxially grown on monocrystalline rutile $TiO_2$(001) substrates by means of pulsed laser deposition. The temperature dependence of resistance of the $VO_2$ devices for different gate biases was reported (see Fig. 23). At high bias, it was observed that the temperature dependence of channel resistance and the MIT were suppressed. The gate bias dependence of channel resistance at 260 K showed hysteretic switching.

The authors proposed that electrostatic charging at a surface drives all the previously localized charge carriers in the bulk $VO_2$ material into motion giving rise to collective carrier delocalization, leading to the emergence of a 3D metallic ground state.

Jeong et al. [146] showed similar temperature dependence of resistivity for different ionic liquid gate biases and similar hysteretic gate bias dependence at constant temperature in similar devices as Nakano et al. [145]. The hysteretic gate bias dependence was reported in Ref. [144] as well, in which the modulation was ascribed to water contamination. Jeong et al. argued that electrolyte gating of $VO_2$ leads not to electrostatically induced bulk carriers as proposed in Ref. [145] but instead to the electric field–induced creation of oxygen vacancies, with migration of oxygen from the oxide film into the ionic liquid. The devices were gated to the metallic state in vacuum and reverse-gated to recover to the insulating state in an $^{18}O_2$ ambient. The $^{18}O_2$ was

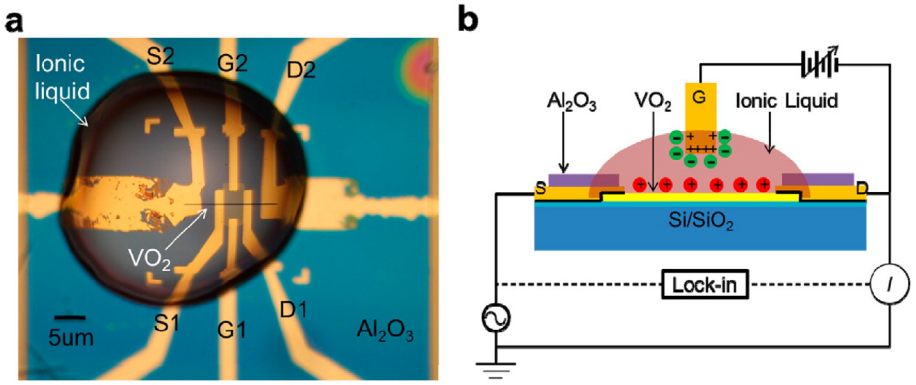


**Fig. 22.** a) Optical micrograph of an ionic liquid–gated EDLT device. (b) Schematic cross-section of an EDLT device. Adapted with permission from Ref. [144]. Copyright 2012 American Chemical Society. EDLT, electric double-layer transistor.

found to be incorporated in the $VO_2$ films by means of SIMS. XPS observations indicated a reduction in the oxidation state of V from $V^{4+}$ towards $V^{3+}$ after gating. It was also observed that the gate bias dependence of conductance depends on oxygen pressure, with gating absent at higher oxygen pressure. Jeong et al. showed that oxygen migration occurs during ionic liquid gating.

Belyaev et al. deposited 100 nm of amorphous vanadium oxide at room temperature by magnetron sputtering, on a Si substrate with a 100 nm $SiO_2$ gate dielectric followed by a 10 m Torr, 520 °C post deposition anneal [147]. These solid gated FET structures showed a temperature-induced MIT with a resistivity jump of about 2 orders of magnitude. The $VO_2$ channel resistance was found to weakly depend on gate bias, showing a change with only tenths of a percent for an oxide field strength of $10^7$ V/cm.

Martens et al. investigated the field effect on devices with ultrathin layers of $VO_2$ epitaxially deposited by pulsed laser deposition on single crystalline $TiO_2$ [148]. These films were combined with ultrathin high-quality gate dielectrics, among which ALD $HfO_2$. These structures allowed the measurement of the $VO_2$ field effect. The 3- to 9-nm thick single crystalline $VO_2$ films avoided large unmodulated 'bulk' conduction which has made measuring the small $VO_2$ field effect problematic. Owing to the high dielectric breakdown strength and high k value of the ALD $HfO_2$ films, $VO_2$ FET devices could attain a charge density of ~$5 \times 10^{13}$cm$^{-2}$, which is similar to the density quoted in Ref. [145] for ionic liquid gating, $5.6 \times 10^{13}$cm$^{-2}$at 0.9 V.

The gate bias modulation of channel conductance was found to be low (<0.6%/V), and no gate bias–induced MITs were observed. Depletion behaviour was found to be strongly suppressed, as observed in both subdued field effect modulation of channel current and capacitance. No signatures of defect dominated behaviour were encountered in admittance spectroscopy of gate capacitance and channel conductance, and scanning tunneling microscopy (STM). The mobility of the field-induced carriers was derived at 80 K–400 K. Based on the low, thermally activated field-induced carrier mobility (~$1 \times 10^{-3}$ cm$^2$/V at 300 K), these excess carriers were concluded to be strongly localized. The excess charge mobility was in agreement with that of small polarons described by an adiabatic Holstein polaron model with an extracted optical phonon frequency of the expected magnitude, $\hbar\omega = 8$–$22$ meV for hopping distances of a = 0.3–0.5 nm, fitted to the observed activation energy Ea = 0.11 eV. The low mobility of the field-induced carriers

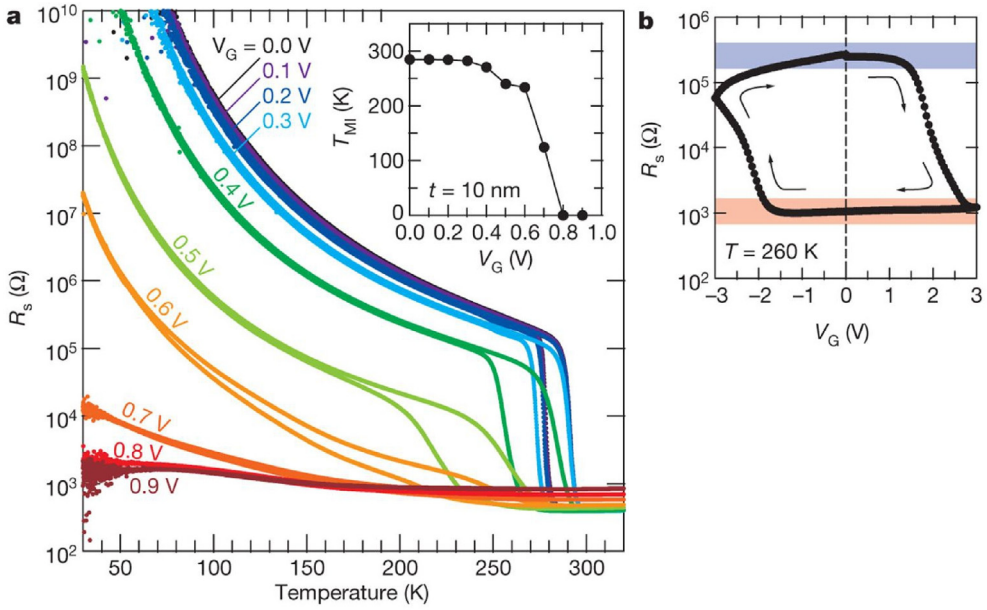


**Fig. 23.** a) Temperature dependence of channel resistance of a $VO_2$ EDLT device for different gate biases and (b) gate bias dependence at 260 K. Reprinted with permission from Nature [145]. EDLT, electric double-layer transistor.

provides an explanation for the strongly subdued field effect found in $VO_2$.

Yajima et al. [149] grew $VO_2$ on top of single crystalline Nb:$TiO_2$ with PLD. As an 'inverse-Schottky gate', the $VO_2$ channel was regarded as a metal electrode and $TiO_2$ as a semiconductor. The inverse–Schottky gate geometry allows electron densities of more than $1 \times 10^{14}$ $cm^{-2}$ to accumulate in $VO_2$ at the $VO_2$/Nb:$TiO_2$ interface.

The hysteretic temperature dependence of channel conductivity across the MIT was measured for different gate biases. A gate bias dependence of the derived transition temperatures was observed. Accumulating ~$9.0 \times 10^{13}$$cm^{-2}$ gate–induced carriers resulted in an observed change in $T_{MIT}$ of ~1 K. The small transition temperature shifts observed were found to be inconsistent with Joule heating. It was argued that the current modulation was taking place not only in the vicinity of the interface but also in the whole $VO_2$ film and hence that a carrier delocalization effect is taking place as proposed in Ref. [145].

Wei et al. [150] found that the modulation of $VO_2$ nanowire channel resistance near the MIT temperature by a gate was significantly larger than that of larger thin film–based FETs. The authors proposed that the enhanced resistance modulation of the nanowire channels was primarily due to the expansion of metallic nanofractions in an insulating matrix by applying gate bias especially at the edge of the channel where the electric field was higher.

There is plenty left to be learned and confirmed about the field effect in $VO_2$. A significant modulation of $VO_2$ by means of a transverse electric field has been observed in ionic liquid–gated devices and was ascribed to oxygen migration. Cyclability and speed of this effect remain to be further investigated for applications. The field effect in solid gated devices has so far largely appeared to be subdued. Improvements in film quality and defect content, especially near the gate dielectric–$VO_2$ interface, the careful avoidance or control of Joule heating, gate leakage and electrochemical effects and the use of advanced characterization techniques may lead to further understanding of the physics and the development of the application potential of the $VO_2$ field effect.

### 5.3. $VO_2$ applications and ALD $VO_2$ challenges

Electronic switching applications for $VO_2$ that have been proposed so far include the following: selector elements for cross bar array memories [140,151–155], RF switches [156–158], steep threshold devices [159], non-Boolean computing [160,161], reconfigurable photonic devices [162–166], plasmonics [167,168], terahertz applications [169–172], metamaterials [173,174] and others.

A key challenge across $VO_2$-based electronics and photonics is the compatibility with commercial and industrial operating temperature range requirements (70–85 °C) and the even more challenging range of military and automotive applications. To comply with these requirements, the $VO_2$ film transition temperature would need to be sufficiently above the operating temperature range, to avoid switching all $VO_2$ when the chip temperature is at the higher end of the operating range. During electronic switching, the local device temperature is then brought above the operating temperature range to switch the device. A workaround would be to provide temperature control of the nanoelectronics or photonics chip which keeps global chip temperature below the transition temperature. This might be feasible for some specific applications, but not for all, especially when competing with alternatives that do not require such temperature control. To address the operating temperature range challenge, ALD $VO_2$ films might be strained [176] or doped to raise the transition temperature. Ti doping has been reported by some to lead to higher transition temperature [177] or to have little influence on the transition temperature by others [178,179]. While raising the transition temperature sufficiently, the abruptness and magnitude of the resistivity change across the transition should be maintained or even improved.

Another key ALD challenge is improving the $VO_2$ ALD film quality to reach similar magnitudes of resistivity change across the transition as those obtained in the best reported $VO_2$ material. Control of crystallinity, stoichiometry, and defects in $VO_2$ films are key to obtain the desired electronic properties.

ALD forms an attractive technology to deposit thin (<50 nm) $VO_2$ films suitable for mass manufacturing, and further progress in film quality, change in conductivity across the transition and transition temperature tuning, could enable $VO_2$ applications.

## 6. Thermochromic windows—principle of operation

Approximately half of the energy that reaches the surface of the Earth from the Sun is in near-infrared wavelengths, which are invisible to humans [180]. Developing adaptive coatings that modulate this particular part of the terrestrial solar spectrum is presenting us with an excellent opportunity to balance the energy needs for the heating and cooling of buildings, without affecting the visual perception and comfort of their inhabitants [181]. In this regard, the purpose of a smart thermochromic coating is to regulate the amount of solar radiation that is transmitted through the windows of a building, depending upon the ambient temperature. During hot weather (hot-state), a smart window should ideally reject the majority of the Sun's infrared radiation and pass all or part (in cases where a diming effect is desirable) of the incident visible radiation; thus, the need for air conditioning is limited. During cooler weather (cold-state), both infrared and visible radiation should fully be transmitted, minimising heating and lighting energy loads, Fig. 24. Vanadium dioxide is the prime material choice for thermochromic window applications due to its favourable intrinsic properties, summarised in the following: (i) the material exhibits a substantial change to its optical properties when switching from one phase to the other (see also discussion on $VO_2$ refractive index in the following section). This change is more prominent in the infrared wavelengths (>700 nm), inducing a large modulation to the transmittance of near infrared (NIR) radiation between the cold and hot states; (ii) the transition temperature of

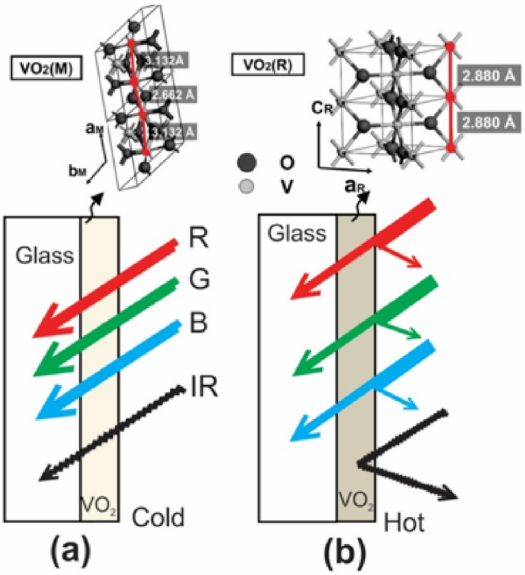


**Fig. 24.** Illustration of thermochromic window functionality: (a) Cold state enabling both visible and infrared radiation to be transmitted through. (b) Hot state that cuts off infrared radiation and part of visible radiation.

$VO_2$ can be tuned over a broad range, and hence, the properties of thermochromic coatings can be tailored to the specific climatic conditions of a particular geographic location; (iii) a large number of deposition methods and precursor materials for $VO_2$ thin-films are already available, some compatible with widely deployed, scalable manufacturing processes. This promises a short path from research to the market; and finally, (iv) vanadium is a relatively abundant material and is already in use on industrial scale. There are largely two lines of research in association with $VO_2$ smart window technologies under intense investigation at present. The first uses thin-films of $VO_2$ to control NIR radiation, most commonly via modulation of a window's reflectance [182]. The second exploits the changes in the absorption cross-section of $VO_2$ nanoparticles to regulate the solar heat gain through a window's surface. The latter area, frequently termed nanothermochromics [183], will not be the subject of this review as there is no evidence of conjunction with ALD processes in the literature. Instead, we will focus on the former area, where we believe that most of the breakthroughs may come about by application of ALD methods.

### 6.1. Optical constants in hot and cold state

As mentioned in previous sections of this review, $VO_2$ behaves as a semiconductor with monoclinic crystalline structure below the transition temperature *Tt*, ($T < Tt$), while it transforms into a rutile-like, semi-metallic phase for $T > Tt$. We therefore expect the real and imaginary parts, ($n$,$k$), of its refractive index to vary quite distinctly between these two states. It is, in fact, the drastic variation in the optical constants of $VO_2$ that is responsible for its striking properties that make it a suitable material for smart window applications. Despite numerous studies having been devoted to the evaluation of the wavelength dependent $VO_2$ refractive index [73,184–186], the literature has yet to converge to an accurate and commonly agreed set of values. This is primarily because the quality of the measurements is affected by deviations on the density and morphology of the produced films, as well as the concurrent presence of other oxide polymorphs. The inherent anisotropic nature of crystalline $VO_2$ may imply at first that the complete refractive index tensor needs be quantified. Nonetheless, most films produced in practice consist of polycrystalline domains, giving rise to an isotropic effective index over sufficiently long range. Although substantial discrepancies between the absolute values of the reported optical constants are met among different studies, all published data still share the same qualitative characteristics. Fig. 25 shows the values for both hot and cold states, obtained by spectrometric ellipsometry [186]. The cold state is consistent with a semiconductor structure with a bandgap of 2.5 eV (~495 nm), arising from the separation between the oxygen 2p-orbitals and the vanadium 3d-bands in the monoclinic phase and additional absorption peaks at around 3 eV and 4 eV due to interband transitions within the vanadium 3d-bands [184]. These features manifest as an abrupt increase in the extinction coefficient for wavelengths <500 nm, which accounts for increased losses in this region. This is undesirable, as it is responsible for the yellow-brownish colouration of typical $VO_2$ films, which is generally considered unattractive for commercial purposes. The relatively large values (>2.3) of the refractive index across the whole visible spectrum contribute to high reflectance in this spectral region, which is also undesirable as natural light is equally blocked in hot and cold states. An additional absorption peak is observed at ~1.2–1.3 eV, consistent with the literature [73,184,185], which is responsible for the milder and broader peak in the extinction coefficient around 1000 nm. In the hot state, purely metallic behaviour is observed for energies higher than 2 eV (~620 nm) and a stark increase in the free-carrier absorption with a concomitant increase in the extinction coefficient in the infrared occurs. The consequence of this behaviour is dramatic, as far as smart window applications are concerned. Vanadium-dioxide thin films exhibit a surge in their reflectivity [182], whereas $VO_2$ nanoparticles exhibit acute enhancement to their absorption cross-section [183], as the temperature increases past the transition threshold and the material undergoes the SMT. Thereupon, the amount of radiation that is transmitted through a smart window can substantially be modulated, with this effect being more prominent for NIR wavelengths, as already mentioned before.

### 6.2. Metrics for thermochromic window performance

Before discussing the synergies between thermochromic coating research and ALD in more detail, it is useful to introduce some key metrics that are used extensively to characterise the performance of smart windows [181–183]. It is customary to use spectrally weighted average transmission quantities and assess the performance of the window in the visible wavelengths, associated with human comfort aspects, separately. Consequently, the luminous transmittance $T^{c,h}_{\mathrm{lum}}$ and solar transmittance $T^{c,h}_{\mathrm{sol}}$ metrics are defined in the cold and hot states as follows:

$$T^{c,h}_{\mathrm{lum,sol}} = \frac{\int \phi_{\mathrm{lum,sol}}(\lambda) T^{c,h}(\lambda)\, \mathrm{d}\lambda}{\int \phi_{\mathrm{lum,sol}}(\lambda)\, \mathrm{d}\lambda},$$

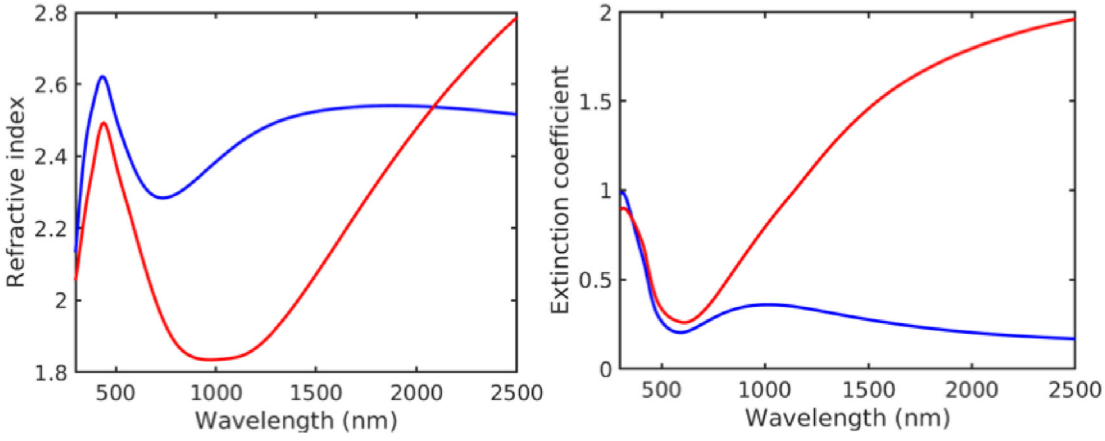


**Fig. 25.** Spectroscopic analysis of $VO_2$ refractive index: (left) real part, (right) imaginary part. Data reproduced from Ref. [186].

where $T^c(\lambda)$ is the transmittance at wavelength λ in the cold state and $T^h(\lambda)$ in the hot state correspondingly, $\phi_{lum}$ is the photopic spectral sensitivity of the light-adapted eye (CIE 2008, 380 nm < λ < 780 nm) and $\phi_{sol}$ is the solar irradiance spectrum for air mass 1.5 standard (280 nm < λ < 2500 nm). The solar transmittance modulation ($\Delta T_{sol}$) can then be deduced from the above as $\Delta T_{sol} = (T^c_{sol} - T^h_{sol})/T^c_{sol}$. This parameter outlines the potential of a thermochromic coating to regulate the admitted solar radiation in the summer and winter months. As a general rule of thumb, efficient thermochromic coatings should be designed to simultaneously maximize $T^{c,h}_{lum}$ and $\Delta T_{sol}$. We mention in passing that the transmittance based metrics presented above are not the only parameters that smart window researchers need to consider when developing next generation coatings. Equally important, albeit broadly overlooked in the literature, are the hysteresis width and gradient of the coatings, which need to be tightly controlled or otherwise the performance of the windows may be inexorably compromised [187].

After several decades of research, a smart window product has yet to appear in the market, unveiling the hurdles still needed to be overcome to commercially translate the work in this area. The key and often conflicting challenges facing thermochromic coating research are (a) the refractive index of $VO_2$ admits large values across the entire solar spectrum, as already discussed in the previous section. This results in high reflectance in both hot and cold states, limiting $T^{c,h}_{lum}$ and suppressing $\Delta T_{sol}$. (b) The solution that usually is advanced to improve $\Delta T_{sol}$ is to increase the thickness of $VO_2$ layers. This has the adverse effect of diminishing $T^{c,h}_{lum}$, pointing to a critical trade-off between $T^{c,h}_{lum}$ and $\Delta T_{sol}$ the difficulty in concurrently maximizing both; (c) the native transition temperature of $VO_2$ is 68 °C, which is impractical for real life applications and needs to be brought closer to room temperature; (d) steep switching promotes higher energy savings and hence, the hysteresis and the gradient of the transition curve have to be kept to a minimum; (e) the unappealing colouration of $VO_2$ coatings needs to be addressed to produce aesthetically desirable products; (f) durability is an issue of prime importance, as coatings need to survive harsh conditions over prolonged periods of time. The two most common threats encountered by $VO_2$ coatings are oxidation when exposed to air and weak adhesion to substrates; (g) as a final remark, we note that additional multifunctionality (for example, self-cleaning, oil-repellence, high-conductivity, scratch resistance, ice nucleation delay, photocatalytic and antimicrobial activity and other) is desirable for add on value and creation of high-end products.

### 6.3. Role of ALD in smart window research and future outlook

ALD is emerging as a promising technology platform to address some or all of the key challenges encountered in smart window research. As a first example, ultrathin layers of amorphous $Al_2O_3$ were deposited atop $VO_2$ films by Wang et al. in Ref. [188] as protective layers. In this study, it was found that $Al_2O_3$ layers as thin as 5 nm were sufficient to prevent oxidation of $VO_2$, even when samples were heated up to 350 °C for over 1 h. This was in complete contrast with the control sample that was fully oxidised to $V_2O_5$ and lost its thermochromic properties when subjected to the same heat treatment. Such protective layers can, in the future, be used as barriers to prevent oxidation but also to improve the durability and wearability of thermochromic films [189]. As far as the issues associated with the transition temperature and aesthetics of the $VO_2$ coatings are concerned, researchers have traditionally sought solutions in elemental doping. This is a very vibrant area of work and over 60 elements have been investigated by theory or experiment at present, as potential dopants to improve the optical properties of $VO_2$ films [190]. The complete coverage of the subject is outside the scope of this review but the general strategies to lower by doping aim to increase the carrier concentration and to

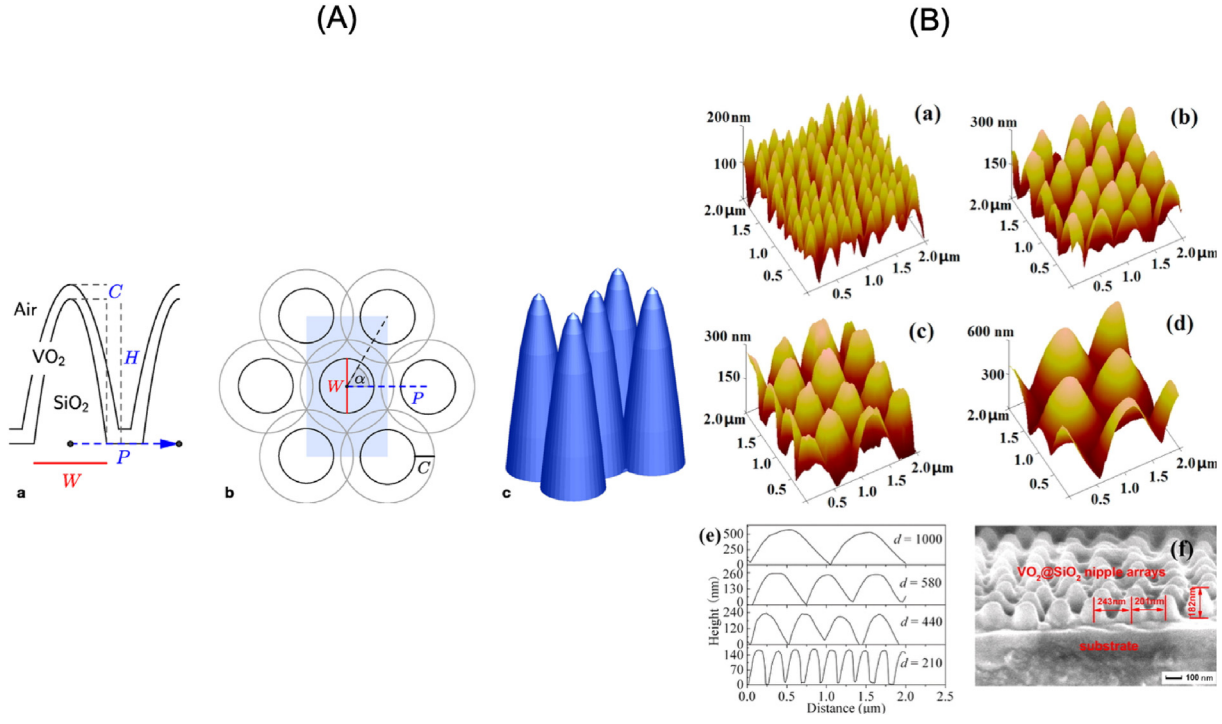


**Fig. 26.** Bioinspired, antireflective, superhydrophobic thermochromic concept. (A) Side and top elevations of nanotextured surfaces with hexagonally arranged paraboloid cones that were simulated in Ref. [195]. © 2013 Optical Society of America. (B) Fabricated moth-eye $VO_2$ structures. Adapted with permission from Ref. [196]. Copyright 2014 American Chemical Society.

induce directed internal strain, both of which have shown to decrease the energy barrier for the SMT. The prototypical dopant is W, a higher valency (+5) transition metal, which was shown to lower the transition temperature by ~20 K/at% [191]. On the other hand, doping with Mg was used to widen (blue shift) the bandgap of $VO_2$ to 2.32 eV [192], which had a beneficial effect on the hue and the $T_{lum}^{c,h}$ of the films. ALD can play an important role as a means to a controlled and precise doping, as has been demonstrated with the nanolaminate technique [193]. According to this method, ultrathin nanolaminates of different materials are alternately deposited by successive ALD cycles and doping is facilitated upon high-temperature annealing via interlayer diffusion. A first attempt in the context of smart windows was made by Lv et al. in Ref. [194], where doping with Mo up to levels of 10 at% was examined and results were encouraging.

A popular method to surpass the trade-off barrier between luminous transmittance and solar modulation is by using multilayer, antireflective films [197–199]. By carefully optimising the optical path in each layer, constructive interference conditions can be attained for the transmitted field suppressing reflections and thus, enhancing $T_{lum}^{c,h}$ and $\Delta T_{sol}$. A triple-layer $TiO_2/VO_2/TiO_2$ made by magnetron sputtering in Ref. [197] reported $T_{lum}^{c} = 63\%$ and $T_{lum}^{h} = 57\%$, compared with $T_{lum}^{c} = 47\%$ and $T_{lum}^{h} = 42.5\%$, for a single $VO_2$ layer deposited under identical conditions and on a similar substrate. Another triple layer $SiO_2/VO_2/TiO_2$ structure [199] demonstrated additional photocatalytic activity, showcasing the possibility of combining thermochromicity with extra functionalities. The broadband and incoherent nature of sunlight poses a great challenge to the design and fabrication of multilayer structures for thermochromic applications. Any system designed needs to maintain steady performance over a broad range of wavelengths and, crucially, be insensitive to the incident polarisation as well as the angle of incidence. Such demanding design rules can only be met by systems comprising a large number of layers [200], the thickness of each one of which needs to very precisely be controlled as even miniscule errors aggregate rapidly across the full stack. This imposes stringent requirements to the fabrication processes. ALD is a very attractive method for this purpose, as it provides with a highly repeatable, accurate, scalable and automated route for the uniform deposition of multiple material layers in a single batch [201].

The outlook of ALD in thermochromic window research is bright, as argued in the previous paragraphs. It is our belief, however, that the full potential of ALD will truly be harnessed only when it combines with the rapid advances in nanotechnology and nanofabrication. The first step to merge the worlds of smart

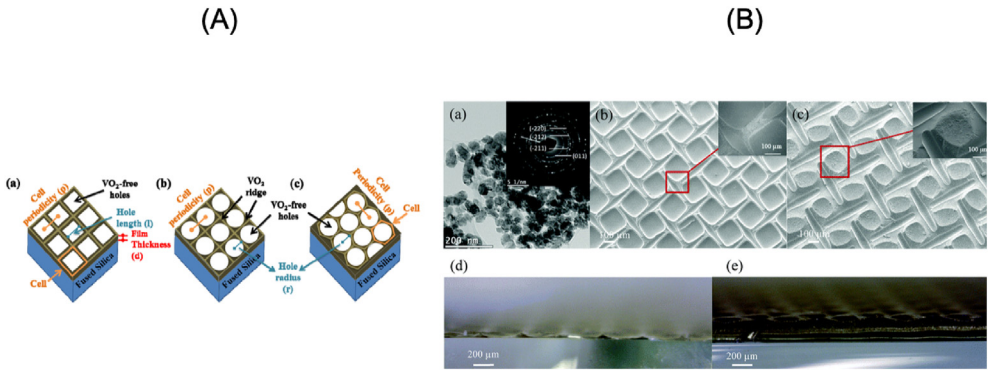


**Fig. 27.** (A) Nanogrid thermochromic modelled in Ref. [202]. © 2015 Optical Society of America. (B) Fabricated microgrid patterns in Ref. [203]—published by the Royal Society of Chemistry.

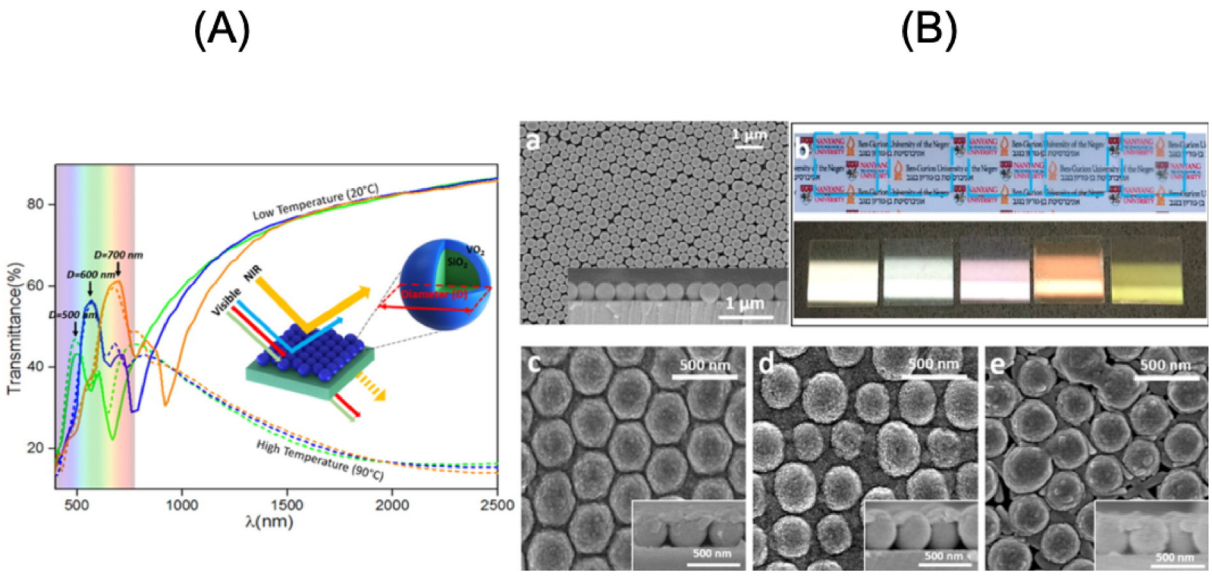


**Fig. 28.** Photonic crystal–based thermochromic windows. Adapted with permission from [206]. Copyright 2016 American Chemical Society.

windows and nanotechnology was taken by Taylor et al., [195], with the design shown in Fig. 26(A). In their article, it was shown theoretically that $T^c_{lum} > 70\%$ and $\Delta T_{sol} > 15\%$ are achievable by using bioinspired, antireflective structures in a glass substrate, conformally coated with ultrathin layers (10–20 nm) of $VO_2$. Moreover, this design satisfies the requirements for broadband operation, is agnostic to the polarisation and angle of the incident light and introduces virtually no haze to the smart window. Finally, such moth-eye structures are well known to induce extreme superhydrophobicity, ice formation delay, omniphobicity and other functionalities when their surface energy is lowered by silanization or other processes [204,205]. Along similar lines, Liu et al. [202] proposed a design, whereby a $SiO_2$ substrate patterned on a nanogrid array showed theoretical values of $T^c_{lum} > 78\%$ and $\Delta T_{sol} > 15\%$, when coated with $VO_2$ layers of ~300 nm, Fig. 27(A). Thermochromic coatings were also combined with opal photonic crystals in Ref. [206] where theoretical results of $T^c_{lum} > 49\%$ and $\Delta T_{sol} > 11\%$ were obtained. However, the real strength of photonic crystals lies in the ability to tune their photonic bandgap, which can be leveraged to achieve virtually any desired tint, as was demonstrated in this publication, Fig. 28. Some attempts to fabricate the aforementioned structures were made in the literature [196,203] where in all cases, sol-gel processes were used to deposit the $VO_2$ coatings. Despite best efforts, all experimental systems exhibited suboptimal results compared with their theoretical counterparts, mainly because the fabricated structures could not match the explicit design requirements arose from modelling. This reveals the unique opportunity for ALD, as the only known process that can provide ultrathin, carefully doped, conformal and high–aspect ratio coatings, to meet the demanding requirements of nanotechnology and produce highly efficient, multifunctional thermochromic coatings that can outperform almost any other design.

## 7. Conclusions

The ALD of vanadium oxide has been addressed from various perspectives. A close look at the processing chemistry reveals the availability of vanadium precursors where the cation features the oxidation state III, IV and V. Considering the volatility of these precursors near room temperature and their thermal stability, two precursors can be distinguished in terms of reaction with various typical reactants. Thermal ALD using water vapour or ozone as a reactant and plasma-enhanced ALD using molecular oxygen are readily enabled using TEMAV and VTOP. The ALD-required saturating chemisorption of these precursors was reported. The absence of a consensus regarding the thermolysis temperature of VTOP and the growth per cycle at saturation with TEMAV is noteworthy. Nonetheless, VTOP presents clear handling advantage and high volatility at room temperature, whereas TEMAV features a conveniently high thermolysis temperature. A considerable number of commercially available volatile vanadium compounds were not reported so far as ALD precursors. The ALD-made vanadium oxide layers are typically amorphous, and the postdeposition treatment is essential for the attainment of a single crystalline film consisting of one phase only. A thorough review in this respect shows a tight dependence of the crystallisation kinetics on the nature of the substrate, gas-phase composition, pressure, temperature, content and nature of contaminants in the film and film thickness. *In situ* monitoring has played a major role for the establishment of phase-formation diagrams to rationalize the processing of the various vanadium oxide phases. The processing-induced morphological impact is substantial, and it its complexity is worth of dedicated investigations. Among vanadium oxides phases, the Wadsley series presents a particular interest for the electrochemical energy storage. The implementation of ALD leverages the potential of these coatings by the possibility to target amorphous, nanocrystalline or polycrystalline oxides; uniformly coating powders or CNTs and by the possibility to engineer core/shell architectures. The reported investigations display improved performance and stability. The interest towards $VO_2$ that features a semiconductor to metal transition was reviewed for microelectronics and thermochromic windows. This near room-temperature transition, 68 °C, finds pertinent application for switching and light modulation. For microelectronic applications, an understanding of the electronic control of the transition with its thermal shifting above 85 °C is suitable. In contrast, decreasing it around 30 °C is essential for glazing applications. The ALD-based development for thermochromic $VO_2$ windows is emphasized by the introduction of bioinspired surface structuration.

## Acknowledgements

This article is based on work from COST Action MP1402 'Hooking together European research in atomic layer deposition (HERALD)', supported by COST (European Cooperation in Science and Technology). Vasu Prasad Prasadam and Naoufal Bahlawane would like to acknowledge funding through the MASSENA Pride program of the Luxembourg National Research Fund (FNR). Ioannis Papakonstantinou acknowledges support from the European Research Council for Starting Grant Intelglazing, project ID: 679891, and from Horizon H2020 for project EENSULATE, grant No. 723868. Felix Mattelaer, Geert Rambelberg and Christophe Detavernier would like to thank BOF-UGent for GOA funding and FWO-Vlaanderen for project funding. Y.Z. Jiang would like to thank the National Natural Science Foundation of China (Grant no. 51722105), Zhejiang Provincial Natural Science Foundation of China (LR18B030001) and the Fundamental Research Funds for the Central Universities (2018XZZX002-08) for their support. Koen Martens would like to thank FWO-Vlaanderen for project funding. IPP thanks EPSRC for award of Grant EP/L017709/1.

## References

[1] M. Liu, B. Su, Y. Tang, X. Jiang, A. Yu, Recent advances in nanostructured vanadium oxides and composites for energy conversion, Adv. Energy Mater. (2017), https://doi.org/10.1002/aenm.201700885.
[2] J.B. Goodenough, Anomalous properties of the vanadium oxides, Annu. Rev. Mater. Sci. 1 (1971) 101–138, https://doi.org/10.1146/annurev.ms.01.080171.000533.
[3] S. Surnev, M.G. Ramsey, F.P. Netzer, Vanadium oxide surface studies, Prog. Surf. Sci. 73 (2003) 117–165, https://doi.org/10.1016/j.progsurf.2003.09.001.
[4] K. Kosuge, The phase diagram and phase transition of the $V_2O_3$–$V_2O_5$, system, J. Phys. Chem. Solids 28 (1967) 1613–1621. https://doi.org/10.1016/0022-3697(67)90293-4.
[5] Z. Yang, C.Y. Ko, S. Ramanathan, Oxide electronics utilizing ultrafast metal-insulator transitions, Annu. Rev. Mater. Res. 41 (2011) 337–367, https://doi.org/10.1146/annurev-matsci-062910-100347.
[6] M. Brahlek, L. Zhang, J. Lapano, H.T. Zhang, R. Engel-Herbert, N. Shukla, S. Datta, H. Paik, D.G. Schlom, Opportunities in vanadium-based strongly correlated electron systems, Mrs Commun. 7 (2017) 27–52, https://doi.org/10.1557/mrc.2017.2.
[7] C.Z. Wu, F. Feng, Y. Xie, Design of vanadium oxide structures with controllable electrical properties for energy applications, Chem. Soc. Rev. 42 (2013) 5157–5183, https://doi.org/10.1039/c3cs35508j.
[8] T.C. Chang, X. Cao, S.H. Bao, S.D. Ji, H.J. Luo, P. Jin, Review on thermochromic vanadium dioxide based smart coatings: from lab to commercial application, Adv. Manuf. 6 (2018) 1–19, https://doi.org/10.1007/s40436-017-0209-2.
[9] T.A. Kainulainen, M.K. Niemela, A.O.I. Krause, Ethene hydroformylation on $Co/SiO_2$ catalysts, Catal. Lett. 53 (1998) 97–101.
[10] M. Kamalisarvestani, R. Saidur, S. Mekhilef, F.S. Javadi, Performance, materials and coating technologies of thermochromic thin films on smart windows, Renew. Sustain. Energy Rev. 26 (2013) 353–364, https://doi.org/10.1016/j.rser.2013.05.038.
[11] B.M. Weckhuysen, D.E. Keller, Chemistry, spectroscopy and the role of supported vanadium oxides in heterogeneous catalysis, Catal. Today 78 (2003) 25–46, https://doi.org/10.1016/s0920-5861(02)00323-1.
[12] L. Zhang, Y.J. Zhou, L. Guo, W.W. Zhao, A. Barnes, H.T. Zhang, C. Eaton, Y.X. Zheng, M. Brahlek, H.F. Haneef, N.J. Podraza, M.H.W. Chan, V. Gopalan,

K.M. Rabe, R. Engel-Herbert, Correlated metals as transparent conductors, Nat. Mater. 15 (2016) 204, https://doi.org/10.1038/nmat4493.
[13] H.T. Zhang, M. Brahlek, X.Y. Ji, S.M. Lei, J. Lapano, J.W. Freeland, V. Gopalan, R. Engel-Herbert, High-quality LaVO3 films as solar energy conversion material, ACS Appl. Mater. Interfaces 9 (2017) 12556–12562, https://doi.org/10.1021/acsami.6b16007.
[14] N. Bahlawane, D. Lenoble, Vanadium oxide compounds: structure, properties, and growth from the gas phase, Chem. Vap. Depos. 20 (2014) 299–311, https://doi.org/10.1002/cvde.201400057.
[15] S. Beke, A review of the growth of $V_2O_5$ films from 1885 to 2010, Thin Solid Films 519 (2011) 1761–1771, https://doi.org/10.1016/j.tsf.2010.11.001.
[16] S.F. Wang, M.S. Liu, L.B. Kong, Y. Long, X.C. Jiang, A.B. Yu, Recent progress in VO2 smart coatings: strategies to improve the thermochromic properties, Prog. Mater. Sci. 81 (2016) 1–54, https://doi.org/10.1016/j.pmatsci.2016.03.001.
[17] R.L. Puurunen, A short history of atomic layer deposition: Tuomo Suntolaś atomic layer epitaxy, Chem. Vap. Depos. 20 (2014) 332–344, https://doi.org/10.1002/cvde.201402012.
[18] E. Ahvenniemi, A.R. Akbashev, S. Ali, M. Bechelany, M. Berdova, S. Boyadjiev, D.C. Cameron, R. Chen, M. Chubarov, V. Cremers, A. Devi, V. Drozd, L. Elnikova, G. Gottardi, K. Grigoras, D.M. Hausmann, C.S. Hwang, S.H. Jen, T. Kallio, J. Kanervo, I. Khmelnitskiy, D.H. Kim, L. Klibanov, Y. Koshtyal, A.O.I. Krause, J. Kuhs, I. Karkkanen, M.L. Kaariainen, T. Kaariainen, L. Lamagna, A.A. Lapicki, M. Leskela, H. Lipsanen, J. Lyytinen, A. Malkov, A. Malygin, A. Mennad, C. Militzer, J. Molarius, M. Norek, C. Ozgit-Akgun, M. Panov, H. Pedersen, F. Piallat, G. Popov, R.L. Puurunen, G. Rampelberg, R.H.A. Ras, E. Rauwel, F. Roozeboom, T. Sajavaara, H. Salami, H. Savin, N. Schneider, T.E. Seidel, J. Sundqvist, D.B. Suyatin, T. Torndahl, J.R. van Ommen, C. Wiemer, O.M.E. Ylivaara, O. Yurkevich, Recommended reading list of early publications on atomic layer deposition-Outcome of the “Virtual Project on the History of ALD”, J. Vac. Sci. Technol. A 35 (2017) https://doi.org/10.1116/1.4971389.
[19] S.M. George, Atomic layer deposition: an overview, Chem. Rev. 110 (2010) 111–131, https://doi.org/10.1021/cr900056b.
[20] R.L. Puurunen, Surface chemistry of atomic layer deposition: a case study for the trimethylaluminum/water process, J. Appl. Phys. 97 (2005), 121301, https://doi.org/10.1063/1.1940727.
[21] M. Ritala, V. Miikkulainen, R.L. Puurunen, M. Leskela, Crystallinity of inorganic films grown by atomic layer deposition: overview and general trends, J. Appl. Phys. 113 (2013), 021301, https://doi.org/10.1063/1.4757907.
[22] C. Detavernier, J. Dendooven, S.P. Sree, K.F. Ludwig, J.A. Martens, Tailoring nanoporous materials by atomic layer deposition, Chem. Soc. Rev. 40 (2011) 5242–5253, https://doi.org/10.1039/c1cs15091j.
[23] U.K. Urs, K.C. Anitha, K.L. Raghunathan, S.A. Shivashankar, W.T. Robinson, T.N.G. Row, Low-temperature oxobis(2,2,6,6-tetramethyl-3,5-heptanedionato) vanadium(IV), Acta Crystallogr. Section E-Struct. Rep. Online 57 (2001) m242–m243, https://doi.org/10.1107/s1600536801007760.
[24] M.A.K. Ahmed, H. Fjellvag, A. Kjekshus, B. Klewe, New oxovanadium(IV) complexes with mixed ligands synthesis, thermal stability, and crystal structure of (VO)(2)(acac)(2)(mu-OEt)(2) and (VO)(2)(thd)(2)(mu-OEt)(2), Zeitschrift Fur Anorganische Und Allgemeine Chemie 630 (2004) 2311–2318, https://doi.org/10.1002/zaac.200400369.
[25] I.P. Malkerova, A.M. Makarevich, A.S. Alikhanyan, N.P. Kuz'mina, Volatility and thermal stability of vanadyl β-diketonate complexes, Russ. J. Inorg. Chem. 62 (2017) 818–821, https://doi.org/10.1134/S0036023617060134.
[26] T. Moeller, Vanadium(IV) Oxy(acetylacetonate), 1957, https://doi.org/10.1002/9780470132364.ch30.
[27] J. Keranen, A. Auroux, S. Ek-Harkonen, L. Niinisto, Calorimetric measurements of the acidity of supported vanadium oxides prepared by ALE and impregnation, Thermochim. Acta 379 (2001) 233–239, https://doi.org/10.1016/s0040-6031(01)00621-9.
[28] P. Dagur, A.U. Mane, S.A. Shivashankar, Thin films of $VO_2$ on glass by atomic layer deposition: microstructure and electrical properties, J. Cryst. Growth 275 (2005) E1223–E1228, https://doi.org/10.1016/j.jcrysgro.2004.11.144.
[29] J. Keranen, A. Auroux, S. Ek, L. Niinisto, Preparation, characterization and activity testing of vanadia catalysts deposited onto silica and alumina supports by atomic layer deposition, Appl. Catal. Gen. 228 (2002) 213–225, https://doi.org/10.1016/s0926-860x(01)00975-9.
[30] E. Ostreng, K.B. Gandrud, Y. Hu, O. Nilsen, H. Fjellvag, High power nanostructured $V_2O_5$ thin film cathodes by atomic layer deposition, J. Mater. Chem. 2 (2014) 15044–15051, https://doi.org/10.1039/c4ta00694a.
[31] E. Ostreng, O. Nilsen, H. Fjellvag, Optical properties of vanadium pentoxide deposited by ALD, J. Phys. Chem. C 116 (2012) 19444–19450, https://doi.org/10.1021/jp304521k.
[32] H. Kanai, T. Yoshikawa, T. Sone, Y. Nishimura, Preparation and characterization of highly dispersed $V_2O_5/SiO_2$ prepared by a CVD method, React. Kinet. Catal. Lett. 75 (2002) 213–224, https://doi.org/10.1023/A:1015282409268.
[33] J.C. Badot, S. Ribes, E.B. Yousfi, V. Vivier, J.P. Pereira-Ramos, N. Baffier, D. Lincot, Atomic layer epitaxy of vanadium oxide thin films and electrochemical behavior in presence of lithium ions, Electrochem. Solid State Lett. 3 (2000) 485–488.
[34] Safety data sheet vanadium triisopropoxide oxide, Mater. Saf. Data Sheet 4 (2015) 7.
[35] W. Priebsch, D. Rehder, Oxovanadium alkoxides - structure, reactivity, and v-51 NMR characteristics - crystal and molecular-structures of $VO(OCH_2CH_2Cl)_3$ and $VOCl_2(THF)_2H_2O$, Inorg. Chem. 29 (1990) 3013–3019, https://doi.org/10.1021/ic00341a032.
[36] H. Langbein, A. Polte, On the hydrolysis of trisalkoxyvanadyl compounds, Zeitschrift fur Naturforschung - Section B J. Chem. Sci. 46 (1991) 1509–1514, https://doi.org/10.1515/znb-1991-1109.
[37] J. Musschoot, D. Deduytsche, H. Poelman, J. Haemers, R.L.V. Meirhaeghe, S.V. den Berghe, C. Detavernier, Comparison of thermal and plasma-enhanced ALD/CVD of vanadium pentoxide, J. Electrochem. Soc. 156 (2009) P122–P126, https://doi.org/10.1149/1.3133169.
[38] X. Chen, E. Pomerantseva, P. Banerjee, K. Gregorczyk, R. Ghodssi, G. Rubloff, Ozone-based atomic layer deposition of crystalline $V_2O_5$ films for high performance electrochemical energy storage, Chem. Mater. 24 (2012) 1255–P1261, https://doi.org/10.1021/cm202901z.
[39] A. Mantoux, J.C. Badot, N. Baffier, J. Farcy, J.P. Pereira-Ramos, D. Lincot, H. Groult, Structural and Electrochemical Properties of V2O5 Thin Films Obtained by Atomic Layer Chemical Vapor Deposition (ALCVD), 2002, https://doi.org/10.1007/978-94-010-0389-6_42.
[40] R. Baddour-Hadjean, V. Golabkan, J.P. Pereira-Ramos, A. Mantoux, D. Lincot, A Raman study of the lithium insertion process in vanadium pentoxide thin films deposited by atomic layer deposition, J. Raman Spectrosc. 33 (2002) 631–638, https://doi.org/10.1002/jrs.893.
[41] H. Groult, E. Balnois, A. Mantoux, K.L. Van, D. Lincot, Two-dimensional recrystallisation processes of nanometric vanadium oxide thin films grown by atomic layer chemical vapor deposition (ALCVD) evidenced by AFM, Appl. Surf. Sci. 252 (2006) 5917–5925, https://doi.org/10.1016/j.apsusc.2005.08.014.
[42] J.C. Badot, A. Mantoux, N. Baffier, O. Dubrunfaut, D. Lincot, Submicro- and nanostructural eff ects on electrical properties of $Li0.2V_2O_5$ thin films obtained by atomic layer deposition (ALD), J. Phys. Chem. Solids 67 (2006) 1270–1274, https://doi.org/10.1016/j.jpcs.2006.01.098.
[43] K.L. Van, H. Groult, A. Mantoux, L. Perrigaud, F. Lantelme, R. Lindstrom, R. Badour-Hadjean, S. Zanna, D. Lincot, Amorphous vanadium oxide films synthesised by ALCVD for lithium rechargeable batteries, J. Power Sources 160 (2006) 592–601, https://doi.org/10.1016/j.jpowsour.2006.01.049.
[44] J.C. Badot, A. Mantoux, N. Baffier, O. Dubrunfaut, D. Lincot, Electrical properties of $V_2O_5$ thin films obtained by atomic layer deposition (ALD), J. Mater. Chem. 14 (2004) 3411–3415, https://doi.org/10.1039/b410324f.
[45] G.Y. Song, C. Oh, S. Sinha, J. Son, J. Heo, Facile phase control of multivalent vanadium oxide thin films (V2O5 and VO2) by atomic layer deposition and postdeposition annealing, ACS Appl. Mater. Interfaces 9 (2017) 23909–23917, https://doi.org/10.1021/acsami.7b03398.
[46] A.M. Johnson, B.R. Quezada, L.D. Marks, P.C. Stair, Influence of the metal oxide substrate structure on vanadium oxide monomer formation, Top. Catal. 57 (2014) 177–187, https://doi.org/10.1007/s11244-013-0174-3.
[47] I.E. Rauda, V. Augustyn, L.C. Saldarriaga-Lopez, X. Chen, L.T. Schelhas, G.W. Rubloff, B. Dunn, S.H. Tolbert, Nanostructured pseudocapacitors based on atomic layer deposition of $V_2O_5$ onto conductive nanocrystal-based mesoporous ITO scaffolds, Adv. Funct. Mater. 24 (2014) 6717–6728, https://doi.org/10.1002/adfm.201401284.
[48] S. Fleischmann, A. Tolosa, M. Zeiger, B. Kruner, N.J. Peter, I. Grobelsek, A. Quade, A. Kruth, V. Presser, Vanadia-titania multilayer nanodecoration of carbon onions via atomic layer deposition for high performance electrochemical energy storage, J. Mater. Chem. A 5 (2017) 2792–2801, https://doi.org/10.1039/c6ta09890h.
[49] P. Banerjee, X.Y. Chen, K. Gregorczyk, L. Henn-Lecordier, G.W. Rubloff, Mixed mode, ionic-electronic diode using atomic layer deposition of V2O5 and ZnO films, J. Mater. Chem. 21 (2011) 15391–15397, https://doi.org/10.1039/c1jm12595h.
[50] X. Chen, E. Pomerantseva, K. Gregorczyk, R. Ghodssi, G. Rubloff, Cathodic ALD V2O5 thin films for high-rate electrochemical energy storage, RSC Adv. 3 (2013) 4294–4302, https://doi.org/10.1039/c3ra23031g.
[51] J.S. Daubert, N.P. Lewis, H.N. Gotsch, J.Z. Mundy, D.N. Monroe, E.C. Dickey, M.D. Losego, G.N. Parsons, Effect of meso- and micro-porosity in carbon electrodes on atomic layer deposition of pseudocapacitive $V_2O_5$ for high performance supercapacitors, Chem. Mater. 27 (2015) 6524–6534, https://doi.org/10.1021/acs.chemmater.5b01602. internal-pdf://2459727014/daubert2015.pdf.
[52] J.S. Daubert, R.C. Wang, J.S. Ovental, H.F. Barton, R. Rajagopalan, V. Augustyn, G.N. Parsons, Intrinsic limitations of atomic layer deposition for pseudocapacitive metal oxides in porous electrochemical capacitor electrodes, J. Mater. Chem. A 5 (2017) 13086–13097, https://doi.org/10.1039/c7ta02719b. internal-pdf://3362911818/daubert2017.pdf.
[53] S. Fleischmann, N. Jaeckel, M. Zeiger, B. Kruener, I. Grobelsek, P. Formanek, S. Choudhury, D. Weingarth, V. Presser, Enhanced electrochemical energy storage by nanoscopic decoration of endohedral and exohedral carbon with vanadium oxide via atomic layer deposition, Chem. Mater. 28 (2016) 2802–2813, https://doi.org/10.1021/acs.chemmater.6b00738.
[54] T. Singh, S. Wang, N. Aslam, H. Zhang, S. Hoffmann-Eifert, S. Mathur, Atomic layer deposition of transparent VOx thin films for resistive switching applications, Chem. Vap. Depos. 20 (2014) 291–297, https://doi.org/10.1002/cvde.201407122.
[55] X. Sun, C. Zhou, M. Xie, T. Hu, H. Sun, G. Xin, G. Wang, S.M. George, J. Lian, Amorphous vanadium oxide coating on graphene by atomic layer deposition

for stable high energy lithium ion anodes, Chem. Commun. 50 (2014) 10703–10706, https://doi.org/10.1039/c4cc04580g.
[56] M. Xie, X. Sun, H. Sun, T. Porcelli, S.M. George, Y. Zhou, J. Lian, Stabilizing an amorphous $V_2O_5$/carbon nanotube paper electrode with conformal $TiO_2$ coating by atomic layer deposition for lithium ion batteries, J. Mater. Chem. 4 (2016) 537–544, https://doi.org/10.1039/c5ta01949d.
[57] S. Fleischmann, D. Leistenschneider, V. Lemkova, B. Kruener, M. Zeiger, L. Borchardt, V. Presser, Tailored mesoporous carbon/vanadium pentoxide hybrid electrodes for high power pseudocapacitive lithium and sodium intercalation, Chem. Mater. 29 (2017) 8653–8662, https://doi.org/10.1021/acs.chemmater.7b02533.
[58] B.-C. Kan, J.-H. Boo, I. Lee, F. Zaera, Thermal chemistry of tetrakis(ethylmethylamido)titanium on Si(100) surfaces, J. Phys. Chem. A 113 (2009) 3946–3954, https://doi.org/10.1021/jp8102172.
[59] I.J. Raaijmakers, Low-temperature metal-organic chemical-vapor-deposition of advanced barrier layers for the microelectronics industry, Thin Solid Films 247 (1994) 85–93, https://doi.org/10.1016/0040-6090(94)90479-0.
[60] H. Park, B. Kim, S.H. Lee, H. Kim, Study of a vanadium precursor for VO2 thin-film growth in the atomic layer deposition process by multiscale simulations, J. Phys. Chem. C 120 (2016) 28193–28203, https://doi.org/10.1021/acs.jpcc.6b06347.
[61] D.C. Bradley, M.H. Chisholm, Transition-metal dialkylamides and disilylamides, Accounts Chem. Res. 9 (1976) 273–280, https://doi.org/10.1021/ar50103a005.
[62] D.C. Bradley, R.H. Moss, K.D. Sales, Electron spin resonance studies on quadrivalent vanadium compounds, J. Chem. Soc. D Chem. Commun. (1969) 1255–1256. 10.1039/C29690001255.
[63] T. Blanquart, J. Niinisto, M. Gavagnin, V. Longo, M. Heikkila, E. Puukilainen, V.R. Pallem, C. Dussarrat, M. Ritala, M. Leskela, Atomic layer deposition and characterization of vanadium oxide thin films, RSC Adv. 3 (2013) 1179–1185. 10.1039/c2ra22820c.
[64] P. Bonnefond, R. Feurer, A. Reynes, F. Maury, B. Chansou, R. Choukroun, P. Cassoux, Thermal decomposition of V(NEt(2))(4) in an MOCVD reactor: a low-temperature route to vanadium carbonitride coatings, J. Mater. Chem. 6 (1996) 1501–1506. 10.1039/jm9960601501.
[65] F. Mattelaer, K. Geryl, G. Rampelberg, T. Dobbelaere, J. Dendooven, C. Detavernier, Atomic layer deposition of vanadium oxides for thin-film lithium-ion battery applications, RSC Adv. 6 (2016) 114658–114665. 10.1039/c6ra25742a.
[66] G. Rampelberg, D. Deduytsche, B.D. Schutter, P.A. Premkumar, M. Toeller, M. Schaekers, K. Martens, I. Radu, C. Detavernier, Crystallization and semiconductor-metal switching behavior of thin $VO_2$ layers grown by atomic layer deposition, Thin Solid Films 550 (2014) 59–64. 10.1016/j.tsf.2013.10.039.
[67] G. Rampelberg, M. Schaekers, K. Martens, Q. Xie, D. Deduytsche, B.D. Schutter, N. Blasco, J. Kittl, C. Detavernier, Semiconductor-metal transition in thin $VO_2$ films grown by ozone based atomic layer deposition, Appl. Phys. Lett. 98 (2011), https://doi.org/10.1063/1.3579195 internal-pdf: 0744364709/2011-APL-Rampelberg-Semiconductor-metaltransit.pdf.
[68] P.A. Premkumar, M. Toeller, I.P. Radu, C. Adelmann, M. Schaekers, J. Meersschaut, T. Conard, S.V. Elshocht, Process study and characterization of VO2 thin films synthesized by ALD using TEMAV and O-3 precursors, ECS J. Solid State Sci. Technol. 1 (2012) P169–P174, https://doi.org/10.1149/2.009204jss.
[69] A.P. Peter, K. Martens, G. Rampelberg, M. Toeller, J.M. Ablett, J. Meersschaut, D. Cuypers, A. Franquet, C. Detavernier, J.-P. Rueff, M. Schaekers, S.V. Elshocht, M. Jurczak, C. Adelmann, I.P. Radu, Metal-insulator transition in ALD $VO_2$ ultrathin films and nanoparticles: morphological control, Adv. Funct. Mater. 25 (2015) 679–686. 10.1002/adfm.201402687.
[70] F. Cerbu, H.S. Chou, I.P. Radu, K. Martens, A.P. Peter, V.V. Afanasév, A. Stesmans, Band alignment and effective work function of atomic-layer deposited $VO_2$ and $V_2O_5$ films on $SiO_2$ and $Al_2O_3$, Phys. Status Solidi C: Current Topics in Solid State Physics 12 (1–2 12) (2015) 238–241. 10.1002/pssc.201400037.
[71] M.J. Tadjer, V.D. Wheeler, B.P. Downey, Z.R. Robinson, D.J. Meyer, C.R. Eddy Jr., F.J. Kub, Temperature and electric field induced metal-insulator transition in atomic layer deposited $VO_2$ thin films, Solid State Electron. 136 (2017) 30–35. 10.1016/j.sse.2017.06.018.
[72] B.P. Downey, V.D. Wheeler, D.J. Meyer, Localized phase change of VO2 films grown by atomic-layer deposition on InAlN/AlN/GaN heterostructures, APEX 10 (2017). 10.7567/apex.10.061101.
[73] M. Currie, M.A. Mastro, V.D. Wheeler, Characterizing the tunable refractive index of vanadium dioxide, Opt. Mater. Express 7 (2017) 1697–1707. 10.1364/ome.7.001697.
[74] A.C. Kozen, H. Joress, M. Currie, V.R. Anderson, C.R. Eddy Jr., V.D. Wheeler, Structural characterization of atomic layer deposited vanadium dioxide, J. Phys. Chem. C 121 (2017) 19341–19347. 10.1021/acs.jpcc.7b04682.
[75] M. Tangirala, K. Zhang, D. Nminibapiel, V. Pallem, C. Dussarrat, W. Cao, T.N. Adam, C.S. Johnson, H.E. Elsayed-Ali, H. Baumgart, Physical analysis of $VO_2$ films grown by atomic layer deposition and RF magnetron sputtering, ECS J. Solid State Sci. Technol. 3 (2014) N89–N94. 10.1149/2.006406jss.
[76] K. Zhang, M. Tangirala, D. Nminibapiel, W. Cao, V. Pallem, C. Dussarrat, H. Baumgart, Synthesis of VO2 thin films by atomic layer deposition with TEMAV as precursor, Atom. Layer Depos. Appl. 8 (50) (2012) 175–182. 10.1149/05013.0175ecst.
[77] H.H. Park, T.J. Larrabee, L.B. Ruppalt, J.C. Culbertson, S.M. Prokes, Tunable electrical properties of vanadium oxide by hydrogen-plasma-treated atomic layer deposition, ACS Omega 2 (2017) 1259–1264. 10.1021/acsomega.7b00059.
[78] X. Wang, Z. Guo, Y. Gao, J. Wang, Atomic layer deposition of vanadium oxide thin films from tetrakis(dimethylamino)vanadium precursor, J. Mater. Res. 32 (2017) 37–44. 10.1557/jmr.2016.303.
[79] Y. Gao, Y. Shao, L. Yan, H. Li, Y. Su, H. Meng, X. Wang, Efficient charge injection in organic field-effect transistors enabled by low-temperature atomic layer deposition of ultrathin VOx interlayer, Adv. Funct. Mater. 26 (2016) 4456–4463. 10.1002/adfm.201600482.
[80] X. Lv, Y. Cao, L. Yan, Y. Li, L. Song, Atomic layer deposition of VO2 films with Tetrakis-dimethyl-amino vanadium (IV) as vanadium precursor, Appl. Surf. Sci. 396 (2017) 214–220. 10.1016/j.apsusc.2016.10.044.
[81] B.S. Lim, A. Rahtu, J.S. Park, R.G. Gordon, Synthesis and characterization of volatile, thermally stable, reactive transition metal amidinates, Inorg. Chem. 42 (2003) 7951–7958. 10.1021/ic0345424.
[82] R.G. Gordon, Introduction to ALD precursors and reaction mechanisms, Proc. AVS Atom. Layer Depos. Conf. (2011).
[83] M.S. Weimer, I.S. Kim, G. Peijun, R.D. Schaller, A.B.F. Martinson, A.S. Hock, Oxidation state discrimination in the atomic layer deposition of vanadium oxides, Chem. Mater. 29 (2017) 6238–6244. 10.1021/acs.chemmater.7b01130.
[84] R.F. McCarthy, M.S. Weimer, R.T. Haasch, R.D. Schaller, A.S. Hock, A.B.F. Martinson, VxIn(2-x)S3 intermediate band Absorbers deposited by atomic layer deposition, Chem. Mater. 28 (2016) 2033–2040. 10.1021/acs.chemmater.5b04402.
[85] S. Passerini, J.J. Ressler, D.B. Le, B.B. Owens, W.H. Smyrl, High rate electrodes of V2O5 aerogel, Electrochim. Acta 44 (1999) 2209–2217. 10.1016/s0013-4686(98)00346-6.
[86] D.B. Le, S. Passerini, J. Guo, J. Ressler, B.B. Owens, W.H. Smyrl, High surface area V2O5 aerogel intercalation electrodes, J. Electrochem. Soc. 143 (1996) 2099–2104. 10.1149/1.1836965.
[87] F. Mattelaer, K. Geryl, G. Rampelberg, J. Dendooven, C. Detavernier, Amorphous and crystalline vanadium oxides as high-energy and high-power cathodes for three-dimensional thin-film lithium ion batteries, ACS Appl. Mater. Interfaces 9 (2017) 13121–13131. 10.1021/acsami.6b16473.
[88] F.J. Morin, Oxides which show a metal-to-insulator transition at the neel temperature, Phys. Rev. Lett. 3 (1959) 34–36. 10.1103/PhysRevLett.3.34.
[89] J. Musschoot, D. Deduytsche, R.L.V. Meirhaeghe, C. Detavernier, ALD of vanadium oxide, Atom. Layer Depos. Appl. 5 (25) (2009) 29–37. 10.1149/1.3205040.
[90] R. Geert, B.D. Schutter, W. Devulder, M. Schaekers, K. Martens, C. Dussarrat, C. Detavernier, Semiconductor-metal Transition in ALD Deposited Vanadium Oxide Thin Films and Nanoparticles, 2016.
[91] H.A. Wriedt, The O-V (Oxygen-Vanadium) system, Bull. Alloy Phase Diagrams 10 (1989) 271–277.
[92] Y.-B. Kang, Critical evaluation and thermodynamic optimization of the VO-VO2.5 system, J. Eur. Ceram. Soc. 32 (2012) 3187–3198. 10.1016/j.jeurceramsoc.2012.04.045.
[93] G. Rampelberg, B.D. Schutter, W. Devulder, K. Martens, I. Radu, C. Detavernier, In situ X-ray diffraction study of the controlled oxidation and reduction in the V-O system for the synthesis of $VO_2$ and $V_2O_3$ thin films, J. Mater. Chem. C 3 (2015) 11357–11365. 10.1039/c5tc02553b.
[94] X. Chen, H. Zhu, Y.-C. Chen, Y. Shang, A. Cao, L. Hu, G.W. Rubloff, MWCNT/$V_2O_5$ core/shell sponge for high areal capacity and power density Li-ion cathodes, ACS Nano 6 (2012) 7948–7955, https://doi.org/10.1021/nn302417x, internal-pdf, 1021881756/chen2012.pdf.
[95] A. Pan, H.B. Wu, L. Yu, X.W. Lou, Template-free synthesis of $VO_2$ hollow microspheres with various interiors and their conversion into $V_2O_5$ for lithium-ion batteries, Angew. Chem. Int. Ed. 52 (2013) 2226–2230. 10.1002/anie.201209535.
[96] R.J. Cava, A. Santoro, D.W. Murphy, S.M. Zahurak, R.M. Fleming, P. Marsh, R.S. Roth, The structure of the lithium-inserted metal-oxide delta-Li$V_2O_5$, J. Solid State Chem. 65 (1986) 63–71. 10.1016/0022-4596(86)90089-7.
[97] X.-F. Zhang, K.-X. Wang, X. Wei, J.-S. Chen, Carbon-coated $V_2O_5$ nanocrystals as high performance cathode material for lithium ion batteries, Chem. Mater. 23 (2011) 5290–5292. 10.1021/cm202812z.
[98] Z. Chen, V. Augustyn, J. Wen, Y. Zhang, M. Shen, B. Dunn, Y. Lu, High-performance supercapacitors based on intertwined CNT/$V_2O_5$ nanowire nanocomposites, Adv. Mater. 23 (2011) 791. 10.1002/adma.201003658.
[99] B. Yan, X. Li, Z. Bai, Y. Zhao, L. Dong, X. Song, D. Li, C. Langford, X. Sun, Crumpled reduced graphene oxide conformally encapsulated hollow $V_2O_5$ nano/microsphere achieving brilliant lithium storage performance, Nano Energy 24 (2016) 32–44. 10.1016/j.nanoen.2016.04.002.
[100] S. Guan, Y. Wei, J. Zhou, J. Zheng, C. Xu, A method for preparing manganese-doped $V_2O_5$ films with enhanced cycling stability, J. Electrochem. Soc. 163 (2016) H541–H545. 10.1149/2.0761607jes.
[101] C. Liu, N. Kim, G.W. Rubloff, S.B. Lee, High performance asymmetric $V_2O_5$-$SnO_2$ nanopore battery by atomic layer deposition, Nanoscale 9 (2017) 11566–11573. 10.1039/c7nr02151h.
[102] R. Carter, L. Oakes, N. Muralidharan, A.P. Cohn, A. Douglas, C.L. Pint, Polysulfide anchoring mechanism revealed by atomic layer deposition of $V_2O_5$ and sulfur-filled carbon nanotubes for lithium-sulfur batteries, ACS Appl. Mater. Interfaces 9 (2017) 7185–7192. 10.1021/acsami.6b16155.

[103] J.M. Tarascon, M. Armand, Issues and challenges facing rechargeable lithium batteries, Nature 414 (2001) 359–367. 10.1038/35104644.
[104] M. Armand, J.M. Tarascon, Building better batteries, Nature 451 (2008) 652–657. 10.1038/451652a.
[105] Y.-M. Chiang, Building a better battery, Science 330 (2010) 1485–1486. 10.1126/science.1198591.
[106] J.B. Goodenough, Y. Kim, Challenges for rechargeable Li batteries, Chem. Mater. 22 (2010) 587–603. 10.1021/cm901452z.
[107] P.G. Bruce, S.A. Freunberger, L.J. Hardwick, J.-M. Tarascon, Li-O-2 and Li-S batteries with high energy storage, Nat. Mater. 11 (2012) 19–29. 10.1038/nmat3191.
[108] B.J. Landi, M.J. Ganter, C.D. Cress, R.A. DiLeo, R.P. Raffaelle, Carbon nanotubes for lithium ion batteries, Energy Environ. Sci. 2 (2009) 638–654. 10.1039/b904116h.
[109] A. Pearse, T. Schmitt, E. Sahadeo, D.M. Stewart, A. Kozen, K. Gerasopoulos, A.A. Talin, S.B. Lee, G.W. Rubloff, K.E. Gregorczyk, Three-dimensional solid-state lithium-ion batteries fabricated by conformal vapor-phase chemistry, ACS Nano 12 (2018) 4286–4294. 10.1021/acsnano.7b08751.
[110] H. Xia, Z. Luo, J. Xie, Nanostructured LiMn2O4 and their composites as high-performance cathodes for lithium-ion batteries, Prog. Nat. Sci.-Mater. Int. 22 (2012) 572–584. 10.1016/j.pnsc.2012.11.014.
[111] L.-H. Hu, F.-Y. Wu, C.-T. Lin, A.N. Khlobystov, L.-J. Li, Graphene-modified LiFePO4 cathode for lithium ion battery beyond theoretical capacity, Nat. Commun. 4 (2013). 10.1038/ncomms2705.
[112] X. Dai, A. Zhou, J. Xu, Y. Lu, L. Wang, C. Fan, J. Li, Extending the high-voltage capacity of $LiCoO_2$ cathode by direct coating of the composite electrode with $Li_2CO_3$ via magnetron sputtering, J. Phys. Chem. C 120 (2016) 422–430. 10.1021/acs.jpcc.5b10677.
[113] S. Zhou, X.G. Yang, Y.J. Lin, J. Xie, D.W. Wang, A nanonet-enabled Li ion battery cathode material with high power rate, high capacity, and long cycle lifetime, ACS Nano 6 (2012) 919–924. 10.1021/nn204479n.
[114] K. West, B. Zachauchristiansen, M.J.L. Ostergard, T. Jacobsen, Vanadium-oxides as electrode materials for rechargeable lithium cells, J. Power Sources 20 (1987) 165–172. 10.1016/0378-7753(87)80107-6.
[115] C. Delmas, H. Cognacauradou, J.M. Cocciantelli, M. Menetrier, J.P. Doumerc, The lix$V_2O_5$ system - an overview of the structure modifications induced by the lithium intercalation, Solid State Ionics 69 (1994) 257–264. 10.1016/0167-2738(94)90414-6.
[116] C. Leger, S. Bach, P. Soudan, J.P. Pereira-Ramos, Structural and electrochemical properties of omega-Li(x)V(2)O(5) (0.4 <= x <= 3) as rechargeable cathodic material for lithium batteries, J. Electrochem. Soc. 152 (2005) A236–A241. 10.1149/1.1836155.
[117] J.-Y. Luo, W.-J. Cui, P. He, Y.-Y. Xia, Raising the cycling stability of aqueous lithium-ion batteries by eliminating oxygen in the electrolyte, Nat. Chem. 2 (2010) 760–765. 10.1038/nchem.763.
[118] N.A. Chernova, M. Roppolo, A.C. Dillon, M.S. Whittingham, Layered vanadium and molybdenum oxides: batteries and electrochromics, J. Mater. Chem. 19 (2009) 2526–2552. 10.1039/b819629j.
[119] M. Kurttepeli, S. Deng, F. Mattelaer, D.J. Cott, P. Vereecken, J. Dendooven, C. Detavernier, S. Bals, Heterogeneous TiO2/$V_2O_5$/carbon nanotube electrodes for lithium ion batteries, ACS Appl. Mater. Interfaces 9 (2017) 8055–8064. 10.1021/acsami.6b12759.
[120] A. Gonzalez, E. Goikolea, J.A. Barrena, R. Mysyk, Review on supercapacitors: technologies and materials, Renew. Sustain. Energy Rev. 58 (2016) 1189–1206. 10.1016/j.rser.2015.12.249.
[121] S. Boukhalfa, K. Evanoff, G. Yushin, Atomic layer deposition of vanadium oxide on carbon nanotubes for high-power supercapacitor electrodes, Energy Environ. Sci. (5) (2012) 6872–6879.
[122] M. Ritala, Atomic layer deposition of oxide thin films with metal alkoxides as oxygen sources, Science 288 (5464) (2000) 319–321, https://doi.org/10.1126/science.288.5464.319.
[123] R. Chau, B. Doyle, S. Datta, J. Kavalieros, K. Zhang, Integrated nanoelectronics for the future, Nat. Mater. 6 (11) (2007) 810–812, https://doi.org/10.1038/nmat2014.
[124] D.-H. Kwon, K.M. Kim, J.H. Jang, J.M. Jeon, M.H. Lee, G.H. Kim, X.-S. Li, G.-S. Park, B. Lee, S. Han, M. Kim, C.S. Hwang, Atomic structure of conducting nanofilaments in $TiO_2$ resistive switching memory, Nat. Nanotechnol. 5 (2) (2010) 148–153, https://doi.org/10.1038/nnano.2009.456.
[125] A. Javey, H. Kim, M. Brink, Q. Wang, A. Ural, J. Guo, P. McIntyre, P. McEuen, M. Lundstrom, H. Dai, High-κ dielectrics for advanced carbon-nanotube transistors and logic gates, Nat. Mater. 1 (4) (2002) 241–246, https://doi.org/10.1038/nmat769.
[126] C. Ko, S. Ramanathan, Observation of electric field-assisted phase transition in thin film vanadium oxide in a metal-oxide-semiconductor device geometry, Appl. Phys. Lett. 93 (25) (2008) 252101, https://doi.org/10.1063/1.3050464.
[127] H.-T. Kim, B.-G. Chae, D.-H. Youn, S.-L. Maeng, G. Kim, K.-Y. Kang, Y.-S. Lim, Mechanism and observation of Mott transition in VO 2 -based two- and three-terminal devices, New J. Phys. 6 (2004) 52, https://doi.org/10.1088/1367-2630/6/1/052.
[128] G. Gopalakrishnan, D. Ruzmetov, S. Ramanathan, On the triggering mechanism for the metal–insulator transition in thin film VO2 devices: electric field versus thermal effects, J. Mater. Sci. 44 (19) (2009) 5345–5353, https://doi.org/10.1007/s10853-009-3442-7.
[129] Z. Yang, S. Hart, C. Ko, A. Yacoby, S. Ramanathan, Studies on electric triggering of the metal-insulator transition in VO 2 thin films between 77 K and 300 K, J. Appl. Phys. 110 (3) (2011) 33725, https://doi.org/10.1063/1.3619806.
[130] G. Stefanovich, A. Pergament, D. Stefanovich, Electrical switching and Mott transition in $VO_2$, J. Phys. Condens. Matter 12 (41) (2000) 8837–8845, https://doi.org/10.1088/0953-8984/12/41/310.
[131] J. Leroy, A. Crunteanu, A. Bessaudou, F. Cosset, C. Champeaux, J.-C. Orlianges, High-speed metal-insulator transition in vanadium dioxide films induced by an electrical pulsed voltage over nano-gap electrodes, Appl. Phys. Lett. 100 (21) (2012) 213507, https://doi.org/10.1063/1.4721520.
[132] Y. Zhang, S. Ramanathan, Analysis of “on” and “off” times for thermally driven $VO_2$ metal-insulator transition nanoscale switching devices, Solid State Electron. 62 (1) (2011) 161–164, https://doi.org/10.1016/j.sse.2011.04.003.
[133] A. Joushaghani, J. Jeong, S. Paradis, D. Alain, J. Stewart Aitchison, J.K.S. Poon, Voltage-controlled switching and thermal effects in $VO_2$ nano-gap junctions, Appl. Phys. Lett. 104 (22) (2014) 221904, https://doi.org/10.1063/1.4881155.
[134] T.S. Jordan, S. Scott, D. Leonhardt, J.O. Custer, C.T. Rodenbeck, S. Wolfley, C.D. Nordquist, Model and characterization of $VO_2$ thin-film switching devices, IEEE Trans. Electron Devices 61 (3) (2014) 813–819, https://doi.org/10.1109/TED.2014.2299549.
[135] A. Zimmers, L. Aigouy, M. Mortier, A. Sharoni, S. Wang, K.G. West, J.G. Ramirez, I.K. Schuller, Role of thermal heating on the voltage induced insulator-metal transition in $VO_2$, Phys. Rev. Lett. 110 (5) (2013), https://doi.org/10.1103/PhysRevLett.110.056601.
[136] S. Kumar, M.D. Pickett, J.P. Strachan, G. Gibson, Y. Nishi, R.S. Williams, Local temperature redistribution and structural transition during joule-heating-driven conductance switching in $VO_2$, Adv. Mater. 25 (42) (2013) 6128–6132, https://doi.org/10.1002/adma.201302046.
[137] E. Freeman, G. Stone, N. Shukla, H. Paik, J.A. Moyer, Z. Cai, H. Wen, R. Engel-Herbert, D.G. Schlom, V. Gopalan, S. Datta, Nanoscale structural evolution of electrically driven insulator to metal transition in vanadium dioxide, Appl. Phys. Lett. 103 (26) (2013) 263109, https://doi.org/10.1063/1.4858468.
[138] D. Li, A.A. Sharma, D.K. Gala, N. Shukla, H. Paik, S. Datta, D.G. Schlom, J.A. Bain, M. Skowronski, Joule heating-induced metal–insulator transition in epitaxial $VO_2$/$TiO_2$ devices, ACS Appl. Mater. Interfaces 8 (20) (2016) 12908–12914, https://doi.org/10.1021/acsami.6b03501.
[139] M.A. Belyaev, P.P. Boriskov, A.A. Velichko, A.L. Pergament, V.V. Putrolainen, D.V. Ryabokon, G.B. Stefanovich, V.I. Sysun, S.D. Khanin, Switching channel development dynamics in planar structures on the basis of vanadium dioxide, Phys. Solid State 60 (3) (2018) 447–456, https://doi.org/10.1134/S1063783418030046.
[140] I.P. Radu, B. Govoreanu, S. Mertens, X. Shi, M. Cantoro, M. Schaekers, M. Jurczak, S. De Gendt, A. Stesmans, J.A. Kittl, M. Heyns, K. Martens, Switching mechanism in two-terminal vanadium dioxide devices, Nanotechnology 26 (16) (2015) 165202, https://doi.org/10.1088/0957-4484/26/16/165202.
[141] M.J. Tadjer, V.D. Wheeler, B.P. Downey, Z.R. Robinson, D.J. Meyer, C.R. Eddy, F.J. Kub, Temperature and electric field induced metal-insulator transition in atomic layer deposited $VO_2$ thin films, Solid-State Electron. 136 (2017) 30–35, selected Papers from ISDRS 2016, https://doi.org/10.1016/j.sse.2017.06.018, http://www.sciencedirect.com/science/article/pii/S0038110117304264.
[142] J.C. Duchene, M.M. Terraillon, M. Pailly, G.B. Adam, Initiation of switching in VO 2 coplanar devices, IEEE Trans. Electron Devices 18 (12) (1971) 1151–1155, https://doi.org/10.1109/T-ED.1971.17347.
[143] D. Ruzmetov, G. Gopalakrishnan, C. Ko, V. Narayanamurti, S. Ramanathan, Three-terminal field effect devices utilizing thin film vanadium oxide as the channel layer, J. Appl. Phys. 107 (11) (2010) 114516, https://doi.org/10.1063/1.3408899.
[144] H. Ji, J. Wei, D. Natelson, Modulation of the electrical properties of $VO_2$ nanobeams using an ionic liquid as a gating medium, Nano Lett. 12 (6) (2012) 2988–2992, https://doi.org/10.1021/nl300741h.
[145] M. Nakano, K. Shibuya, D. Okuyama, T. Hatano, S. Ono, M. Kawasaki, Y. Iwasa, Y. Tokura, Collective bulk carrier delocalization driven by electrostatic surface charge accumulation, Nature 487 (2012) 459. https://doi.org/10.1038/nature11296. http://10.0.4.14/nature11296. https://www.nature.com/articles/nature11296#supplementary-information.
[146] J. Jeong, N. Aetukuri, T. Graf, T.D. Schladt, M.G. Samant, S.S.P. Parkin, Suppression of metal-insulator transition in $VO_2$ by electric field-induced oxygen vacancy formation, Science 339 (6126) (2013) 1402–1405, https://doi.org/10.1126/science.1230512.
[147] M.A. Belyaev, V.V. Putrolaynen, A.A. Velichko, G.B. Stefanovich, A.L. Pergament, Field-effect modulation of resistance in $VO_2$ thin film at lower temperature, Japanese, J. Appl. Phys. 53 (11) (2014) 111102, https://doi.org/10.7567/JJAP.53.111102.
[148] K. Martens, J. Jeong, N. Aetukuri, C. Rettner, N. Shukla, E. Freeman, D. Esfahani, F. Peeters, T. Topuria, P. Rice, A. Volodin, B. Douhard, W. Vandervorst, M. Samant, S. Datta, S. Parkin, Field effect and strongly localized carriers in the metal-insulator transition material $VO_2$, Phys. Rev. Lett. 115 (19) (2015), https://doi.org/10.1103/PhysRevLett.115.196401.
[149] T. Yajima, T. Nishimura, A. Toriumi, Positive-bias gate-controlled metal–insulator transition in ultrathin $VO_2$ channels with $TiO_2$ gate dielectrics, Nat. Commun. 6 (1) (2015), https://doi.org/10.1038/ncomms10104.

[150] T. Wei, T. Kanki, M. Chikanari, T. Uemura, T. Sekitani, H. Tanaka, Enhanced electronic-transport modulation in single-crystalline $VO_2$ nanowire-based solid-state field-effect transistors, Sci. Rep. 7 (1) (2017), https://doi.org/10.1038/s41598-017-17468-x.

[151] M.-J. Lee, Y. Park, D.-S. Suh, E.-H. Lee, S. Seo, D.-C. Kim, R. Jung, B.-S. Kang, S.-E. Ahn, C. Lee, D. Seo, Y.-K. Cha, I.-K. Yoo, J.-S. Kim, B. Park, Two series oxide resistors applicable to high speed and high density nonvolatile memory, Adv. Mater. 19 (22) (2007) 3919–3923, https://doi.org/10.1002/adma.200700251.

[152] C.-R. Cho, S. Cho, S. Vadim, R. Jung, I. Yoo, Current-induced metal–insulator transition in VOx thin film prepared by rapid-thermal-annealing, Thin Solid Films 495 (1–2) (2006) 375–379, https://doi.org/10.1016/j.tsf.2005.08.241.

[153] M. Son, J. Lee, J. Park, J. Shin, G. Choi, S. Jung, W. Lee, S. Kim, S. Park, H. Hwang, Excellent selector characteristics of nanoscale $VO_2$ for high-density bipolar ReRAM applications, IEEE Electron. Device Lett. 32 (11) (2011) 1579–1581, https://doi.org/10.1109/LED.2011.2163697.

[154] K. Martens, I.P. Radu, S. Mertens, X. Shi, L. Nyns, S. Cosemans, P. Favia, H. Bender, T. Conard, M. Schaekers, S. De Gendt, V. Afanas'ev, J.A. Kittl, M. Heyns, M. Jurczak, The $VO_2$ interface, the metal-insulator transition tunnel junction, and the metal-insulator transition switch On-Off resistance, J. Appl. Phys. 112 (12) (2012) 124501, https://doi.org/10.1063/1.4767473.

[155] I.P. Radu, B. Govoreanu, K. Martens, M. Toeller, A.P. Peter, M.R. Ikram, L.Q. Zhang, H. Hody, W. Kim, P. Favia, T. Conard, H.Y. Chou, B. Put, V.V. Afanasiev, A. Stesmans, M. Heyns, S. De Gendt, M. Jurczak, (Invited) Vanadium dioxide for selector applications, ECS Trans. 58 (7) (2013) 249–258, https://doi.org/10.1149/05807.0249ecst.

[156] A. Crunteanu, J. Givernaud, J. Leroy, D. Mardivirin, C. Champeaux, J.-C. Orlianges, A. Catherinot, P. Blondy, Voltage- and current-activated metal–insulator transition in $VO_2$ -based electrical switches: a lifetime operation analysis, Sci. Technol. Adv. Mater. 11 (6) (2010) 65002, https://doi.org/10.1088/1468-6996/11/6/065002.

[157] C. Hillman, P.A. Stupar, Z. Griffith, $VO_2$ switches for millimeter and submillimeter-wave applications, in: 2015 IEEE Compound Semiconductor Integrated Circuit Symposium (CSICS), IEEE, 2015, pp. 1–4, https://doi.org/10.1109/CSICS.2015.7314528.

[158] H. Madan, H.-T. Zhang, M. Jerry, D. Mukherjee, N. Alem, R. Engel-Herbert, S. Datta, 26.5 Terahertz electrically triggered RF switch on epitaxial $VO_2$-on-Sapphire (VOS) wafer, in: 2015 IEEE International Electron Devices Meeting (Iedm), IEEE, 2015, pp. 9.3.1–9.3.4, https://doi.org/10.1109/IEDM.2015.7409661.

[159] J. Frougier, N. Shukla, D. Deng, M. Jerry, A. Aziz, L. Liu, G. Lavallee, T.S. Mayer, S. Gupta, S. Datta, Phase-Transition-FET exhibiting steep switching slope of 8mV/decade and 36% enhanced ON current, in: 2016 IEEE Symposium on VLSI Technology, IEEE, 2016, pp. 1–2, https://doi.org/10.1109/VLSIT.2016.7573445.

[160] S. Datta, N. Shukla, M. Cotter, A. Parihar, A. Raychowdhury, Neuro inspired computing with coupled relaxation oscillators, in: The 51th Annual Design Automation Conference, ACM Press, 2014, pp. 1–6, https://doi.org/10.1145/2593069.2596685.

[161] N. Shukla, A. Parihar, E. Freeman, H. Paik, G. Stone, V. Narayanan, H. Wen, Z. Cai, V. Gopalan, R. Engel-Herbert, D.G. Schlom, A. Raychowdhury, S. Datta, Synchronized charge oscillations in correlated electron systems, Sci. Rep. 4 (1) (2014), https://doi.org/10.1038/srep04964.

[162] J.D. Ryckman, K.A. Hallman, R.E. Marvel, R.F. Haglund, S.M. Weiss, Ultra-compact silicon photonic devices reconfigured by an optically induced semiconductor-to-metal transition, Optic Express 21 (9) (2013) 10753, https://doi.org/10.1364/OE.21.010753.

[163] J.D. Ryckman, V. Diez-Blanco, J. Nag, R.E. Marvel, B.K. Choi, R.F. Haglund, S.M. Weiss, Photothermal optical modulation of ultra-compact hybrid Si-$VO_2$ ring resonators, Optic Express 20 (12) (2012) 13215, https://doi.org/10.1364/OE.20.013215.

[164] P. Markov, K. Appavoo, R.F. Haglund, S.M. Weiss, Hybrid Si-$VO_2$-Au optical modulator based on near-field plasmonic coupling, Optic Express 23 (5) (2015) 6878, https://doi.org/10.1364/OE.23.006878.

[165] A.B. Pevtsov, D.A. Kurdyukov, V.G. Golubev, A.V. Akimov, A.A. Meluchev, A.V. Sel'kin, A.A. Kaplyanskii, D.R. Yakovlev, M. Bayer, Ultrafast stop band kinetics in a three-dimensional opal- $VO_2$ photonic crystal controlled by a photoinduced semiconductor-metal phase transition, Phys. Rev. B 75 (15) (2007), https://doi.org/10.1103/PhysRevB.75.153101.

[166] R.M. Briggs, I.M. Pryce, H.A. Atwater, Compact silicon photonic waveguide modulator based on the vanadium dioxide metal-insulator phase transition, Optic Express 18 (11) (2010) 11192, https://doi.org/10.1364/OE.18.011192.

[167] M. Maaza, O. Nemraoui, C. Sella, A.C. Beye, B. Baruch-Barak, Thermal induced tunability of surface plasmon resonance in Au–$VO_2$ nano-photonics, Optic Commun. 254 (1–3) (2005) 188–195, https://doi.org/10.1016/j.optcom.2004.08.056.

[168] L.A. Sweatlock, K. Diest, Vanadium dioxide based plasmonic modulators, Optic Express 20 (8) (2012) 8700, https://doi.org/10.1364/OE.20.008700.

[169] Y.-G. Jeong, H. Bernien, J.-S. Kyoung, H.-R. Park, H. Kim, J.-W. Choi, B.-J. Kim, H.-T. Kim, K.J. Ahn, D.-S. Kim, Electrical control of terahertz nano antennas on $VO_2$ thin film, Optic Express 19 (22) (2011) 21211, https://doi.org/10.1364/OE.19.021211.

[170] M. Seo, J. Kyoung, H. Park, S. Koo, H.-s. Kim, H. Bernien, B.J. Kim, J.H. Choe, Y.H. Ahn, H.-T. Kim, N. Park, Q.-H. Park, K. Ahn, D.-s. Kim, Active terahertz nanoantennas based on $VO_2$ phase transition, Nano Lett. 10 (6) (2010) 2064–2068, https://doi.org/10.1021/nl1002153.

[171] Y. Zhao, J. Hwan Lee, Y. Zhu, M. Nazari, C. Chen, H. Wang, A. Bernussi, M. Holtz, Z. Fan, Structural, electrical, and terahertz transmission properties of VO 2 thin films grown on c-, r-, and m-plane sapphire substrates, J. Appl. Phys. 111 (5) (2012) 53533, https://doi.org/10.1063/1.3692391.

[172] M. Liu, H.Y. Hwang, H. Tao, A.C. Strikwerda, K. Fan, G.R. Keiser, A.J. Sternbach, K.G. West, S. Kittiwatanakul, J. Lu, S.A. Wolf, F.G. Omenetto, X. Zhang, K.A. Nelson, R.D. Averitt, Terahertz-field-induced insulator-to-metal transition in vanadium dioxide metamaterial, Nature 487 (7407) (2012) 345–348, https://doi.org/10.1038/nature11231.

[173] M.J. Dicken, K. Aydin, I.M. Pryce, L.A. Sweatlock, E.M. Boyd, S. Walavalkar, J. Ma, H.A. Atwater, Frequency tunable near-infrared metamaterials based on $VO_2$ phase transition, Optic Express 17 (20) (2009) 18330, https://doi.org/10.1364/OE.17.018330.

[174] M.D. Goldflam, T. Driscoll, B. Chapler, O. Khatib, N. Marie Jokerst, S. Palit, D.R. Smith, B.-J. Kim, G. Seo, H.-T. Kim, M.D. Ventra, D.N. Basov, Reconfigurable gradient index using $VO_2$ memory metamaterials, Appl. Phys. Lett. 99 (4) (2011) 44103, https://doi.org/10.1063/1.3615804.

[176] J.H. Park, J.M. Coy, T.S. Kasirga, C. Huang, Z. Fei, S. Hunter, D.H. Cobden, Measurement of a solid-state triple point at the metal–insulator transition in $VO_2$, Nature 500 (7463) (2013) 431–434, https://doi.org/10.1038/nature12425.

[177] B.G. Chae, H.T. Kim, S.J. Yun, Characteristics of W- and Ti-doped $VO_2$ thin films prepared by sol-gel method, Electrochem. Solid State Lett. 11 (6) (2008) D53, https://doi.org/10.1149/1.2903208.

[178] F. Beteille, J. Livage, Optical switching in $VO_2$ thin films, J. Sol. Gel Sci. Technol. 13 (1–3) (1998) 915–921.

[179] I.P. Radu, K. Martens, S. Mertens, C. Adelmann, X. Shi, H. Tielens, M. Schaekers, G. Pourtois, S. Van Elshocht, S. De Gendt, M. Heyns, J.A. Kittl, (Invited) Vanadium oxide as a memory material, in: 219th ECS Meeting, 2011, pp. 233–243, https://doi.org/10.1149/1.3568865.

[180] AM1.5 Spectra, According to the AM1.5 Standard Available Online from NREL the Relative Division of Energy between the Different Spectral Bands of the Solar Radiation Is; UV (<400nm)=0.7%, Vis (400nm-700nm)=48.3%, NIR (>700nm) = 51%. . URL https://www.nrel.gov/grid/solar-resource/spectra-am1.5.html.

[181] M. Saeli, C. Piccirillo, I.P. Parkin, R. Binions, I. Ridley, Energy modelling studies of thermochromic glazing, Energy Build. 42 (10) (2010) 1666–1673.

[182] S.-Y. Li, G.A. Niklasson, C.G. Granqvist, Thermochromic vanadium oxide thin films: electronic and optical properties, J. Phys. Conf. Ser. 559 (2014), 012001.

[183] S. Li, G.A. Niklasson, C.G. Granqvist, Nanothermochromics with $VO_2$-based core-shell structures: calculated luminous and solar optical properties, J. Appl. Phys. 113515 (2011) 1–6, https://doi.org/10.1063/1.3592350 (2014).

[184] H.W. Verleur, A.S. Barker, C.N. Berglund, Optical properties of $VO_2$ between 0.25 and 5 eV, Phys. Rev. 172 (1968) 788–798.

[185] H. Kakiuchida, P. Jin, S. Nakao, M. Tazawa, Optical properties of vanadium dioxide film during semiconductive-metallic phase transition, Japanese J. Appl. Phys. Part 2 Lett. 46 (4–7) (2007) 113–116, https://doi.org/10.1143/JJAP.46.L113.

[186] Thermochromic $VO_2$-$SiO_2$ nanocomposite smart window coatings with narrow phase transition hysteresis and transition gradient width submitted Sol. Energy Mater. Sol. Cells.

[187] C. Sol, J. Schläfer, I.P. Parkin, I. Papakonstantinou, Mitigation of hysteresis due to a pseudo-photochromic effect in thermochromic smart window coatings, Sci. Rep. 8 (1) (2018) 13249, https://doi.org/10.1038/s41598-018-31519-x. http://www.nature.com/articles/s41598-018-31519-x.

[188] W. Xiao, C. Yunzhen, Y. Chao, Y. Lu, L. Ying, Vanadium dioxide film protected with an atomic-layer-deposited Al $_2O_3$thin film, J. Vac. Sci. Technol. Vacuum, Surfaces, Films 34 (2016), 01A106. 10.1116/1.4931723.

[189] G.T. Pan, Y.L. Yang, S. Chong, N. Arjun, T.C. Yang, Y.C. Lai, The durability study of thermochromic vanadium dioxide films with the addition of barrier coatings, Vacuum 145 (2017) 158–168, https://doi.org/10.1016/j.vacuum.2017.08.028. https://doi.org/10.1016/j.vacuum.2017.08.028.

[190] Y. Cui, Y. Ke, C. Liu, Z. Chen, N. Wang, L. Zhang, Y. Zhou, S. Wang, Y. Gao, Y. Long, Thermochromic $VO_2$ for energy-efficient smart windows, Joule (2018) 1–40, https://doi.org/10.1016/j.joule.2018.06.018. https://linkinghub.elsevier.com/retrieve/pii/S2542435118302836.

[191] R. Binions, G. Hyett, C. Piccirillo, I.P. Parkin, Doped and un-doped vanadium dioxide thin films prepared by atmospheric pressure chemical vapour deposition from vanadyl acetylacetonate and tungsten hexachloride: the effects of thickness and crystallographic orientation on thermochromic properties, J. Mater. Chem. 17 (44) (2007) 4652–4660, https://doi.org/10.1039/b708856f.

[192] S.-y. Li, G.A. Niklasson, C.G. Granqvist, Thermochromic undoped and Mg-doped $VO_2$ thin films and nanoparticles : optical properties and performance limits for energy efficient windows, J. Appl. Phys. (2014), 053513, https://doi.org/10.1063/1.4862930.

[193] Y. Geng, L. Guo, S.-S. Xu, Q.-Q. Sun, S.-J. Ding, H.-L. Lu, D.W. Zhang, Influence of Al doping on the properties of ZnO thin films grown by atomic layer deposition, J. Phys. Chem. C 115 (25) (2011) 12317–12321, https://doi.org/10.1021/jp2023567. https://doi.org/10.1021/jp2023567.

[194] X. Lv, Y. Cao, L. Yan, Y. Li, Y. Zhang, L. Song, Atomic layer deposition of V 1–xMoxO2Thin films, largely enhanced luminous transmittance, solar modulation, ACS Appl. Mater. Interfaces (2018), https://doi.org/10.1021/acsami.7b16479.

[195] A. Taylor, I. Parkin, N. Noor, C. Tummeltshammer, M.S. Brown, I. Papakonstantinou, A bioinspired solution for spectrally selective thermochromic $VO_2$ coated intelligent glazing, Optic Express 21 (Suppl 5) (2013) A750–A764, https://doi.org/10.1364/OE.21.00A750. http://www.ncbi.nlm.nih.gov/pubmed/24104571.

[196] X. Qian, N. Wang, Y. Li, J. Zhang, Z. Xu, Y. Long, Bioinspired multifunctional vanadium dioxide: improved thermochromism and hydrophobicity, Langmuir 30 (35) (2014) 10766–10771, https://doi.org/10.1021/la502787q.

[197] N.R. Mlyuka, G. a. Niklasson, C.G. Granqvist, Thermochromic multilayer films of $VO_2$ and $TiO_2$ with enhanced transmittance, Sol. Energy Mater. Sol. Cell. 93 (9) (2009) 1685–1687, https://doi.org/10.1016/j.solmat.2009.03.021. https://doi.org/10.1016/j.solmat.2009.03.021.

[198] C. Liu, S. Wang, Y. Zhou, H. Yang, Q. Lu, D. Mandler, S. Magdassi, C.Y. Tay, Y. Long, Index-tunable anti-reflection coatings: maximizing solar modulation ability for vanadium dioxide-based smart thermochromic glazing, J. Alloy. Comp. 731 (2018) 1197–1207, https://doi.org/10.1016/j.jallcom.2017.10.045.

[199] M.J. Powell, R. Quesada-Cabrera, A. Taylor, D. Teixeira, I. Papakonstantinou, R.G. Palgrave, G. Sankar, I.P. Parkin, Intelligent multifunctional $VO_2/SiO_2/TiO_2$ coatings for self-cleaning, energy-saving window panels, Chem. Mater. 28 (5) (2016) 1369–1376, https://doi.org/10.1021/acs.chemmater.5b04419. https://doi.org/10.1021/acs.chemmater.5b04419.

[200] Y. Fink, J. Winn, S. Fan, C. Chen, A dielectric omnidirectional reflector, Science 1679 (1998), https://doi.org/10.1126/science.282.5394.1679. http://www.sciencemag.org/content/282/5394/1679.short.

[201] A. Szeghalmi, M. Helgert, R. Brunner, F. Heyroth, U. Gösele, M. Knez, Atomic layer deposition of $Al_2O_3$ and $TiO_2$ multilayers for applications as bandpass filters and antireflection coatings, Appl. Optic. 48 (9) (2009) 1727, https://doi.org/10.1364/AO.48.001727. https://www.osapublishing.org/abstract.cfm?URI=ao-48-9-1727.

[202] C. Liu, I. Balin, S. Magdassi, I. Abdulhalim, Y. Long, Vanadium dioxide nanogrid films for high transparency smart architectural window applications, Optic Express 23 (3) (2015) A124, https://doi.org/10.1364/OE.23.00A124. https://www.osapublishing.org/abstract.cfm?URI=oe-23-3-A124.

[203] Q. Lu, C. Liu, N. Wang, S. Magdassi, D. Mandler, Y. Long, Periodic micropatterned $VO_2$ thermochromic films by mesh printing, J. Mater. Chem. C 4 (36) (2016) 8385–8391, https://doi.org/10.1039/c6tc02694j.

[204] A. Checco, A. Rahman, C. Black, Robust superhydrophobicity in large-area nanostructured surfaces defined by block-copolymer self assembly, Adv. Mater. (2013) 1–6, https://doi.org/10.1002/adma.201304006. http://onlinelibrary.wiley.com/doi/10.1002/adma.201304006/full.

[205] T. Maitra, M.K. Tiwari, C. Antonini, P. Schoch, S. Jung, P. Eberle, D. Poulikakos, On the nanoengineering of superhydrophobic and impalement resistant surface textures below the freezing temperature, Nano Lett. 14 (1) (2014) 172–182, https://doi.org/10.1021/nl4037092. http://www.ncbi.nlm.nih.gov/pubmed/24320719.

[206] Y. Ke, I. Balin, N. Wang, Q. Lu, A.I.Y. Tok, T.J. White, S. Magdassi, I. Abdulhalim, Y. Long, Two-dimensional $SiO_2/VO_2$ photonic crystals with statically visible and dynamically infrared modulated for smart window deployment, ACS Appl. Mater. Interfaces 8 (48) (2016) 33112–33120, https://doi.org/10.1021/acsami.6b12175.

### 3.1.2 Synthesis of $VO_2$ thin films by ALD process.

$VO_2$ features a reversible transition from semiconducting to metallic state as a response to temperature, electrical field, optical, magnetic field, or strain. The induced reversible characteristics can be exploited for applications such as electrical switches, oscillators, thermal sensors, optical switches, and metamaterials.

TEMAV or TDMAV are the most widely used precursors to grow $VO_2$ film as vanadium is in the +4 oxidation state in the precursor state. Nevertheless, handling these precursors is critical due to their high sensitivity to moisture. In this context, the VTOP was considered despite the +5 oxidation state of vanadium, as it features a vapour pressure that is comparable to that of TEMAV, while presenting less sensitivity to moisture. Post-annealing treatments are needed to reach crystalline $VO_2$, starting with ALD, irrespective of the precursors used.

ALD optimization using VTOP precursor results in amorphous vanadium oxide films. Post-deposition annealing converts the film into vanadium dioxide phase with discontinuous rough morphology. Argon plasma treatment before the annealing treatment resulted in a full covering $VO_2$ phase with reduced roughness. Semiconductor-Metal transition at 67˚C is noticed for obtained $VO_2$ phase.

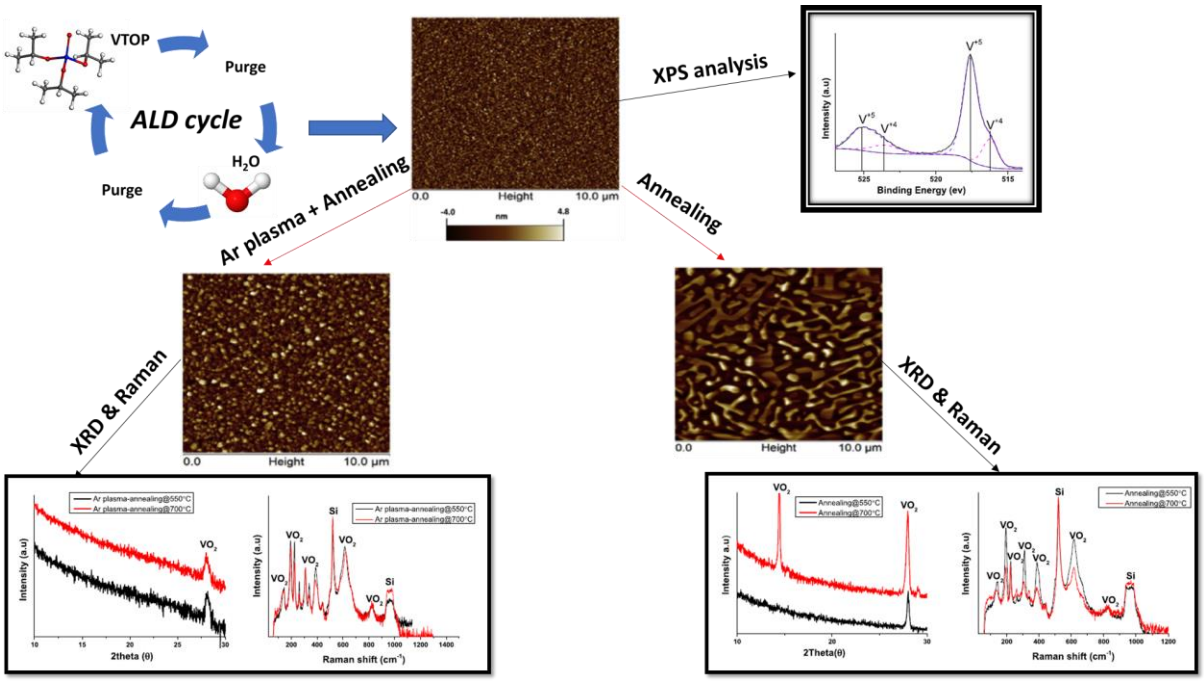

Materials Today Chemistry 12 (2019) 332–342

Contents lists available at ScienceDirect

Materials Today Chemistry

journal homepage: www.journals.elsevier.com/materials-today-chemistry/

# Study of $VO_2$ thin film synthesis by atomic layer deposition

V.P. Prasadam, B. Dey, S. Bulou, T. Schenk, N. Bahlawane*

*Material Research and Technology Department, Luxembourg Institute of Science and Technology, Rue du Brill, L-4422, Belvaux, Luxembourg*

ARTICLE INFO

*Article history:*
Received 11 February 2019
Received in revised form
16 March 2019
Accepted 16 March 2019

*Keywords:*
ALD
Vanadyl triisopropoxide
Vanadium dioxide
Semiconductor-to-metal transition

ABSTRACT

Vanadium dioxide emerges as an appealing material for smart thermal management and electrical/optical switching owing to its abrupt semiconductor-to-metal transition (SMT) at near room temperature. The application potential of this material should be leveraged by the implementation of the atomic layer deposition (ALD), a method that enables an unequaled control over the thickness and film conformality on complex substrate structures by virtue of self-limiting growth mechanism. Here, the vanadium oxide thin films are synthesized from vanadyl (V) triisopropoxide (VTOP) as the vanadium precursor and $H_2O$ as the reactant. The thermal decomposition threshold of VTOP was observed at 90 °C, and temperature window with a constant growth rate was observed at 50–90 °C. The saturation behavior of the ALD half reactions was demonstrated at 80 °C, yielding the optimized ALD cycle conditions of 8 s VTOP/15 s purge/6 s $H_2O$/15 s purge with a growth rate of 0.047 nm/cycle. The as-grown amorphous films convert into $VO_2$ via a 4-h heat treatment under $10^{-5}$ mbar at 550 °C. The formed $VO_2$ features a sudden and reversible change in the total hemispherical reflectance in UV-VIS-NIR region at 68 °C, confirming its SMT behavior. The conversion process induces, however, a surface roughening, which was considerably suppressed by a postdeposition treatment in plasma environment prior the annealing treatment.



## 1. Introduction

Vanadium oxides have interesting properties because of the 'd' orbital electrons, which might behave as localized or free electrons due to the crystal field splitting [1]. Because vanadium features various oxidation states, i.e., +5, +4, +3, +2, it can co-ordinate to oxygen in different polyhedral structures [2]. Polyhedral co-ordination and electron-electron correlation drive the properties of vanadium oxide and give rise to applications in varied fields such as catalysis [3], batteries [4], thermochromic smart windows [5], and microelectronics [6]. Vanadium in the oxide phase exists either in a single or in mixed oxidation states as in the Magneli ($V_nO_{2n-1}$) and Wadsley ($V_nO_{2n+1}$) series [7,8]. These compounds are formed because of the varied oxygen vacancies and small difference between their formation energy [9]. Several vanadium oxide phases, such as $V_2O_3$, $V_3O_5$, and $VO_2$ show semiconductor-to-metal transition (SMT) as a response to external stimuli such as temperature [10]. Among these oxides, $VO_2$ undergoes a reversible transition between the metallic and semiconducting states as a response to change of temperature, electrical field, optical, magnetic field, or strain [6,11]. The induced reversible change in the properties of $VO_2$ thin films can be useful in applications such as electrical switches [10,12,13], oscillators [14,15], thermal sensors [16,17], optical switches [18,19], and metamaterials [20–22].

Several processes were developed for the growth of vanadium dioxide, such as sputtering, pulsed laser deposition [23–25], sol-gel [26–28], and chemical vapor deposition, [29–31]. A comprehensive review of vanadium oxide deposition process can be seen in the literature [32–34]. Atomic layer deposition (ALD) yields pure films with precise control of the thickness and conformality on complex substrates such as carbon nanotubes (CNTs) and high-aspect-ratio structures [35–37].

Previously, Weimer et al. [38] have demonstrated the ALD of $VO_2$ using a precursor where vanadium is in the +3 oxidation state, i.e., vanadium tris (*N*,*N*′-diisopropylacetamidinate) ($V(amd)_3$), which presents a vapor pressure of 6.6 Pa at 70 °C. Nevertheless, this precursor is not commercially available. Rampelberg et al. [39] and Premkumar et al. [40] have implemented a +4-oxidation state vanadium precursor, i.e., tetrakis[ethylmethyamino]vanadium (TEMAV). The precursor is available commercially, and it features a vapor pressure of 57 Pa at 82 °C. This precursor has, however, a narrow ALD window because the thermal decomposition of the precursor starts at 100 °C. The deposition temperature window is also restricted by the evaporation temperature of the precursor. The ALD of vanadium oxide was also reported using another $V^{+4}$-

* Corresponding author.
*E-mail address:* Naoufal.bahlawane@list.lu (N. Bahlawane).

https://doi.org/10.1016/j.mtchem.2019.03.005
2468-5194/

precursor, tetrakis[dimethyamino]vanadium (TDMAV), which is solid at room temperature and features a vapor pressure of 133 Pa at 64 °C [41,42]. The implementation of this precursor requires heating to raise the vapor pressure, and the high sensitivity to moisture is associated with cumbersome precaution measures.

The vapor pressure of the vanadyl (V) triisopropoxide (VTOP), 268 Pa at 82 °C, is high enough to allow evaporation at room temperature. VTOP is mostly studied for the growth of vanadium pentoxide films with different reactants such as $H_2O$ [43–47], $O_3$ [48], and plasma $O_3$ [49]. Song et al. [50] and Kim et al. [51] have produced vanadium dioxide films using VTOP but have not demonstrated the characteristic self-limited half reactions that differentiate CVD from ALD. Postdeposition treatments are common to all ALD processes to convert the as-deposited amorphous film into crystalline $VO_2$. This involves either thermal annealing in ultra high vacuum (UHV), [52–58], $H_2$ [51,59,60], or in inert $N_2$ atmospheres [61]. Reduction through electron bombardment, X-rays [53], and $H_2$ plasma [62–64] were also proven successful. The postdeposition annealing generally deteriorates the morphology of the films, and the impact is even stronger for ultrathin films [65], with consequent impact on the SMT properties [66,67].

In this report, we demonstrate the formation of continuous thin film $VO_2$ down to a thickness of 20 nm, which exhibit the SMT behavior.

## 2. Experiment

Vanadium oxide films are deposited on 4-inch silicon substrates using a thermal homebuilt ALD reactor. Before depositions, vacuum leak tests were performed using Pfeiffer Smart test HL572 with alpha 2 helium test gas. The measured leak rate, $10^{-9}$ mbar l/s, is equivalent to ultrahigh vacuum vessels. VTOP is used as the precursor, along with $H_2O$ for the hydrolysis. Both the water and VTOP sources are maintained at room temperature during deposition. alpha 2 argon (99.9999%), filtered using a gas purifier (Gatekeeper; Entegris), was used as a carrier gas for VTOP and used as the purge gas with a flow rate of 50 sscm (standard cubic centimeter per minute) for the removal of unreacted species from the reactor. VTOP and $H_2O$ are introduced into the reactor chamber sequentially followed by purging steps, and the ALD cycle is optimized by adjusting the exposures and purge times. The deposition pressure was maintained at ~0.2 mbar. Unless otherwise stated, the deposition temperature was set at 80 °C.

Various postdeposition treatments have been investigated for the film conversion into crystalline $VO_2$:

- Four hours of annealing in a vacuum furnace (AS micro; AnnealSys) at 550 or 700 °C was used with a residual air pressure of $10^{-5}$ mbar. Heating and cooling were performed with a ramp of 5 °C/min.
- Plasma treatment before annealing was performed during 30 min under a 50-sccm flow of either Ar or $H_2$. Radiofrequency (RF) electron cyclotron wave resonance (ECWR) plasma source (COPRA® 200 DN CF; CCR Technology GmbH) was used in this study. This specific plasma source consists in a single-turn RF-driven electrode and a small transverse static magnetic field (≈tens of Gauss) to generate a high-density plasma even at low pressure [68]. A quasi-neutral beam (composed of electron, ions, and neutral species) diffuses through the reactor chamber and interacts with the coated substrate. ECWR plasma sources are of major interest for material processing because they can provide a high plasma density up to $n_e = 10^{11}$ $cm^{-3}$ and a dissociation degree of diatomic gases up to 80% [69]. The plasma treatments were performed at $5.10^{-3}$ mbar using a power of 400 W, and the substrates, initially kept at room temperature, reach 50 °C after 30-min exposure to the remote plasma species.

The films thicknesses were assessed using a multiwavelength ellipsometer (Film Sense) with the Cauchy model, whereas X-ray diffraction (Bruker D8), with Cu-$K_\alpha$ as the X-ray source, was used to identify the crystalline phases of vanadium oxide. Data were collected in the grazing incidence mode from 20° to 60° with a step size of 0.02°. Raman spectroscopy was performed using an inVia Raman spectrometer from Renishaw with a 532-nm laser. X-ray photoelectron spectroscopy (XPS) experiments were performed using a Kratos Axis Ultra DLD using monochromatic Al-$K_\alpha$ radiation (E = 1,486.6eV), photoelectron emission take-off angle at 0° with respect to the surface normal. X-ray reflectivity (XRR) was performed using a PANalytical X'Pert Pro with Cu-$K_\alpha$ radiation ($\lambda = 0.154$ nm). GenX software was used to fit the data using a stack of Si, native $SiO_2$ (typically fitted to be 2 nm or less), and a $VO_x$. The cross-sectional morphology of the films was inspected using the FEI Helios Nanolab 650 scanning electron microscope (SEM) at a working distance of 5.7 mm with 5–10 V voltage. The surface morphology of the obtained films was investigated using atomic force microscopy (AFM; Innova; Bruker) in tapping mode with an etched single crystal silicon probe tip having a radius curvature <10 nm. The optical measurements were carried out in a reflection configuration using LAMBDA 1050 UV-Vis-NIR spectrophotometer from Perkin Elmer with a 100-mm Spectralon integration sphere. Measurements were performed in the UV-Vis-NIR spectral range (250–2,500 nm), whereas the surface temperature was cycled between 25 °C and 95 °C.

## 3. Results

### 3.1. ALD growth of vanadium oxide

The deposition of vanadium oxide was performed on silicon substrates using the thermally activated hydrolysis reaction of VTOP. It is worth mentioning that the hydrolysis reaction enables a ligand exchange with no change of the oxidation state.

This vanadium source was intensively investigated as a single-source precursor for the growth of vanadium oxide by chemical vapor deposition [70,71]. Nevertheless, the lowest temperature enabling the CVD growth is not reported. The occurrence of a self-limiting growth, a prerequisite for the optimization of the ALD process, is only expected below this critical temperature. Therefore, a systematic study was conducted to define this temperature via the *ex situ* determination of the thickness, by ellipsometry, after 240 cycles of exposure to VTOP in the absence of water vapor and at various temperatures. As shown in Fig. 1, no measurable growth was noticed up to 90 °C, and a substantial increase of the deposited thickness was observed starting 100 °C. The resulting films have a refractive index of 2.35 at $\lambda = 633$ nm that corresponds to the $V_2O_5$ phase [72].

A second experimental confirmation was performed using a sequential exposure of the silicon surface to both VTOP (8 s) and $H_2O$ (5 s) with a purge time of 10 s. The growth rate per cycle is found to be temperature insensitive within the 60–90 °C range. The difficulty of evacuating water vapor from the deposition reactor below 60 °C during the 10 s of purge is presumably the reason why CVD deposition occurs below 60 °C. The condensation of VTOP precursor can be ruled out because the VTOP was evaporated at room temperature. The enhanced growth rate at ≥100 °C in the presence of water vapor confirms the CVD growth. The ALD temperature window using VTOP-$H_2O$ is therefore clearly identified within the 60–90 °C range. The obtained ALD growth rate of 0.047 nm/cycle is slightly high relative to the already reported value of 0.03 nm/cycle, but it is still below the monolayer of $V_2O_5$, i.e., 0.2 nm/cycle [73]. It is worth mentioning that most ALD studies of vanadium oxide from VTOP are reported at temperatures exceeding

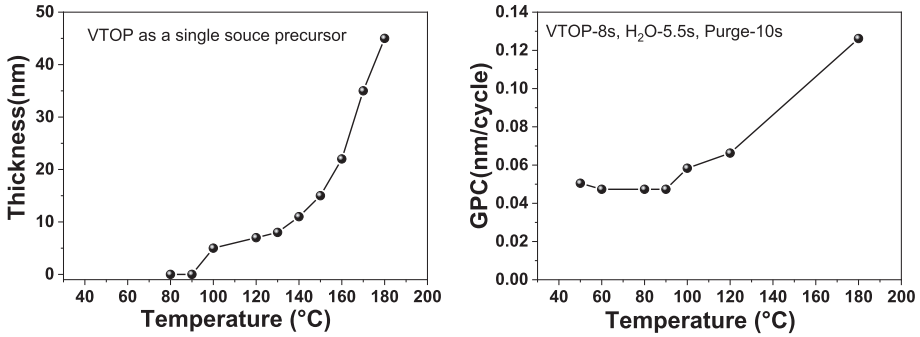


**Fig. 1.** Deposited thickness of vanadium oxide as a result of VTOP thermolysis (left) and hydrolysis (right) as a function of the substrate temperature. GPC, growth per cycle; VTOP, vanadyl triisopropoxide.

100 °C, a temperature that is seemingly outside the ALD range, as demonstrated in Fig. 1. The extent of parasitic CVD contribution in the ALD process due to the precursor decomposition increases with the temperature and also with the precursor pulse duration [74,75]. To reduce the parasitic CVD contribution, precursor pulse durations are usually kept short [76,77], which is an efficient strategy as long as no highly structured substrates are involved.

During the VTOP exposure, the surface sites are occupied by the chemisorbed precursor, and unreacted species are evacuated during the purging time. The available vanadium ligands are converted to OH groups along the hydrolysis process in the subsequent $H_2O$ exposure. A systematic study was performed to estimate the necessary time to attain ALDs self-limited half reactions with VTOP and $H_2O$ pulses. Here, we have extended the individual VTOP and water pulses for long durations while keeping the same number of ALD cycles.

Extending the surface exposure to VTOP, up to 8 s at 80 °C, leads to an increase of the growth per cycle (GPC). Saturation is observed beyond 8 s, as displayed in Fig. 2. The obtained GPC, 0.047 nm/cycle, corresponds to 23% of a monolayer. The VTOP surface coverage is therefore strongly limited by the size of the ligand sphere and probably by the charge transfer between the adsorbate and surface.

The hydrolysis of VTOP shows a clear self-limitation behavior after 5 s at 80 °C (Fig. 2), whereas 0.5s was sufficient at 120 °C (results not shown). The here-observed slow hydrolysis was related in previous reports to the ligands' steric hindrance [43,44,78,79]. With a VTOP exposure time of 2 s, the saturation of the hydrolysis reaction at 120 °C was noticed at 0.02 nm/cycle. Such a behavior can be associated with a decrease of OH surface concentrations at higher temperatures affecting the surface coverage during the adsorption of VTOP [78,80].

The optimized saturating conditions yield less than 1-nm deviation in thickness throughout the substrate on the 4-inch silicon wafer. An efficient deposition conformity is expected even on highly structured substrates under the ALD self-limiting conditions. The aforementioned optimized saturation conditions, 8 s VTOP/15 s purge/6 s $H_2O$/15 s purge, were therefore implemented to coat a 4-μm-thick film of CVD-grown CNT ($\phi = 10$ nm) [81]. Fig. 3 shows the cross-sectional micrograph of the CNT layer featuring an aspect ratio equivalent to 400, before and after the ALD of a conformal 15-nm-thick vanadium oxide film. The CNTs initially featuring a diameter of 10 nm clearly thicken after vanadium oxide deposition and exhibit a diameter of ~40 nm. The SEM inspection of the cross section shows clearly that both CNTs at the surface and interface with silicon substrate are coated with the same thickness of vanadium oxide, which is a clear demonstration of the conformal nature of ALD deposits in the optimized conditions.

### 3.2. Characterization of the as-deposited $VO_x$

The structural characterization was performed on a 70-nm-thick vanadium oxide resulting from 1,500 ALD cycles on silicon substrate at 80 °C using the saturating ALD conditions. The as-grown films are X-ray diffraction (XRD) amorphous and show no Raman scattering bands. The XPS analysis reveals a mixed oxidation state for vanadium. The deconvolution of the $V_{2p}$ peak (Fig. 4) fits with two peaks at 517.3 and 516.1 eV that can be attributed to the oxidation states +5 and + 4, respectively [82]. The quantitative interpretation reveals a dominant (79%) +5 oxidation state, which is similar to that the implemented precursor. The presence of small fraction of $V^{+4}$ might be due to the surface reduction of vanadium oxide films by the creation of oxygen vacancies upon exposure to X-rays under ultrahigh vacuum conditions [53]. The XPS analysis shows no trace of carbon excluding its presence with concentrations above 1 at% that is the detection limit with XPS. Therefore, VTOP ligands are efficiently hydrolyzed during the surface

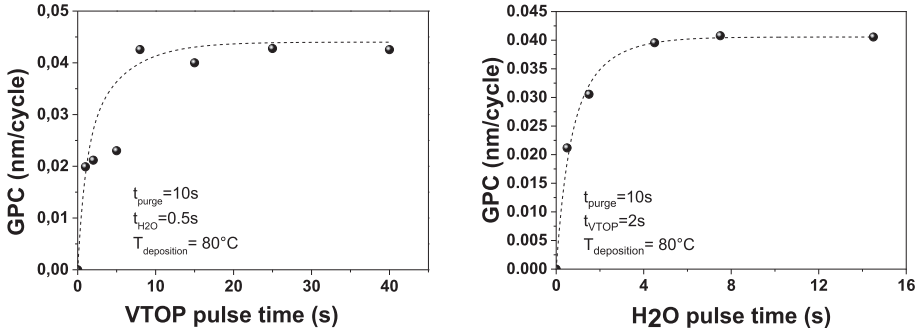


**Fig. 2.** ALD self-limitation behavior at 80 °C using a sequential surface exposure to VTOP and $H_2O$. ALD, atomic layer deposition; GPC, growth per cycle; VTOP, vanadyl triisopropoxide.

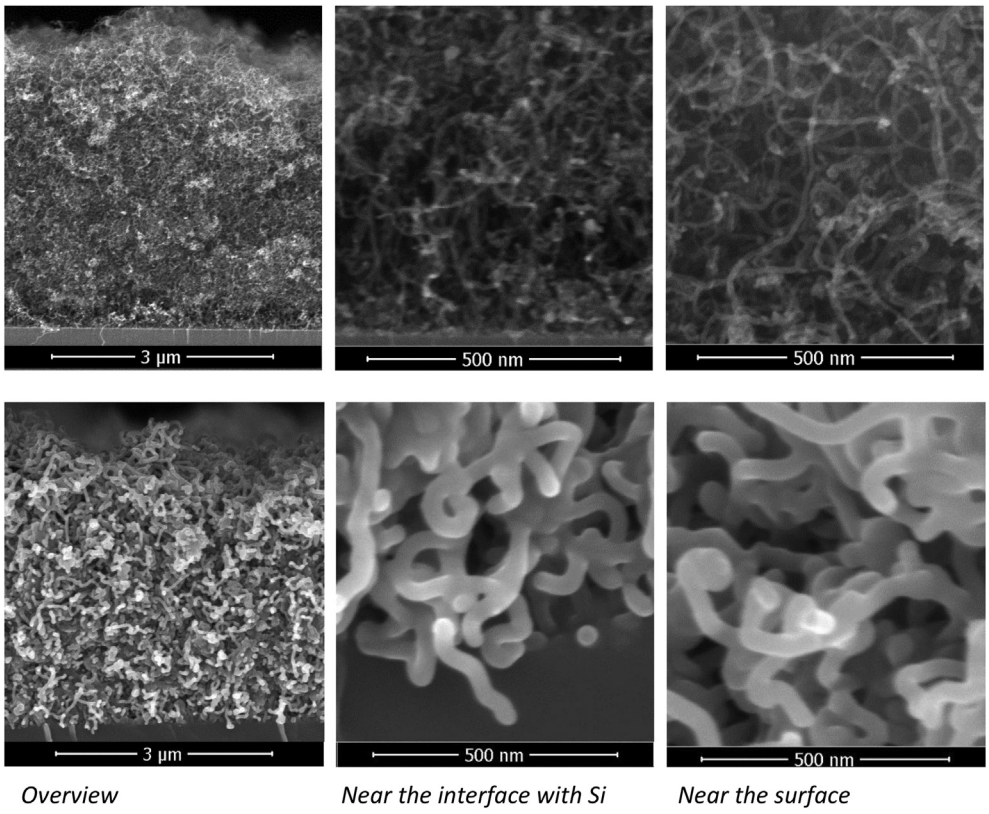


**Fig. 3.** Cross-sectional scanning electron micrographs of the CNT film before (above) and after (below) the ALD of vanadium oxide. ALD, atomic layer deposition; CNT, carbon nanotube.

exposure to $H_2O$ vapor at 80 °C [83]. This result contrasts with the growth at 150 °C, where 6% carbon contamination was detected [44]. The contamination in this case is presumably associated with the excessive and non-selective thermal decomposition of the precursor.

From the XRR measurement and corresponding fit curve of the as-grown films, Fig. 5, a film density of 2.7 g/cm$^3$ can be derived, which is low relative to bulk polycrystalline $V_2O_5$ (3.39 g/cm$^3$). Reduced density in amorphous films is not unusual for as-grown ALD-made films [84].

Thermal postdeposition treatment is achieved to convert the amorphous as-grown films into crystalline $VO_2$. Hereby, the vanadium cations reduce to form exclusively $V^{+4}$. Previous investigations showed that annealing treatment under ambient air or oxygen converts the as-grown amorphous vanadium oxide into crystalline $V_2O_5$ phase [43,44,85]. Reducing atmospheres are therefore needed to yield a $VO_2$ phase [86,87].

### 3.3. Characterization of the postannealed $VO_x$

#### 3.3.1. Annealing in vacuum

The as-grown films were annealed 4 h under vacuum, $10^{-5}$ mbar (without any reducing gases), at various temperatures. The XRD analysis, Fig. 6, provides evidence that films annealed at ≥550 °C feature a monoclinic $VO_2$ phase (PDF card no 03-065-2358). The diffractogram of the annealed film at 550 °C reveals a peak at $2\theta = 27.9°$, corresponding to (011) plane, whereas the annealed films at 700 °C show additionally the presence of the (001) plane with comparable intensity.

Raman scattering, Fig. 6, shows bands at 141, 194, 222, 259, 306, 336, 385, 440, 613, and 825 cm$^{-1}$, all of which can be assigned to the monoclinic $VO_2$ phase [82,88]. The low-frequency phonon bands at 141, 194, and 222 cm$^{-1}$ represent the lattice V-V vibrations, and the rest of the frequency modes represent vibrations of V-O bonds [82].

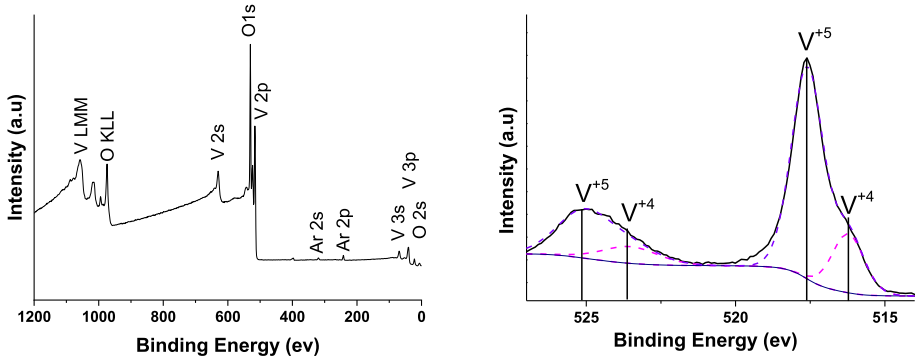


**Fig. 4.** XPS survey spectrum of the as-deposited vanadium oxide (left) and the deconvolution of the V2p into +5 and + 4 components (right).

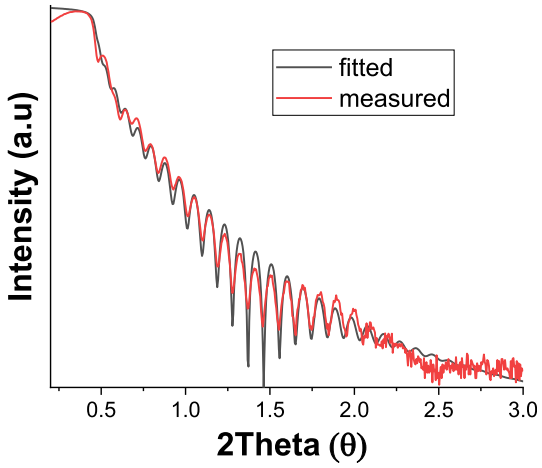


**Fig. 5.** XRR pattern fitted with the model of as-grown $VO_x$. XRR, X-ray reflectivity.

The obtained results are in line with previous works conducted on $VO_2$ by CVD [31].

The $O_2$ temperature-programmed desorption ($O_2$-TPD) is a characterization technique heavily implemented for the characterization of catalysts. In this method, the temperature of the materials is typically increased at a ramp of 10 K/min under ultrahigh vacuum, and the desorbed oxygen is monitored. This method was reported for the investigation of $V_2O_5$ on silicon oxide [52,53,89,90]. The $O_2$-TPD features two peaks: the α peak with a maximum slightly below 450 °C was attributed to the desorption of the surface oxygen, whereas the β peak above 600 °C was attributed to the desorption of the lattice oxygen of $V_2O_5$. Based on this literature, it is clear that the selected temperature in our experiments, 550 °C, is high enough to induce a fast desorption of the surface oxygen and a slow desorption of the lattice oxygen. Oxygen partial pressure is the most crucial part in obtaining the $VO_2$ phase [86,87]. The Ellingham diagram illustrates this effect and shows that oxygen partial pressure below $10^{-4}$ mbar is necessary to attain $VO_2$ [10]. This condition is also satisfied in the designed vacuum annealing test.

Vanadium dioxide features an SMT at 68 °C that is accompanied by a structural transition from the semiconducting monoclinic to the metallic rutile structure [91]. The optical properties feature a substantial change at the transition temperature, which finds relevant application for thermochromic smart windows [5,92,93]. The optical property of 20-nm $VO_2$ films, obtained by annealing the ALD-made amorphous layer at 550 °C for 4 h in vacuum of $10^{-5}$ mbar was investigated using temperature-dependent total hemispherical reflectance (THR) in the UV-VIS-NIR (λ: 250–2,500 nm). As displayed in Fig. 7, the THR of the film shows a sudden increase at the transition temperature, i.e., 68 °C. If we categorize the optical spectrum in two regions, i.e., UV-VIS and NIR, we measure a significant increase in the reflectance in the NIR region relative to UV-VIS region, i.e., with a ΔR ~8% in the NIR vs. 2% in the UV-VIS region. The obtained result is in line with the observed 10% reflection change for a 35-nm-thick vanadium oxide film made by ALD on sapphire substrates [94]. The change in the optical properties, as shown in previous studies [95], follows the Beer-Lambert law as a function of the thickness. In Fig. 7, a hysteresis width of $\Delta T = 6$ °C is observed upon heating and cooling across the SMT. The width of the hysteresis depends on the crystallinity, grain size, and grain boundary conditions [68,96,97]. The obtained narrow hysteresis and high amplitude of reflectance change hint at the high quality of the attained ultrathin films.

Relative to the as-grown vanadium oxide films, the AFM-assessed surface morphology of the obtained $VO_2$ shows a substantial surface roughening already after annealing at 550 °C, and a severe dewetting from the silicon substrate occurs upon annealing at 700 °C. Similar surface roughening was previously reported upon reduction of $V_2O_5$ films to $VO_2$ films [40,57,61,65,98]. This effect was attributed to the desorption of lattice oxygen that generates strain in the films, leading to the grain growth, especially for a low-melting-point oxides such as $V_2O_5$, where thermally induced elemental diffusion is significant. The combination of strain and thermally activated diffusion results in a substantial morphological change, which is seen as roughening and dewetting [99]. The extent of dewetting depends on the nature of the substrate, gas-phase composition, thickness of the films, and temperature. The 70-nm-thick $VO_x$ film produced a $VO_2$ film with a roughness of 21 nm after annealing at 550 °C. This roughness rises to 46 nm when the conversion is performed at 700 °C (Fig. 8).

Among the vanadium oxide phases, $V_2O_5$ and $V_nO_{2n+1}$ in general have melting points between 690 °C and 720 °C, Fig. 9, which means that the thermally activated elemental diffusion would be high during the conversion to $VO_2$ with a consequent dewetting. The resulting discontinuous $VO_2$ films are of a limited suitability for a number of applications. Therefore, inducing oxygen desorption at low temperatures would be suitable for the attainment of smooth $VO_2$ film. Various plasma treatments were considered for the generation of oxygen deficiency in the as-grown film before annealing.

### 3.3.2. Hydrogen plasma treatment/annealing in vacuum

After 30 min of hydrogen plasma treatment, the as-grown films remain amorphous; nevertheless, their refractive index at 633 nm decreased from 2.35 to 2.23. This change might indicate the occurrence of a bulk oxygen desorption during the plasma treatment. The potentially formed vanadium oxide with lower oxidation state is metallic at room temperature and has lower refractive

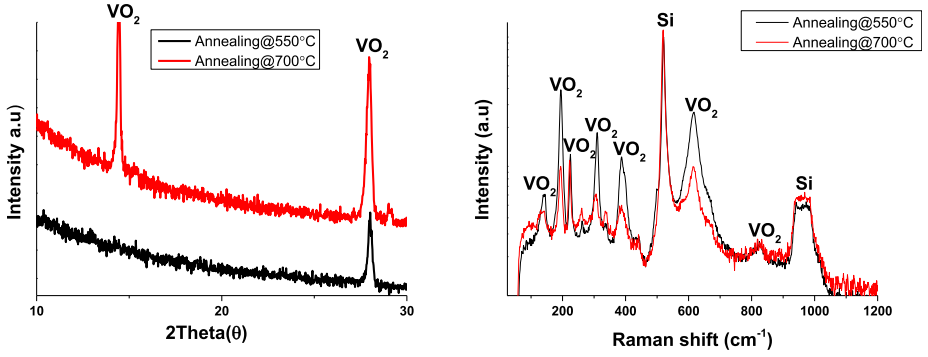


**Fig. 6.** XRD (left) and Raman (right) characterization of thermally treated vanadium oxide films. XRD, X-ray diffraction.

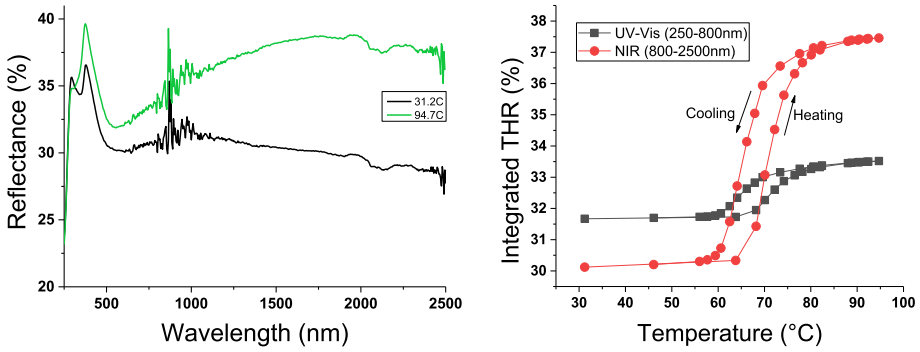


**Fig. 7.** Temperature-dependent total hemispherical reflectance (THR) of 20-nm $VO_2$ films upon heating as a function of the wavelength for (left) and the variation in the integrated THR in the UV-Vis and in the NIR across the transition temperature upon consecutive heating and cooling (right). $VO_2$ films are obtained by annealing at 550 °C for 4 h under air residual pressure of $10^{-5}$ mbar.

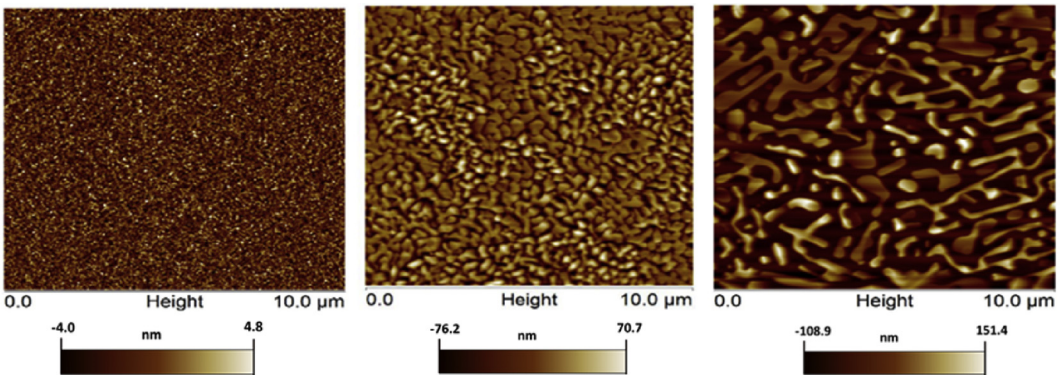


**Fig. 8.** AFM images of as-deposited vanadium oxide film with a roughness of 1.5 nm and a thickness of 70 nm (left), with postdeposition thermal treatment at 550 °C with roughness of Rq = 21 nm (middle) and 700 °C with roughness of Rq = 46 nm (right). The film is deposited on silicon substrate. AFM, atomic force microscopy. (For interpretation of the references to colour in this figure legend, the reader is referred to the Web version of this article.)

index. Subsequent 4-h annealing in vacuum was performed at 550 and 700 °C to induce crystallization. The obtained films after annealing at 550 °C are dominated by the presence of $V_nO_{2n-1}$ phase as shown by the XRD analysis (Fig. 10), whereas the Raman scattering shows a minor presence of $VO_2$. The fraction of $VO_2$ is enhanced after annealing at 700 °C (Fig. 10).

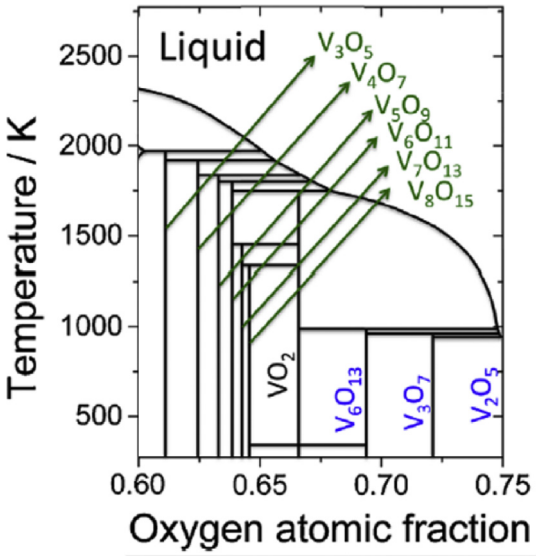


**Fig. 9.** Fraction of the V-O binary diagram (Reproduced with permission for Kang [100], Copyright 2012, Elsevier B. V.).

It is worth mentioning that no Raman scattering signature is expected from $V_nO_{2n-1}$ at room temperature because they exhibit metallic states [9]. The formation of $V_nO_{2n-1}$ was also reported upon a remote RF $H_2$ plasma treatment of $V_2O_5$ films [64]. Authors have attributed the occurrence of a mixed phase after annealing at 700 °C to the decomposition of $V_nO_{2n-1}$ into $VO_2$ and $V_3O_5$ [9].

The impact of $H_2$ plasma on surface morphology is substantial as it can be appreciated in Fig. 11. Films annealed at 550 °C remain smooth and exhibit a roughness of 4 nm. For annealing at 700 °C, the roughness increases to 18 nm because of grain growth but remains reasonable and the dewetting is largely suppressed. The formation of the lower oxidation state of vanadium (+3 in the $V_nO_{2n-1}$) witnesses the higher reduction potential of $H_2$ plasma as the $V_nO_{2n-1}$ phases feature a significantly higher melting temperature, see Fig. 9, which explains the limited dewetting [99].

### 3.3.3. Argon plasma treatment/annealing in vacuum

As noticed with hydrogen, 30 min of Ar plasma treatment does not induce any crystallization; nevertheless, the refractive index at 633 nm featured an increase to 2.45 starting from 2.35, a value that corresponds to ALD-made $V_2O_5$ [72]. Increase of the refractive index can be associated with the formation of lower oxidation phase, such as $VO_2$ [94]. The subsequent 4-h annealing in vacuum was performed at 550 and 700 °C to induce crystallization. As depicted in Fig. 12, the Ar plasma–treated $VO_x$ samples convert to $VO_2$ after annealing at 550 and 700 °C. XRD and Raman analysis results, shown in Fig. 12, confirm the formation of the monoclinic $VO_2$ phase. Both temperatures yield similar XRD and Raman patterns.

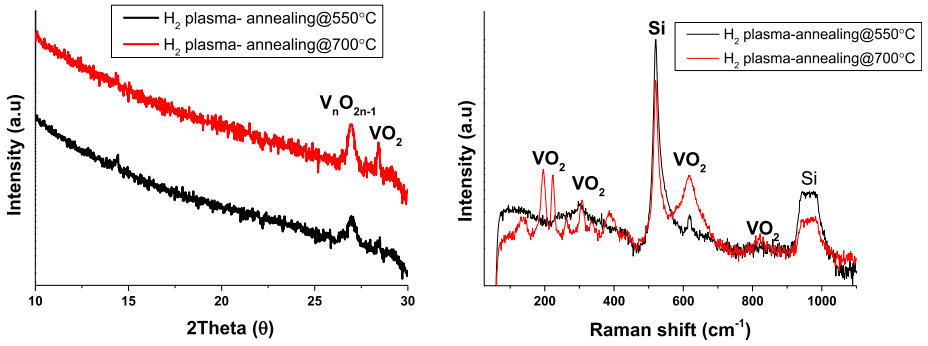


**Fig. 10.** XRD (left) and Raman (right) characterization of vanadium oxide film treated with $H_2$ plasma followed by thermal treatment at 550 and 700 °C. XRD, X-ray diffraction.

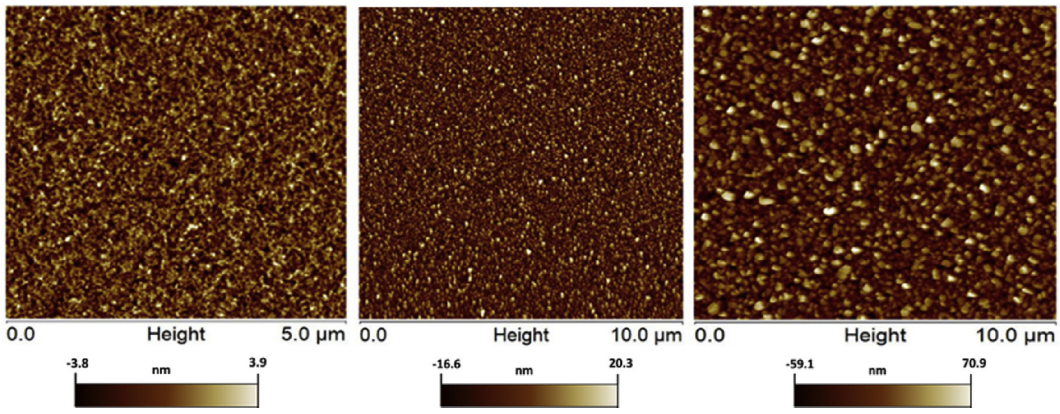


**Fig. 11.** AFM micrographs of $H_2$ plasma–treated vanadium oxide film (roughness: 1.2 nm) (left), a subsequent annealing at 550 °C that yields a roughness of 4 nm (middle), and a roughness of 18 nm is obtained after annealing at 700 °C (right). AFM, atomic force microscopy.

The observed narrower diffraction peak after annealing at 700 °C is noteworthy, and it hints at the formation of larger crystallites.

The assessed morphology by AFM shows a substantial improvement (Fig. 13). Ar plasma–treated samples are smooth with a roughness of 1.89 nm, very close to that of the as-grown films. Annealing at 550 °C induces a slight roughening to 2.5 nm, which greatly contrasts with the measured roughness of 21 nm without plasma treatment. The benefit of the plasma treatment is less significant in terms of roughness when films were treated at 700 °C, although the dewetting is substantially lower. Based on these observations, it can be assumed that argon plasma treatment is efficient at creating oxygen deficiency in the as-grown films, making them less vulnerable to elemental diffusion and the consequent dewetting. The benefit at low crystallization temperature (550 °C) is substantial as smooth crystalline $VO_2$ could be achieved. Relative to the strongly reducing $H_2$ plasma, the argon plasma enables the formation of a single $VO_2$ monoclinic phase.

Although the plasma treatment is performed at room temperature, a significant oxygen deficiency is generated, but there is no enough thermal energy to drive crystallization. Therefore, further thermal annealing at 550 °C is needed to induce the crystallization of the oxygen-deficient film into $VO_2$. In contrast, the hydrogen plasma treatment generates an excessive oxygen deficiency and the

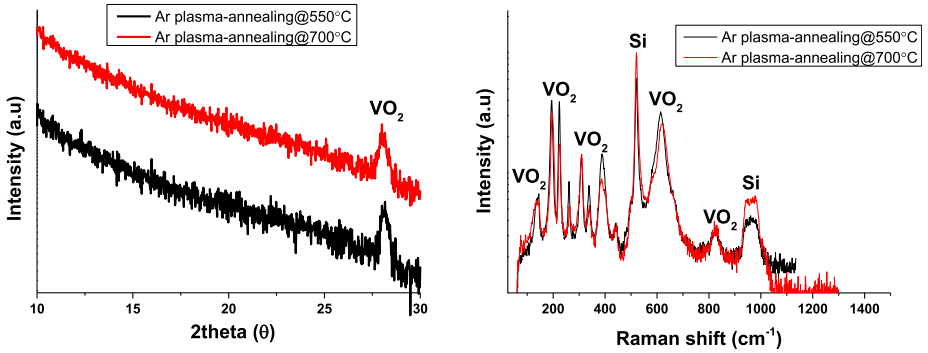


**Fig. 12.** XRD (left) and Raman (right) characterization of vanadium oxide films post-treated in Ar plasma followed by thermal treatment at varied temperatures. XRD, X-ray diffraction.

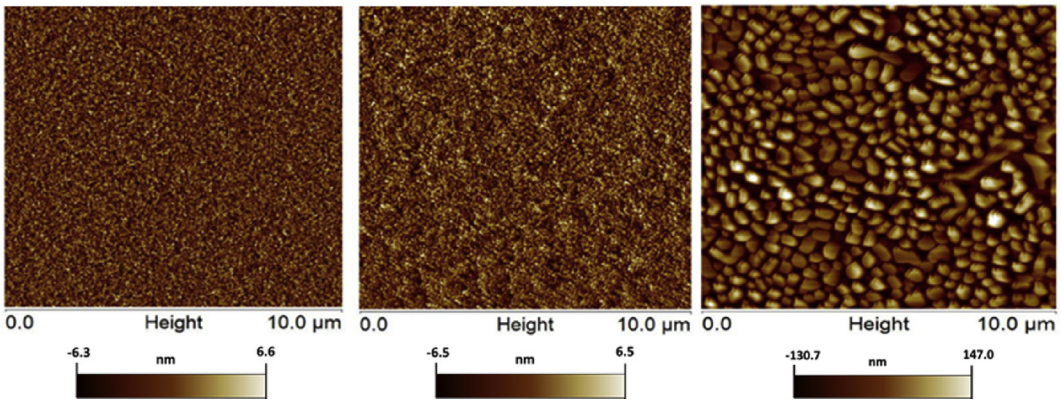


**Fig. 13.** AFM micrographs of Ar plasma–treated ALD-$VO_x$ film on Si substrate, featuring a roughness of 1.89 nm (left), and annealed at 550 °C (roughness of 2.5 nm/middle) or at 700 °C (roughness of 43 nm/right). AFM, atomic force spectroscopy; ALD, atomic layer deposition.

**Table 1**
XRR measured density and roughness values of $VO_x$ film.

| Condition | Density (XRR) ($g/cm^3$) | Roughness (XRR) (nm) | Roughness (AFM) (nm) |
|---|---|---|---|
| As-grown $VO_x$ | 2.7 ± 0.1 | 1.8 ± 0.1 | 1.3 ± 0.1 |
| Direct annealing at 550 °C | 3.4 ± 0.1 | 9.1 ± 0.4 | 21.3 ± 0.1 |
| Ar plasma treatment on as-grown | 2.6 ± 0.1 | 2.4 ± 0.1 | 1.5 ± 0.1 |
| Ar plasma + annealing at 550 °C | 4.1 ± 0.1 | 2.9 ± 0.1 | 1.8 ± 0.1 |

AFM, atomic force microscopy; XRR, X-ray reflectivity.

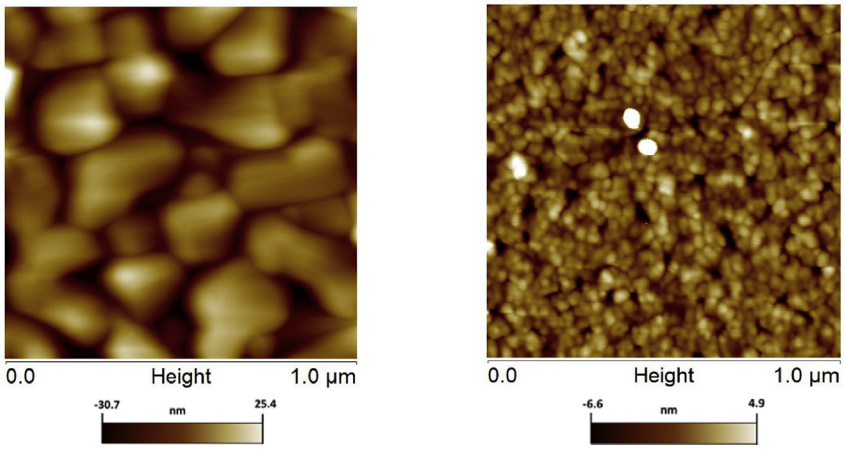


**Fig. 14.** AFM micrographs of 20-nm-thick $VO_2$ films formed after thermal treatment at 550 °C, with (roughness of 1.9 nm/right) and without (roughness of 8 nm/left) prior Ar plasma treatment. AFM, atomic force microscopy.

thermal treatment favors the formation of crystalline Magneli phases instead of $VO_2$.

Based on the XRR data summarized in Table 1, the post-deposition treatment involving Ar plasma has a marginal impact on the surface roughness and film density. Nevertheless, the subsequent thermal annealing enables the conversion of amorphous vanadium oxide into $VO_2$ pure phase with improved density surface morphology. Continuous $VO_2$ films, down to a thickness of 20 nm, could be achieved with the Ar plasma treatment process.

Fig. 14 shows the morphology of a 20-nm-thick film after 4 h of annealing in vacuum at 550 °C with and without a prior Ar plasma treatment. While both films are pure-phase $VO_2$, the suppression of grain growth is evidenced in the plasma-treated sample, which maintains the roughness at the level of the as-grown film after conversion to $VO_2$.

## 4. Conclusion

The ALD of the $VO_2$ starting from the hydrolysis reaction of VTOP was investigated. VTOP shows a clear thermal decomposition above 90 °C, which sets the upper limit for the ALD process. The ALD self-limiting half reactions were demonstrated, enabling a constant growth rate of 0.047 nm/cycle between 60 and 90 °C and a conformal deposition on CNTs with high aspect ratio. The as-grown films are amorphous and vanadium cations exhibit a dominant +5 oxidation state.

Postdeposition thermal treatment of these films yields polycrystalline $VO_2$. Nevertheless, the morphology undergoes a substantial roughening and significant dewetting. Both issues were addressed using argon plasma treatment before thermal treatment. The implementation of hydrogen plasma reduces excessively the

films and forms $V_nO_{2n-1}$ phases. The combination of ALD/Ar plasma treatment/thermal annealing at 550 °C allowed a dense, smooth, and pure-phase $VO_2$.

## Acknowledgments

V.P.P. and N.B. would like to acknowledge funding through the MASSENA Pride program of the Luxembourg National Research Fund (FNR).

## References

[1] John B. Goodenough, Anomalous properties of the vanadium oxides, Annu. Rev. Mater. Sci. 1 (1971) 101–138, https://doi.org/10.1146/annurev.ms.01.080171.000533.
[2] P.Y. Zavalij, M.S. Whittingham, Structural chemistry of vanadium oxides with open frameworks, Acta Crystallogr. Sect. B Struct. Sci. 55 (5) (1999) 627–663, https://doi.org/10.1107/S0108768199004000.
[3] B.M. Weckhuysen, D.E. Keller, Chemistry , spectroscopy and the role of supported vanadium oxides in heterogeneous catalysis 78 (2003) 25–46.
[4] M.S. Whittingham, Y. Song, S. Lutta, P.Y. Zavalij, N.A. Chernova, Some transition metal (oxy)phosphates and vanadium oxides for lithium batteries, J. Mater. Chem. 15 (33) (2005) 3362–3379, https://doi.org/10.1039/b501961c.
[5] T.C. Chang, X. Cao, S.H. Bao, S.D. Ji, H.J. Luo, P. Jin, Review on thermochromic vanadium dioxide based smart coatings: from lab to commercial application, Adv. Manuf. 6 (1) (2018) 1–19, https://doi.org/10.1007/s40436-017-0209-2.
[6] Z. Yang, C. Ko, S. Ramanathan, Oxide electronics utilizing ultrafast metal-insulator transitions, Annu. Rev. Mater. Res. 41 (1) (2011) 337–367, https://doi.org/10.1146/annurev-matsci-062910-100347.
[7] U. Schwingenschlögl, V. Eyert, The vanadium Magnéli phases $V_nO_{2n-1}$, Ann. Phys. 13 (9) (2004) 475–510, https://doi.org/10.1002/andp.200410099.
[8] K. Kosuge, The phase diagram and phase transition of the $V_2O_3$-$V_2O_5$, system, J. Phys. Chem. Solids 28 (8) (1967) 1613–1621, https://doi.org/10.1016/0022-3697(67)90293-4.
[9] B.N. Bahlawane, D. Lenoble, Vanadium Oxide Compounds: Structure, Properties , and Growth from the Gas Phase, 2014, pp. 299–311, https://doi.org/10.1002/cvde.201400057.
[10] M. Brahlek, L. Zhang, J. Lapano, et al., Opportunities in vanadium-based strongly correlated electron systems, MRS Commun 7 (1) (2017) 27–52, https://doi.org/10.1557/mrc.2017.2.
[11] A. Pergament, A. Crunteanu, A. Beaumont, Vanadium Dioxide: Metal-Insulator Transition, Electrical Switching and Oscillations. A Review of State of the Art and Recent Progress, 2015, pp. 9–12.
[12] N. Shukla, A.V. Thathachary, A. Agrawal, et al., A steep-slope transistor based on abrupt electronic phase transition, Nat. Commun. 6 (1) (2015) 7812, https://doi.org/10.1038/ncomms8812.
[13] N. Shukla, A. Parihar, M. Cotter, et al., Pairwise coupled hybrid vanadium dioxide-MOSFET (HVFET) oscillators for non-boolean associative computing, in: 2014 IEEE International Electron Devices Meeting, IEEE, 2014, https://doi.org/10.1109/IEDM.2014.7047129, 28.7.1-28.728.7.4.
[14] A. Beaumont, J. Leroy, J.C. Orlianges, A. Crunteanu, Current-induced electrical self-oscillations across out-of-plane threshold switches based on $VO_2$ layers integrated in crossbars geometry, J. Appl. Phys. 115 (15) (2014), https://doi.org/10.1063/1.4871543.
[15] Q. Gu, A. Falk, J. Wu, L. Ouyang, H. Park, Current-driven phase oscillation and domain-wall propagation in $W_xV_{1-x}O_2$ nanobeams, Nano Lett. 7 (2) (2007) 363–366, https://doi.org/10.1021/nl0624768.
[16] B.-J. Kim, Y.W. Lee, B.-G. Chae, et al., Temperature dependence of the first-order metal-insulator transition in $VO_2$ and programmable critical temperature sensor, Appl. Phys. Lett. 90 (2) (2007), 023515, https://doi.org/10.1063/1.2431456.
[17] Z. Yang, C. Ko, V. Balakrishnan, G. Gopalakrishnan, S. Ramanathan, Dielectric and carrier transport properties of vanadium dioxide thin films across the phase transition utilizing gated capacitor devices, Phys. Rev. B 82 (20) (2010) 205101, https://doi.org/10.1103/PhysRevB.82.205101.
[18] M. Rini, Z. Hao, R.W. Schoenlein, et al., Optical switching in $VO_2$ films by below-gap excitation, Appl. Phys. Lett. 92 (18) (2008), https://doi.org/10.1063/1.2921784.
[19] M.F. Becker, A.B. Buckman, R.M. Walser, T. Lépine, P. Georges, A. Brun, Femtosecond laser excitation of the semiconductor-metal phase transition in $VO_2$, Appl. Phys. Lett. 65 (12) (1994) 1507–1509, https://doi.org/10.1063/1.112974.
[20] M. Seo, J. Kyoung, H. Park, et al., Active terahertz nanoantennas based on $VO_2$ phase transition, Nano Lett. 10 (6) (2010) 2064–2068, https://doi.org/10.1021/nl1002153.
[21] K. Sun, C.A. Riedel, A. Urbani, et al., $VO_2$ Thermochromic metamaterial-based smart optical solar reflector, ACS Photonics 5 (6) (2018) 2280–2286, https://doi.org/10.1021/acsphotonics.8b00119.
[22] M.J. Dicken, K. Aydin, I.M. Pryce, et al., Frequency tunable near-infrared metamaterials based on $VO_2$ phase transition, Opt Express 17 (20) (2009) 18330, https://doi.org/10.1364/OE.17.018330.
[23] M. Nazari, Y. Zhao, V. Hallum, A.A. Bernussi, Z.Y. Fan, M. Holtz, Finite size effect on the phase transition of vanadium dioxide, Appl. Phys. Lett. 103 (4) (2013), https://doi.org/10.1063/1.4816507.
[24] G. Garry, O. Durand, A. Lordereau, Structural, electrical and optical properties of pulsed laser deposited $VO_2$ thin films on R- and C-sapphire planes, Thin Solid Films 453–454 (2004) 427–430, https://doi.org/10.1016/j.tsf.2003.11.118.
[25] H. Koo, S. Yoon, O.-J. Kwon, et al., Effect of lattice misfit on the transition temperature of $VO_2$ thin film, J. Mater. Sci. 47 (17) (2012) 6397–6401, https://doi.org/10.1007/s10853-012-6565-1.
[26] X. Qian, N. Wang, Y. Li, J. Zhang, Z. Xu, Y. Long, Bioinspired multifunctional vanadium dioxide: improved thermochromism and hydrophobicity, Langmuir 30 (35) (2014) 10766–10771, https://doi.org/10.1021/la502787q.
[27] D.P. Partlow, S.R. Gurkovich, K.C. Radford, L.J. Denes, Switchable vanadium oxide films by a sol-gel process, J. Appl. Phys. 70 (1) (1991) 443–452, https://doi.org/10.1063/1.350272.
[28] S.W. Lu, L.S. Hou, F.X. Gan, Structure and optical property changes of sol-gel derived $VO_2$ thin films, Adv Mater 9 (3) (1997) 244–246, https://doi.org/10.1002/adma.19970090313.
[29] H.K. Kim, H. You, R.P. Chiarello, H.L.M. Chang, T.J. Zhang, D.J. Lam, Finite-size effect on the first-order metal-insulator transition in $VO_2$ films grown by metal-organic chemical-vapor deposition, Phys. Rev. B 47 (19) (1993) 12900–12907, https://doi.org/10.1103/PhysRevB.47.12900.
[30] T. Maruyama, Y. Ikuta, Vanadium dioxide thin films prepared by chemical vapour deposition from vanadium(III) acetylacetonate, J. Mater. Sci. 28 (18) (1993) 5073–5078, https://doi.org/10.1007/BF00361182.
[31] S. Kumar, F. Maury, N. Bahlawane, Electrical switching in semiconductor-metal self-assembled $VO_2$ Disordered metamaterial coatings, Sci. Rep. 6 (August) (2016) 1–13, https://doi.org/10.1038/srep37699.
[32] S. Beke, A review of the growth of $V_2O_5$ films from 1885 to 2010, Thin Solid Films 519 (6) (2011) 1761–1771, https://doi.org/10.1016/j.tsf.2010.11.001.
[33] M. Liu, B. Su, Y. Tang, X. Jiang, A. Yu, Recent Advances in Nanostructured Vanadium Oxides and Composites for Energy Conversion, Adv. Energy Mater. (2017) 1–34, https://doi.org/10.1002/aenm.201700885, 1700885.
[34] M. Kamalisarvestani, R. Saidur, S. Mekhilef, F.S. Javadi, Performance , materials and coating technologies of thermochromic thin films on smart windows, Renew. Sustain. Energy Rev. 26 (2013) 353–364, https://doi.org/10.1016/j.rser.2013.05.038.
[35] S.M. George, Atomic layer deposition: an overview, Chem. Rev. 110 (1) (2009) 111–131, https://doi.org/10.1021/cr900056b.
[36] C. Marichy, N. Pinna, Carbon-nanostructures coated/decorated by atomic layer deposition: growth and applications, Coord. Chem. Rev. 257 (23–24) (2013) 3232–3253, https://doi.org/10.1016/j.ccr.2013.08.007.
[37] R.W. Johnson, A. Hultqvist, S.F. Bent, A brief review of atomic layer deposition: from fundamentals to applications, Mater. Today 17 (5) (2014) 236–246, https://doi.org/10.1016/j.mattod.2014.04.026.
[38] M.S. Weimer, I.S. Kim, P. Guo, R.D. Schaller, A.B.F. Martinson, A.S. Hock, Oxidation state discrimination in the atomic layer deposition of vanadium oxides, Chem. Mater. 29 (15) (2017) 6238–6244, https://doi.org/10.1021/acs.chemmater.7b01130.
[39] M. Schaekers, K. Martens, Q. Xie, et al., Semiconductor-metal transition in thin $VO_2$ films grown by ozone based atomic layer deposition, Appl. Phys. Lett. 98 (16) (2011) 162902, https://doi.org/10.1063/1.3579195.
[40] P.A. Premkumar, M. Toeller, I.P. Radu, et al., Process study and characterization of $VO_2$ thin films synthesized by ALD using TEMAV and $O_3$ precursors, ECS J Solid State Sci Technol 1 (4) (2012) P169–P174, https://doi.org/10.1149/2.009204jss.
[41] X. Lv, Y. Cao, L. Yan, Y. Li, L. Song, Atomic layer deposition of $VO_2$ films with Tetrakis-dimethyl-amino vanadium (IV) as vanadium precursor, Appl. Surf. Sci. 396 (2017) 214–220, https://doi.org/10.1016/j.apsusc.2016.10.044.
[42] X. Wang, Z. Guo, Z. Guo, J. Wang, Atomic layer deposition of vanadium oxide thin films from tetrakis(dimethylamino)vanadium precursor, J. Mater. Res. 32 (1) (2017) 37–44, https://doi.org/10.1557/jmr.2016.303.
[43] J.C. Badot, S. Ribes, E.B. Yousfi, et al., Atomic layer epitaxy of vanadium oxide thin films and electrochemical behavior in presence of lithium ions, Electrochem. Solid State Lett. 3 (10) (2000) 485–488, https://doi.org/10.1149/1.1391187.
[44] J. Musschoot, D. Deduytsche, H. Poelman, et al., Comparison of thermal and plasma-enhanced ALD/CVD of vanadium pentoxide, J. Electrochem. Soc. 156 (7) (2009) P122, https://doi.org/10.1149/1.3133169.
[45] X. Chen, E. Pomerantseva, K. Gregorczyk, R. Ghodssi, G. Rubloff, Cathodic ALD $V_2O_5$ thin films for high-rate electrochemical energy storage, RSC Adv. 3 (13) (2013) 4294, https://doi.org/10.1039/c3ra23031g.
[46] M. Xie, X. Sun, H. Sun, et al., Stabilizing an amorphous $V_2O_5$/carbon nanotube paper electrode with conformal $TiO_2$ coating by atomic layer deposition for lithium ion batteries, J. Mater. Chem. 4 (2) (2016) 537–544, https://doi.org/10.1039/C5TA01949D.
[47] S. Fleischmann, N. Jäckel, M. Zeiger, et al., Enhanced electrochemical energy storage by nanoscopic decoration of endohedral and exohedral carbon with vanadium oxide via atomic layer deposition, Chem. Mater. 28 (8) (2016) 2802–2813, https://doi.org/10.1021/acs.chemmater.6b00738.
[48] X. Chen, E. Pomerantseva, P. Banerjee, K. Gregorczyk, R. Ghodssi, G. Rubloff, Ozone-Based atomic layer deposition of crystalline $V_2O_5$ films for high

performance electrochemical energy storage, Chem. Mater. 24 (7) (2012) 1255–1261, https://doi.org/10.1021/cm202901z.
[49] S. Fleischmann, D. Leistenschneider, V. Lemkova, et al., Tailored mesoporous carbon/vanadium pentoxide hybrid electrodes for high power pseudocapacitive lithium and sodium intercalation, Chem. Mater. 29 (20) (2017) 8653–8662, https://doi.org/10.1021/acs.chemmater.7b02533.
[50] G.Y. Song, C. Oh, S. Sinha, J. Son, J. Heo, Facile phase control of multivalent vanadium oxide thin films ($V_2O_5$ and $VO_2$) by atomic layer deposition and postdeposition annealing, ACS Appl. Mater. Interfaces 9 (28) (2017) 23909–23917, https://doi.org/10.1021/acsami.7b03398.
[51] C.Y. Kim, S.H. Kim, S.J. Kim, K.S. An, $VO_2$ (110) film formation on $TiO_2$ (110) through post-reduction of ALD grown vanadium oxide, Appl. Surf. Sci. 313 (2014) 368–371, https://doi.org/10.1016/j.apsusc.2014.05.216.
[52] M.N. Colpaert, P. Clauws, L. Flermans, J. Vennik, Thermal and low energy electron bombardment induced oxygen loss of $V_2O_5$ single crystals: Transition into $V_6O_{13}$, Surface Science 36 (1973) 513–525.
[53] S. Guimond, J.M. Sturm, D. Göbke, et al., Well-ordered $V_2O_5$ (001) thin films on Au (111): growth and thermal stability, J. Phys. Chem. C 112 (001) (2008) 11835–11846.
[54] D.S. Su, R. Schlögl, Thermal decomposition of divanadium pentoxide $V_2O_5$: towards a nanocrystalline $V_2O_3$ phase, Catal. Lett. 83 (3–4) (2002) 115–119, https://doi.org/10.1023/A:1021042232178.
[55] D.Q. Liu, W.W. Zheng, H.F. Cheng, H.T. Liu, Thermochromic $VO_2$ thin film prepared by post annealing treatment of $V_2O_5$ thin film, Adv. Mater. Res. 79–82 (2009) 747–750, https://doi.org/10.4028/www.scientific.net/AMR.79-82.747.
[56] M. Ibisate, D. Golmayo, C. López, Vanadium dioxide thermochromic opals grown by chemical vapour deposition, J. Opt. A Pure Appl. Opt. 10 (12) (2008), https://doi.org/10.1088/1464-4258/10/12/125202.
[57] Y.F. Wu, L.L. Fan, S.M. Chen, S. Chen, C.W. Zou, Z.Y. Wu, Spectroscopic analysis of phase constitution of high quality $VO_2$ thin film prepared by facile sol-gel method, AIP Adv. 3 (4) (2013) 0–10, https://doi.org/10.1063/1.4802981.
[58] B.-G. Chae, H.-T. Kim, S.-J. Yun, et al., Highly oriented $VO_2$ thin films prepared by sol-gel deposition, Electrochem. Solid State Lett. 9 (1) (2006) C12, https://doi.org/10.1149/1.2135430.
[59] S.A. Corr, M. Grossman, J.D. Furman, et al., Controlled reduction of vanadium oxide nanoscrolls: crystal structure, morphology, and electrical properties, Chem. Mater. 20 (20) (2008) 6396–6404, https://doi.org/10.1021/cm801539f.
[60] O. Monfort, T. Roch, L. Satrapinskyy, et al., Reduction of $V_2O_5$ thin films deposited by aqueous sol-gel method to $VO_2$ (B) and investigation of its photocatalytic activity, Appl. Surf. Sci. 322 (2014) 21–27, https://doi.org/10.1016/j.apsusc.2014.10.009.
[61] Q. Shi, W. Huang, J. Yan, et al., Preparation and phase transition characterization of $VO_2$ thin film on single crystal Si (100) substrate by sol-gel process, J. Sol. Gel Sci. Technol. 59 (3) (2011) 591–597, https://doi.org/10.1007/s10971-011-2533-5.
[62] H.H. Park, T.J. Larrabee, L.B. Ruppalt, J.C. Culbertson, S.M. Prokes, Tunable electrical properties of vanadium oxide by hydrogen-plasma-treated atomic layer deposition, ACS Omega 2 (4) (2017) 1259–1264, https://doi.org/10.1021/acsomega.7b00059.
[63] V.S. Aliev, V.N. Votentsev, A.K. Gutakovskii, S.M. Maroshina, D.V. Shcheglov, Morphological transformations of vanadium oxide films during low-temperature reduction in hydrogen electron cyclotron resonance plasma, J. Surf. Investig. X-ray Synchrotron Neutron Tech. 1 (4) (2007) 454–461, https://doi.org/10.1134/S1027451007040167.
[64] A.L. Pergament, A.A. Velichko, O.Y. Berezina, E.L. Kazakova, N.A. Kuldin, D.V. Artyukhin, Influence of doping on the properties of N A Kuldin and D V Artyukhin, 422204, 2008, pp. 1–5, https://doi.org/10.1088/0953-8984/20/42/422204.
[65] G. Rampelberg, D. Deduytsche, B. De Schutter, et al., Crystallization and semiconductor-metal switching behavior of thin $VO_2$ layers grown by atomic layer deposition, Thin Solid Films 550 (2014) 59–64, https://doi.org/10.1016/j.tsf.2013.10.039.
[66] S. Lysenko, V. Vikhnin, A. Rua, F. Fernandez, H. Liu, Size-dependent phase transition of $VO_2$ nanostructures induced by light excitation, Phys. Proc. 13 (2011) 18–23, https://doi.org/10.1016/j.phpro.2011.02.005.
[67] J. Narayan, V.M. Bhosle, Phase transition and critical issues in structure-property correlations of vanadium oxide, J. Appl. Phys. 100 (10) (2006) 103524, https://doi.org/10.1063/1.2384798.
[68] H. Oechsner, Theoretical background and some applications of ECWR-plasmas, Vacuum 83 (4) (2008) 727–731, https://doi.org/10.1016/j.vacuum.2008.05.018.
[69] M. Weiler, K. Lang, E. Li, J. Robertson, Deposition of tetrahedral hydrogenated amorphous carbon using a novel electron cyclotron wave resonance reactor, Appl. Phys. Lett. 72 (11) (1998) 1314–1316, https://doi.org/10.1063/1.121069.
[70] S. Kumar, D. Lenoble, F. Maury, N. Bahlawane, Synthesis of vanadium oxide films with controlled morphologies: impact on the metal-insulator transition behaviour, Phys. Status Solid Appl. Mater. Sci. 212 (7) (2015) 1582–1587, https://doi.org/10.1002/pssa.201532325.
[71] S. Mathur, T. Ruegamer, I. Grobelsek, Phase-selective CVD of vanadium oxide nanostructures, Chem. Vap. Depos. 13 (1) (2007) 42–47, https://doi.org/10.1002/cvde.200606578.
[72] E. Ostreng, O. Nilsen, H. Fjellvag, Optical properties of vanadium pentoxide deposited by ALD, J. Phys. Chem. 116 (2012) 19444–19450, https://doi.org/10.1021/jp304521k.
[73] M.B. Sreedhara, J. Ghatak, B. Bharath, C.N.R. Rao, Atomic layer deposition of ultrathin crystalline epitaxial films of $V_2O_5$, ACS Appl. Mater. Interfaces 9 (3) (2017) 3178–3185, https://doi.org/10.1021/acsami.6b14882.
[74] Pamela R. Fischer, Dieter Pierreux, Olivier Rouault, Jacky Sirugue, Peter M. Zagwijn, Eva Tois, Suvi Haukka, Batch Atomic Layer Deposition of HfO2 and ZrO2 Films Using Cyclopentadienyl Precursors, ECSTrans. 16 (4) (2008) 135–148.
[75] R.J. Potter, P.R. Chalker, T.D. Manning, et al., Deposition of $HfO_2$, $Gd_2O_3$ and $PrO_x$ by liquid injection ALD techniques, Chem. Vap. Depos. 11 (3) (2005) 159–169, https://doi.org/10.1002/cvde.200406348.
[76] J.W. Elam, Coatings on high aspect ratio structures, in: Atomic Layer Deposition of Nanostructured Materials, Wiley-VCH Verlag GmbH & Co. KGaA, Weinheim, Germany, 2012, pp. 227–249, https://doi.org/10.1002/9783527639915.ch10.
[77] R.G. Gordon, D. Hausmann, E. Kim, J. Shepard, A Kinetic Model for Step Coverage by Atomic Layer Deposition in Narrow Holes or Trenches, 2003. https://faculty.chemistry.harvard.edu/files/gordon/files/model.pdf. (Accessed 24 October 2018).
[78] C. Guerra-Nuñez, M. Döbeli, J. Michler, I. Utke, Reaction and growth mechanisms in $Al_2O_3$ deposited via atomic layer deposition: elucidating the hydrogen source, Chem. Mater. 29 (20) (2017) 8690–8703, https://doi.org/10.1021/acs.chemmater.7b02759.
[79] R.L. Puurunen, Surface chemistry of atomic layer deposition: a case study for the trimethylaluminum/water process, J. Appl. Phys. 97 (12) (2005), https://doi.org/10.1063/1.1940727.
[80] Marika Juppo, Antti Rahtu, Mikko Ritala, Markku Leskelä, In situ mass spectrometry study on surface reactions in atomic layer deposition of $Al_2O_3$ thin films from trimethylaluminum and water, Langmuir 16 (8) (2000) 4034–4039, https://doi.org/10.1021/la991183.
[81] H.J. Basheer, C. Pachot, U. Lafont, X. Devaux, N. Bahlawane, Low-temperature thermal CVD of superblack carbon nanotube coatings, Adv Mater Interfaces 4 (18) (2017) 1700238, https://doi.org/10.1002/admi.201700238.
[82] F. Ureña-Begara, A. Crunteanu, J.P. Raskin, Raman and XPS characterization of vanadium oxide thin films with temperature, Appl. Surf. Sci. 403 (2017) 717–727, https://doi.org/10.1016/j.apsusc.2017.01.160.
[83] P. Boryło, K. Matus, K. Lukaszkowicz, et al., The influence of atomic layer deposition process temperature on ZnO thin film structure, Appl Surf Sci (March 2018), https://doi.org/10.1016/j.apsusc.2018.03.169.
[84] F. Mattelaer, K. Geryl, G. Rampelberg, J. Dendooven, C. Detavernier, Amorphous and crystalline vanadium oxides as high-energy and high-power Cathodes for three-dimensional thin-film lithium ion batteries, ACS Appl. Mater. Interfaces 9 (15) (2017) 13121–13131, https://doi.org/10.1021/acsami.6b16473.
[85] F. Mattelaer, K. Geryl, G. Rampelberg, T. Dobbelaere, J. Dendooven, C. Detavernier, Atomic layer deposition of vanadium oxides for thin-film lithium-ion battery applications, RSC Adv. 6 (115) (2016) 114658–114665, https://doi.org/10.1039/C6RA25742A.
[86] R. Dziembaj, Oxygen equilibrium pressure above $V_2O_{5-x}$ and thermodynamic properties of this oxide system, J. Solid State Chem. 26 (2) (1978) 159–165, https://doi.org/10.1016/0022-4596(78)90146-9.
[87] J. Haber, M. Witko, R. Tokarz, Vanadium pentoxide I. Structures and properties, Appl. Catal. Gen. 157 (1–2) (1997) 3–22, https://doi.org/10.1016/S0926-860X(97)00017-3.
[88] C. Marini, E. Arcangeletti, D. Di Castro, et al., Optical properties of $V_{1-x}Cr_xO_2$ compounds under high pressure, Phys. Rev. B 77 (23) (2008) 235111, https://doi.org/10.1103/PhysRevB.77.235111.
[89] M.M. Koranne, J.G. Goodwin, G. Marcelin, Characterization of silica- and alumina-supported vanadia catalysts using temperature programmed reduction, J. Catal. 148 (1) (1994) 369–377, https://doi.org/10.1006/jcat.1994.1217.
[90] Y. Liu, C. Jiang, W. Chu, W. Sun, Z. Xie, Novel F-$V_2O_5$/$SiO_2$ catalysts for oxidative dehydrogenation of propane, React. Kinet. Mech. Catal. 101 (1) (2010) 141–151, https://doi.org/10.1007/s11144-010-0207-x.
[91] F.J. Morin, Oxides which show a metal-to-insulator transition at the neel temperature, Phys. Rev. Lett. 3 (1) (1959) 34–36, https://doi.org/10.1103/PhysRevLett.3.34.
[92] Y. Gao, S. Wang, H. Luo, et al., Enhanced chemical stability of $VO_2$ nanoparticles by the formation of $SiO_2$/$VO_2$ core/shell structures and the application to transparent and flexible $VO_2$-based composite foils with excellent thermochromic properties for solar heat control, Energy Environ. Sci. 5 (3) (2012) 6104–6110, https://doi.org/10.1039/c2ee02803d.
[93] Y. Ji, Thermochromic $VO_2$ -Based Materials for Smart Windows, 2018.
[94] M. Currie, M.A. Mastro, V.D. Wheeler, Characterizing the tunable refractive index of vanadium dioxide, Opt. Mater. Express 7 (5) (2017) 1697, https://doi.org/10.1364/OME.7.001697.
[95] M. Taha, S. Walia, T. Ahmed, et al., Insulator-metal transition in substrate-independent $VO_2$ thin film for phase-change devices, Sci. Rep. 7 (1) (2017) 1–10, https://doi.org/10.1038/s41598-017-17937-3.
[96] J.Y. Suh, R. Lopez, L.C. Feldman, R.F. Haglund, Semiconductor to metal phase transition in the nucleation and growth of $VO_2$ nanoparticles and thin films Micro-optical switch device based on semiconductor-to-metallic phase transition characteristics of W-doped $VO_2$ smart coatings, Cit J Appl Phys 96 (2004) 971, https://doi.org/10.1063/1.1762995.

[97] L. Kang, Y. Gao, Z. Zhang, et al., Effects of annealing parameters on optical properties of thermochromic $VO_2$ films prepared in aqueous solution, J. Phys. Chem. C 114 (4) (2010) 1901–1911, https://doi.org/10.1021/jp909009w.
[98] C. Zhang, W. Cao, A.V. Adedeji, H.E. Elsayed-Ali, Preparation and properties of $VO_2$ thin films by a novel sol–gel process, J. Sol. Gel Sci. Technol. 69 (2) (2014) 320–324, https://doi.org/10.1007/s10971-013-3220-5.
[99] D. Kim, A.L. Giermann, C.V. Thompson, Solid-state dewetting of patterned thin films, Appl. Phys. Lett. 95 (25) (2009) 1–36, https://doi.org/10.1063/1.3268477.
[100] Youn-Bae Kang, Critical evaluation and thermodynamic optimization of the VO-$VO_{2.5}$ system, J. Eur. Ceram. Soc. 32 (2012) 3187–3198. https://doi.org/10.1007/s11663-014-0193-x.

### 3.1.3 MWCNT-$VO_2$ for the solar thermal application.

Execution of carbon nanotubes (CNTs) and vanadium dioxide ($VO_2$) as constituents to design smart absorbing coatings was investigated. CNTs attribute a near-perfect blackbody absorption. However, their sole introduction is insufficient to harvest solar energy because CNTs are also excellent thermal emitters. Whereas, $VO_2$ promote sudden change in its optoelectronic properties across its semiconductor-to-metal transition that occurs at 67 °C. As a matter of fact, metals are typically good infrared (IR) reflectors, and semiconductors are mostly infratred transparent.

MWCNTs grown by single pot CVD process are conformally coated with nanocrystalline $V_2O_5$ through optimized ALD process. Post-deposition annealing was used to convert the oxide layer into the $VO_2$ phase. The morphology of the obtained $VO_2$ layer correlates with the thickness of the as-grown $V_2O_5$. Discontinuous $VO_2$ nanoparticle structure results from thin $V_2O_5$ while thick $V_2O_5$ layer resulted in a full-covering $VO_2$ shell. Optical modulation across the semiconductor-metal transition is influenced by the morphology of the $VO_2$ phase. $VO_2$ nanoparticles on the MWCNT structure illustrates an enhancement in the thermal emissivity across the SMT temperature. A contrasting optical modulation is displayed by the continuous $VO_2$ layer on MWCNT.

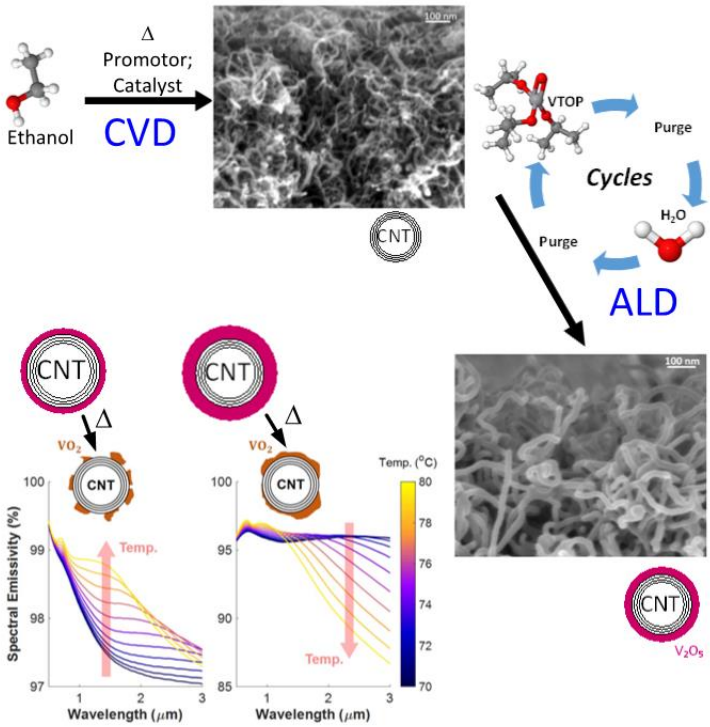

ACS APPLIED NANO MATERIALS

www.acsanm.org

Article

# Thermoresponsive Black $VO_2$–Carbon Nanotube Composite Coatings for Solar Energy Harvesting

Vasu Prasad Prasadam, Francisco V. Ramirez, Ioannis Papakonstantinou, Ivan P. Parkin, and Naoufal Bahlawane*

Cite This: *ACS Appl. Nano Mater.* 2020, 3, 8848–8857

Read Online

ACCESS | Metrics & More | Article Recommendations | Supporting Information

**ABSTRACT:** Solar energy harvesting is an essential component for a clean and sustainable future energy supply. Hereby, solar–thermal energy conversion is of a significant importance, and the role of absorbing layers is pivotal. Nanoscale design of thermally responsive absorbing nanocomposite coatings is addressed in this study with the objective to tailor the light absorption behavior. While carbon nanotubes (CNTs) act as perfect black absorbers, vanadium dioxide ($VO_2$) shows a semiconductor-to-metal transition (SMT) at 67 °C with an abrupt change in the optical properties. Combining the properties of these two nanometric building blocks is investigated as an approach to design smart black nanocomposite films. The CNTs feature either an upward or a downward thermal emissivity switching across the SMT depending on the morphology of the overgrown $VO_2$ nanolayer. Decorated CNTs with $VO_2$ nanoparticles feature an enhancement of the thermal emissivity above the SMT, whereas $VO_2$-covered CNTs feature a decrease of thermal emissivity when they turn metallic above the SMT. The results were successfully explained by a theoretical model based on effective media approximations. By means of this model, the percolation threshold for the $VO_2$ inclusions was identified. $VO_2$ inclusions below this threshold are mostly confined in small domains, and near/mid-infrared light absorption dominates in the metallic phase as a consequence of the localized surface plasmons' excitation. Above the percolation threshold, $VO_2$ inclusions form large continuous domains that are more reflective in the metallic phase. The percolation threshold is the result of surface-energy-driven dewetting that can be influenced by the implemented thermal treatment. The developed $VO_2$–CNT nanocomposite films hold appealing properties for the design of smart absorbers for solar energy harvesting and thermal management as well as photothermal actuators.

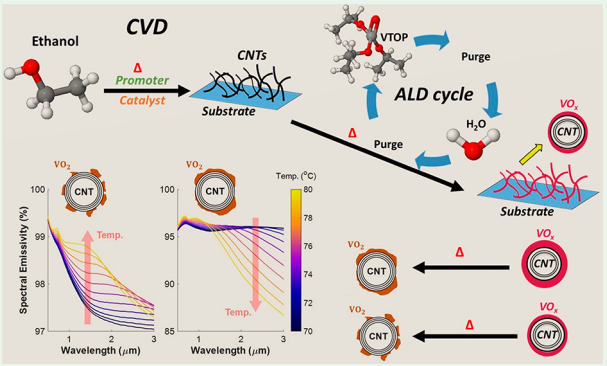


**KEYWORDS:** *solar absorbers, thermal radiation, smart absorber, smart radiators, nanocomposite coatings, CNT, SMT, vanadium oxide, CVD, ALD*



## INTRODUCTION

The continuous growth of the global electricity demand implies a consequent rise of energy production, leading to a record $CO_2$ emission increase of +1.7%/annum in 2018.[1] The sun, which is the most abundant clean source for energy, can be harnessed through a direct conversion to electricity (photovoltaics) or through thermal energy. The approach of adjusting or modulating solar energy gave rise to valuable applications such as solar selective absorber in thermoelectric devices,[2] solar–thermal radiator for cooling devices,[3] and smart coatings for energy efficient windows.[4] Generally, these nanocomposite coatings incorporate materials with contrasting optical properties to engineer the targeted functionality.

The implementation of carbon nanotubes (CNTs) and vanadium dioxide ($VO_2$) as building blocks to design smart absorbing coatings sounds appealing in this context. CNTs feature a near-perfect blackbody absorption;[5] nevertheless, their sole implementation is not sufficient to harvest solar energy, as CNTs are also great thermal emitters. On the other hand, $VO_2$ features an abrupt change in its optoelectronic properties across its semiconductor-to-metal transition, which takes place at 67 °C.[6,7] In fact, metals are typical good infrared (IR) reflectors, and semiconductor are mostly NIR transparent.

A simulation study reported by Voti et al. reveals that stacks involving $VO_2$ and metallic layers can be engineered to optimize an up- and downward thermal emissivity (E) depending on their architectures.[8] The expected downward emissivity modulation, i.e., $(E_{hot} - E_{cold}) < 0$, is reported by using $VO_2$ film with a thickness exceeding 100 nm on different IR-transmitting

**Received:** June 14, 2020
**Accepted:** August 25, 2020
**Published:** August 25, 2020

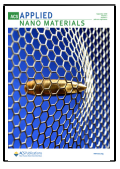







https://dx.doi.org/10.1021/acsanm.0c01630
*ACS Appl. Nano Mater.* 2020, 3, 8848–8857

**Scheme 1. Illustration of the Hybrid CVD/ALD Experimental Setup for the Growth of the CNT-Based Nanocomposite**[a]

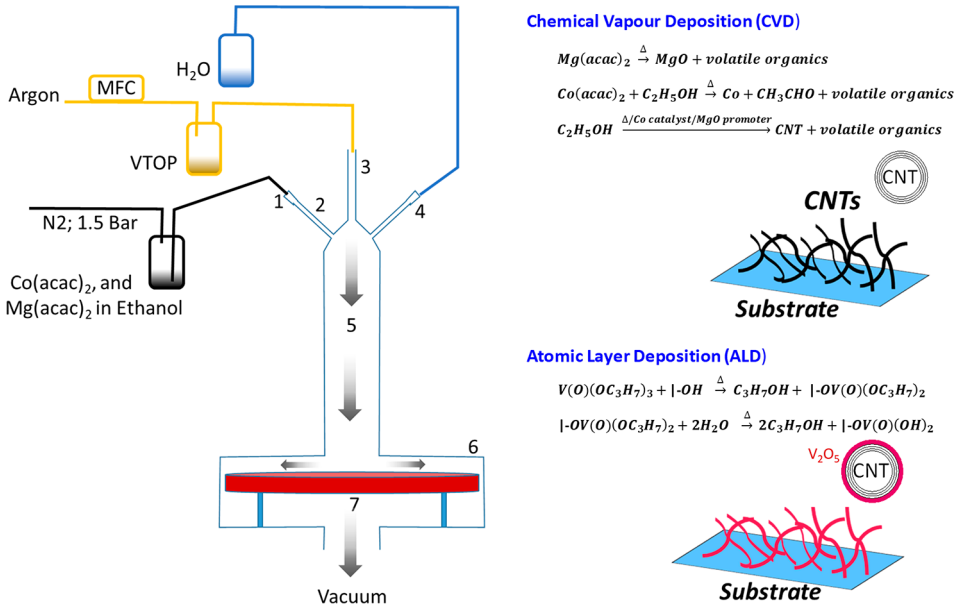


[a]The right-hand side presents the involved two steps: the corresponding chemical reactions and the materials structure. (left) 1: pulsed spray injector (opening time 4 ms; frequency 4 Hz; rate 1 mL/min); 2: evaporation tube (at 200 °C); 3: VTOP gas vapor inlet; 4: $H_2O$ gas vapor inlet; 5: transport tube (at 200 °C); 6: vacuum deposition chamber; 7: hot substrate holder.

substrates like Si,[9] quartz,[10] graphene,[11] TiN,[12] and $Al_2O_3$.[13] An upward emissivity modulation, i.e., $(E_{hot} - E_{cold}) > 0$, was however reported by using IR-reflecting substrates.[14] Incorporating an intermediate dielectric layer in the last case amplifies the emissivity modulation response.[15,16] Surfaces featuring textures with high aspect ratios are particularly appealing as the amplitude of the optical modulation is expected to be more prominent.[17,18] Based on the emissivity modulation down- or upward, the resulting composites might be used in different applications like smart windows[19] and smart radiators[20] for terrestrial and space application, respectively.

Vanadium dioxide−carbon composites have potential application in various fields as electrode materials for energy storage,[21,7] gas sensors,[22] infrared detectors,[23] thermal camouflage,[11] and photothermal actuators.[24−27] In the above-mentioned literature, $VO_2$ is grown on carbon films by chemical sol−gel and physical vapor deposition. To grow conformal $VO_2$ layers on the high aspect ratio structures, atomic layer deposition (ALD) is the most reported process.[7]

In this study, a strongly correlated material ($VO_2$) is applied on highly textured black absorber coating, CNTs, to investigate the optical modulation behavior based on fundamentally contrasting classical and plasmonic optical response. The chemical vapor deposition (CVD) process is used for the growth of CNT layers, whereas the atomic layer deposition process (ALD) was used to grow conformal $VO_2$ layers around the individual CNTs of the film.

## EXPERIMENTAL METHODS

The deposition of carbon nanotubes on silicon substrates was performed by using the thermal CVD process. Hereby an ethanol solution of $0.65 \times 10^{-3}$ mol $L^{-1}$ of cobalt acetylacetonate ($Co(acac)_2$) and $0.65 \times 10^{-3}$ mol $L^{-1}$ of magnesium acetylacetonate ($Mg(acac)_2$) was implemented as a single precursor feedstock. The formation of CNTs is obtained at 485 °C and a pressure of 10 mbar with ethanol vapor as the carbon source in the presence of a cobalt catalyst and MgO growth promoter; both form in situ during deposition. The CVD of CNT is illustrated in Scheme 1. The layer is composed of randomly oriented CNTs featuring an adjustable density.[28] The implemented CNT films in this study have an average thickness of 3 $\mu$m and a density of 0.8−1 mg/$cm^3$, whereas the outer diameter of the CNT is around 10 nm. It is worth mentioning that the obtained film density is 3 orders of magnitude lower relative to densely packed CNTs. Further details regarding the process are reported earlier.[29]

Vanadium oxide films are deposited on CNTs by using thermal ALD via the sequential hydrolysis with deionized water of vanadium(V) triisopropoxide (VTOP) at 80 °C and a pressure of 0.4 mbar. All depositions were performed by using ALD cycles composed of (a) 8 s exposure to VTOP, (b) 15 s of argon purge gas with a flow rate of 50 sccm, (c) 6 s exposure to water vapor, and (d) 15 s argon purge. The as-grown films were identified as amorphous or poorly crystalline $V_2O_5$. Details of the ALD optimization on planar Si substrates were reported earlier.[30] The ALD consecutive reactions are displayed in Scheme 1.

Postdeposition annealing was performed in a vacuum ($10^{-2}$ mbar) at 500 °C for 4 h to convert the as-grown film to crystalline $VO_2$−CNTs. The thickness of $VO_x$ on silicon was assessed by using a multi-wavelength ellipsometer (Film Sense) with the Cauchy model, whereas X-ray diffraction (Bruker D8), with Cu K$\alpha$ as the X-ray source, was used to identify the crystalline phases of vanadium oxide. Data were collected in the grazing incidence mode at 0.5° and a detector scanning from 20° to 60° with a step size of 0.02°.

All XRD reflexes of $VO_2$, except the (011) plane at 27.83°, can be attributed to overlapping planes, which complicates the implementation of the Williamson−Hall method to assess the strain and crystallite size values. Hence, the single peak analysis method was used. The broadening of the XRD peak is a combined contribution from the instrumental broadening, strain in the lattice, and the size of the crystallites. Thereby we defined 0.173 as the instrumental broadening measured using a single crystal silicon wafer. We fit the $VO_2$(011) peak to the pseudo-Voigt function, which is a linear combination of Lorentzian and Gaussian functions. The peak deconvolution provides the broadening resulting from the size effect (Lorentz component with $\beta_L$) and that resulting from the strain effect (Gauss component with $\beta_G$). Both are the corrected full width at half-maximum (FWHM) of both components from the instrumental broadening as follows: $FWHM_L = \beta_L + \beta_I$ and $(FWHM_G)^2 = (\beta_G)^2 + (\beta_I)^2$.



https://dx.doi.org/10.1021/acsanm.0c01630
ACS Appl. Nano Mater. 2020, 3, 8848−8857

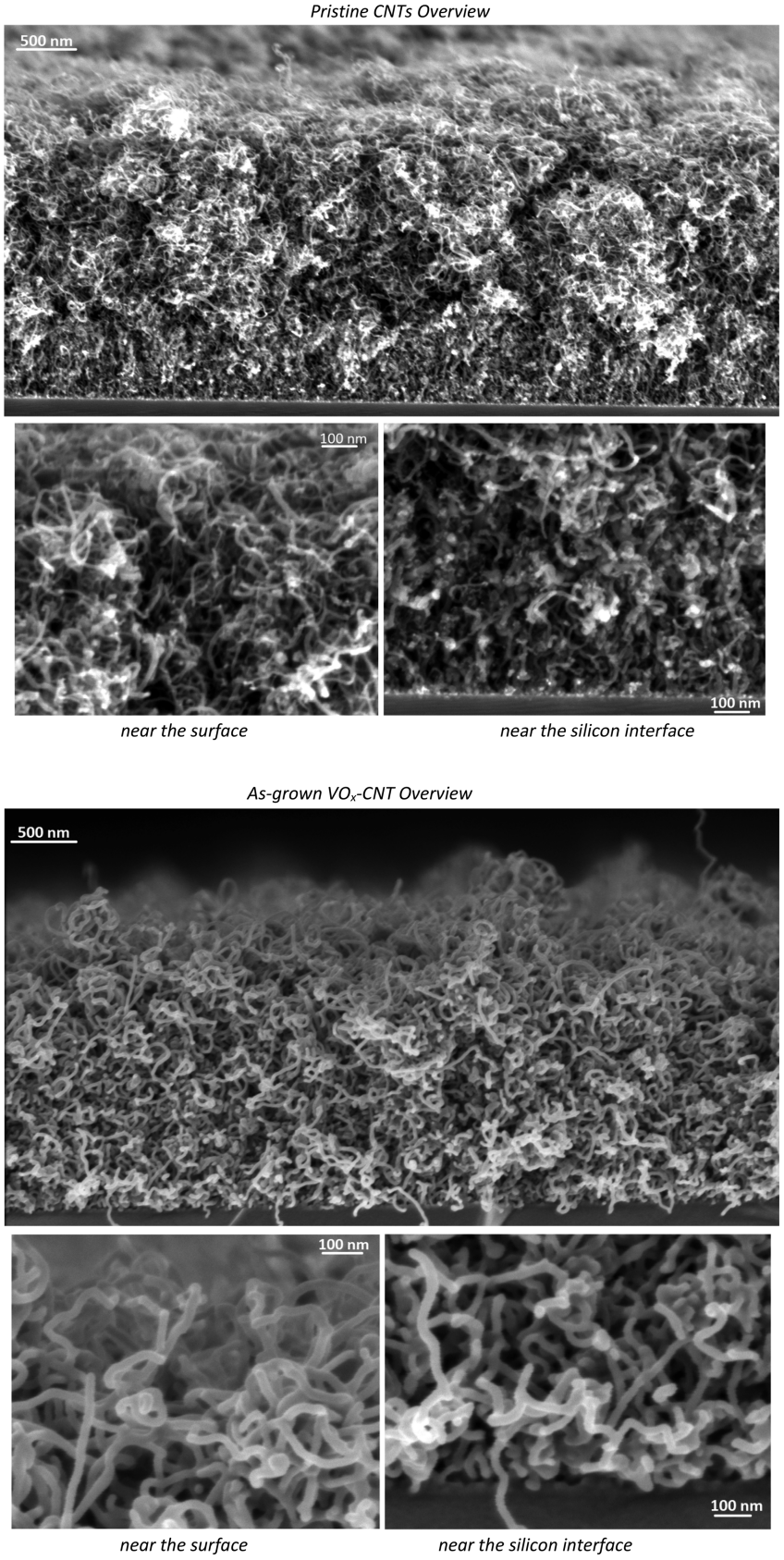


**Figure 1.** SEM cross-section inspection of pristine CNTs with a thickness of 3 $\mu$m ($\varphi_{CNT}$ = 10 nm) with high-magnification view in the near surface and interface regions (top). A similar observation is displayed for ALD-coated CNTs with 327 cycles of $VO_x$ showing an apparent CNT diameter increase to reach ~25 nm both near the surface and the silicon interface (bottom).



https://dx.doi.org/10.1021/acsanm.0c01630
ACS Appl. Nano Mater. 2020, 3, 8848−8857

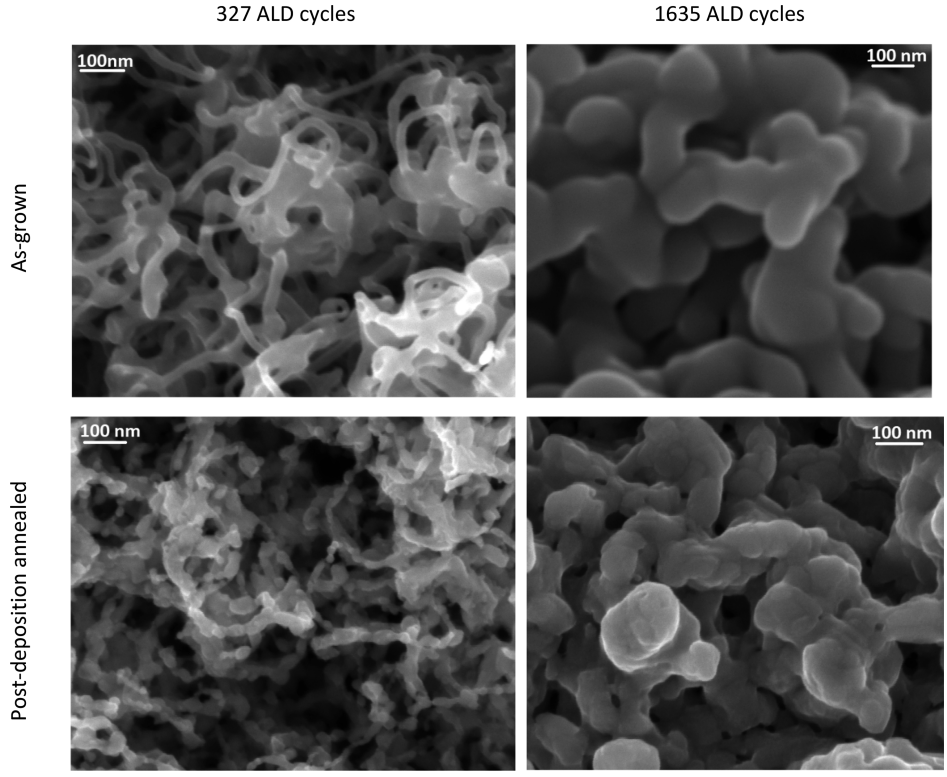


**Figure 2.** SEM surface inspection of the ALD grown $VO_x$ on CNT: 327 cycles ($VO_2$ decorated) (left), 1635 cycles ($VO_2$ covered) (right), before (top) and after (bottom) conversion to $VO_2$.

The crystallite size, $d$, and the strain, $\varepsilon$, are computed via the following equations:

$$d = \frac{K\lambda}{\beta_L \cos\theta}; \quad \varepsilon = \frac{\beta_G}{4\tan\theta} \tag{1}$$

We assume $k = 0.94$ and $\lambda = 0.154$ nm (Cu K$\alpha$).

Raman scattering was performed by using an InVia Raman spectrometer from Renishaw with a 633 nm laser and a power density of 87 $\mu W/cm^2$. The morphology of the films was inspected by using the FEI Helios Nanolab 650 scanning electron microscope (SEM) at a working distance of 5 mm and by using 2−5 V as the acceleration voltage.

The surface emissivity was measured by a FLIR X6580SC thermal camera operating in the 3−5 $\mu$m spectral range. The pristine CNTs coating was taken as a reference perfect black in these measurements. The emissivity measurement was performed along three consecutive heating and cooling cycles between 30 and 85 °C by using a ramping rate of 2 °C/min. The optical measurements were performed in a reflection configuration with a LAMBDA 1050 UV−vis−NIR spectrophotometer from PerkinElmer with a 100 mm Spectralon integration sphere. Measurements were performed in the 300−2300 nm spectral range, while the surface temperature was cycled between 25 and 95 °C.

## THEORETICAL METHODS

The effective permittivity of the 2D array of CNTs is estimated by[31]

$$\varepsilon_\perp^{\text{eff}} = \varepsilon_h\left(1 + f_{CNT}\frac{\alpha}{1 - f_{CNT}L\alpha}\right) \tag{2a}$$

$$\varepsilon_\parallel^{\text{eff}} = f_{CNT}\varepsilon_o + (1 - f_{CNT})\varepsilon_h \tag{2b}$$

where $\varepsilon_h$ is the host material surrounding the CNT, $f_{CNT}$ is the filling fraction of the CNT, $L = 1/2$ is the depolarization factor, and $\alpha$ is the 2D polarizability of the CNT:[32]

$$\alpha = \frac{2}{1-\rho^2}\frac{(\varepsilon_e\Delta - 1)(\varepsilon_e\Delta + \varepsilon_h)\rho^{2\Delta} - (\varepsilon_e\Delta - \varepsilon_h)(\varepsilon_e\Delta + 1)}{(\varepsilon_e\Delta - 1)(\varepsilon_e\Delta - \varepsilon_h)\rho^{2\Delta} - (\varepsilon_e\Delta + \varepsilon_h)(\varepsilon_e\Delta + 1)} \tag{3}$$

Here, $\rho = r/R_{CNT}$ is the ratio between the inner, $r$, and outer, $R_{CNT}$, CNT radius. The parameters $\varepsilon_0$ and $\varepsilon_e$ are the dielectric constant of graphite at the ordinary (perpendicular) and extraordinary (parallel) axis, respectively, and $\Delta = \sqrt{\varepsilon_o/\varepsilon_e}$. The filling fraction is determined by[33]

$$f_{CNT} = \pi\left(\frac{R_{CNT}}{a}\right)^2(1 - \rho^2)$$

where $\alpha$ is the lattice constant of the 2D array.

Equation 2 is based on a 2D array of CNTs, and therefore it represents an anisotropic media. For low CNT filling fractions, the effective permittivity of CVD-grown films can be approximated by[34]

$$\varepsilon_{\text{eff}} = \frac{1}{3}\varepsilon_\perp^{\text{eff}} + \frac{2}{3}\varepsilon_\parallel^{\text{eff}} \tag{4}$$

The change in the optical properties induced by the $VO_2$ inclusions is included by the dielectric constant of the host material, $\varepsilon_h$, by using Bruggerman's effective media theory for a $VO_2$−air composite:[35]

$$f^*\frac{\varepsilon_{VO_2} - \varepsilon_h}{\varepsilon_{VO_2} + 2\varepsilon_h} + (1 - f^*)\frac{\varepsilon_{air} - \varepsilon_h}{\varepsilon_{air} + 2\varepsilon_h} = 0 \tag{5}$$



https://dx.doi.org/10.1021/acsanm.0c01630
ACS Appl. Nano Mater. 2020, 3, 8848−8857

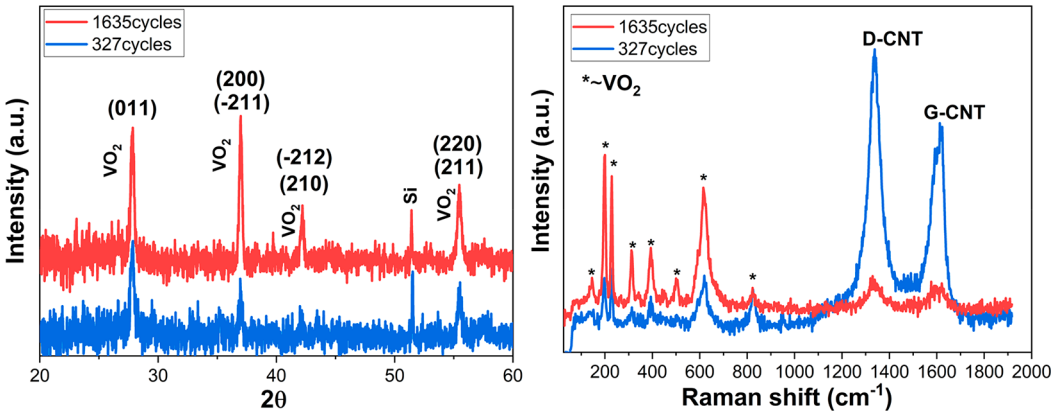


**Figure 3.** XRD (left) and Raman scattering (right) on $VO_2$ decorated (327 cycles) and covered (1635 cycles) CNTs.

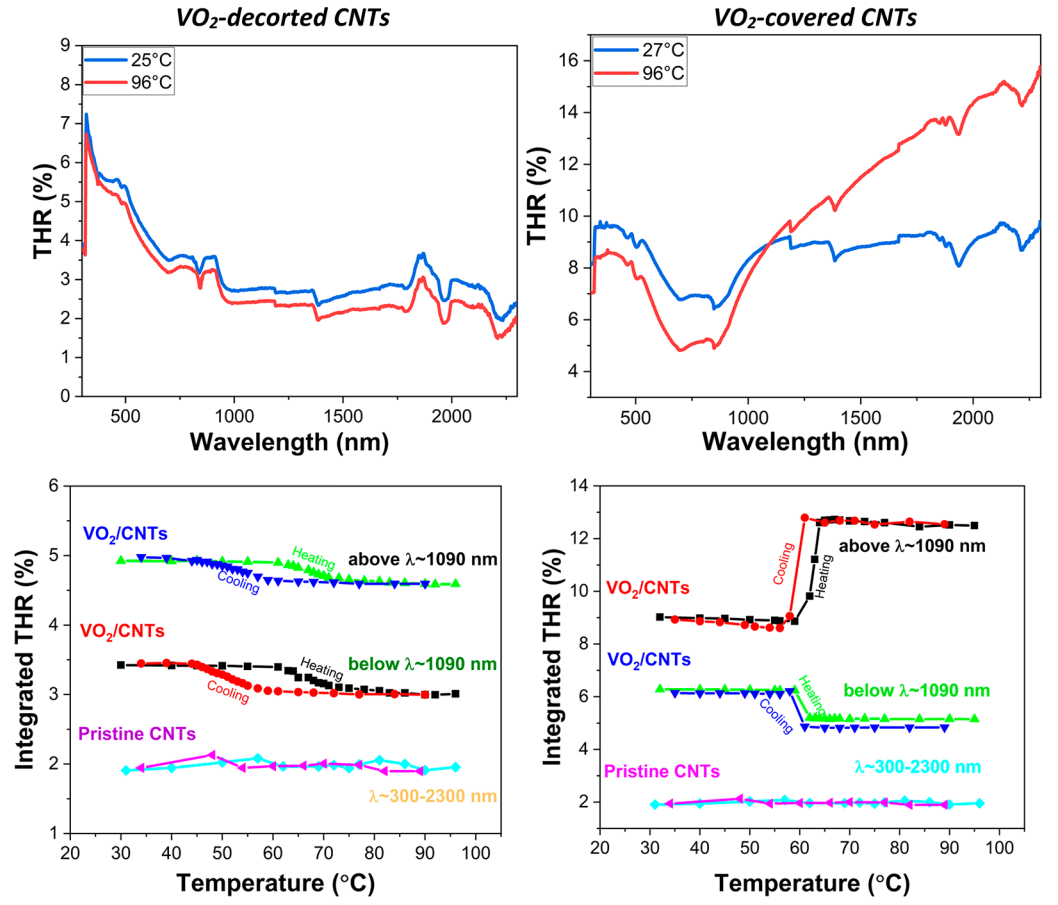


**Figure 4.** Temperature-dependent total hemispherical reflectance (THR) upon heating as a function of the wavelength and the variation of the integrated THR at the inflecting point across the transition temperature upon consecutive heating and cooling of $VO_2$-decorated CNTs (left) and $VO_2$-covered CNTs (right).

where $\varepsilon_{air} = 1$ is the dielectric constant of air, $\varepsilon_{VO_2}$ is the dielectric constant of $VO_2$, and $f^* = \frac{1}{1-\pi(R_{CNT}/a)^2} f_{VO_2}$ corresponds to a fraction of $VO_2$ relative to the volume outside the CNTs. The filling fraction of $VO_2$ relative to the unit cell, $f_{VO_2}$, is given by

$$f_{VO_2} = \frac{\pi[(R_{CNT} + t_{VO_2})^2 - {R_{CNT}}^2]}{a^2}$$

where $t_{VO_2}$ is the thickness of the ALD-deposited $VO_2$ layer (assuming the coating is uniformly distributed over the CNT surface), which is estimated by the product of the ALD deposition rate and number of cycles. Here and in the rest of the paper, the term "filling fraction" corresponds to $f_{VO_2}$.

The radiative properties of the $VO_2$−CNT composite film, i.e., emissivity ($E$) and reflectance ($R$), were computed by using the transfer matrix method for incoherent light.[36] The assumption of incoherent light transport in the CNT film is justified because of multiple scattering of light as a result of the large porosity of film. The model considers a 3 $\mu$m thick film over a semi-infinite silica substrate. Thus, the emissivity is computed as $E = 1 - R$. All the results are based on unpolarized



https://dx.doi.org/10.1021/acsanm.0c01630
ACS Appl. Nano Mater. 2020, 3, 8848−8857

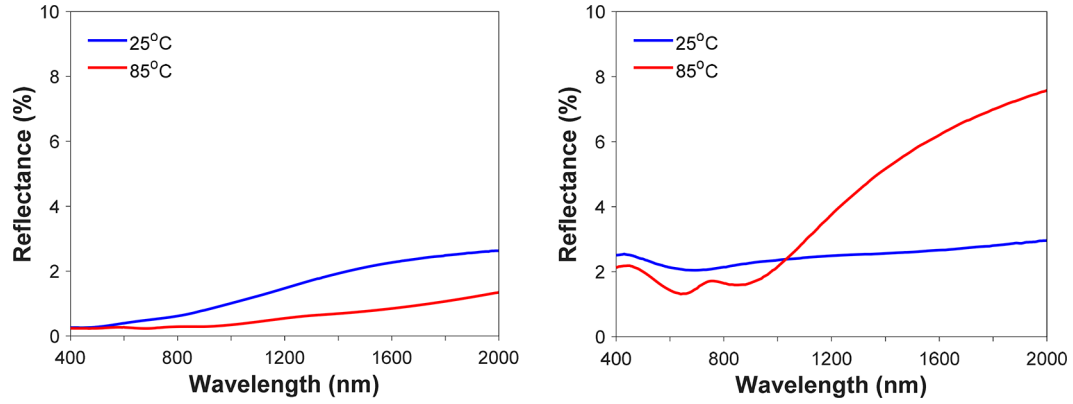


**Figure 5.** Simulated reflectance at normal incidence for (left) $VO_2$-decorated (625 cycles) and (right) $VO_2$-covered (1365 cycles).

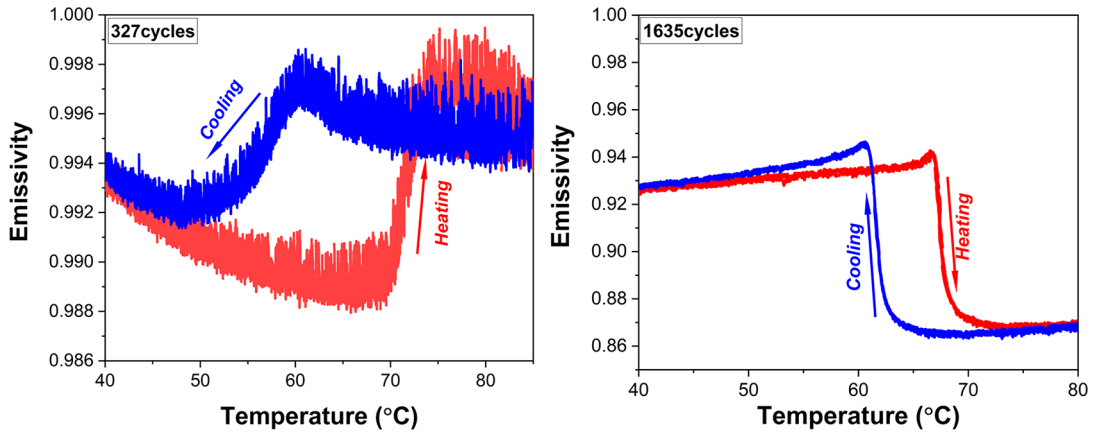


**Figure 6.** Emissivity measurements of the $VO_2$-decorated CNTs (left) and $VO_2$-covered CNTs (right) nanocomposite films.

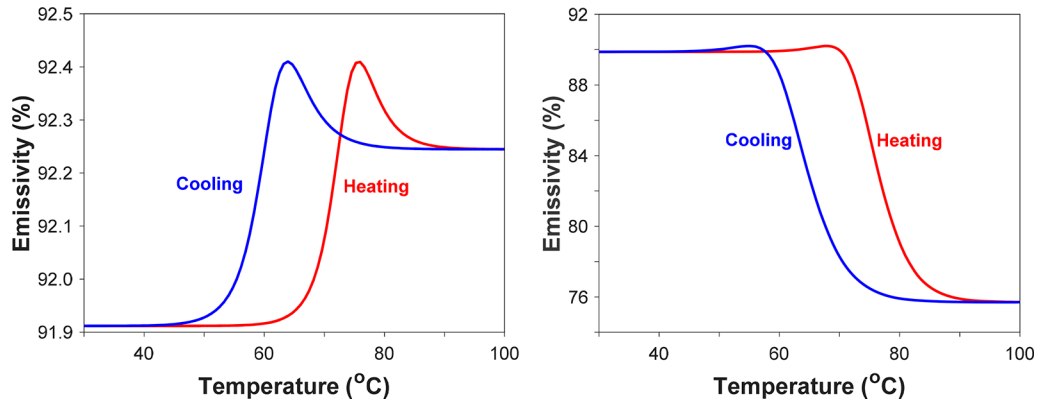


**Figure 7.** Simulated spectral and hemispherical averaged emissivity as a function of temperature for (left) $VO_2$-decorated (327 cycles) and (right) $VO_2$-coated (1635 cycles). Results consider a complete heating and cooling cycle.

light, i.e., $R = {}^1/_2(R^{(s)} + R^{(p)})$, where s and p represent the two polarizations.

The optical properties of graphite[37] and silicon[38] are reported elsewhere. The dielectric constant of $VO_2$, together with the temperature-dependent model for hysteresis, were extracted from Wan et al.[39] In all the calculations, $\rho = 0.2$ and $R_{CNT} = 5$ nm, estimated from previously reported CVD grown CNTs films.[29] The lattice constant was estimated as $a = 20R_{CNT}$ (~0.8% filling fraction) by fitting the spectral-averaged reflectance of the pristine CNT film (eq 4, with $f_{VO_2} = 0$), with the reflectance from measurements for as-grown CNT (~2.5%).

## RESULTS AND DISCUSSION

The vanadium oxide layer is grown directly without any prior treatment of the CNTs. The present defect sites on the surface of CNTs[29,28] likely act as the growth centers for the ALD of oxides.[40] Figure 1 displays the morphology of the cut cross section of pristine and ALD-coated CNTs with a high-magnification view at the surface and interface regions. The average diameter of the CNT, ~10 nm prior the ALD of $VO_x$, increases to ~25 nm across the thickness of the CNT film as shown in Figure 1. The CNTs retain their randomly oriented morphology, tubular structure, and smooth surface. Furthermore, the apparent diameter is similar at the surface and deep at



https://dx.doi.org/10.1021/acsanm.0c01630
ACS Appl. Nano Mater. 2020, 3, 8848−8857

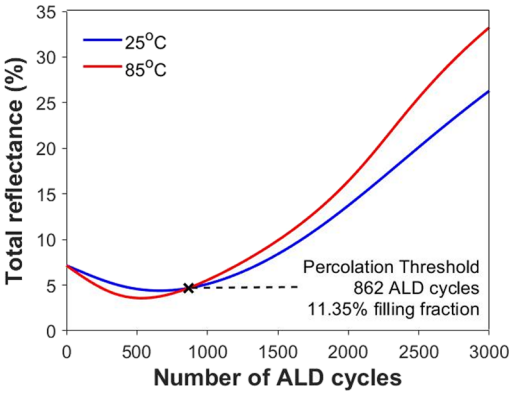


**Figure 8.** Estimation of the percolation threshold. Average spectral and hemispherical total reflectance for hot and cold states of $VO_2$−CNT films as a function of the number of ALD cycles.

the interface with the substrate. These observations confirm the conformal nature of the vanadium oxide ALD deposition and the total infiltration across the porous CNT coating. The $VO_x$/CNTs radius was then monitored as a function of the number of $VO_x$−ALD cycles. A linear increase with the number of ALD cycles is observed with neither surface promotion nor inhibition of the growth as displayed in Figure S1. A deposition rate of 0.017 nm/cycle is measured on CNT while a higher growth rate of 0.03 nm/cycles is observed on a planar silicon substrate. The relatively slow growth on the CNT might be attributed to the reduced density of nucleation sites on CNT.

The as-grown films on CNTs are identified as amorphous or poorly crystalline $V_2O_5$ (Figure S2). Once the CNTs/$V_2O_5$ core/shell structure is obtained, a postdeposition treatment is necessary to secure the conversion to CNTs/$VO_2$. For this purpose, heat treatment in a vacuum ($10^{-2}$ mbar) at 500 °C was performed. The density of the as-grown vanadium oxide is likely to be similar to that of $V_2O_5$, 3.36 g/cm$^3$, or slightly lower. Whereas after conversion to crystalline $VO_2$, the film density would increase to 4.57 g/cm$^3$. This change in the density was quantified in an earlier study devoted to the ALD of $VO_x$ on planar silicon substrates.[30] As a consequence, annealing might cause a significant surface morphology change such as roughening and dewetting.[41,42] In line with these expectations, significant surface roughening was observed as a result of postdeposition annealing as displayed in Figure 2. Annealing thin $VO_x$ (327 cycles) film results in a discontinuous $VO_2$ layer decorating the CNTs, whereas thick layer of $VO_x$ (1635 cycles) on CNTs yields continuous $VO_2$ layer on CNTs with perceptible surface roughening.

Raman analysis provides evidence that postdeposition annealing in a vacuum has converted films into the $VO_2$ phase. The appearance of Raman V−V low-frequency vibrational modes at 146, 196, and 227 cm$^{-1}$ in addition to the V−O high-frequency vibrational modes 313, 394, and 617 cm$^{-1}$ are in line with the presence of the $VO_2$ phase,[30] as shown in Figure 3. The detection of CNTs' "D" vibrational modes at 1337 cm$^{-1}$ and "G" vibrational modes at 1612 cm$^{-1}$ confirms the preservation of CNTs after annealing at high temperatures in the CNTs/$VO_2$ core/shell structure. Here the "G" mode corresponds to the in-plane oscillation of the crystalline graphite, and the "D" mode corresponds to the oscillation of the defective amorphous carbon.[29] The bands attributed to $VO_2$ intensify with the number of ALD cycles at the expense of the CNT bands.

XRD analysis of annealed films, as shown in Figure 3, confirms the formation of polycrystalline $VO_2$ monoclinic phase (pdf no. 04-003-2035[28]). Single-peak analysis as described in the Experimental Methods section was implemented to extract the crystallite size by fitting the (011) peak at 27.83° to the pseudo-Voigt1 function.[43] The calculated crystallite size for the discontinuous nanostructure $VO_2$ (327 cycles) is ∼55 nm, whereas a plateau at ∼120 nm is observed for continuous $VO_2$ layers on CNTs as shown in Figure S3. This result reasonably fits to the observed morphology by SEM.

The grain boundary area ($\gamma$) depends on both the crystallite size and the film thickness, featuring an exponential decay when crystallites are assumed to exhibit a spherical shape.[44] Here the calculated $\gamma$ was normalized to the volume of $VO_2$ layer to obtain the GB = $\gamma$/volume. In Figure S3, we can see that the GB decreases gradually with increased number of $VO_x$ ALD cycles, while the crystallite size features a saturation behavior.

$VO_2$-decorated CNTs (327 cycles) feature a low strain relative to $VO_2$-covered CNTs (>625 cycles), as shown in Figure S3. Referring to the evaluated uncertainty on the determination of the strain, the observed difference as a function of the number of ALD cycles can be considered marginal for all $VO_2$-covered CNTs (>625 ALD cycles of vanadium oxide). Here we assume that strain in ultrathin $VO_2$ (327 cycle) film is relaxed by the formation of disconnected nanoparticles on the CNT surface. The calculated strain values for $VO_2$-covered CNTs are in a similar range as the one measured for the strained

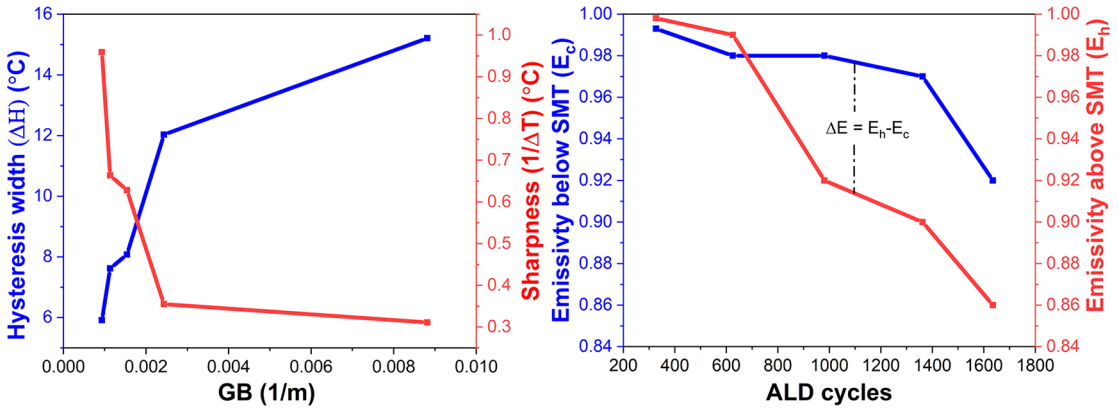


**Figure 9.** Hysteresis width ($\Delta H$) and transition sharpness ($1/\Delta T$) variation with the ALD cycles (left). Emissivity modulation amplitude across SMT for varied ALD cycles composite film (right).



https://dx.doi.org/10.1021/acsanm.0c01630
ACS Appl. Nano Mater. 2020, 3, 8848−8857

$VO_2$ nanobeams on a $SiO_2$ substrate.[45] The type of strain can hardly be obtained from the XRD measurement where the peak shift $2\theta$ value is very small relative to unstrained single-crystal $VO_2$. The Raman peak in the $VO_2$−CNT nanocomposite shifts, however, toward higher frequencies ($cm^{-1}$) relative to the single-crystal $VO_2$,[46] which is attributed to the presence of compressive strain in the film. The "$c$" lattice parameter features an abrupt change from 5.755 Å in the semiconducting to 5.700 Å in the metallic $VO_2$ across the transition, which is due to the orbital occupancy at the Fermi level. As the SMT comes with a shrinkage of the lattice, it is favored at lower temperatures when the semiconducting phase features a compressive strain.[47] As is reported earlier, the SMT temperature increases above 67 °C for the tensile strained films and decreases below 67 °C for the compressive strain in $VO_2$ films,[48,45] which is in line with the observed behavior in Figure S3.

The temperature-dependent optical properties of the nanocomposite $VO_2$/CNT shell/core coating were investigated by using a thermal camera and a UV−vis−NIR spectrometer. As these composite films are opaque and porous in nature, the total hemispherical reflection (THR) is well suited to investigate their diffuse optical properties. The SMT behavior of $VO_2$/CNTs was monitored in the spectral range from 300 to 2300 nm. The resulting temperature-dependent measurements are displayed in Figure 4 for $VO_2$-decorated and $VO_2$-covered CNTs.

$VO_2$-covered CNTs show an increase in the reflectance for $\lambda >$ 1100 nm in the near-infrared and a decrease for $\lambda <$ 1100 nm in the UV−vis−NIR region across the SMT, while the $VO_2$-decorated CNTs show a decrease of the total hemispherical reflectance in the entire investigated spectral range.

The reflectance curves from modeling (Figure 5) show a qualitatively good agreement with the experiments (Figure 4). A major discrepancy between the results from simulation and experiments is observed in the decorated CNTs case; the former shows a monotonic growth with the wavelength, as opposed to the latter. The discrepancy is a consequence of the effective media model considered (eqs 2a and 2b), which neglects near-field interactions between the CNTs. In the case of covered CNTs the discrepancy becomes less evident, as the optical response becomes more dominated by the optical properties from $VO_2$, which are more accurately represented by Brugermann's model (eq 5).

The simulations allow to explain the experimental observations and their relation to the filling fraction of $VO_2$. Indeed, the filling fraction of $VO_2$ in the $VO_2$-decorated CNTs is below the percolation threshold, and the coating is mainly distributed in small domains.[35] The larger absorption in the hot (metallic) phase is thus a consequence of localized surface plasmons excitation, induced by the interaction of light and the confined $VO_2$ domains. In the case of $VO_2$-covered CNTs the filling fraction of $VO_2$ is above the percolation threshold, forming large domains that behave as a continuum.[35] Thus, the coating becomes more reflective in the hot (metallic) phase as compared to the cold phase.

Next, thermal emissivity as a function of temperature of $VO_2$-decorated and $VO_2$-covered CNTs films is investigated (Figure 6). The results consider the spectral and hemispherical averaged emissivity in the mid-infrared region, i.e., $\lambda = 3-5\ \mu$m. The SMT transition in $VO_2$ in both cases induces a modulation of the emissivity ($\Delta E = E^{hot} - E^{cold}$). The modulation is either upward ($\Delta E > 0$) for decorated (low number of ALD cycles) or downward ($\Delta E < 0$) for covered (high number of ALD cycles) CNTs. These results are consistent with the aforementioned observations for the reflectance measurements in the 0.4−2 $\mu$m spectral range. Similar emissivity modulation results are obtained for decorated/covered $VO_2$ films on a silicon substrate (Figure S4).

Additionally, both emissivity curves show a peak near the transition region. The results for calculated spectral and hemispherical average emissivity are consistent with the results from measurements (Figure 7) and able to capture the most relevant features of the phenomenon, i.e., degree and sign of emissivity modulation, and maximum peak near the transition. The difference in the transition temperatures and the hysteresis width ($\Delta H$) are due to the hysteresis model considered.[39] Similar to the aforementioned observation from the reflectance plots (Figure 5), the switching in the emissivity modulation ($\Delta E > 0$ for decorated samples and $\Delta E < 0$ for covered samples) is a consequence of the filling fraction of $VO_2$ in relation to the percolation threshold. Interestingly the peak in the emissivity near the transition region is clearly displayed from the model. This peak corresponds to localized surface plasmon resonances induced by the small metallic domains present at the metastable phase across the semiconductor-to-metallic transition, in line with previously reported measurements.[9,49,50]

The percolation threshold marks a turning point for modulation of the optical properties in $VO_2$−CNT composites. It is therefore customary to predict the threshold based on the theoretical model. However, given the complexity of eq 2, the solution cannot be determined analytically, and thus the value is estimated from graphical results. The percolation threshold is estimated as 11.35% filling fraction which corresponds to 862 ALD cycles, based on the crossing of the hot and cold state curves of the spectral and hemispherical average reflectance as a function of the number of ALD cycles (Figure 8). From Figure 9, it can be noticed that experimentally the percolation threshold value corresponds to 625 ALD cycles, based on the crossing of hot and cold state hemispherical emissivity (3−5 $\mu$m). For lower ALD cycles, the average hemispherical reflectance (emissivity) decreases (increases), while in the case of higher ALD cycles the average hemispherical reflectance (emissivity) increases (decreases).

Temperature-triggered emissivity modulation features a hysteresis, the derivative of which ($dE/dT$) is used to extract characteristic parameters. The sharpness of the SMT is discussed referring to the parameter $1/\Delta T$. Earlier report correlates sharp transitions (high $1/\Delta T$ values) and narrow hysteresis to a large grain sizes ($r$) and low grain boundary area ($\gamma$).[51] The estimated GB decreases with the increased number of ALD cycles of $VO_x$ on the CNTs (Figure S3). A low GB is therefore associated with low defect concentration, as defects are more likely to occur at the interface between grains forming the film. In line with this reasoning, we observed narrow hysteresis ($\Delta H$) and sharper transitions ($1/\Delta T$) with decreased GB, as shown in Figure 9.

Here we addressed the challenge of establishing a design approach to trigger an upward and downward emissivity modulation while using the same building blocks. Simulation efforts were also implemented to link this behavior to the percolation threshold and the physics of metallic nanoparticles versus bulk films. Further developments toward efficient implementation would require the optimization of the modulation amplitude. In this respect, introducing an intermediate dielectric layer[15,16] is expected to play a significant role. If the $VO_2$/CNT nanocomposite film is implemented as a smart solar absorber, the abrupt upward emissivity modulation


https://dx.doi.org/10.1021/acsanm.0c01630
ACS Appl. Nano Mater. 2020, 3, 8848−8857

across the SMT would slow down the surface heating as a response to heating above the transition. An increased heat capture is, however, expected for nanocomposites featuring a downward emissivity modulation. The last would therefore feature an enhanced solar selective absorption above the SMT.

## CONCLUSION

$VO_2$−CNT nanocomposite films are developed by using a hybrid CVD/ALD process with the objective to tailor the light absorption behavior. The modulation of the optical properties induced by the phase change on $VO_2$ inclusions appeared to be strongly dependent on the filling fraction. Thus, at small numbers of ALD cycles the emissivity(reflectivity) of the film was switched upward (downward) across the SMT, while the opposite was observed at large numbers of ALD cycles. The results were successfully explained by effective media theory, and a theoretical model to predict the optical response of the $VO_2$−CNT composite film was derived. The model allowed to determine the percolation threshold over which the $VO_2$ inclusions start forming a continuum domain with bulklike behavior. Below this threshold, the $VO_2$ inclusions are confined in small domains that feature a larger absorption in the IR region at the metallic phase due to the excitation of localized surface plasmons. Above the threshold the $VO_2$ inclusions form a large continuum that becomes more reflective in the metallic phase. The developed nanocomposite coatings can be implemented in different applications as a smart absorber or smart radiator, temperature sensors, and photothermal actuators.

## ASSOCIATED CONTENT

### Supporting Information

The Supporting Information is available free of charge at https://pubs.acs.org/doi/10.1021/acsanm.0c01630.

Figures S1−S4 (PDF)

## AUTHOR INFORMATION


### Corresponding Author

**Naoufal Bahlawane** − *Material Research and Technology Department, Luxembourg Institute of Science and Technology, L-4422 Belvaux, Luxembourg;* orcid.org/0000-0003-1094-2512; Email: naoufal.bahlawane@list.lu

### Authors

**Vasu Prasad Prasadam** − *Material Research and Technology Department, Luxembourg Institute of Science and Technology, L-4422 Belvaux, Luxembourg;* orcid.org/0000-0001-6969-933X

**Francisco V. Ramirez** − *Photonic Innovations Lab, Department of Electronic and Electrical Engineering, University College London, London WC1E 7JE, U.K.;* orcid.org/0000-0001-8863-8735

**Ioannis Papakonstantinou** − *Photonic Innovations Lab, Department of Electronic and Electrical Engineering, University College London, London WC1E 7JE, U.K.;* orcid.org/0000-0002-1087-7020

**Ivan P. Parkin** − *Photonic Innovations Lab, Department of Electronic and Electrical Engineering, University College London, London WC1E 7JE, U.K.;* orcid.org/0000-0002-4072-6610

Complete contact information is available at: https://pubs.acs.org/10.1021/acsanm.0c01630


### Notes

The authors declare no competing financial interest.

## ACKNOWLEDGMENTS

V.P.P. and N.B. acknowledge funding through the MASSENA Pride program of the Luxembourg National Research Fund (project ID: FNR PRIDE/MASSENA/15/10935404). F.V.R. and I.P. thank the European Research Council for a starting grant ERC-StG-IntelGlazing, project ID: 679891. I.P.P. thanks the EPSRC for grant EP/L015862/1.

## REFERENCES


(1) IEA. Global Energy & $CO_2$ Status Report: Emissions. Iea.org. **2019**:15. https://webstore.iea.org/global-energy-co2-status-report-2017 (accessed May 23, 2019).

(2) Granqvist, C. G. Spectrally selective coatings for energy efficiency and solar applications. *Phys. Scr.* **1985**, *32* (4), 401−407.

(3) Wang, L. P.; Lee, B. J.; Wang, X. J.; Zhang, Z. M. Spatial and temporal coherence of thermal radiation in asymmetric Fabry-Perot resonance cavities. *Int. J. Heat Mass Transfer* **2009**, *52* (13−14), 3024−3031.

(4) Granqvist, C. G. Energy-Efficient Windows: Present and Forthcoming Technology. In *Materials Science for Solar Energy Conversion Systems*; Pergamon: 1991; pp 106−167.

(5) Bahlawane, N.; Pachot, C.; Lafont, U. Innovative CNT-based composite coatings for the stray light reduction. *Proc. SPIE - Int. Soc. Opt Eng.* **2016**, 1−9.

(6) Bahlawane, N.; Lenoble, D. Vanadium Oxide Compounds: Structure, Properties, and Growth from the Gas Phase. *Chem. Vap. Deposition* **2014**, *20*, 299−311.

(7) Prasadam, V. P.; Bahlawane, N.; Mattelaer, F.; Rampelberg, G.; Detavernier, C.; Fang, L.; Jiang, Y.; Martens, K.; Parkin, I. P.; Papakonstantinou, I. Atomic layer deposition of vanadium oxides: process and application review. *Mater. Today Chem.* **2019**, *12*, 396−423.

(8) Voti, R. L.; Larciprete, M. C.; Leahu, G.; Sibilia, C.; Bertolotti, M. Optimization of thermochromic $VO_2$ based structures with tunable thermal emissivity. *J. Appl. Phys.* **2012**, *112* (3), 034305.

(9) Kumar, S.; Maury, F.; Bahlawane, N. Light modulation in phase change disordered metamaterial - A smart cermet concept. *Mater. Today Phys.* **2017**, *3*, 41−47.

(10) Wang, S.; Liu, G.; Hu, P.; Zhou, Y.; Ke, Y.; Li, C.; Chen, J.; Cao, T.; Long, Yi. Largely Lowered Transition Temperature of a $VO_2$/Carbon Hybrid Phase Change Material with High Thermal Emissivity Switching Ability and Near Infrared Regulations. *Adv. Mater. Interfaces* **2018**, *5* (21), 1−8.

(11) Xiao, L.; Ma, H.; Liu, J.; Zhao, W.; Jia, Y.; Zhao, Q.; Liu, K.; Wu, Y.; Wei, Y.; Fan, S.; Jiang, K. Fast Adaptive Thermal Camouflage Based on Flexible $VO_2$/Graphene/CNT Thin Films. *Nano Lett.* **2015**, *15* (12), 8365−8370.

(12) Yang, L.; Zhou, P.; Huang, T.; Zhen, G.; Zhang, L.; Bi, L.; Weng, X.; Xie, J.; Deng, L. Broadband thermal tunable infrared absorber based on the coupling between standing wave and magnetic resonance. *Opt. Mater. Express* **2017**, *7* (8), 2767.

(13) Gomez-Heredia, C. L.; Ramirez-Rincon, J. A.; Ordonez-Miranda, J.; Ares, O.; Alvarado-Gil, J. J.; Champeaux, C.; Dumas-Bouchiat, F.; Ezzahri, Y.; Joulain, K. Thermal hysteresis measurement of the $VO_2$ emissivity and its application in thermal rectification. *Sci. Rep.* **2018**, *8* (1), 1−11.

(14) Benkahoul, M.; Chaker, M.; Margot, J.; Haddad, E.; Kruzelecky, R.; Wong, B.; Jamroz, W.; Poinas, P. Thermochromic $VO_2$ film deposited on Al with tunable thermal emissivity for space applications. *Sol. Energy Mater. Sol. Cells* **2011**, *95* (12), 3504−3508.

(15) Hendaoui, A.; Émond, N.; Dorval, S.; Chaker, M.; Haddad, E. $VO_2$-based smart coatings with improved emittance-switching properties for an energy-efficient near room-temperature thermal control of spacecrafts. *Sol. Energy Mater. Sol. Cells* **2013**, *117*, 494−498.

(16) Sun, K.; Riedel, C. A.; Urbani, A.; Simeoni, M.; Mengali, S.; Zalkovskij, M.; Bilenberg, B.; De Groot, C. H.; Muskens, O. L. $VO_2$ Thermochromic Metamaterial-Based Smart Optical Solar Reflector. *ACS Photonics* **2018**, *5* (6), 2280−2286.
(17) Taylor, A.; Parkin, I.; Noor, N.; Tummeltshammer, C.; Brown, M. S.; Papakonstantinou, I. A bioinspired solution for spectrally selective thermochromic $VO_2$ coated intelligent glazing. *Opt. Express* **2013**, *21* (S5), A750.
(18) Wu, S. H.; Chen, M.; Barako, M. T.; Jankovic, V.; Hon, P.W. C.; Sweatlock, L. A.; Povinelli, M. Thermal homeostasis using microstructured phase-change materials. *Optica.* **2017**, *4* (11), 1390.
(19) Powell, M. J.; Quesada-Cabrera, R.; Taylor, A.; Teixeira, D.; Papakonstantinou, I.; Palgrave, R.; Sankar, G.; Parkin, I. P. Intelligent Multifunctional $VO_2/SiO_2/TiO_2$ Coatings for Self-Cleaning, Energy-Saving Window Panels. *Chem. Mater.* **2016**, *28* (5), 1369−1376.
(20) Haddad, E.; Kruzelecky, R. V.; Wong, B.; Jamroz, W.; Soltani, M.; Benkahoul, M.; Chaker, M.; Poinas, P. Multilayer Tuneable Emittance Coatings with Low Solar Absorptance for Improved Smart Thermal Control in Space Applications. *SAE Technol. Pap. Ser.* **2009**, 1.
(21) Chao, D.; Zhu, C.; Xia, X.; et al. Graphene quantum dots coated $VO_2$ arrays for highly durable electrodes for Li and Na ion batteries. *Nano Lett.* **2015**, *15* (1), 565−573.
(22) Evans, G. P.; Powell, M. J.; Johnson, I. D.; Howard, D.; Bauer, D.; Darr, J. A.; Parkin, I. P. Room temperature vanadium dioxide−carbon nanotube gas sensors made via continuous hydrothermal flow synthesis. *Sens. Actuators, B* **2018**, *255*, 1119−1129.
(23) Ma, H.; Zhang, X.; Zhang, Z.; Wang, Y.; Wang, G.; Liu, F.; Cui, R.; Huang, C.; Wang, M.; Wei, Y.; Jiang, K.; Pan, L.; Liu, K. Infrared micro-detectors with high sensitivity and high response speed using $VO_2$-coated helical carbon nanocoils. *J. Mater. Chem. C* **2019**, *7* (39), 12095−12103.
(24) Ma, H.; Hou, J.; Wang, X.; Zhang, J.; Yuan, Z.; Xiao, L.; Wei, Y.; Fan, S.; Jiang, K.; Liu, K. Flexible, all-inorganic actuators based on vanadium dioxide and carbon nanotube bimorphs. *Nano Lett.* **2017**, *17* (1), 421−428.
(25) Wang, Y.; Zhang, L.; Wang, P. Self-Floating Carbon Nanotube Membrane on Macroporous Silica Substrate for Highly Efficient Solar-Driven Interfacial Water Evaporation. *ACS Sustainable Chem. Eng.* **2016**, *4* (3), 1223−1230.
(26) Wang, T.; Torres, D.; Fernández, F. E.; Wang, C.; Sepúlveda, N. Maximizing the performance of photothermal actuators by combining smart materials with supplementary advantages. *Sci. Adv.* **2017**, *3* (4), 1−10.
(27) Ma, H.; Zhang, X.; Cui, R.; Liu, F.; Wang, M.; Huang, C.; Hou, J.; Wang, G.; Wei, Y.; Jiang, K.; Pan, L.; Liu, K. Photo-driven nanoactuators based on carbon nanocoils and vanadium dioxide bimorphs. *Nanoscale* **2018**, *10* (23), 11158−11164.
(28) Basheer, H. J.; Baba, K.; Bahlawane, N. Thermal Conversion of Ethanol into Carbon Nanotube Coatings with Adjusted Packing Density. *ACS Omega.* **2019**, *4* (6), 10405−10410.
(29) Basheer, H. J.; Pachot, C.; Lafont, U.; Devaux, X.; Bahlawane, N. Low-Temperature Thermal CVD of Superblack Carbon Nanotube Coatings. *Adv. Mater. Interfaces* **2017**, *4* (18), 1−9.
(30) Prasadam, V. P.; Dey, B.; Bulou, S.; Schenk, T.; Bahlawane, N. Study of $VO_2$ thin film synthesis by atomic layer deposition. *Mater. Today Chem.* **2019**, *12*, 332−342.
(31) García-Vidal, F. J.; Pitarke, J. M.; Pendry, J. B. Effective medium theory of the optical properties of aligned Carbon nanotubes. *Phys. Rev. Lett.* **1997**, *78* (22), 4289−4292.
(32) Henrard, L.; Lambin, P. Calculation of the energy loss for an electron passing near giant fullerenes. *J. Phys. B: At., Mol. Opt. Phys.* **1996**, *29* (21), 5127−5141.
(33) García-Vidal, F. J.; Pitarke, J. M. Optical absorption and energy-loss spectra of aligned carbon nanotubes. *Eur. Phys. J. B* **2001**, *22* (2), 257−265.
(34) Banhegyi, G. Comparison of electrical mixture rules for composites. *Colloid Polym. Sci.* **1986**, *264* (12), 1030−1050.
(35) Cai, W.; Shalaev, V. *Optical Metamaterials: Fundamentals and Applications*; Springer: 2009.
(36) Katsidis, C. C.; Siapkas, D. I. General transfer-matrix method for optical multilayer systems with coherent, partially coherent, and incoherent interference. *Appl. Opt.* **2002**, *41* (19), 3978.
(37) Djurišić, A. B.; Li, E. H. Optical properties of graphite. *J. Appl. Phys.* **1999**, *85* (10), 7404−7410.
(38) Palik, E. D.; Ghosh, G. *Handbook of Optical Constants of Solids*, 1st ed.; Academic Press: 1998.
(39) Wan, C.; Zhang, Z.; Woolf, D.; Hessel, C.; Rensberg, J.; Hensley, J. M.; Xiao, Y.; Shahsafi, A.; Salman, J.; Richter, S.; Sun, Y.; Qazilbash, M. M.; Schmidt-Grund, R.; Ronning, C.; Ramanathan, S.; Kats, M. A. On the Optical properties of thin-film vanadium dioxide from the visible to the far infrared. *Ann. Phys.* **2019**, *531*, 1−7.
(40) Stano, K. L.; Carroll, M.; Padbury, R.; McCord, M.; Jur, J. S.; Bradford, P. D. Conformal atomic layer deposition of alumina on millimeter tall, vertically-aligned carbon nanotube arrays. *ACS Appl. Mater. Interfaces* **2014**, *6* (21), 19135−19143.
(41) Rampelberg, G.; Deduytsche, D.; De Schutter, B.; Premkumar, P. A.; Toeller, M.; Schaekers, M.; Martens, K.; Radu, I.; Detavernier, C. Crystallization and semiconductor-metal switching behavior of thin $VO_2$ layers grown by atomic layer deposition. *Thin Solid Films* **2014**, *550*, 59−64.
(42) Peter, A. P.; Martens, K.; Rampelberg, G.; Toeller, M.; Ablett, J.; Meersschaut, J.; Cuypers, D.; Franquet, A.; Detavernier, C.; Rueff, J. P.; Schaekers, M.; Van Elshocht, S.; Jurczak, M.; Adelmann, C.; Radu, I. P. Metal-insulator transition in ALD $VO_2$ ultrathin films and nanoparticles: Morphological control. *Adv. Funct. Mater.* **2015**, *25* (5), 679−686.
(43) De Keijser, T. H.; Langford, J. I.; Mittemeijer, E. J.; Vogels, A. B. P. Use of the Voigt function in a single-line method for the analysis of X-ray diffraction line broadening. *J. Appl. Crystallogr.* **1982**, *15*, 308.
(44) Siegel, R. W.; Thomas, G. J. Grain boundaries in nanophase materials. *Ultramicroscopy* **1992**, *40* (3), 376−384.
(45) Park, J. H.; Coy, J. M.; Kasirga, T. S.; Huang, C.; Fei, Z.; Hunter, S.; Cobden, D. H. Measurement of a solid-state triple point at the metal-insulator transition in $VO_2$. *Nature* **2013**, *500* (7463), 431−434.
(46) Parker, J. C. Raman scattering from $VO_2$ single crystals: A study of the effects of surface oxidation. *Phys. Rev. B: Condens. Matter Mater. Phys.* **1990**, *42* (5), 3164−3166.
(47) Aetukuri, N. B.; Gray, A. X.; Drouard, M.; Cossale, M.; Gao, L.; Reid, A. H.; Kukreja, R.; Ohldag, H.; Jenkins, C. A.; Arenholz, E.; Roche, K. P.; Dürr, H. A.; Samant, M.; Parkin, S. S. P. Control of the metal-insulator transition in vanadium dioxide by modifying orbital occupancy. *Nat. Phys.* **2013**, *9* (10), 661−666.
(48) Atkin, J. M.; Berweger, S.; Chavez, E. K.; Raschke, M. B.; Cao, J.; Fan, W.; Wu, J. Strain and temperature dependence of the insulating phases of $VO_2$ near the metal-insulator transition. *Phys. Rev. B: Condens. Matter Mater. Phys.* **2012**, *85* (2), 1−4.
(49) Kats, M. A.; Sharma, D.; Lin, J.; Genevet, P.; Blanchard, R.; Yang, Z.; Qazilbash, M. M.; Basov, D. N.; Ramanathan, S.; Capasso, F. Ultra-thin perfect absorber employing a tunable phase change material. *Appl. Phys. Lett.* **2012**, *101* (22), 221101.
(50) Kats, M. A.; Blanchard, R.; Zhang, S.; Genevet, P.; Ko, C.; Ramanathan, S.; Capasso, F. Vanadium dioxide as a natural disordered metamaterial: Perfect thermal emission and large broadband negative differential thermal emittance. *Phys. Rev. X* **2013**, *3* (4), 1−7.
(51) Narayan, J.; Bhosle, V. M. Phase transition and critical issues in structure-property correlations of vanadium oxide. *J. Appl. Phys.* **2006**, *100* (10), 103524.


https://dx.doi.org/10.1021/acsanm.0c01630
ACS Appl. Nano Mater. 2020, 3, 8848−8857

# Thermo-responsive Black $VO_2$-Carbon Nanotubes Composite Coatings for Solar Energy Harvesting

Vasu Prasad Prasadam, Francisco V. Ramirez,[a] Ioannis Papakonstantinou,[a] Ivan P. Parkin,[a] Naoufal Bahlawane

*Material Research and Technology Department,* Luxembourg Institute of Science and Technology, Rue du Brill, L-4422 Belvaux, Luxembourg

[a] Photonic Innovations Lab, Department of Electronic and Electrical Engineering, University College London, Torrington Place, London, WC1E 7JE, UK

The ALD kinetics of vanadium oxide was investigated on silicon substrates and on CNTs. Ellipsometry was implemented to assess the thickness on Si, whereas the SEM was used to measure the evolution of the CNTs' outer diameter with the number of deposition cycles. A linear increase with the number of ALD cycles is observed with neither surface promotion nor inhibition of the growth as displayed in the figure S1. A deposition rate of 0.017 nm/cycle is measured on CNT while a higher growth rate of 0.03 nm/cycles is observed on planar silicon substrate. The relatively slow growth on the CNT might be attributed to the reduced density of nucleation sites on CNT.

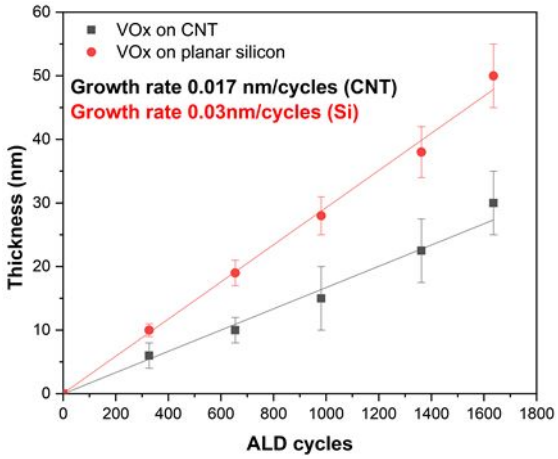


*Figure S1. ALD growth kinetics of $VO_x$ on planar silicon and on CNTs at 80˚C substrate temperature with ALD cycle composed of 8s VTOP/15s purge/6s H2O/15s purge.*

As-grown $VO_2$ on CNTs surfaces are poorly crystalline as indicated by XRD and Raman scattering analyses. XRD and Raman analyses show no sign of distinctive vanadium oxide phase as depicted in figure S2. From the XPS analysis reported earlier, we observe the presence of vanadium +5 oxidation state for the as-grown films on silicon substrate[1].

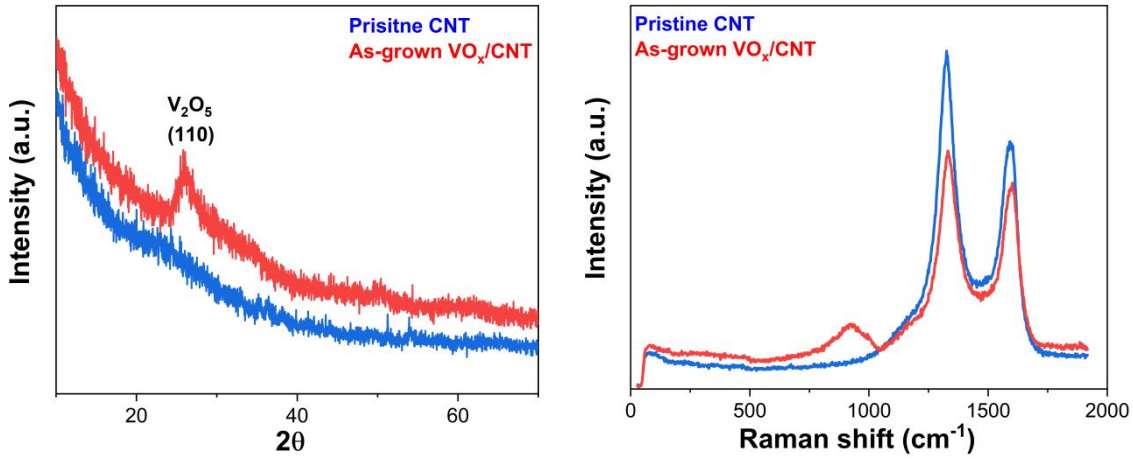


*Figure S2. XRD (left) and Raman scattering (right) of pristine CNTs and as-grown $VO_x$/CNT. The major $V_2O_5$ phase peaks are missing in both XRD, Raman. However, Obtained broad XRD peak overlaps with (110) peak of $V_2O_5$ phase.*

The grain boundary area (GB) decreases gradually with increased number of $VO_x$ ALD cycles, while the crystallite size features a saturation behaviour as shown in figure S3. $VO_2$-decorated CNTs (327 cycles) feature a low strain relative to $VO_2$ covered CNTs (>625 cycles). The decrease of the SMT might be associated with the defect concentration that scale with the GB. Furthermore, the presence of compressive strain might further contribute to the decrease of the SMT temperature. [2,3]

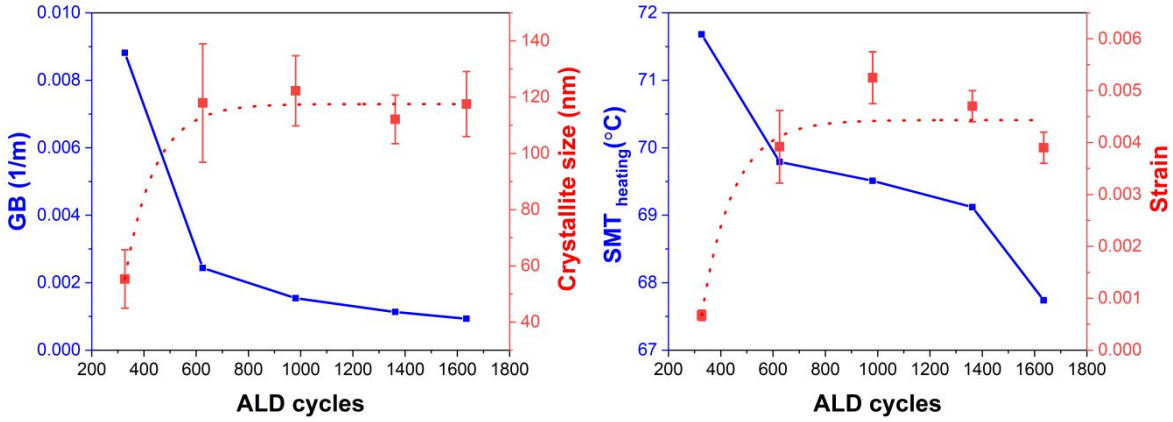


*Figure S3. Crystallite size and GB extracted from (011) reflex for different ALD cycles (right), of $VO_2$-CNTs nanocomposite films (left); Impact of strain on the SMT transition (right).*

In figure S4, we observed the emissivity modulation across the SMT for decorated and covered $VO_2$ films on silicon substrate. Here similar optical modulation characteristics are noticed as shown on $VO_2$-CNT nanocomposite of figure 5.

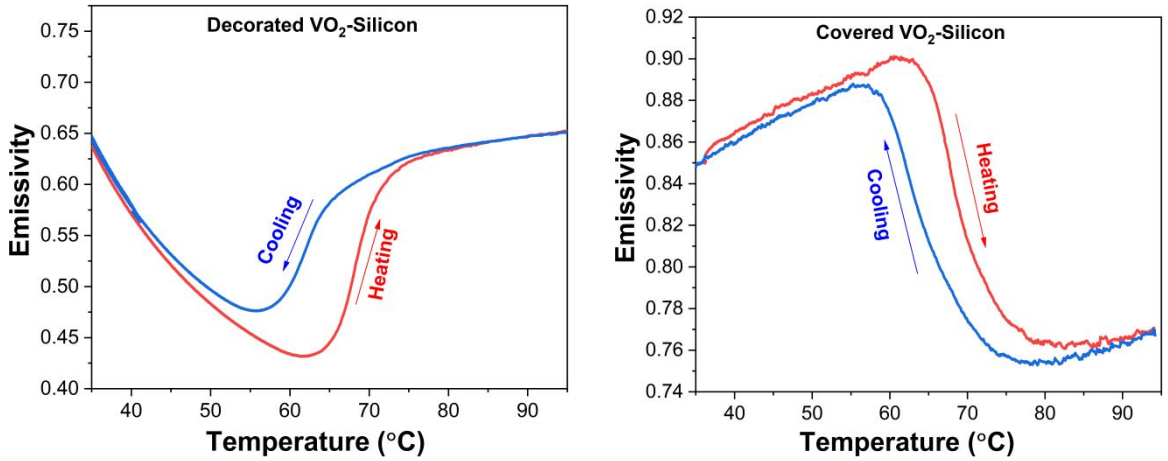


*Figure S4. Emissivity across the SMT of decorated $VO_2$ (left), covered $VO_2$ (right) on silicon substrates.*

References

1. Prasadam, V.P.; Dey, B.; Bulou, S.; Schenk, T.; Bahlawane, N. Study of $VO_2$ thin film synthesis by atomic layer deposition. *Mater Today Chem*. 2019;12:332-342. doi:10.1016/j.mtchem.2019.03.005

2. Atkin, J.M.; Berweger, S.; Chavez, E.K.; Raschke, M.B.; Cao, J.; Fan, W.; Wu, J. Strain and temperature dependence of the insulating phases of $VO_2$ near the metal-insulator transition. *Phys Rev B - Condens Matter Mater Phys*. 2012;85(2):1-4. doi:10.1103/PhysRevB.85.020101

3. Park, J.H.; Coy, J.M.; Serkan, K.T.;Huang, C.; Fei, Z.; Hunter, S.; Cobden, D.H. Measurement of a solid-state triple point at the metal-insulator transition in $VO_2$. *Nature*. 2013;500(7463):431-434. doi:10.1038/nature12425

### 3.1.4 MWCNT-ZnO for the solar selective thermal application

Execution of carbon nanotubes (CNTs) and Al doped zinc oxide (AZO) as primary constituents to design solar selective coatings are addressed in this section. Transparent conducting oxides (TCO) such as AZO have immense capability because they attribute high transparency in the solar spectrum region and reflectance in IR region.

CVD deposited MWCNTs were conformally coated with aluminium doped zinc oxide (AZO) using an optimized ALD process. Nanoengineering of AZO layer to achieve the desired optical properties requires an appropriate Al dopant concentration (4.7 at %). The thermal stability of the engineered MWCNT-AZO is limited at 1000 K under vacuum. The interface between ZnO and MWCNT is thermodynamically unstable above 670 K resulting in the carbothermal reduction of the ZnO film. However, a thin $Al_2O_3$ layer prior to the deposition of AZO stabilizes the interface with MWCNTs. A core-double shell structure, i.e., CNT-$Al_2O_3$-AZO withstands thermal treatment at 1000 K for 72 h.

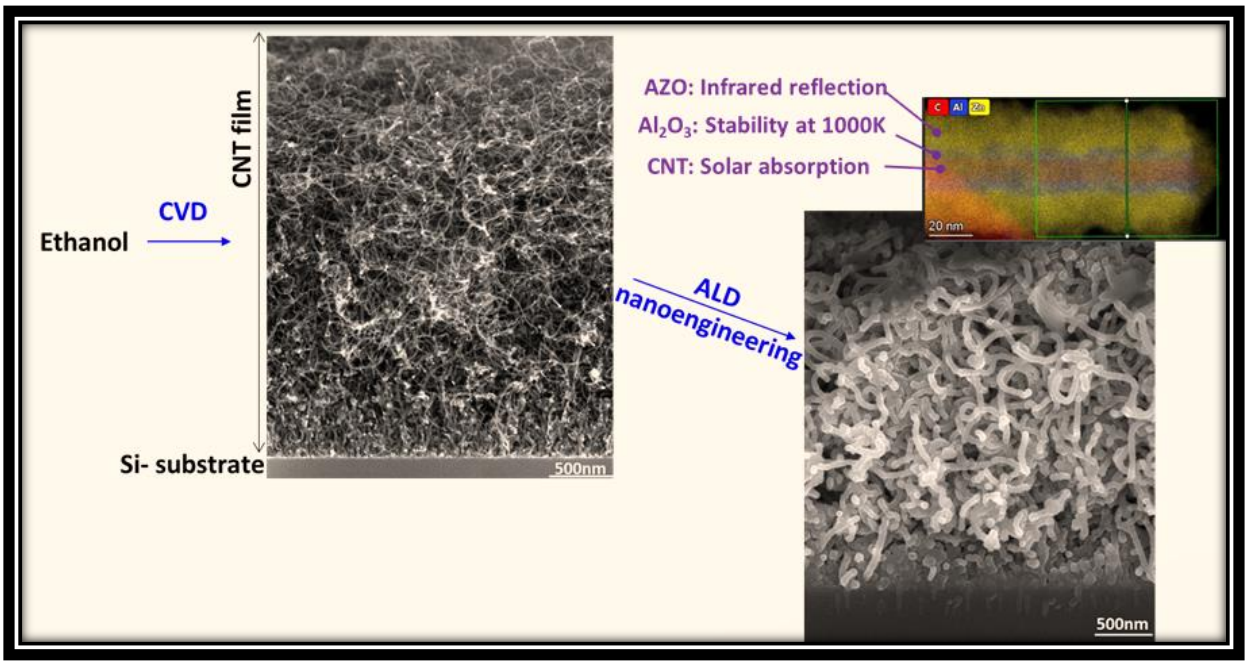

Materials Today Communications 28 (2021) 102552

Contents lists available at ScienceDirect

Materials Today Communications

journal homepage: www.elsevier.com/locate/mtcomm

# CNT nanoengineering for thermally stable selective solar absorption

Vasu Prasad Prasadam [a], Nicolas Gautier [b], Naoufal Bahlawane [a,*]

[a] Material Research and Technology Department, Luxembourg Institute of Science and Technology, Rue du Brill, L-4422 Belvaux, Luxembourg
[b] Université de Nantes, CNRS, Institut des Matériaux Jean Rouxel, IMN, F-44000 Nantes, France

ARTICLE INFO

*Keywords:*
Nanomaterials
Nanoengineering
Carbon nanotubes
Transparent conducting oxides
Solar-thermal energy harvesting
Chemical vapor deposition
Atomic layer deposition

ABSTRACT

Solar thermal electricity generation is an appealing green concept, which the efficiency enhancement requires the development of appropriate solar absorbers using an up-scalable processing technique. Here, we report on the nanoengineering of carbon nanotubes (CNT) as an approach to design high-performance solar absorbers using oxide materials in a core/shell architecture. Gas-phase synthesis is deployed for the growth of modified CNT cores with infra-red reflecting and low refractive index shell layers. The designed coating fully benefits from the high absorbance of CNTs and the infrared-reflecting properties of *Al*-doped ZnO irrespective of the nature of the underlying substrate. The nano-engineered CNT-metal oxide design withstands extended exposure to 1000 *K*.

## 1. Introduction

Solar energy has a great potential to meet the global energy demand while reducing the carbon emission footprint [1]. The ultimate target of harnessing this clean energy source retains the attention of researchers worldwide. Despite the improvement in materials technologies and governmental subsidies, solar energy harvesting still faces challenges related to the high cost and low yield relative to energy production from fossil fuels. Solar power might be classified into photovoltaics (PV) and solar thermal [2]. In the last case, the thermal efficiency improves greatly with the temperature of the hot source [3]. Hereby, a central role is played by the solar absorbers that are ideally selective, i.e. total absorbance in the solar spectrum ($\alpha = 1$) and no thermal emittance ($\varepsilon = 0$) [4]. Selective solar absorption might be intrinsic or attained using various approaches such as semiconductor-metal tandems, multilayers, cermets and surface texturing [4,5]. Cermet based solar absorbers were studied intensively, due to their potential high temperature stability [6,7]. Next generation solar thermal harvesters are expected to operate above 923 *K*, a temperature at which both the solar absorbance and thermal emittance of most cermets degrade due to diffusion, agglomeration and/or oxidation of the embedded metallic nanoparticles [6]. Approaches to improve the thermal stability of solar absorbers have included the implementation of barrier layers on the substrates, non-metallic substrates and embedded noble metal or bi-metallic particles in the matrix. Despite the above-mentioned efforts, cermets still represent an unfavorable performance-thermal stability trade-off [6]. Bulk metal carbide ($Ti_3SiC_2$) is a promising intrinsic solar selective absorber with a significant stability in air at 900 *K* [8]. Early large-scale applications have involved Pyromark 2500 black, a paint that features a long term thermal durability at 1000 *K* but it does not exhibit solar selectivity [9]. Several carbon based tandem solar absorbers were recently proposed for the high temperature solar absorber application [10–13], provided the adhesion strength can be improved [14] and the absorption can be made solar selective. Here, implementing a metallic substrate ensures a low thermal emittance.

Carbon nanotubes (CNT) have a high absorbance (low reflectance) in a broad spectrum i.e. 0.25–200 $\mu m$ [15–18], which is attributed to the inter band and $\pi$-$\pi^*$ transitions [19,20]. Furthermore, CNTs feature a very low reflectance owing to the low refractive index resulting from their porous structure [21], and exhibit an outstanding thermal stability in vacuum [22] and in argon atmosphere [23]. The adhesion issue, which is challenging for CNT coatings in general, can be addressed and an adhesion strength exceeding 8 N/cm can be achieved via the application of an ultrathin metal oxide layer with ALD [15]. These characteristics make their implementation appealing as a building block for the design of high temperature selective absorbers in association with infrared reflecting materials. In this respect, transparent conducting oxides (TCO) have a great potential as they feature a high transparency in the solar spectrum while reflecting IR radiations [24]. A solar selective absorbing paint composed of CNT, indium tin oxide (ITO) and aluminum hydroxide enabled 80% of solar absorbance and 12% emittance [25], which makes the concept promising. ITO is nevertheless an

* Corresponding author.
*E-mail address:* naoufal.bahlawane@list.lu (N. Bahlawane).

https://doi.org/10.1016/j.mtcomm.2021.102552
Received 10 February 2021; Received in revised form 21 May 2021; Accepted 14 June 2021
Available online 16 June 2021

expensive alternative due to the scarcity of Indium that represents ~0.25 ppm of the earth crust. Aluminum doped ZnO (AZO) is another promising TCO materials with a substantially higher elemental abundance. AZO films are studied quite intensely for transparent electronics using various dry synthesis techniques including atomic layer deposition (ALD) [26] that is highly suitable for the growth of conformal layers on challenging structured surfaces as CNT [27]. A hybrid ALD-CVD approach is investigated in the present study to demonstrate, for the first time, the potential of CNT/AZO porous core/shell architecture for the selective solar absorption.

## 2. Experimental studies

### 2.1. Synthesis of CNT

CNT coatings were prepared by thermal CVD using a single ethanol precursor solution containing 0.65 × $10^{-3}$ *mol* $L^{-1}$ of cobalt acetylacetonate ($Co(acac)_2$) and 0.65 × $10^{-3}$ *mol* $L^{-1}$ of magnesium acetylacetonate ($Mg(acac)_2$). The temperature of the substrate was kept at 485 °*C* during deposition and the pressure was adjusted at 10 mbar. At this temperature $Mg(acac)_2$ undergoes thermolysis and forms MgO. On the other side $Co(acac)_2$ is reduced by ethanol at elevated temperatures to form metallic cobalt or cobalt carbide [28]. Finally, ethanol vapor acts as the carbon source, in the presence of cobalt catalytic nanoparticles and MgO growth promoter, for the growth of CNT films as illustrated in Scheme 1. Further details are reported elsewhere [18,29].

### 2.2. Synthesis of AZO film

*Al* doped ZnO films are prepared by thermal ALD via the sequential hydrolysis of diethyl zinc (DEZ) and trimethylaluminum (TMA) precursors. All precursors were kept at room temperature and the substrate temperature was adjusted for the optimization of the ALD process. AZO films were made by introducing "m" TMA-$H_2O$ cycle for every "n" DEZ-$H_2O$ cycles. The thickness of AZO films was controlled by varying the number of macro cycles "N", where one macro-cycle corresponds to "n" DEZ-$H_2O$ cycles and "m" TMA-$H_2O$ cycles as illustrated in Scheme 2, whereas the aluminum doping concentration was varied by changing "n" and "m". A descriptive annotation will be given as AZO N(n:m).

### 2.3. Characterization

The thickness measurement of the oxide layers was performed with a multi-wavelength Ellipsometer (Film Sense) with the Cauchy model. For this purpose, deposition was performed on silicon substrates. The structural characterization was performed using X-ray diffraction (Bruker D8), with *Cu-*$K_\alpha$ ($\lambda = 0.154$ nm) as the X-ray source, where the data were collected in the grazing incidence, 0.5°, and a detector scan from 20° to 80° with 0.02° steps. Crystallite size "D" was calculated using the Williamson-Hall method (Eq. (1)).

$$(FWHM) * cos\theta = \frac{(K * \lambda)}{D} + 4 * strain * sin\theta \quad (1)$$

The width of the XRD peak (FWHM) is a combined contribution from the instrumental broadening, lattice strain and size of the crystallites. We measured 0.173 as the instrumental broadening using a single crystal silicon wafer and we consider a crystallite shape factor "*k*" of 0.94. The morphology of the films was inspected using the FEI Helios Nanolab 650 scanning electron microscope (SEM) at a working distance of 5 mm and using 2–5 *V* as the acceleration voltage. Aluminum atomic concentration in AZO was determined using EDX measurement at an acceleration voltage of 15 *V*.

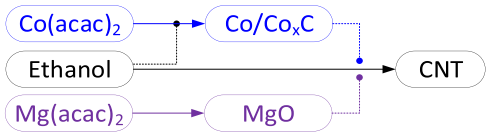


**Scheme 1.** Illustration of the thermally induced chemical conversions in the CVD of CNT coatings.

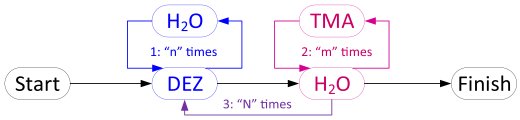


**Scheme 2.** Illustration of AZO deposition recipe.

Texture coefficient "TC" of the film was calculated from the Eq. (2), using the observed 5 XRD reflections, here M = 5.

$$TC\ (hkl) = \frac{I_{(hkl)}/Io_{(hkl)}}{\frac{1}{M}\sum_{M} I_{(hkl)}/Io_{(hkl)}} \quad (2)$$

The electrical resistivity was measured using the four-probe analysis and Hall probe measurement to determine the charge carrier concentration and mobility. For this purpose, the films were grown on glass substrates. Optical properties were measured using LAMBDA 1050 UV–VIS–NIR spectrophotometer from Perkin Elmer and Bruker FTIR spectrometer. Spectralon integration sphere was used to measure the total hemispherical reflectance in UV–Vis–NIR, $\lambda$: 0.25–2.5 μ*m*, whereas a gold-coated integration sphere was used in the IR, $\lambda$: 1–25 μ*m*. The solar absorbance ($\alpha_s$) and thermal emittance ($\varepsilon$) were calculated from Eqs. (3) and (4) respectively.

$$\alpha_s = \frac{\int_{0.25}^{2.5}{}_{\mu m}^{\mu m} I_{Am1.5}\ _{(\lambda)} * (1 - R\ _{(\lambda)}) \cdot d\lambda}{\int_{0.25}^{2.5}{}_{\mu m}^{\mu m} I_{Am1.5}\ _{(\lambda)} \cdot d\lambda} \quad (3)$$

$$\varepsilon = \frac{\int_{2.5}^{25}{}_{\mu m}^{\mu m} I_{BB}\ _{(\lambda,T)} * (1 - R\ _{(\lambda)}) \cdot d\lambda}{\int_{2.5}^{25}{}_{\mu m}^{\mu m} I_{BB}\ _{(\lambda,T)} \cdot d\lambda} \quad (4)$$

"$I_{Am1.5}$" is the solar radiance with atmospheric absorption at AM1.5; "R" is the total hemispherical reflectance and "$I_{BB}$" is the black body radiation at the given temperature. The surface emissivity was measured by a FLIR X6580SC thermal camera operating in the 3–5 μm spectral range. Linkam stage was used to control the temperature and the emissivity of pristine CNTs coating was taken as a reference perfect black body in these measurements. A built-in software from the FLIR camera program is used for calculating the emissivity value.

Solar absorber efficiency is given in the form of figure of merit ($\eta$) as shown in Eq. (5).

$$\eta = [\alpha Q - (\sigma \varepsilon T^4)]/Q \quad (5)$$

$\alpha$ is solar absorbance, $Q$ is irradiance on absorber *(1000* $W/m^2$*)*, $\sigma$ is Stefan–Boltzmann constant *(5.67×*$10^{-8}$*W/*$m^2$ $K^{-4}$*)*, $T$ is surface temperature *(300 K) and* $\varepsilon$ *is thermal emittance measured.* The deposited oxides on CNT were characterized using transmission electron microscopy (S/TEM Themis Z G3, 300 *kV*, Thermo Fisher Scientific). The elemental mapping was performed using a combined EDX (energy dispersive X-ray spectrometer) analysis and high-angle annular dark-field scanning transmission electron microscopy (HAADF-STEM, 29.5 mrad, probe corrected). The coated CNTs were sampled, by scratching the surface, and deposited on lacey carbon grids.

## 3. Results and discussion

Upon surface exposure to DEZ, the precursor molecules chemisorb on the surface until saturation occurs, and the unreacted excess is purged from the reactor. The chemisorbed DEZ is then converted to Zn-OH groups during the subsequent exposure to water vapor. These sequential reactions are self-terminating, and the growth per cycle (GPC)

remains constant even after extended exposures to DEZ or $H_2O$ [30]. The saturation kinetics was investigated starting by arbitrary fixing the $H_2O$ exposure time at 40 ms and varying the exposure time to DEZ. The results displayed in Fig. 1a show that a DEZ exposure time of 1s is required to reach saturation. This condition was then implemented in Fig. 1b to define the $H_2O$ exposure time required for the self-limited reaction. Therefore, one ALD cycle for ZnO growth consists of 1s exposure to DEZ; 1s of $H_2O$ exposure and 29 s for the Ar purges. The last was kept intentionally long to address the growth on highly structured substrates as CNTs. Identical deposition conditions were used for the ALD of ZnO and $Al_2O_3$. Here the growth rate of ZnO and $Al_2O_3$ films was measured at 0.25 and 0.16 nm/cycle respectively. It is worth noting that the coverage at saturation depends generally on the ligand size and the surface density of active sites [31]. The obtained growth rate for ZnO is in line with reported values, but the $Al_2O_3$ growth rate is slightly higher [32,33].

We observed an ALD window for AZO at 120–150 °*C* with a constant GPC at 0.25 nm/cycle as shown in the Supplementary Materials. A decay of the GPC was noticed by decreasing the temperature below 120 °*C*, presumably due to the partial DEZ hydrolysis. A similar decay was observed by increasing the deposition temperature above 150 °*C*, which might be attributed to the thermally activated desorption of the precursor in the purge stage. The optimized ALD conditions for AZO film show a linear thickness increase with the number of cycles with neither induction time nor surface activation as depicted in Fig. S1*b*. Such a behavior is favorable for the precise control of the thickness.

The deposition temperature has also a direct impact on the thermal emittance of the resulting AZO films. The thermal emittance of the AZO (10:1) film is displayed in the Supplementary Materials (Fig. S2) as a function of the deposition temperature. The obtained thermal emittance features a minimum for films deposited at 150 °*C*, although the same number of deposition cycles was applied. The change of thermal emittance with the deposition temperature is presumably attributed to a variation of the *Al* doping concentration or to a contrasting distribution of aluminum in the film. These phenomena are due to a difference in the growth rate of ZnO and $Al_2O_3$ at high temperature [34], and to the thermally activated Al-diffusion respectively. In this context, Al segregation occurs at the grain boundary leading to a decrease in the charge carrier concentration as discussed in electrical property section. Reduced thermal emittance at 150 °*C* is correlated to the observed higher charge carrier concentration relative to films grown at high temperature. It is well admitted that a rise of charge carrier concentration favors the IR reflection, with a consequent decrease of the thermal emittance.

The ALD of AZO was performed using m = 1 and n = varying from 5 to 50. The XRD characterization of the resulting *Al* doped zinc oxide films is displayed in Fig. 2a. ZnO film features an average crystallite size of 33 nm that exhibits a single decay trend with the incorporation of $Al^{+3}$ to reach 8 nm for 8.5 at.% (Fig. 2b). As it might be anticipated, doping introduces defects in the ZnO lattice, which hinders the growth of large crystallites. Pure zinc oxide films feature a Wurtzite hexagonal crystal structure with a preferred (002) orientation, which is in line with the associated low surface energy [35,36]. Upon Al doping, the unit cell features a nearly linear contraction from ZnO (c = 5.20 Å; a = 3.23 Å) to AZO (8.5 at.% *Al:* c = 5.09 Å; a = 3.23 Å) as shown in Fig. 2c. This contraction is attributed to the substitution of $Al^{+3}$ on $Zn^{2+}$ sites [37]. The ionic radius of $Al^{+3}$ (0.54 Å) is small relative to $Zn^{+2}$ (0.72 Å), and the electroneutrality suggests the creation of cationic vacancies. Beyond the change observed on the lattice parameter, the preferred orientation of the film evolves from the (002) to (100) when *Al* concentration was raised to 3 at.% as illustrated in Fig. 2d, e. This is reasonably correlated to a change of the surface energy due to the intermixing of *Al* and *Zn* cations that disrupts the surface charges. Rising aluminum concentration above 3 at.% no longer influences the crystal orientation, which is in line with a reported maximal (002) peak intensity for 3 at.% *Al* doping in ZnO [38].

The electrical properties of AZO films were measured on glass substrates using the Van der Pauw configuration. A similar film thickness was used, (57 ± 2) nm, to focus on the composition effect. The electrical resistivity ($\rho$) decreases from 167 $m\Omega{\cdot}cm$ for pure ZnO, to a minimum of 5 $m\Omega{\cdot}cm$ at 4.7 at.% *Al* doping, as depicted in Fig. 3a. The calculated charge carrier concentration shows a 2 orders of magnitude increase from $1.26 \times 10^{18}$ $cm^{-3}$ for pure ZnO film, to a maximum at $2.41 \times 10^{20}$ $cm^{-3}$ for 4.7 at.% aluminum doping (Fig. 3b), whereas the charge mobility features a continuous decay with nearly one order of magnitude as illustrated in Fig. 3c. The last is attributed to the charge carrier scattering by impurity atoms and by grain boundaries, which is in line with the composition, and crystallite size trend displayed in Fig. 2b. It is noteworthy that the impact of *Al*-doping on the charge carrier concentration is dominant relative to their mobility. Above the optimal 4.7 at.% of *Al*-doping concentration, amorphous clusters of $AlO_x$ might form at grain boundaries as presumed in a previous report [39], which correlates reasonably with the solubility limit of *Al* in ZnO [40]. This phase would act as an electrons trap with a consequent decrease of charge carrier concentration and rise of the electrical resistivity. In line with the charge carrier concentration, the measured thermal emittance ($\varepsilon$) shows a minimum at the aluminum concentration of 4.7 at.%, as displayed in the Supplementary Materials. The uncoated substrate features an emittance of $\varepsilon$~0.94 that decreases to 0.87 when coated with ZnO. While preserving the same number of deposition cycles, *Al*-doping yields to a minimum emittance of $\varepsilon$~0.63.

The optical properties of the grown AZO on glass substrates were measured in the UV–VIS–NIR and the results are displayed in Fig. 4a. At first glance, aluminum doping induces a blue shift of the absorption edge

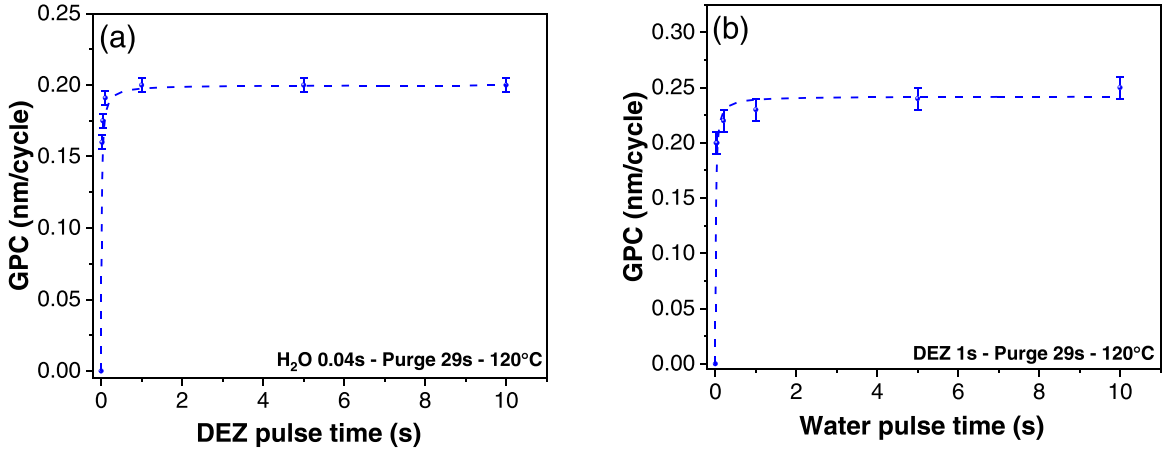


**Fig. 1.** ALD saturation curves for DEZ (a) and $H_2O$ (b) exposures.

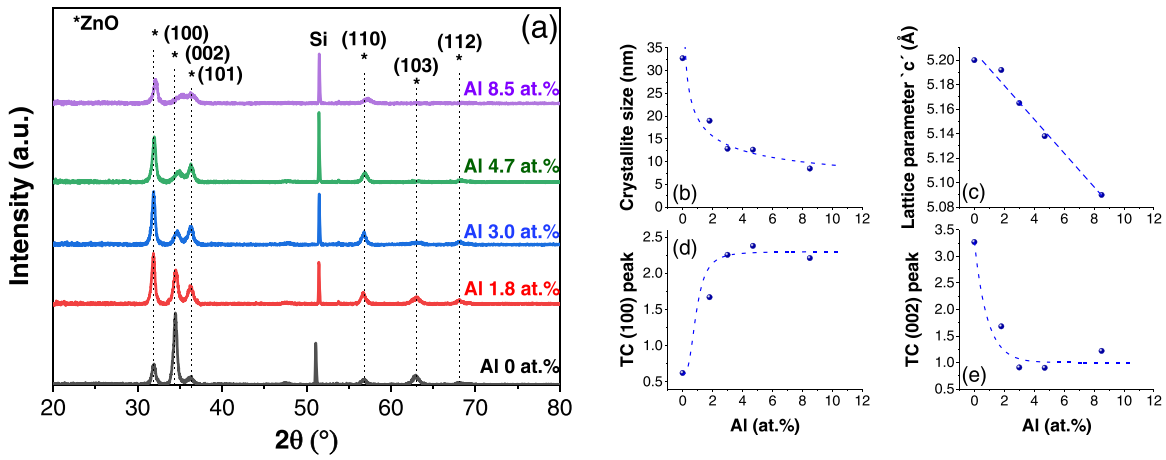


**Fig. 2.** XRD patterns of *Al*-doped ZnO films with Wurtzite (*hkl*) reference reflexes (a), and the extracted structural properties as a function of doping concentration (b–e).

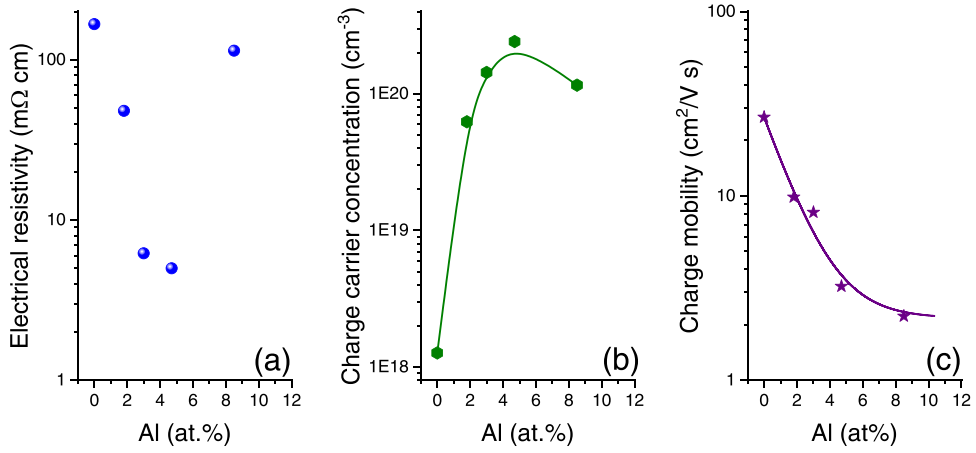


**Fig. 3.** Effect of the *Al* doping concentration on the electrical properties of AZO.

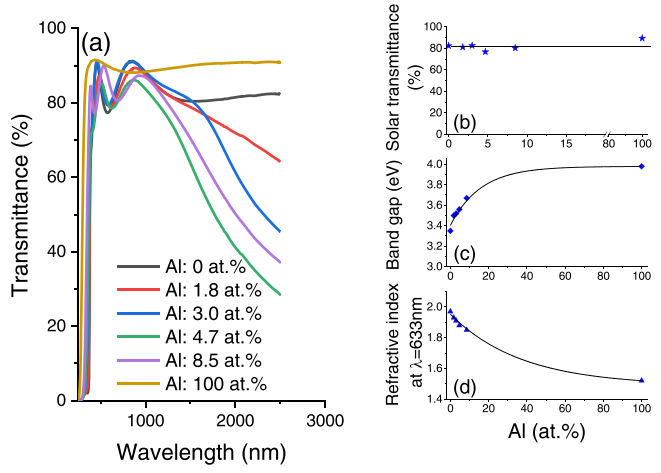


**Fig. 4.** Total integrated transmittance of AZO films on glass substrates (a) and the resulting optical parameters (b–d). (For interpretation of the references to colour in this figure, the reader is referred to the web version of this article.)

and a lower transmittance of the near-IR radiation, while a marginal change occurs in the visible range. The calculated solar transmittance, Fig. 4b, confirms a value of 80–90% irrespective of the film composition ZnO, AZO and $Al_2O_3$. Therefore, the transparency towards visible radiation is not significantly sensitive to aluminum doping. Nevertheless, the NIR transmittance features a minimum at an aluminum concentration of 4.7 at.%, which provides a similar trend as the emissivity (Supplementary Materials). This is associated to the free charge carrier absorption and scattering that occur in NIR for degenerate semiconductors.

The assessed band gap using Tauc plot, Fig. 4c, features an increasing trend with aluminum concentration from $E_g = 3.35$ eV (*Al:* 0 at.%) to $E_g = 3.68$ eV (*Al:* 8.5 at.%), which agrees with the measured increase of the charge carrier concentration. In fact, higher conduction band occupation leads to an increase of the fermi level according to Burstein-Moss effect, which explains the rise of the band gap [26]. The refractive index ($n$), assessed using ellipsometry, features a value of $n = 1.97$ for pure ZnO. This value decreases gradually with aluminum content to reach $n = 1.85$ with a concentration of 8.5 at.%, see Fig. 4d.

The investigated ALD process shows an efficient incorporation of Al into the ZnO lattice, which was demonstrated by a linear shrinkage of the lattice parameter "c", and a single trend in the variation of the bandgap, refractive index and electron mobility. These modifications are accompanied by a continuous decrease of the crystallite size and a change of their orientation, without impacting the solar transmittance. *Al* doping concentration of 4.7 at.% features an optimum in terms of concentration of charge carrier and thermal emittance, which encourages the use of this composition for further investigations.

The effect of the film thickness on the optical properties was investigated for films grown on glass substrates. The measured thermal

emittance decreases gradually from $\varepsilon = 0.94$ for non-coated glass, to $\varepsilon = 0.55$ for the deposition of 1750 cycles. The deposition of thicker AZO film does not further influence the thermal emittance as displayed in Fig. 5a. Therefore, it is reasonable to consider this emittance value as being the intrinsic property of ALD-made AZO. This emittance value agrees with the reported $\varepsilon = 0.6$ for 120 nm-thick AZO made by ALD [41].

The transmittance of visible light (400–700 nm), displayed in Fig. 5a, decreases from 91% for glass to 80% irrespective of the number of deposition cycles. This slight decrease of transmittance might be attributed to the higher refractive index of AZO relative to glass. Therefore, glass substrates remain significantly transparent after the deposition of AZO films. Results displayed in Fig. 5a confirm the relevance of implementing AZO as a transparent infrared reflecting layer for glazing application, and as a building block for the engineering of solar selective absorbers.

Thermal CVD was implemented to form a porous 3.5 $\mu m$-thick layer of randomly oriented CNTs as shown in the SEM inspection of the cross section in the Supplementary Materials. The formed CNTs, featuring an average diameter of ~10 nm, were used to grow AZO by ALD taking advantage of surface defects and the conformal nature of the ALD process. After ALD deposition of AZO, the morphology of the CNT film remained unchanged although a clear increase of the nanotube diameter can be noticed. Similar tubes' diameter can be noticed throughout the CNT layer, indicating a complete infiltration of the film (data shown in the Supplementary Information). The TEM characterization and electron diffraction, Fig. 6a, show AZO crystallites with various orientations around the tubular structure. The characteristic parallel walls of the CNT are also visible in the center of the tube. Further confirmation of the core/shell structure is provided with the HAADF-EDX analysis, which shows a carbon core and a shell composed of Zn, O and Al, Fig. 6b. An outer diameter of 45 nm after 88 deposition cycles, does correspond to the deposition of ~17.5 nm thick shell of AZO around the CNTs. This corresponds to a GPC of 0.2 nm/cycle which is slightly lower relative to the 0.25 nm/cycle measured by ellipsometry for the growth on planar silicon substrates. The outer diameter of CNT-ZnO estimated from the TEM observation agrees with that assessed by SEM inspection throughout the cross-section of the film as displayed in the Supplementary Materials (Fig. S6).

The solar absorbance and thermal emissivity of the CNT-AZO core/shell structure are displayed in Fig. 5b as a function of the shell thickness. Pristine CNT layers feature a solar absorbance of $\alpha_s = 0.9965$ and an emittance of $\varepsilon = 0.96$. The growth of AZO film on the CNTs reduces the emittance down to $\varepsilon = 0.6$, which is nearly the characteristic value for thick ALD-made AZO films on various substrates. Here solar absorbance is based on the measured total hemispherical reflectance (THR) at 0° angle of incidence. Nevertheless, no significant THR variation is observed with the angle of incidence owing to the random orientation of the CNTs [18].

The full potential of AZO in terms of emittance requires the application of 500 ALD cycles on the CNTs that nearly closes the porosity of the CNT layer. It is worth mentioning that the deposition of 1750 ALD cycles of AZO was necessary to reach this plateau on glass substrates (Fig. 5a).

The change of the emittance occurs with a slight loss of the solar absorption, which saturates at $\alpha_s = 0.96$ for thick AZO films. The loss of solar absorption results from the rise of reflection in the high-energy side of the visible spectrum, which is due to the inherent presence of defects in AZO (Fig. S8). ZnO features stable excitonic states just below the conduction band. The band gap of ZnO corresponds to a wavelength of ~370 nm, whereas transitions between the excitonic states and the valence band correspond to wavelengths in the UV spectral range (386–400 nm). The presence of other defects in ZnO such as interstitial oxygen and oxygen vacancies lead to transitions in the visible spectrum [42]. Furthermore, a higher reflection is also expected as AZO features a high refractive index relative to the porous CNT film.

The resulting CNT/AZO, core/shell structure, features an enhanced solar absorbance owing to the presence of a CNT core, and an emittance that corresponds to the applied transparent conducting oxide (AZO) shell. The thermal emissivity of the "CNT-AZO-4000 cycles" sample was measured by an IR camera operating in the 3–5 μm spectral range. Here pristine CNTs coating was taken as a reference perfect black body. The emissivity of the sample is constant up to 300 °C as shown in Fig. S9. A summary of the state of the art regarding carbon containing solar absorbers is displayed in Table S1. All these solar absorbers take advantage of metallic substrates to provide a background overall low emittance. While the performance is substrate-independent in the present case, and the reduced emittance is exclusively associated to the intrinsic properties of the applied composite coating. The implementation of stainless-steel substrates with a CNT coating thickness of 0.5 μm (SS-AZO-CNT) resulted in a higher solar absorbance and a lower thermal emittance relative to Si-CNT-AZO configuration (Table S1).

The thermal stability of the engineered CNT/AZO is however limited for the intended implementation at 1000 K under vacuum. The characteristic Raman bands of AZO ($E_2^1 : 99\ cm^{-1}$; $E_2^2 : 437\ cm^{-1}$) and CNT (D and G) are well identified for the as-grown core/shell structure [43]. The characteristic bands of CNT have completely vanished as a consequence of a 72 h ageing at 1000 $K$, and the coating is no longer black as displayed in Fig. 7a. In fact, the interface between ZnO and carbon is thermodynamically unstable above 670 $K$ where ZnO might undergo a carbothermal reduction, a reaction that converts carbon to CO and $CO_2$. Although the kinetics of this reaction is only relevant above 1200 $K$ [44] for macroscopic Carbon-ZnO powder mixture, an enhancement is expected for smaller particle sizes [45].

Based on thermodynamic considerations, the ALD of a thin $Al_2O_3$ layer (5 nm) was realized prior the deposition of AZO to stabilize the

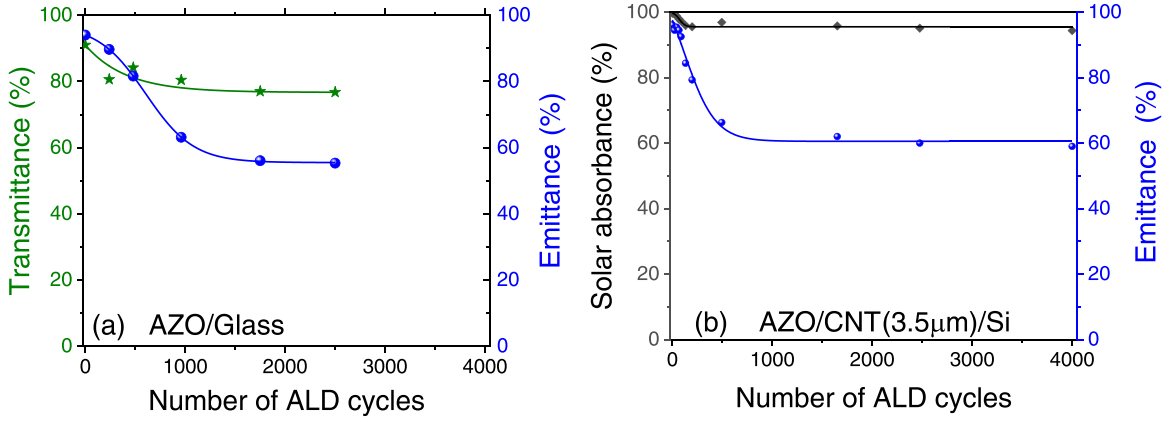


**Fig. 5.** Thermo-optical properties of Al doped ZnO films (4.7 at.% *Al*) on glass (a) and on CNTs (b) as a function of the number of deposition cycles.

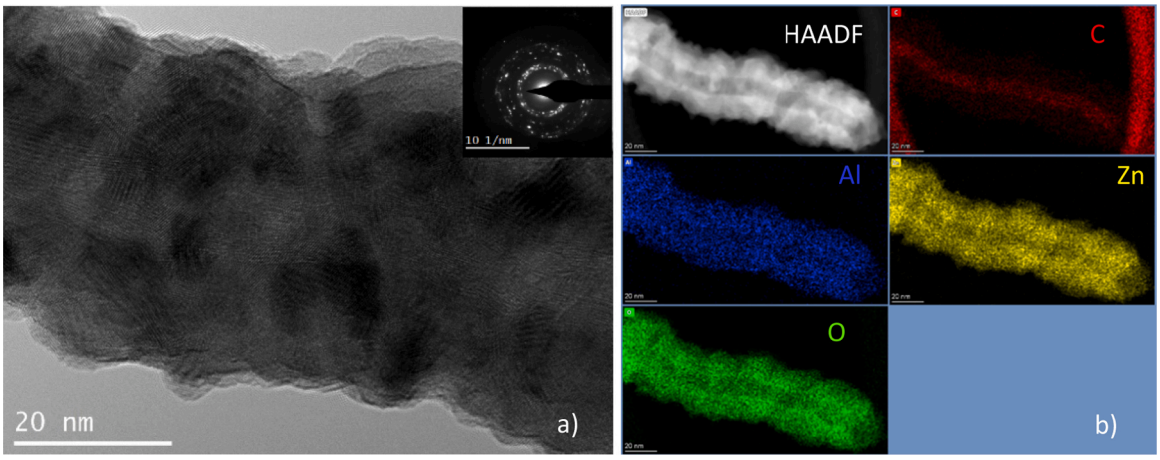


**Fig. 6.** a) TEM image with an insert corresponding to the diffraction pattern b) STEM-HAADF and EDX mapping of elements C, Al, O and Zn of an isolated AZO-coated CNT.

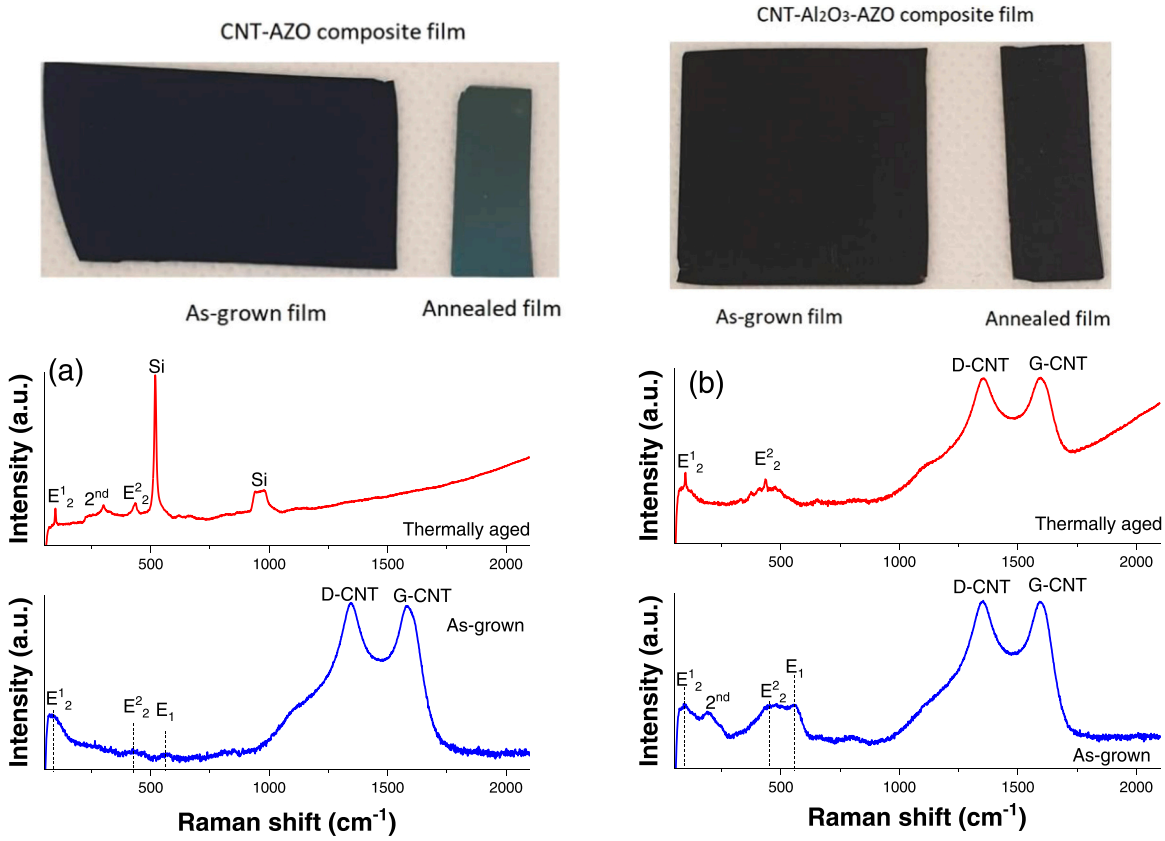


**Fig. 7.** Photo and Raman scattering of AZO coated CNT (a) and $Al_2O_3$-CNT (b) prior and after 72 h ageing at 1000 *K* under vacuum.

interface with CNTs. The TEM inspection (Fig. 8a) reveals a poly-crystalline AZO morphology that is similar to films directly grown on CNTs. The outer diameter is measured at 66 nm, which corresponds to 5 nm of $Al_2O_3$ and 23 nm of AZO around the CNTs. Unlike the direct growth on CNTs, the GPC of AZO on $Al_2O_3$/CNT is similar to the growth on planar *Si*. The obtained double shell structure is further evidenced by the elemental mapping displayed in Fig. 8b. The CNT core features a localized presence of carbon, while the outer shell indicates the presence of *Zn*, *Al* and *O*. A clear presence of *Al* with high intensity is situated at the interface, which confirms the formation of the CNT/$Al_2O_3$/AZO core/double shell structure. This structure withstands ageing at 1000 *K* for 72 *h* as displayed in Fig. 7b, unlike CNT/AZO. The black color of the film remains intact due to preservation of the CNTs after thermal ageing. The thermal emittance of the film, measured by IR camera, remains unchanged after ageing. In contrast, the emissivity of the CNT/AZO film is significantly reduced, Fig. S9, due to the oxidative removal of carbon from the film. The ALD process was implemented to further engineer the individual CNTs in the film as displayed in Fig. 8c, d. The displayed elemental mapping reveals an additional layer on top of AZO, which corresponds to the presence of *Al*, *Si* and oxygen. Here an aluminosilicate layer was applied as an upper layer using ALD. This layer exhibits a refractive index of ~1.5 which is appealing for antireflection.

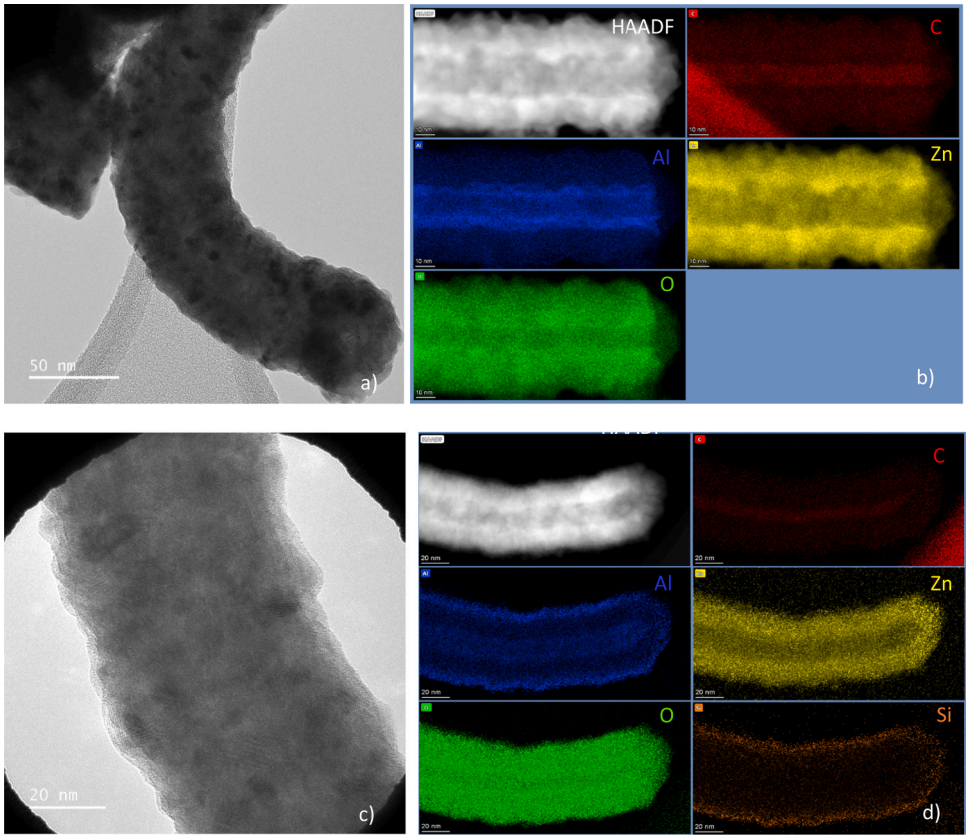


**Fig. 8.** TEM, STEM-HAADF and EDX mapping on coated CNTs with a double $Al_2O_3$/AZO (panels a-b) and triple $Al_2O_3$/AZO/AlSiOx (panels c- d) shell layers.

## 4. Conclusion

Aluminum doping in ZnO was optimized with the objective to minimize the thermal emittance without scarifying the solar transparency. Incorporating 4.7 at.% of *Al* in ZnO enabled a high charge carrier concentration with low electrical resistivity and low thermal emittance. The ALD of AZO was successfully carried out on CNTs to yield a core/shell structure with a CNT-typical high solar absorbance, $\alpha_s \geq 0.96$, and a near bulk thermal emissivity of AZO ($\varepsilon = 0.6$). The resulting core/shell is therefore an appealing building block for the design of high performance solar selective absorbers. An ultrathin aluminum oxide layer was introduced at the interface to overcome the thermal stability that was demonstrated at 1000 *K*, which makes CNT a promising candidate for the nanoengineering of selective solar absorbers for high temperature solar-thermal energy harvesting. Further CNT engineering was demonstrated using an outer low-refractive index layer.

## Declaration of Competing Interest

The authors declare that they have no known competing financial interests or personal relationships that could have appeared to influence the work reported in this paper.

## Acknowledgements

Vasu Prasad Prasadam and Naoufal Bahlawane would like to acknowledge funding through the MASSENA Pride and CORE programs of the Luxembourg National Research Fund (projects ID: FNR PRIDE/MASSENA/15/10935404 and C15/MS/10465305; BlackSelect).

## Appendix A. Supporting information

Supplementary data associated with this article can be found in the online version at doi:10.1016/j.mtcomm.2021.102552.

## References

[1] T.E. Drennen, J.D. Erickson, D. Chapman, Solar power and climate change policy in developing countries, Energy Policy 24 (1996) 9–16.
[2] R. Schmalensee, The future of solar energy: a personal assessment, Energy Econ. 52 (2015) S142–S148.
[3] A. Sharma, A comprehensive study of solar power in India and World, Renew. Sustain. Energy Rev. 15 (2011) 1767–1776.
[4] C.G. Granqvist, Solar energy materials, Adv. Mater. 15 (2003) 1789–1803.
[5] C. Kennedy, Review of Mid- to High- Temperature Solar Selective Absorber Materials, NREL/TP-520-31267, National Renewable Energy Laboratory, 2002. ⟨http://www.osti.gov/bridge⟩.
[6] K. Xu, M. Du, L. Hao, J. Mi, Q.H. Yu, S.J. Li, A review of high-temperature selective absorbing coatings for solar thermal applications, J. Mater. 6 (2020) 167–182.
[7] F. Cao, K. McEnaney, G. Chen, Z. Ren, A review of cermet-based spectrally selective solar absorbers, Energy Environ. Sci. 7 (2014) 1615–1627.
[8] Z.G. Fang, C.H. Lu, C.P. Guo, Y. Lu, D.S. Gao, Y.R. Ni, J.H. Kou, Z.Z. Xu, P.W. Li, Suitability of layered $Ti_3SiC_2$ and $Zr_3[Al(si)]_4C_6$ ceramics as high temperature solar absorbers for solar energy applications, Sol. Energy Mater. Sol. Cells 134 (2015) 252–260.
[9] C.K. Ho, A.R. Mahoney, A. Ambrosini, M. Bencomo, A. Hall, T.N. Lambert, Characterization of Pyromark 2500 paint for high-temperature solar receivers, J. Sol. Energy Eng. Trans. ASME 136 (2014), 014502.
[10] N. Selvakumar, S.B. Krupanidhi, H.C. Barshilia, Carbon nanotube-based tandem absorber with tunable spectral selectivity: transition from near-perfect blackbody absorber to solar selective absorber, Adv. Mater. 26 (2014) 2552–2557.
[11] T. Abendroth, H. Althues, G. Mader, P. Hartel, S. Kaskel, E. Beyer, Selective absorption of Carbon Nanotube thin films for solar energy applications, Sol. Energy Mater. Sol. Cells 143 (2015) 553–556.
[12] Q.H. Liao, P.P. Zhang, H.Z. Yao, H.H. Cheng, C. Li, L.T. Qu, Reduced graphene oxide-based spectrally selective absorber with an extremely low thermal emittance and high solar absorptance, Adv. Sci. 7 (2020), 1903125.
[13] K.T. Lin, H. Lin, T.S. Yang, B.H. Jia, Structured graphene metamaterial selective absorbers for high efficiency and omnidirectional solar thermal energy conversion, Nat. Commun. 11 (2020) 1389.
[14] R.K. Bera, S. Azoubel, S.G. Mhaisalkar, S. Magdassi, D. Mandler, Fabrication of carbon nanotube/indium tin oxide "Inverse Tandem" absorbing coatings with tunable spectral selectivity for solar-thermal applications, Energy Technol. 3 (2015) 1045–1050.

[15] N. Bahlawane, C. Pachot, U. Lafont, International Conference on Space Optics — ICSO 2016, SPIE2017, pp. 1056212.
[16] J. Lehman, C. Yung, N. Tomlin, D. Conklin, M. Stephens, Carbon nanotube-based black coatings, Appl. Phys. Rev. 5 (2018), 011103.
[17] R.Z. Zhang, X.L. Liu, Z.M.M. Zhang, Modeling the optical and radiative properties of vertically aligned carbon nanotubes in the infrared region, J. Heat. Transf. Trans. ASME 137 (2015), 091009.
[18] H.J. Basheer, C. Pachot, U. Lafont, X. Devaux, N. Bahlawane, Low-temperature thermal CVD of superblack carbon nanotube coatings, Adv. Mater. Interfaces 4 (2017), 1700238.
[19] M.E. Itkis, S. Niyogi, M.E. Meng, M.A. Hamon, H. Hu, R.C. Haddon, Spectroscopic study of the Fermi level electronic structure of single-walled carbon nanotubes, Nano Lett. 2 (2002) 155–159.
[20] M.E. Itkis, D.E. Perea, R. Jung, S. Niyogi, R.C. Haddon, Comparison of analytical techniques for purity evaluation of single-walled carbon nanotubes, J. Am. Chem. Soc. 127 (2005) 3439–3448.
[21] Z.-P. Yang, L. Ci, J.A. Bur, S.-Y. Lin, P.M. Ajayan, Experimental observation of an extremely dark material made by a low-density nanotube array, Nano Lett. 8 (2008) 446–451.
[22] X.L. Wei, M.S. Wang, Y. Bando, D. Golberg, Thermal stability of carbon nanotubes probed by anchored tungsten nanoparticles, Sci. Technol. Adv. Mater. 12 (2011), 044605.
[23] Y.A. Kim, H. Muramatsu, T. Hayashi, M. Endo, M. Terrones, M.S. Dresselhaus, Thermal stability and structural changes of double-walled carbon nanotubes by heat treatment, Chem. Phys. Lett. 398 (2004) 87–92.
[24] D. Ginley, H. Hosono, D. Paine. Handbook of Transparent Conductors, Springer, US, 2011.
[25] R.K. Bera, Y. Binyamin, S.G. Mhaisalkar, S. Magdassi, D. Mandler, Highly selective solar thermal sprayable coating based on carbon nanotubes, Sol. RRL 1 (2017), 1700080.
[26] Z.N. Gao, P. Banerjee, Review article: atomic layer deposition of doped ZnO films, J. Vac. Sci. Technol. A 37 (2019), 050802.
[27] V.P. Prasadam, N. Bahlawane, F. Mattelaer, G. Rampelberg, C. Detavernier, L. Fang, Y. Jiang, K. Martens, I.P. Parkin, I. Papakonstantinou, Atomic layer deposition of vanadium oxides: process and application review, Mater. Today Chem. 12 (2019) 396–423.
[28] P.A. Premkumar, A. Turchanin, N. Bahlawane, Effect of solvent on the growth of Co and $Co_2C$ using pulsed-spray evaporation chemical vapor deposition, Chem. Mater. 19 (2007) 6206–6211.
[29] H.J. Basheer, K. Baba, N. Bahlawane, Thermal conversion of ethanol into carbon nanotube coatings with adjusted packing density, ACS Omega 4 (2019) 10405–10410.
[30] A. Yamada, B.S. Sang, M. Konagai, Atomic layer deposition of ZnO transparent conducting oxides, Appl. Surf. Sci. 112 (1997) 216–222.
[31] R.L. Puurunen, Surface chemistry of atomic layer deposition: a case study for the trimethylaluminum/water process, J. Appl. Phys. 97 (2005), 121301.
[32] T. Tynell, M. Karppinen, Atomic layer deposition of ZnO: a review, Semicond. Sci. Technol. 29 (2014), 043001.
[33] M.D. Groner, F.H. Fabreguette, J.W. Elam, S.M. George, Low-temperature $Al_2O_3$ atomic layer deposition, Chem. Mater. 16 (2004) 639–645.
[34] M. Steglich, A. Bingel, G. Jia, F. Falk, Atomic layer deposited ZnO:Al for nanostructured silicon heterojunction solar cells, Sol. Energy Mater. Sol. Cells 103 (2012) 62–68.
[35] N. Fujimura, T. Nishihara, S. Goto, J.F. Xu, T. Ito, Control of preferred orientation for ZnOx films: control of self-texture, J. Cryst. Growth 130 (1993) 269–279.
[36] S.Y. Pung, K.L. Choy, X. Hou, C.X. Shan, Preferential growth of ZnO thin films by the atomic layer deposition technique, Nanotechnology 19 (2008), 435609.
[37] N.P. Dasgupta, S. Neubert, W. Lee, O. Trejo, J.R. Lee, F.B. Prinz, Atomic layer deposition of Al-doped ZnO films: effect of grain orientation on conductivity, Chem. Mater. 22 (2010) 4769–4775.
[38] P. Banerjee, W.J. Lee, K.R. Bae, S.B. Lee, G.W. Rubloff, Structural, electrical, and optical properties of atomic layer deposition Al-doped ZnO films, J. Appl. Phys. 108 (2010), 043504.
[39] Y. Wu, P.M. Hermkens, B.W.H. van de Loo, H.C.M. Knoops, S.E. Potts, M. A. Verheijen, F. Roozeboom, W.M.M. Kessels, Electrical transport and Al doping efficiency in nanoscale ZnO films prepared by atomic layer deposition, J. Appl. Phys. 114 (2013), 024308.
[40] Y.Z. Wu, A.D. Giddings, M.A. Verheijen, B. Macco, T.J. Prosa, D.J. Larson, F. Roozeboom, W.M.M. Kessels, Dopant distribution in atomic layer deposited ZnO: Al films visualized by transmission electron microscopy and atom probe tomography, Chem. Mater. A Publ. Am. Chem. Soc. 30 (2018) 1209–1217.
[41] K. Sun, C.A. Riedel, Y.D. Wang, A. Urbani, M. Simeoni, S. Mengali, M. Zalkovskij, B. Bilenberg, C.H. de Groot, O.L. Muskens, Metasurface optical solar reflectors using AZO transparent conducting oxides for radiative cooling of spacecraft, ACS Photonics 5 (2018) 495–501.
[42] R. Khokhra, B. Bharti, H.N. Lee, R. Kumar, Visible and UV photo-detection in ZnO nanostructured thin films via simple tuning of solution method, Sci. Rep. 7 (2017) 15032.
[43] V. Russo, M. Ghidelli, P. Gondoni, C.S. Casari, A.L. Bassi, Multi-wavelength Raman scattering of nanostructured Al-doped zinc oxide, J. Appl. Phys. 115 (2014), 073508.
[44] B.P. Jalan, V.K. Rao, The reduction of zinc oxide by carbon: non-catalyzed reaction, Can. Metall. Q. 16 (1977) 88–92.
[45] H.K. Chen, Kinetic study on the carbothermic reduction of zinc oxide, Scand. J. Metall. 30 (2001) 292–296.

# Supplementary Information

# CNT nanoengineering for thermally stable selective solar absorption

**Vasu Prasad Prasadam, Nicola Gautier, Naoufal Bahlawane**

The ALD of AZO using the DEZ and TMA hydrolysis gives a constant growth rate window between 120-150 °C as shown in figure S1a. The partial hydrolysis of the precursors is presumably the effect resulting in a decrease of the growth rate below 120 °C. At temperatures above 150 °C, however, the gradual decrease of the growth rate is attributed to the thermal desorption of the precursors and the reduction of surface-active sites. Along with the self-limited reactions in the ALD process, a linear growth was observed with the increase of the number of cycles as displayed in figure S1b.

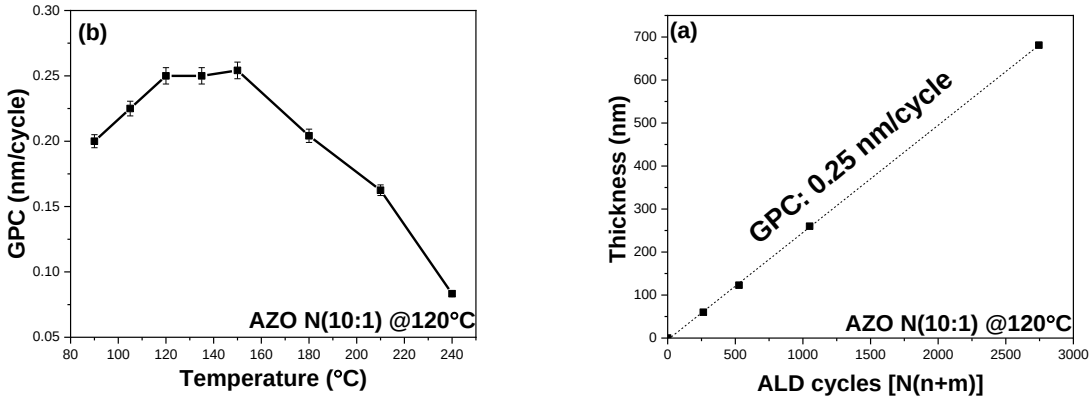


***Figure S1: ALD growth rate for AZO (10:1) at various temperatures (a), and a growth kinetics at 120°C (b). The number of cycles used to assess the GPC refers to*** $[N \cdot (n+m)]$***.***

The thermal emittance of AZO film was measured using the integrated total hemispherical reflectance in the 2.5-25 µm spectral range, and displayed for the AZO (10:1) (4.7 Al at.%) film as a function of the deposition temperature in Figure *S2*. A minimum value for the emittance was measured for films grown at 150°C, even though equal number of ALD cycles were used. The drop of the thermal emittance when increasing the temperature up to 150°C is correlated to the increase of the charge carrier concentration. The correlation between the charge carrier concentration and the thermal emittance is further confirmed when addressing the effect of aluminum doping concentration. Figure S3 displays a minimum in the thermal emittance trend at 4.7 at.% as Al concentration in the ZnO lattice. This agrees with the observed maximum in the charge carrier concentration trend (Figure 3b in the article).

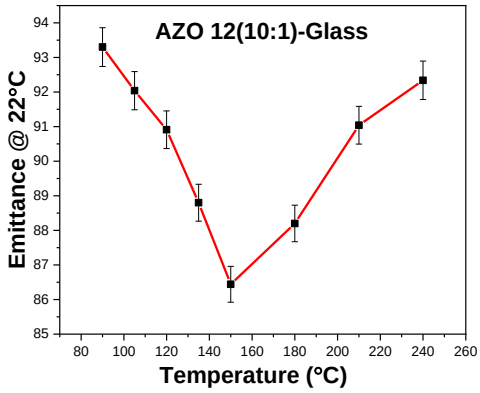


*Figure S2: Thermal emittance of AZO film grown on glass substrates as a function of the deposition temperature.*

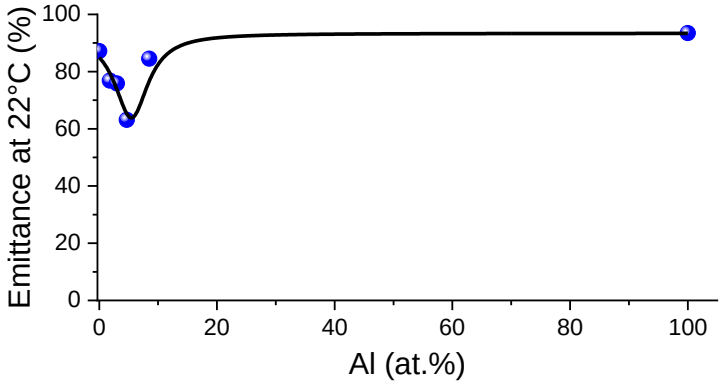


*Figure S3: Thermal emittance of AZO film grown on glass substrates as a function of aluminum doping concentration.*

The UV-VIS-NIR total hemispherical transmittance was measured for the optimal doping concentration (4.7 at.%) as a function of the number of ALD cycles and the results are displayed in Figure S4. A significant decrease of the NIR transmittance with a contraction of the transparency window is observed. A continuous decay of the transmittance was observed within the 1000-2000 nm window, which can be associated to both scattering and absorption by the free charge carriers.

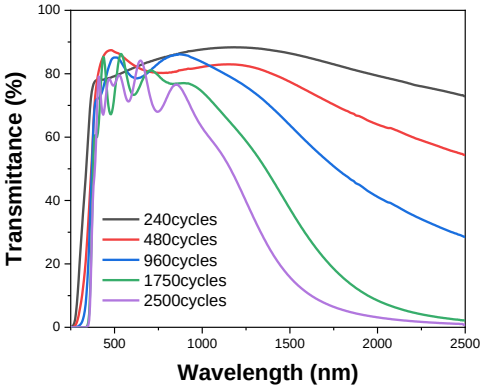


*Figure S4: Thickness effect on the total hemispherical transmittance of Al doped ZnO films (4.7 at.% Al) on glass substrates.*

Randomly oriented CNTs were deposited on silicon substrates using CVD at 450 °C. Figure *S5* shows the scanning electron microscopic inspection over the cross-section of a pristine CNT layer. The layer features a density of 0.4-0.5 mg/cm$^3$ which is more than 2 orders of magnitude lower relative to dense-packed CNTs. This high porosity is considered as an advantage for the present application. The CNT diameter is measured around 10 nm.

*Pristine CNT Overview*


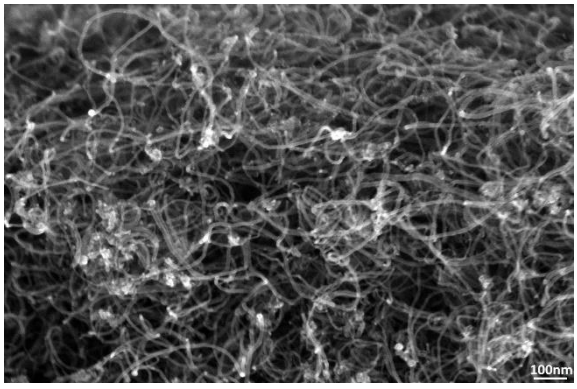


*near the surface*

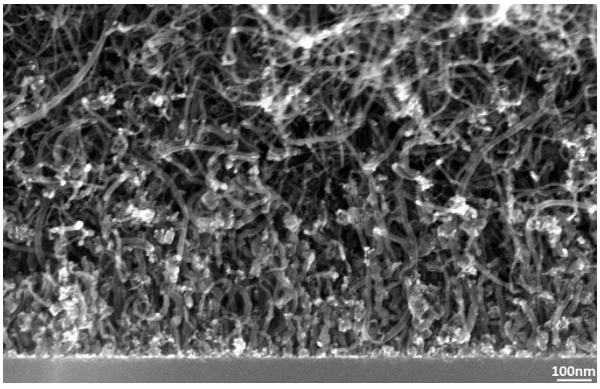


*near the silicon interface*

***Figure S5: SEM cross-section inspection of pristine CNTs with a thickness of 3.5 µm, ($\phi_{CNT}$=10 nm) with high magnification view in the near surface and interface regions.***

ALD coating of AZO on the CVD grown CNTs yields a conformal layer around the individual CNTs. The resulting core-shell structure is illustrated in the SEM inspection by the preservation of the tubular morphology while rising the diameter of the CNTs (figure S6). The growth rate was estimated on the CNT at 0.2 nm/cycle which is 20 % slower relative to deposition on planar silicon substrate. This behavior is attributed to the contrasting surface density of the nucleation sites. The film shows a typical polycrystalline surface morphology.

*As-grown AZO-CNT Overview*

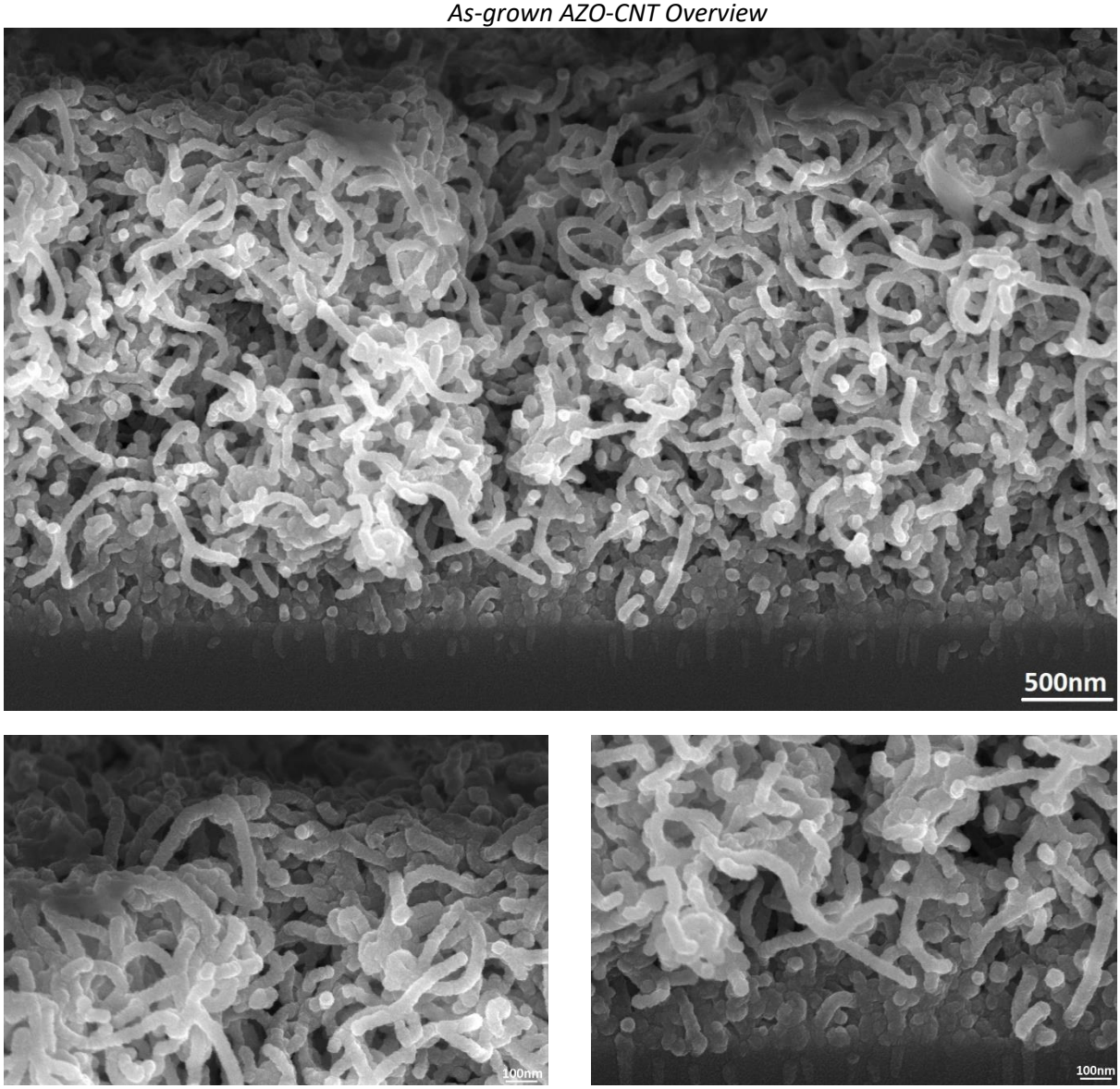


*near the surface* *near the silicon interface*

***Figure S6: SEM cross-section inspection of ALD coated CNTs with 88 cycles of AZO film (4.7 at.% Al) showing an apparent CNT diameter increase to reach ~45 nm both, near the surface and at the interface with silicon.***

Expending the number of AZO cycles leads to a complete densification of the porous CNT structure beyond 500 cycles. Higher number of ALD cycles leads to the formation of an AZO dense layer on top of the AZO-CNT composite as featured in figure S7.

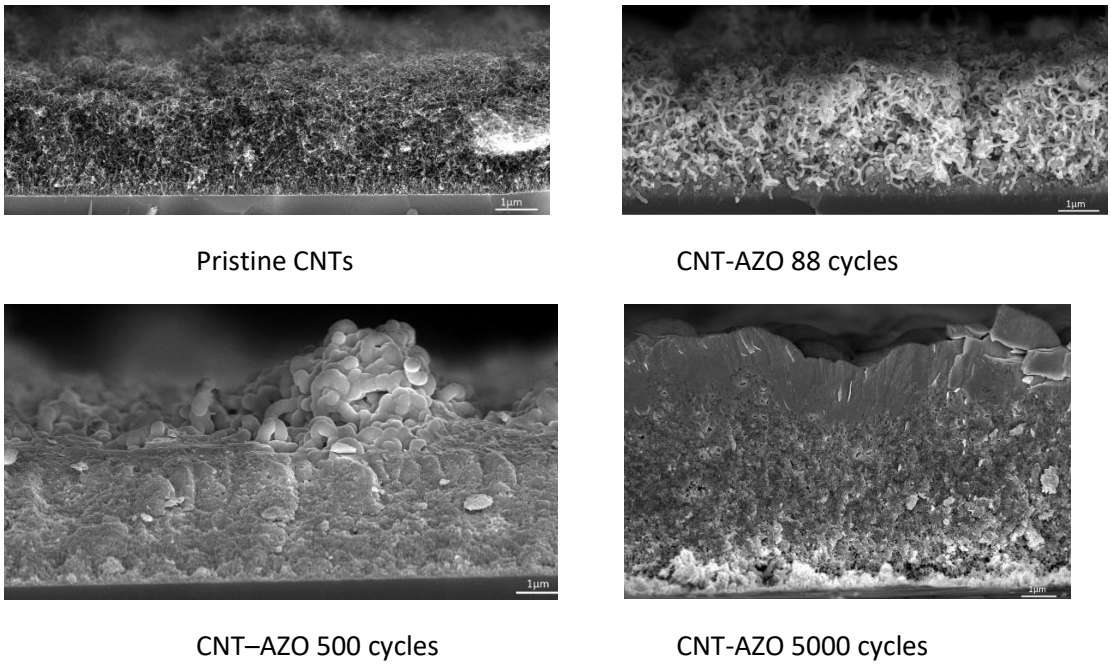


*Figure S7: SEM cross-section inspection of AZO/CNTs with increasing number of ALD cycles (0-5000).*

The UV-vis-NIR total hemispherical reflectance (THR) of CNT-AZO is displayed in Figure S8. Pristine CNTs have a reflection below 1% throughout the solar wavelength region (0.25-2.5 µm). Upon AZO coating on CNT structures, the reflectance increases in the UV side of the spectral window due to the presence of multiple defects in the ZnO lattice. There is a possible contribution of the Fresnel reflection due to the larger refractive index of AZO i.e. (1.85 at 633 nm) relative to porous CNT film.

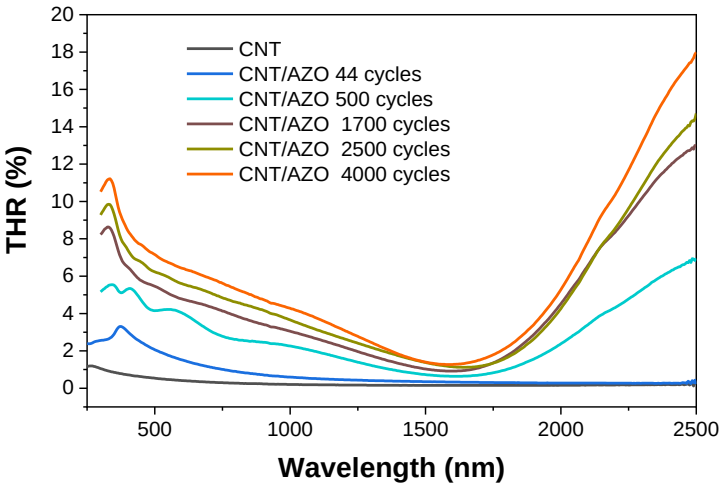


*Figure S8: Total hemispherical reflectance of Al doped ZnO films (4.7 at.% Al) on a 3.5 µm thick CNT layers.*

The thermal emissivity of CNT-AZO as function of the surface temperature is displayed in Figure S9. Emissivity CNT-AZO with/without $Al_2O_3$ interface layer has shown no significant temperature dependency irrespective of the thickness of the AZO layer. However, the emissivity is substantially reduced after thermal ageing at 1000 *K* for 72 *h* in absence of the $Al_2O_3$ interface layer and it becomes temperature dependent. This behavior is attributed to the oxidative removal of the CNT from the composite.

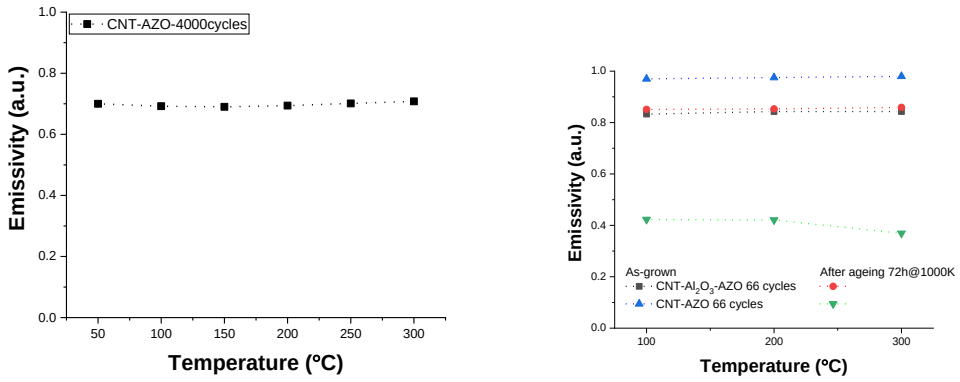


***Figure S9: Thermal emissivity assessed using an IR camera as function of the surface temperature; CNT-AZO-4000 cycles before thermal ageing (left), CNT-AZO-66 cycles with/without $Al_2O_3$ interface before/after thermal ageing at 1000 K for 72 h***

The benchmarking of the CNT/AZO performance as solar absorber is displayed in Table *S1* relative to the state of the art regarding carbon containing coatings.

Table S1: State-of-art of solar selective absorber based on carbon materials.

| Sample | Process | Solar absorbance (α) | Emittance (ε) | Figure of merit ($\alpha Q-\sigma\varepsilon T^4)/Q$ | Ref |
|---|---|---|---|---|---|
| SS-CNT-AlOOH +MTMS | Wet chemistry | 0.9 | 0.3 | 0.762219 | [1] |
| Al-CNT -AlOOH+TMMS | Wet chemistry | 0.98 | 0.9 | 0.566657 | [2] |
| Al-rGO-SiO2 | Wet chemistry | 0.92 | 0.04 | 0.901629 | [3] |
| Metal-black paint | Wet chemistry | 0.97 | 0.90 | 0.556657 | [4] |
| Al-CNT-SiO2 | Wet chemistry | 0.93 | 0.17 | 0.851924 | [5] |
| SS-CNT-SiO2 | Wet chemistry | 0.92 | 0.09 | 0.878666 | [6] |
| SS-Pyromark paint | Wet chemistry | 0.95 | 0.8 | 0.582584 | [7] |
| SS-AlTiO-CoO-CNT | CVD | 0.95 | 0.2 | 0.858146 | [8] |
| SS-CNT-ITO- | Wet chemistry | 0.72 | 0.12 | 0.664888 | [9] |
| Si-CNT | CVD | 0.99 | 0.96 | 0.555101 | Our work |
| Si-CNT-AZO | CVD-ALD | 0.95 | 0.6 | 0.675438 | |
| SS-CNT | CVD | 0.76 | 0.22 | 0.658961 | |
| SS-AZO-CNT | ALD-CVD | 0.97 | 0.24 | 0.859775 | |

Solar absorber efficiency is given in the form of figure of merit ($\eta$) as shown in equation 1

$$\eta = [\alpha Q-(\sigma\varepsilon T^4)]/Q \qquad \text{Eq 1}$$

$\alpha$ is solar absorbance, $Q$ is irradiance on absorber *(1000 W/m$^2$), $\sigma$* is Stefan–Boltzmann constant *(5.67x10$^{-8}$ W/m$^2$ K$^{-4}$)*, *T* is surface temperature *(300 K)*, *$\varepsilon$ is thermal emittance measured.*

Reference


1 Y. Vinetsky, J. Jambu, D. Mandler and S. Magdassi, *Coatings*, 2020, **10**, 1–12.

2 R. K. Bera, Y. Binyamin, C. Frantz, R. Uhlig, S. Magdassi and D. Mandler, *Energy Technol.*, , DOI:10.1002/ente.202000699.

3 Q. Liao, P. Zhang, H. Yao, H. Cheng, C. Li and L. Qu, *Adv. Sci.*, , DOI:10.1002/advs.201903125.

4 R. Harzallah, M. Larnicol, C. Leclercq, A. Herbein and F. Campana, *AIP Conf. Proc.*, , DOI:10.1063/1.5117538.

5 Z. Chen and T. Boström, *Sol. Energy Mater. Sol. Cells*, 2016, **157**, 777–782.

6 T. Abendroth, H. Althues, G. Mäder, P. Härtel, S. Kaskel and E. Beyer, *Sol. Energy Mater. Sol. Cells*, 2015, **143**, 553–556.

7 C. K. Ho, A. R. Mahoney, A. Ambrosini, M. Bencomo, A. Hall and T. N. Lambert, *J. Sol. Energy Eng.*, 2014, **136**, 2014–2017.

8 N. Selvakumar, S. B. Krupanidhi and H. C. Barshilia, *Adv. Mater.*, 2014, **26**, 2552–2557.

9 R. K. Bera, Y. Binyamin, S. G. Mhaisalkar, S. Magdassi and D. Mandler, *Sol. RRL*, 2017, **1**, 1–7.

### 3.1.5 Statements

We have developed ALD process of the metal oxides for planar silicon and 3D porous MWCNT substrate configurations through systematic ALD optimization. Metal oxides are deposited through hydrolysis of metal precursors. Synthesised vanadium dioxide film featured optical transition from semiconducting to metallic (SMT) with an external thermal stimulation. A continuous film morphology with significant improvement in surface roughness for thin film until 20nm thickness was obtained via argon plasma treatment prior to vacuum thermal treatment. Discontinuous $VO_2$ layer on the MWCNT has displayed optical absorption across the SMT, while continuous $VO_2$ layer featured optical reflectance. Morphology of the $VO_2$ layer deposited on the MWCNT surface had significantly influenced optical property of the $VO_2$-CNT composite structure. Optical modulation across the SMT for $VO_2$ decorated sample has shown unique innovative characteristics, which can be used for solar cooling devices. For instance, in solar thermoelectric device, an optimum temperature can always be maintained through $VO_2$ decorated structure to achieve maximum efficiency. Infrared reflectance obtained from metallic $VO_2$ on MWCNT is significantly low. A robust IR reflecting layer with very high transparency in the visible region is therefore required to reduce the overall thermal emissivity. In this context, Al-doped zinc oxide (AZO) is developed through the ALD process using zinc and aluminium alkyl precursors. Al is doped in ZnO lattice by incorporating trimethyl aluminium and water ALD cycle for every "n" number of DEZ, water ALD cycles, which determines the Al dopant ratio. Al dopant of 4.7 at% is considered optimum value because of its minimum electrical resistance and thermal emittance values. The optimised Al-doped zinc oxide films are deposited on the 3D porous MWCNT structures to form a core-shell structure. Systematic optical properties were studied for various AZO layer thicknesses. Solar absorbance decreased insignificantly from 0.995 to 0.96, while thermal emittance decreases significantly from 0.995 to 0.6, with an increase in AZO layer thickness from 0 to140 nm. Further increase in AZO thickness has not demonstrated any improvement of the solar selectivity. However, high temperature annealing under vacuum structure has a detrimental impact on solar absorbance of CNT-AZO core-shell structure. Nevertheless, an $Al_2O_3$ interface layer between CNT and AZO has illustrated thermal stability without any negative impact on solar absorbance and the thermal emittance. Thus, Nano-engineering of hybrid composite material for solar thermal technology application is feasible through the developed CVD-ALD process.

## 3.2 SOLAR $H_2$ ENERGY

Chemical energy storage in the form of $H_2$ produced by solar water splitting stands as a promising technology for long-term storage. In this process, semiconductors play an important role via the capture of photons and driving the water splitting reaction along a photo-electrochemical process. Current photovoltaic materials suffer from poor chemical stability and cost-effectiveness. On the other hand, metal-oxide semiconductors feature a better chemical stability, favourable optical band energies, and high abundance in the earth`s crust. Nevertheless, poor electrical conductivity and short carrier diffusion lengths limits their usage as electrode materials in solar water splitting technologies. In this context, nanostructured metal oxides diminish carrier diffusion limitations, and the addition of MWCNT gives a scope to improve the electrical conductivity.

This section is based on the work of MWCNT-ZnO and MWCNT-$TiO_2$ core-shell structure developed by CVD-ALD process. Photo-electrochemical characterizations are performed to estimate their solar water splitting performance.

### 3.2.1 MWCNT-ZnO for the solar $H_2$ application

Several oxides have been studied intensively as photoanodes, among them ZnO has a high charge mobility 200-300 $cm^2V^{-1}s^{-1}$ and a favourable band alignment relative to water reduction potential (0 $V_{RHE}$) and oxidation potential (1.23 $V_{RHE}$). ALD optimized ZnO layer was conformally coated on the MWCNT. Photoelectrochemical comparison of planar ZnO films and MWCNT-ZnO hybrid nanostructure revealed an improved solar water splitting performance for the hybrid nanostructure. The band alignment of MWCNT-ZnO interface favours a spontaneous electron transfer from ZnO to MWCNT. The difference in performance between Si-ZnO and MWCNT-ZnO was associated with the diminished electron-hole recombination, efficient electron collection and increased relative surface in MWCNT-ZnO core-shell structure.

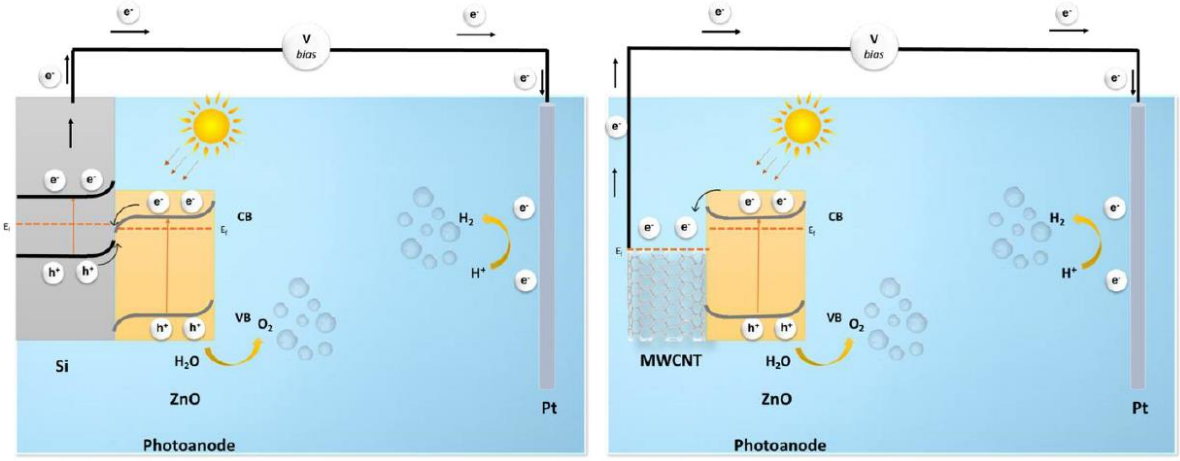

# CNT-ZnO core-shell photoanodes for Photoelectrochemical water splitting

Vasu prasad PRASADAM, Ali Margot HUERTA FLORES, Naoufal BAHLAWANE

*Material Research and Technology Department,* Luxembourg Institute of Science and Technology, Rue du Brill, L-4422 Belvaux, Luxembourg

## Abstract

Solar-driven water splitting is a promising route toward clean $H_2$ energy and the photoelectrochemical approach attracts a strong interest. The oxygen evolution reaction is widely accepted as the performance limiting stage in this technology, which emphasizes the need of innovative anode materials. Metal oxide semiconductors are relevant in this respect owing to their cost-effectiveness and broad availability. The combination of chemical vapor deposition and atomic layer deposition was implemented in this study for the synthesis of randomly oriented CNT-ZnO core-shell nanostructures forming an adhering porous coating. Relative to a directly coated ZnO on Si, the porous structure enables a high interface area with the electrolyte and a resulting 458 % increase of the photocurrent density under simulated solar light irradiation. The photoelectrochemical characterization correlates this performance to the effective electrons withdrawing along the CNTs, and the resulting decrease of the onset potential. In terms of durability, the CNT-ZnO core-shell structure features an enhanced photo-corrosion stability for 8 h under illumination and with a voltage bias.

## Introduction

Most carbon emission is related to the combustion of fossil fuels for transportation and electricity generation, which results in greenhouse effect with the worrying global warming[1]. A widespread implementation of renewable non-fossil fuels is therefore relevant in this context[2]. Hydrogen is a clean energy carrier with enormous potentials for transportation and power generation owing to its high energy density (142 MJ/Kg) relative to gasoline (47 MJ/Kg)[3],[4]. A positive impact on the environment requires however a shift from the current dominance of $H_2$ production from fossil fuels. Clean $H_2$ production is feasible with solar water splitting technology e. g. photovoltaic coupled with electrolyser (PV-EC), photo catalysis (PC) and photo electrochemical catalysis (PEC) [5]. PEC presents advantageous scalability and cost among these technologies, nevertheless, the performance is limited by the availability of efficient photoanode materials that are responsible for the oxygen evolution reaction (OER).

Conventional photovoltaic electrode materials with low band gap energy (1.3-2.4 eV) and high carrier mobility, e.g. transition metal sulphides and selenides, were successfully used in PEC technology. Nevertheless, these materials feature a strong ageing due to photo-corrosion in acidic and alkaline media[6],[7],[8]. Semiconductor metal oxide alternatives are less expensive, non-toxic and abundantly available in the earth`s crust. Several oxides have been studied intensively as photoanodes such as, $BiVO_4$, $TiO_2$, ZnO, $WO_3$ and $Fe_2O_3$ [9],[10]. Among these materials ZnO has a high charge mobility 200-300 $cm^2V^{-1}s^{-1}$ and an electron lifetime exceeding 10 s [11], but it has a limited chemical stability[8]. ZnO features a favourable band alignment with a more negative conduction band (-0.15 $V_{RHE}$) relative to water reduction potential (0 $V_{RHE}$) and a more positive valence band (3.05 $V_{RHE}$) relative to water oxidation potential (1.23 $V_{RHE}$)[12]. $V_{RHE}$ stands for the potential relative to the reversible hydrogen electrode (RHE). The resulting high band gap limits, however, the theoretical photocurrent to ~1.8 mA $cm^{-2}$ [6]. The enhancement of ZnO's performance as a photoanode in PEC water splitting was reported via nano-structuring, doping and the implementation of a co-catalyst[13], but the chemical instability remains a primary issue in highly acidic and highly alkaline media [14]. The dark electrochemical dissolution of ZnO occurs at 2 V versus standard hydrogen electrode[15]. The photo generated surface holes oxidize ZnO in aqueous solutions, which enhances the corrosion. The last might be inhibited by cationic/anionic doping, hybridization with co-catalysts, carbon materials or by forming heterojunctions[16]. The photo-corrosion of the anode material can be reduced in PEC by adding a hole scavenging agent in the electrolyte[17],[18] or by implementing a passivation layer. In this context, $TiO_2$[19], CoO[20],$CoNiO_x$[21], NiO[22] and $Ta_2O_5$[23] confer a long term photo stability to ZnO. Adjusting the thickness of the passivation layer is crucial to optimize the resulting performance [24], which makes Atomic Layer Deposition (ALD) a particularly efficient process [25]. The

implementation of solution-based processes requires the application of an additional hydroxide overlayer [26].

The application of a carbon layer was also proven efficient for the reduction of ZnO photo-corrosion in aqueous solutions[27], and this effect was associated to the improved charge carrier separation. In fact, the work function of ALD grown ZnO is 3.78 eV[28], while that of multiwall CNT (MWCNT) is reported at 4.95 eV[29]. A spontaneous electron transfer is therefore expected from ZnO to MWCNT, followed by the formation of a Schottky barrier, which the height might be reduced via the application of a forward bias, resulting in the promotion of further flow of electrons from ZnO to CNT [30].The high electrical conductivity of carbon prevents electrons from accumulating at the ZnO-carbon junction[31]. Covering ZnO surface with reduced graphene oxide[32],[33] or $C_3N_4$[34] confers few hours protection from photo-corrosion.

Photocurrent densities varying from 0.2 to 0.6 mA $cm^{-2}$(at 1.23 $V_{RHE}$)[35][19][36] were reported for ZnO nanostructures synthesised by wet chemistry, and the reproducibility is noticed as an issue. Chemical vapour deposition (CVD) resulted in a reproducible photocurrent of $I_{ph}$ = 1 mA $cm^{-2}$ (at 1.23 $V_{RHE}$) [37][38], however, the needed high deposition temperature is restrictive in terms of substrates. Atomic layer deposition (ALD) is highly suitable for low temperature deposition of pinhole-free, conformal and crystalline ZnO[37]. These advantages were used to design semiconductor-ZnO heterostructures with core-shell architectures i.e. CdS-ZnO ($I_{ph}$ = 0.55 mA $cm^{-2}$ at 1.5 $V_{RHE}$)[39], $TiO_2$-ZnO ($I_{ph}$ = 0.6 mA $cm^{-2}$ at 1.3 $V_{RHE}$)[40] and N-doped porous silicon-$TiO_2$-ZnO ($I_{ph}$ = 4 mA $cm^{-2}$ at 1.5 $V_{RHE}$)[41]. These heterostructures still however feature photo corrosion. In this study, the ALD is proposed for the design of a CNT-ZnO core-shell architecture and a focus will be given to the photoelectrochemical characterization and stability against photo-corrosion.

## Experimental Section

The synthesis of the CNT-ZnO nanocomposite film involves a single-pot hybrid CVD-ALD process. Multiwalled carbon nanotubes (CNTs) were grown on silicon substrates by thermal chemical vapour deposition (CVD) with a single precursor feedstock [ethanol solution of $0.65 \times 10^{-3}$ mol $L^{-1}$ of cobalt acetylacetonate ($Co(acac)_2$) and $0.65 \times 10^{-3}$ mol $L^{-1}$ of magnesium acetylacetonate ($Mg(acac)_2$)]. This feedstock was introduced into the reactor via an evaporation cylinder at 220 °C, using a pulsed spay with a frequency of 4 Hz and using the opening time of 4 ms. The growth temperature was kept at 485 °C and the pressure at 10 mbar. Further details regarding the process are reported elsewhere[42],[43]. ZnO films are deposited using thermal ALD with the sequential hydrolysis of diethyl zinc (DEZ) precursor. Precursors were kept at room temperature and the substrate temperature was set at 150 °C. One ALD cycle for ZnO growth consists of a separated 1 s exposure to

DEZ and 1 s exposure to $H_2O$ with 29 s of Ar purge. The ALD saturation conditions are reported elsewhere[44].

The thickness of ZnO films grown on silicon substrates was assessed using a multi-wavelength Ellipsometer (Film Sense) with the Cauchy model. The crystallinity was investigated using X-ray diffraction (Bruker D8), with Cu-$K_\alpha$ as the X-ray source. Data were collected in the grazing incidence mode at 0.5° and a detector scanning from 20° to 80° with a step size of 0.02°. Raman scattering was performed using an InVia Raman spectrometer from Renishaw with a 532 nm laser and a power density of 2.35 mW/cm$^2$. The morphology of the films was inspected using the FEI Helios Nanolab 650 scanning electron microscope (SEM) at a working distance of 5 mm and using 5 V as the acceleration voltage.

A standard three-electrode setup was used for the photoelectrochemical measurements with CNT-$TiO_2$ as a working electrode. All voltages were measured versus Ag/AgCl reference electrode and platinum (Pt) was used as the counter electrode. The electrolyte was an aqueous solution of 0.1 M NaOH (pH 12.7). All the potentials from Ag/AgCl reference are converted to RHE based reference by given equation 1.

$$E_{RHE}\,(V) = E_{Ag/AgCl}\,(V) + 0.059 * pH + 0.1976 \qquad \text{Eq 1}$$

The electrode area, 2 cm$^2$, was front-illuminated by a Xe-lamp at 100 mW/cm$^2$. Electrochemical measurements were conducted using an AUTOLAB potentiostat. Steady state current-voltage curves were used for assessing the electrochemical performance.

## Results

The ALD of ZnO has been optimized to secure self-limited reactions upon DEZ and water exposure. The growth rate per cycle was measured at 0.24 nm/cycles, which is in line with the literature[45]. This rate is significantly low when the deposition is applied on the randomly oriented CNTs. Conformal growth of ZnO across the CNT thickness was noticed in the cross-section SEM image displayed in the figure 1. Upon deposition of 130 ALD cycles of ZnO, the outer diameter of the CNTs increases from 10 nm to 40-50 nm. Here the growth rate per cycle (GPC) of ZnO on the CNT surface was approximated to 0.12-0.15 nm/cycles. The low GPC on CNT relative to silicon surface is attributed to a contrast in surface nucleation sites. The porous nature of the CNT-ZnO core-shell configuration was retained still with the deposition of 550 ALD cycles, which corresponds to a ZnO thickness of 74 nm. In contrast, the deposition of 1100 ALD cycles, with an expected ZnO thickness of 150nm, fills the porosity in the CNT film, and results in a compact CNT-ZnO composite film.

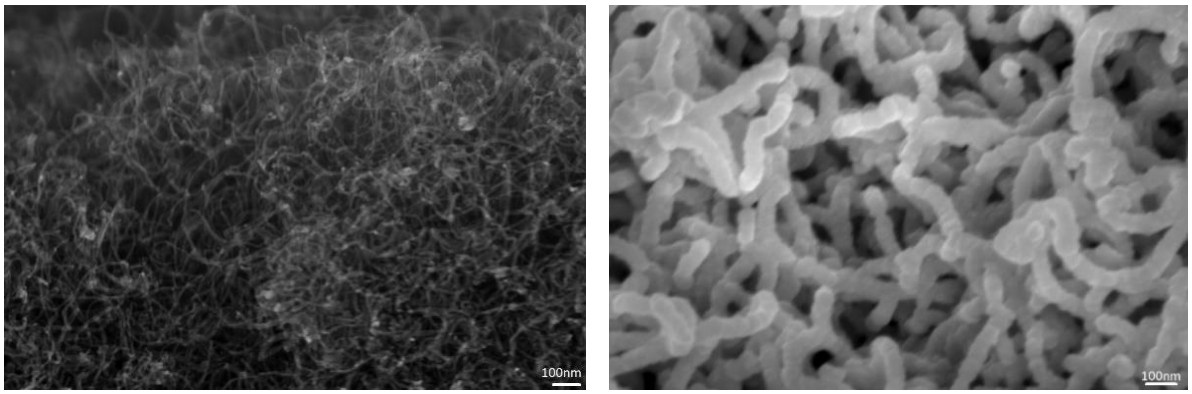


*Figure 1: SEM observation of pristine CNT film (left) and of Si-CNT-ZnO-18 nm (right).*

The grown ZnO on Si-CNT is polycrystalline as shown by the XRD measurements in Figure 2a. The observed peaks and their intensity correspond to the polycrystalline wurtzite ZnO (PDF: 04-015-4060). The crystallite size, calculated from these spectra using the Williamson-Hall method, increases with ZnO thickness to reach a saturation above 550 ALD cycles (Figure 2b). Raman scattering of the CNT-ZnO core-shell structure shows the expected ZnO characteristic peaks at 99 and 438 $cm^{-1}$ that correspond to the $E_2^{low}$ and $E_2^{high}$ modes (Figure 2c). The phonon confinement effect is revealed via the detection of broad first order $A_{1\text{-}LO}$ peaks at 571 $cm^{-1}$ and 2$^{nd}$ order $A_1$ overtones at 203, 333 $cm^{-1}$, and by the decreasing peak intensity ratio (2$^{nd}$ order/1$^{st}$ order) with the thickness of ZnO [46]. The other observed peaks, 1356 and 1595 $cm^{-1}$, correspond to D and G bands of the CNTs[47].

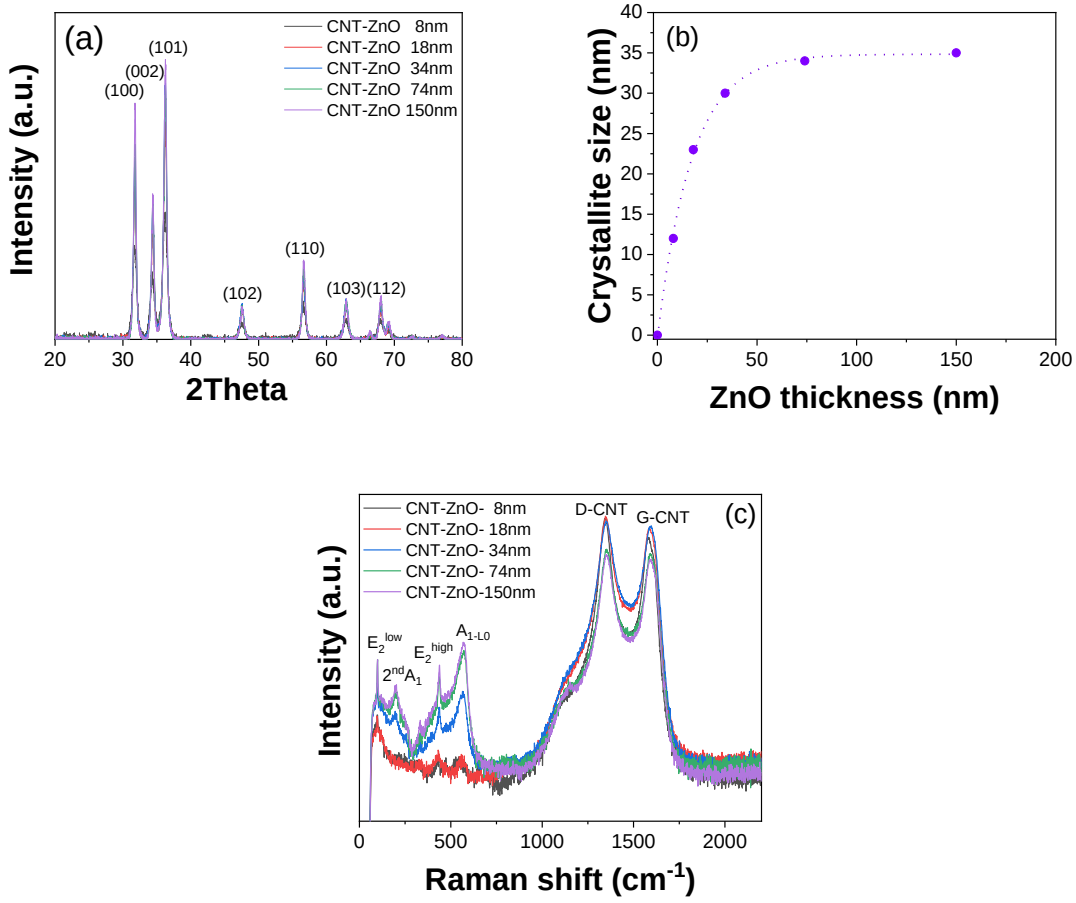

*Figure 2: XRD spectra of the CNT-ZnO coatings on silicon (a) with the extracted crystallite size (b); and their respective Raman spectra (c)*

The synthesized CNT/ZnO core/shell coatings were investigated as anode materials for the photoelectrochemical waster splitting. The oxygen evolution reaction (OER) occurs at the photoanode in PEC technology involving four photogenerated holes ($h^+$) as shown in equation 1. In fact, the generated electron-hole pairs in ZnO upon illumination are separated. While, holes are transferred to the surface of ZnO to contribute to the oxidation of water, electrons are transported via an external electrical circuit to the cathode where they contribute to the hydrogen evolution reaction (HER). Generally, water splitting onset potential occurs over 1.23 $V_{RHE}$ in the absence of catalysts.

$$2H_2O + 4h^+ \rightarrow O_2 + 4H^+ \text{ (OER)} \qquad \text{Eq1}$$

Although the surface area of CNT-ZnO is significantly higher than the planar ZnO on silicon, the photo-electrochemical performance is normalized to the geometric surface area. The photoelectrochemical process, as in this contribution, relies on light absorption to photo-generate charge carriers. In this regard, the reaction is driven by the incident solar radiation that scales with the geometric area. The Si-CNT-ZnO configuration is more suited to trap sunlight but the CNT will strongly compete for the light absorption which generate heat instead of electrical charges. These two effects counteract to result in a trade-off under a constant illumination flux.

The photocurrent density is illustrated in figure 3a for the ALD-grown ZnO on Si and Si-CNT substrates with a comparable ZnO thickness. Bare silicon substrate has shown a very low photocurrent value of 1 μA $cm^{-2}$ in chronoamperometric measurement at 1.23 $V_{RHE}$, versus 2 μA $cm^{-2}$ for pristine Si-CNT. The measurable photocurrent in pristine CNT is presumably attributed to the cobalt particles formed during the CVD process of CNTs, which might convert to cobalt oxide upon interaction with the electrolyte. It is worth reminding that cobalt is used as a catalyst for the growth of CNT films. The photocurrent density in the absence of ZnO remains however marginal in both cases. Si-CNT-ZnO sample featured a photocurrent density of 0.55 mA $cm^{-2}$ at 1.23 $V_{RHE}$, which is 458 % that of Si-ZnO (0.12 mA $cm^{-2}$).

The cyclic voltammetry (CV) was measured under illumination with a sweep rate of 0.1 V/s, and the results are displayed in Figure 3b and 3c. These measurements reveal the need of a bias exceeding 1.5 $V_{RHE}$ to reach a current density of 2 μA/$cm^2$ on silicon substrates. This onset potential, defined as the potential bias needed to reach a photocurrent density of 2 μA $cm^{-2}$, reduces significantly to reach 0.46 $V_{RHE}$ with the deposition of a 62 nm thick ZnO film on Si. Further reduction of the onset potential was observed to reach 0.32 $V_{RHE}$ for ZnO coated Si-CNT with a comparable thickness, which is 140 mV lower relative to Si-ZnO. Similar onset potential was reported for Carbon-ZnO nanocomposite[34].

Pristine Si-CNT shows a very large hysteresis with current densities of 0.5 mA $cm^{-2}$ and -0.25 mA $cm^{-2}$ in the forward and reverse sweep respectively at 1.23 $V_{RHE}$. As this high current density vanishes in

static measurement, chronoamperometry, it is most likely originating from the non-faradaic capacitive charging[48]. This contribution is not evidenced in the other samples, Si, Si-ZnO and Si-CNT-ZnO, as marked by the quasi-absence of a hysteresis in the CV measurement. This observation is in line with the attribution of the capacitive current to the presence of exposed CNT surface to the electrolyte, and their efficient coverage by ZnO.

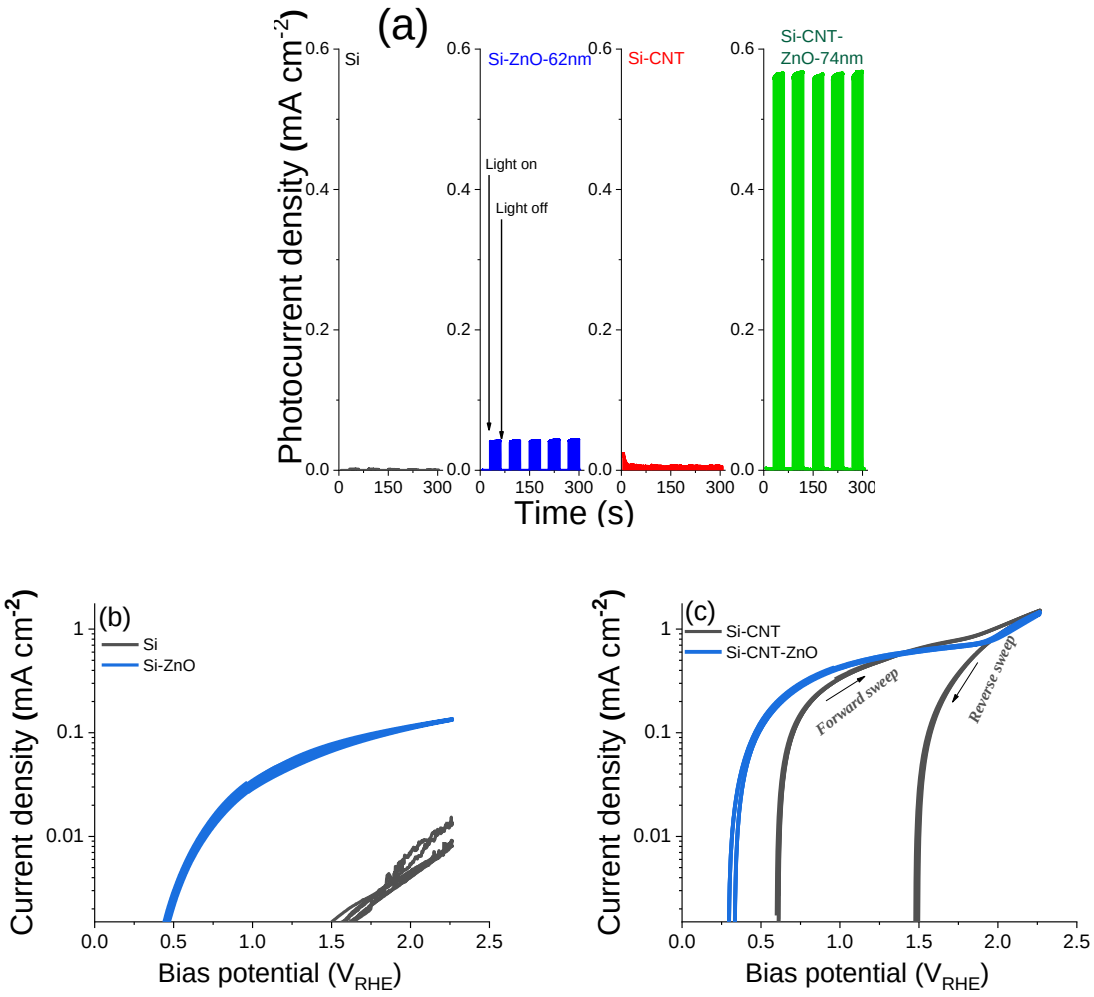


*Figure 3: Chronoamperometric measurements at 1.23 $V_{RHE}$ (a) and the cyclic voltammetry at 0.1V/s sweep rate for the noncoated and ZnO-coated Si (b) and Si-CNT (c) substrates. The thickness of ZnO is 74 nm on the CNTs and of 62 nm on Si.*

The photocurrent density obtained for the Si-CNT-ZnO samples is presented in figure 4 for various ZnO thicknesses. The chronoamperometric measurement at 1.23 $V_{RHE}$ shows a rise of the photocurrent density with ZnO thickness up to a maximum value of 0.55 mA $cm^{-2}$ for 74 nm and a further increase of the thickness leads to a decay in photocurrent density. It is worth reminding that the CNT-ZnO core-shell structure is no longer an appropriate description at, and above a ZnO thickness of 150 nm as the porosity is filled. The amplitude of the photocurrent is directly related to various parameters including the ZnO-electrolyte interface area, effectiveness of the charge separation and the light penetration depth. The last was reported for ZnO at 50-65 nm from λ:280-360 nm respectively[49]. Therefore, increasing the thickness of ZnO, below the light penetration depth, rises the number of photogenerated charge carriers as a higher volume fraction is concerned by the photogeneration of

charges[50]. As a result, a maximum photocurrent can be expected when varying the ZnO film thickness[40],[51]. This behaviour is observed in the case of grown ZnO on Si, where a photocurrent plateau is observed above 100 nm (Figure 4b). The increase of ZnO thickness on CNT, however, can close the porosity that leads to a reduced surface area. Hence, a trade-off is established between the surface area and the light penetration when adjusting the thickness of ZnO on the CNTs.

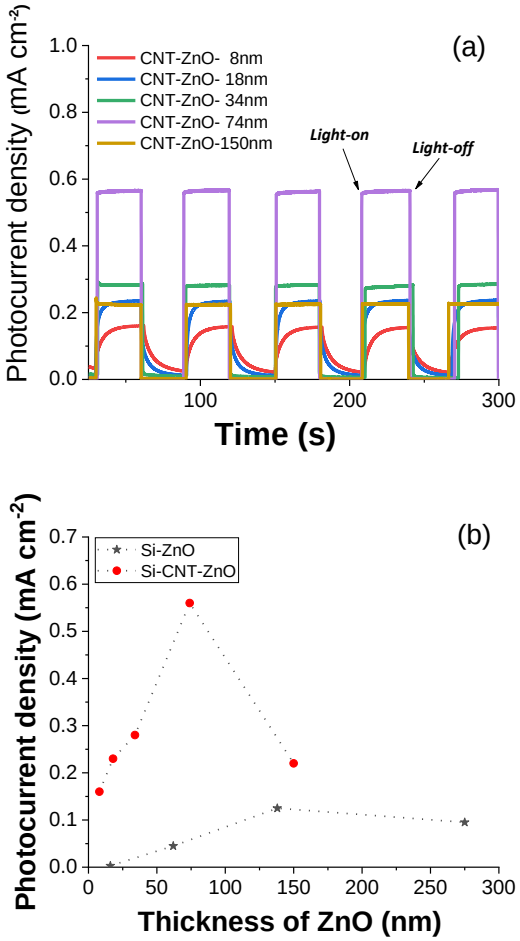


*Figure 4: Chronoamperometric measurements at 1.23 $V_{RHE}$ of various ZnO thicknesses on CNT (a) and the compared thickness-dependent photocurrent with films on planar Si substrates (b).*

The chronoamperometric measurement shows a fast kinetics in response to light switching except for ultra-thin (< 20 nm) ZnO films on the CNTs. This behaviour is neither observed for ultrathin ZnO on silicon substrates nor for uncoated CNT, and it agrees with an eventual influence from the underlying CNT. The spontaneous charge transfer between CNT and ZnO upon contact yields a depletion layer, which the impact on the ZnO-electrolyte interface is most likely for ultrathin ZnO layer. A decisive factor in this case is the thickness of the film relative to the depletion layer thickness. At a first glance, a ZnO thickness of 34 nm is high enough to screen this interference.

The role of CNT is schematically illustrated in Figure 5 by considering the energy band diagrams. When Si-ZnO is illuminated, electron-hole pairs are generated in both ZnO and Si. The band alignment favours the recombination of photoelectrons from ZnO with photo-holes from Si, while, the holes from ZnO migrate to the interface with the electrolyte to contribute to the OER. The observed OER

rate, semi-quantitatively assessed via the photocurrent measurement, contrasts between Si-ZnO and Si-CNT-ZnO which might be associated with the reduced electron-hole recombination, the efficient electron collection and the increased relative surface area in the CNT-ZnO core-shell architecture. The electron transport in the case of Si-CNT-ZnO structure in secured along the CNT network which is highly conductive. The core-shell architecture limits the electron's diffusion distance to the thickness of ZnO, which reduces the bulk recombination of the photogenerated charge carriers. Here the work function of metallic CNTs is reported at 4.95 eV while the electron affinity of ZnO is 3.32 eV[28], which favours a spontaneous electron transfer from ZnO to CNT and the consequent formation of a Schottky junction. Therefore, an external bias at the junction is needed to overcome the Schottky barrier and to favour the flow of electrons from the ZnO conduction band to CNT π-system[52] during the photo-electrochemical reaction. Hereby CNT plays the role of an electron acceptor, and the received electrons are promptly transported to the cathode via the external electrical circuit.

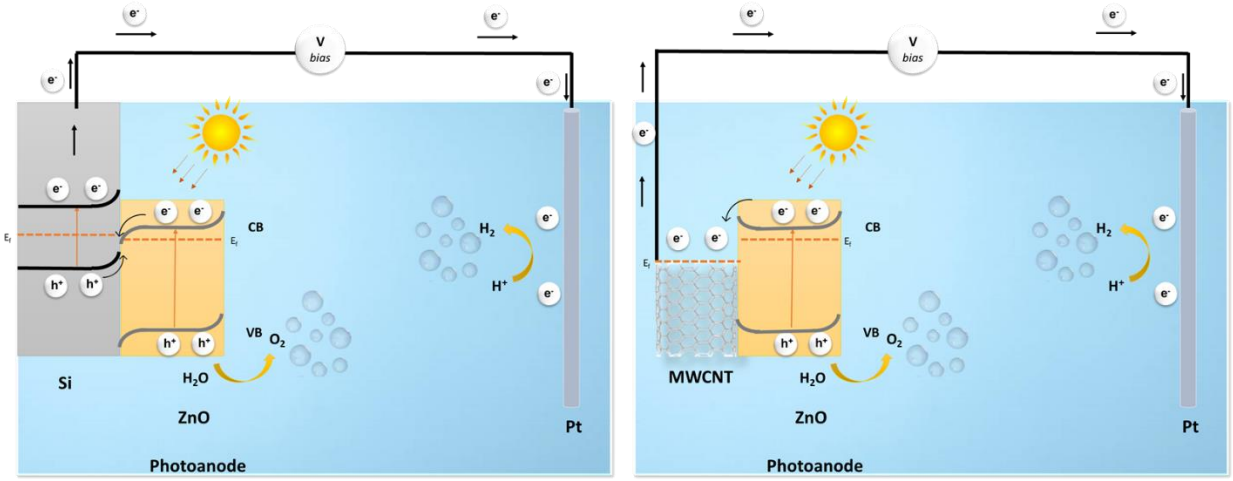


*Figure 5: Schematic of PEC water splitting mechanism for Si-ZnO (left) and CNT-ZnO (right) photoanodes.*

ZnO films are prone to chemical-corrosion, which the extent depends on the pH and the applied bias voltage[19]. The electrochemical-corrosion of ZnO is enhanced under light illumination (photo-corrosion) and is related to the accumulation of photo-holes at the surface. Indeed, holes trapped at the surface follow either of the three possible pathways:

- Transfer across the interface layer for the oxygen evolution reaction (OER) (faradaic process)
- Recombination with electrons at the surface (non-faradaic)
- Promotion of $Zn^{+2}$ dissolution due to the reaction with unsaturated $O^{-2}$ of ZnO[17]. (Photo corrosion)

The high charge transfer resistance in Si-ZnO samples along with the slow OER kinetics lead to the accumulation of charges at the surface, which enhances the photo-corrosion. Various approaches

have been reported, in the context of the photocatalytic organic dye degradation, for the limitation of ZnO photo-corrosion. This includes hybridization with a co-catalyst or with carbon, and the formation of heterojunctions [17]. The photo-corrosion enhances with the application of a bias voltage[19], which makes the ZnO photo-corrosion in water-splitting application more critical. ZnO nanostructures degrade severely under an applied bias voltage and light illumination in different electrolytes such as $Na_2SO_4$[50] and NaOH[39]. The protection of their surface with carbon[29], $C_3N_4$[35], RGO[34],[33] or oxides ($TiO_2$[21], $V_2O_5$[65] and $BiVO_4$[66]) have been reported as a mean to improve the photo stability and at best, a loss of photocurrent was noticed at 40% after 4h of light illumination under a bias voltage.

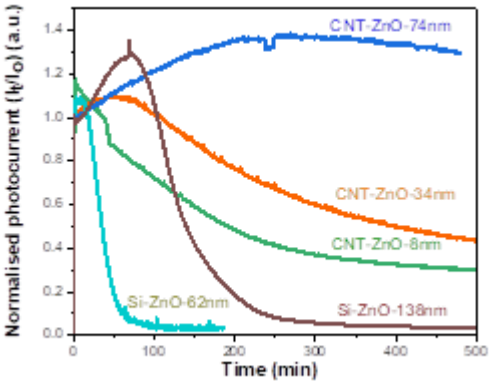


*Figure 6: Photocurrent stability measured in a 0.1 M NaOH solution (pH 12.7), under a 1 sun illumination and a bias of 1.23 $V_{RHE}$, for various ZnO thicknesses on Si and on Si-CNT.*

The heterostructures investigated in the present study are CNT-ZnO core-shell with a direct ZnO exposition to the electrolyte. The photo-corrosion of this heterostructure is compared to Si-ZnO in Figure 6. As far as Si-ZnO is concerned, a loss of 80% of the photocurrent occurs after ~50, 200 and >500 min for the 62, 138 and 275 nm thick ZnO respectively (see supplementary information). Assuming a constant absorption coefficient and a complete light penetration depth, an average ZnO dissolution rate of 0.8 nm/min could be estimated. A substantially higher dissolution rate, 40 nm/min, was reported for ZnO film with a thickness of 800 nm made by a hydrothermal process [53]. This relatively low dissolution rate might be the result of a pin hole free ZnO made by ALD. The ZnO dissolution rate was estimated at 0.024 nm/min for the CNT-ZnO samples, which is substantially low (ultrathin ZnO films: 8 and 34 nm). As no passivation was implemented in this case, the surface kinetics would remain unchanged. The porosity of the CNT-ZnO core-shell structure is suspected to play a determinant role by limiting the $Zn^{+2}$ outward diffusion in the electrolyte which slows-down the coating's degradation. The CNT-ZnO sample with a shell thickness of 74 nm features a photocurrent density of 0.55 mA/cm$^2$ and a stability of 8 hours under 1 sun illumination and a bias voltage of 1.23 $V_{RHE}$. As displayed in Table 1, these results are appealing relative to literature data.

*Table 1: State-of-art of carbon-ZnO composite material studied for photo-corrosion stability*

| Material | Synthesis/Remark | Dimensions | Current density | Reference |
|---|---|---|---|---|
| ZnO thin film covered with nafion | Hydrothermal/ enhancement by (002) crystal facet orientation | ZnO thickness of 800 nm; nafion thickness of 2.5 µm | 0.4 mA/cm$^{-2}$ (1.23 $V_{RHE}$) photocurrent stability for 5 h | [53] |
| ZnO rods covered with $C_3N_4$ layer | Electrodeposition/ enhancement by surface passivation | ZnO rods of 2 µm length; $C_3N_4$ of 15 nm thickness | 0.45 mA/cm$^{-2}$ (1.23 $V_{RHE}$) photocurrent stability for 1 h | [54] |
| ZnO rods covered with $C_3N_4$ sheets in-between | Electrodeposition/ enhancement by surface passivation | 400 nm ZnO rod arrays | 0.4 mA/cm$^{-2}$ (1.23 $V_{RHE}$) photocurrent stability for 1 h | [34] |
| RGO dispersed between ZnO sphere | Solvothermal/ enhancement by heterostructure | 1-2 µm diameter ZnO sphere | 0.1 mA/cm$^{-2}$ (1.23 $V_{RHE}$) photocurrent stability for 3h | [55] |
| ZnO particle on CNT composite | Sol-Gel/ enhancement by heterostructure | 30 nm ZnO particle | 0.45 mA/cm$^{-2}$ (1.23 $V_{RHE}$) photocurrent stability for 20 min | [56] |
| CNT-ZnO core-shell nanocomposite | CVD-ALD/ enhancement by heterostructure | 3 µm thick-CNT film; 74 nm thickness-ZnO shell layer | 0.55 mA/cm$^{-2}$ (1.23 $V_{RHE}$) photocurrent stability for 8 h | Present work |

## Conclusion

Gas-phase CVD-ALD process was used to synthesis porous CNT-ZnO nanocomposite film on silicon substrates. The CNTs deposited via thermal CVD in this work are randomly oriented and feature a low density, whereas the subsequent ALD enables the growth of a polycrystalline wurtzite ZnO shell around the individual CNTs. The photoelectrochemical characteristics of the so formed Si-CNT-ZnO were investigated and compared to a directly grown ZnO on Si (Si-ZnO). The ZnO in these cases was investigated as an anode material for photo-electrochemical water splitting reaction. The Si-CNT-ZnO reveals a nearly 5-fold increase of the photocurrent density relative to Si-ZnO samples, where ZnO features a comparable thickness. This improvement was correlated to the enhancement of electron-hole separation and surface area. CNT acts as an efficient electron collector with a fast 1D transport. Furthermore, the CNT-ZnO core-shell structure features an enhanced photo-corrosion stability relative to bare ZnO.

## Reference


[1] O. K. Varghese and C. A. Grimes, “Appropriate strategies for determining the photoconversion efficiency of water photoelectrolysis cells: A review with examples using titania nanotube array photoanodes,” *Sol. Energy Mater. Sol. Cells*, vol. 92, no. 4, pp. 374–384, 2008.

[2] N. L. Panwar, S. C. Kaushik, and S. Kothari, “Role of renewable energy sources in environmental protection: A review,” *Renew. Sustain. Energy Rev.*, vol. 15, no. 3, pp. 1513–

1524, 2011.

[3] Penn state, “9.4. Hydrogen storage.” [Online]. Available: https://www.e-education.psu.edu/eme812/node/726. [Accessed: 20-Jan-2021].

[4] J. M. Ogden, “Prospects for Building A Hydrogen Energy Infrastructure,” *Annu. Rev. Energy Environ.*, vol. 24, pp. 227–279, 1999.

[5] J. H. Kim, D. Hansora, P. Sharma, J. W. Jang, and J. S. Lee, “Toward practical solar hydrogen production-an artificial photosynthetic leaf-to-farm challenge,” *Chem. Soc. Rev.*, vol. 48, no. 7, pp. 1908–1971, 2019.

[6] C. Ros, T. Andreu, and J. R. Morante, “Photoelectrochemical water splitting: a road from stable metal oxides to protected thin film solar cells,” *J. Mater. Chem. A*, vol. 8, no. 21, pp. 10625–10669, 2020.

[7] J. Li and N. Wu, “Semiconductor-based photocatalysts and photoelectrochemical cells for solar fuel generation: A review,” *Catal. Sci. Technol.*, vol. 5, no. 3, pp. 1360–1384, 2015.

[8] S. Chen and L. W. Wang, “Thermodynamic oxidation and reduction potentials of photocatalytic semiconductors in aqueous solution,” *Chem. Mater.*, vol. 24, no. 18, pp. 3659–3666, 2012.

[9] C. Jiang, S. J. A. Moniz, A. Wang, T. Zhang, and J. Tang, “Photoelectrochemical devices for solar water splitting-materials and challenges,” *Chem. Soc. Rev.*, vol. 46, no. 15, pp. 4645–4660, 2017.

[10] F. E. Osterloh, “Inorganic nanostructures for photoelectrochemical and photocatalytic water splitting,” *Chem. Soc. Rev.*, vol. 42, no. 6, pp. 2294–2320, 2013.

[11] S. G. Kumar and K. S. R. K. Rao, “Zinc oxide based photocatalysis: Tailoring surface-bulk structure and related interfacial charge carrier dynamics for better environmental applications,” *RSC Adv.*, vol. 5, no. 5, pp. 3306–3351, 2015.

[12] A. F. Shaikh, S. S. Arbuj, M. S. Tamboli, S. D. Naik, S. B. Rane, and B. B. Kale, “ZnSe/ZnO Nano-Heterostructures for Enhanced Solar Light Hydrogen Generation,” *ChemistrySelect*, vol. 2, no. 28, pp. 9174–9180, 2017.

[13] J. Kegel, I. M. Povey, and M. E. Pemble, “Zinc oxide for solar water splitting: A brief review of the material’s challenges and associated opportunities,” *Nano Energy*, vol. 54, no. August, pp. 409–428, 2018.

[14] M. E, “Thermodynamics of Corrosion: Pourbaix Diagrams. In: Introduction to Corrosion Science.,” in *Springer, New York, NY*, 2010, p. 328.

[15] J. P. Becker, S. E. Pust, and J. Hüpkes, “Effects of the electrolyte species on the electrochemical dissolution of polycrystalline ZnO:Al thin films,” *Electrochim. Acta*, vol. 112, pp. 976–982, 2013.

[16] B. Weng, M. Y. Qi, C. Han, Z. R. Tang, and Y. J. Xu, “Photocorrosion Inhibition of Semiconductor-Based Photocatalysts: Basic Principle, Current Development, and Future Perspective,” *ACS Catal.*, vol. 9, no. 5, pp. 4642–4687, 2019.

[17] M. Fekete, W. Riedel, A. F. Patti, and L. Spiccia, “Photoelectrochemical water oxidation by screen printed ZnO nanoparticle films: Effect of pH on catalytic activity and stability,” *Nanoscale*, vol. 6, no. 13, pp. 7585–7593, 2014.

[18] C. F. Liu, Y. J. Lu, and C. C. Hu, “Effects of Anions and pH on the Stability of ZnO Nanorods for Photoelectrochemical Water Splitting,” *ACS Omega*, vol. 3, no. 3, pp. 3429–3439, 2018.

[19] M. Liu, C. Y. Nam, C. T. Black, J. Kamcev, and L. Zhang, “Enhancing Water splitting activity and chemical stability of zinc oxide nanowire photoanodes with ultrathin titania shells,” *J. Phys. Chem. C*, vol. 117, no. 26, pp. 13396–13402, 2013.

[20] N. K. Reddy, S. Winkler, N. Koch, and N. Pinna, “Electrochemical water oxidation of ultrathin cobalt oxide-based catalyst supported onto aligned ZnO nanorods,” *ACS Appl. Mater. Interfaces*, vol. 8, no. 5, pp. 3226–3232, Feb. 2016.

[21] M. Shao, F. Ning, M. Wei, D. G. Evans, and X. Duan, “Hierarchical nanowire arrays based on ZnO core-layered double hydroxide shell for largely enhanced photoelectrochemical water splitting,” *Adv. Funct. Mater.*, vol. 24, no. 5, pp. 580–586, 2014.

[22] Y. Mao *et al.*, “Amorphous NiO electrocatalyst overcoated ZnO nanorod photoanodes for enhanced photoelectrochemical performance,” *New J. Chem.*, vol. 40, no. 1, pp. 107–112, 2016.

[23] C. Li, T. Wang, Z. Luo, D. Zhang, and J. Gong, “Transparent ALD-grown Ta2O5 protective layer for highly stable ZnO photoelectrode in solar water splitting,” *Chem. Commun.*, vol. 51, no. 34, pp. 7290–7293, 2015.

[24] A. N. El-Shazly, A. H. Hegazy, M. M. Rashad, M. F. El-Shahat, and N. K. Allam, “Ultrathin ALD TiO2 shells for enhanced photoelectrochemical solar fuel generation,” *J. Alloys Compd.*, vol. 739, pp. 178–183, 2018.

[25] A. G. Scheuermann and P. C. McIntyre, “Atomic Layer Deposited Corrosion Protection: A Path to Stable and Efficient Photoelectrochemical Cells,” *Journal of Physical Chemistry Letters*, vol. 7, no. 14. pp. 2867–2878, 2016.

[26] Z. Li, S. Feng, S. Liu, X. Li, L. Wang, and W. Lu, “A three-dimensional interconnected hierarchical FeOOH/TiO2/ZnO nanostructural photoanode for enhancing the performance of photoelectrochemical water oxidation,” *Nanoscale*, vol. 7, no. 45, pp. 19178–19183, 2015.

[27] H. Fu, T. Xu, S. Zhu, and Y. Zhu, “Photocorrosion inhibition and enhancement of photocatalytic activity for ZnO via hybridization with C60,” *Environ. Sci. Technol.*, vol. 42, no. 21, pp. 8064–8069, 2008.

[28] H. Choi *et al.*, “Tuning the electronic band structure and optoelectrical characteristics of ALD-grown Zn(O,S) buffer layers for SnS solar cells,” *Optik (Stuttg).*, vol. 228, p. 165921, 2021.

[29] M. Shiraishi and M. Ata, “Work function of carbon nanotubes,” *Carbon N. Y.*, vol. 39, no. 12, pp. 1913–1917, 2001.

[30] A. K. Sharma and R. Sharma, “Fabrication and Characterization of Zinc Oxide/Multi-walled Carbon Nanotube Schottky Barrier Diodes,” *J. Electron. Mater.*, vol. 47, no. 5, pp. 3037–3044, 2018.

[31] B. Marinho, M. Ghislandi, E. Tkalya, C. E. Koning, and G. de With, “Electrical conductivity of compacts of graphene, multi-wall carbon nanotubes, carbon black, and graphite powder,” *Powder Technol.*, vol. 221, pp. 351–358, 2012.

[32] W. C. Hu *et al.*, “Reduced graphene oxides-wrapped ZnO with notable photocatalytic property,” *J. Taiwan Inst. Chem. Eng.*, vol. 112, pp. 337–344, 2020.

[33] Z. Zhang *et al.*, “Design and roles of RGO-wrapping in charge transfer and surface passivation

in photoelectrochemical enhancement of cascade-band photoanode," *Nano Res.*, vol. 10, no. 7, pp. 2415–2430, 2017.

[34] C. Liu, Y. Qiu, F. Wang, K. Wang, Q. Liang, and Z. Chen, "Design of Core–Shell-Structured ZnO/ZnS Hybridized with Graphite-Like C3N4 for Highly Efficient Photoelectrochemical Water Splitting," *Adv. Mater. Interfaces*, vol. 4, no. 21, pp. 1–11, 2017.

[35] S. Hernández *et al.*, "Optimization of 1D ZnO@TiO2 core-shell nanostructures for enhanced photoelectrochemical water splitting under solar light illumination," *ACS Appl. Mater. Interfaces*, vol. 6, no. 15, pp. 12153–12167, 2014.

[36] X. Sun, Q. Li, J. Jiang, and Y. Mao, "Morphology-tunable synthesis of ZnO nanoforest and its photoelectrochemical performance," *Nanoscale*, vol. 6, no. 15, pp. 8769–8780, 2014.

[37] K. Jeong, P. R. Deshmukh, J. Park, Y. Sohn, and W. G. Shin, "ZnO-TiO2 Core-Shell Nanowires: A Sustainable Photoanode for Enhanced Photoelectrochemical Water Splitting," *ACS Sustain. Chem. Eng.*, vol. 6, no. 5, pp. 6518–6526, May 2018.

[38] M. A. Hassan, A. Waseem, M. A. Johar, I. V. Bagal, J. S. Ha, and S. W. Ryu, "Single-step fabrication of 3D hierarchical ZnO/ZnS heterojunction branched nanowires by MOCVD for enhanced photoelectrochemical water splitting," *J. Mater. Chem. A*, vol. 8, no. 17, pp. 8300–8312, 2020.

[39] D. Ma *et al.*, "Rational design of CdS@ZnO core-shell structure via atomic layer deposition for drastically enhanced photocatalytic H2 evolution with excellent photostability," *Nano Energy*, vol. 39, no. May, pp. 183–191, 2017.

[40] C. C. Wang, C. Y. Chou, S. R. Yi, and H. D. Chen, "Deposition of heterojunction of ZnO on hydrogenated TiO2 nanotube arrays by atomic layer deposition for enhanced photoelectrochemical water splitting," *Int. J. Hydrogen Energy*, vol. 44, no. 54, pp. 28685–28697, 2019.

[41] M. Kulmas *et al.*, "Composite Nanostructures of TiO2 and ZnO for Water Splitting Application: Atomic Layer Deposition Growth and Density Functional Theory Investigation," *Adv. Funct. Mater.*, vol. 26, no. 27, pp. 4882–4889, 2016.

[42] H. J. Basheer, C. Pachot, U. Lafont, X. Devaux, and N. Bahlawane, "Low-Temperature Thermal CVD of Superblack Carbon Nanotube Coatings," *Adv. Mater. Interfaces*, vol. 4, no. 18, pp. 1–9, 2017.

[43] H. J. Basheer, K. Baba, and N. Bahlawane, "Thermal Conversion of Ethanol into Carbon Nanotube Coatings with Adjusted Packing Density," *ACS Omega*, vol. 4, no. 6, pp. 10405–10410, 2019.

[44] V. P. Prasadam, N. Gautier, and N. Bahlawane, "CNT nanoengineering for thermally stable selective solar absorption," *Mater. Today Commun.*, vol. 28, p. 102552, Sep. 2021.

[45] A. Yamada, B. Sang, and M. Konagai, "Atomic layer deposition of ZnO transparent conducting oxides," *Applied surface science*, vol. 112. pp. 216–222, 1997.

[46] R. P. Wang, G. Xu, and P. Jin, "Size dependence of electron-phonon coupling in ZnO nanowires," *Phys. Rev. B - Condens. Matter Mater. Phys.*, vol. 69, no. 11, pp. 5–8, 2004.

[47] H. J. Basheer, K. Baba, and N. Bahlawane, "Thermal Conversion of Ethanol into Carbon Nanotube Coatings with Adjusted Packing Density," *ACS Omega*, vol. 4, no. 6, pp. 10405–10410, 2019.

[48] A. Doepke *et al.*, “Analysis of the Electrochemical Oxidation of Multiwalled Carbon Nanotube Tower Electrodes in Sodium Hydroxide,” *Electroanalysis*, vol. 24, no. 7, pp. 1501–1508, 2012.

[49] I. E. Paulauskas, G. E. Jellison, L. A. Boatner, and G. M. Brown, “Photoelectrochemical Stability and Alteration Products of n-Type Single-Crystal ZnO Photoanodes,” *Int. J. Electrochem.*, vol. 2011, no. November, pp. 1–10, 2011.

[50] F. L. Souza, K. P. Lopes, E. Longo, and E. R. Leite, “The influence of the film thickness of nanostructured α-Fe 2O3 on water photooxidation,” *Phys. Chem. Chem. Phys.*, vol. 11, no. 8, pp. 1215–1219, 2009.

[51] K. Govatsi, A. Seferlis, S. G. Neophytides, and S. N. Yannopoulos, “Influence of the morphology of ZnO nanowires on the photoelectrochemical water splitting efficiency,” *Int. J. Hydrogen Energy*, vol. 43, no. 10, pp. 4866–4879, 2018.

[52] N. L. W. Septiani *et al.*, “Hollow Zinc Oxide Microsphere-Multiwalled Carbon Nanotube Composites for Selective Detection of Sulfur Dioxide,” *ACS Appl. Nano Mater.*, vol. 3, no. 9, pp. 8982–8996, 2020.

[53] A. U. Pawar, C. W. Kim, M. J. Kang, and Y. S. Kang, “Crystal facet engineering of ZnO photoanode for the higher water splitting efficiency with proton transferable nafion film,” *Nano Energy*, vol. 20, pp. 156–167, 2016.

[54] S. Xie *et al.*, “Enhanced photoactivity and stability of carbon and nitrogen co-treated ZnO nanorod arrays for photoelectrochemical water splitting,” *J. Mater. Chem.*, vol. 22, no. 28, pp. 14272–14275, 2012.

[55] J. Wang, G. Wang, J. Jiang, Z. Wan, Y. Su, and H. Tang, “Insight into charge carrier separation and solar-light utilization: rGO decorated 3D ZnO hollow microspheres for enhanced photocatalytic hydrogen evolution,” *J. Colloid Interface Sci.*, vol. 564, pp. 322–332, 2020.

[56] D. Chaudhary, S. Singh, V. D. Vankar, and N. Khare, “ZnO nanoparticles decorated multi-walled carbon nanotubes for enhanced photocatalytic and photoelectrochemical water splitting,” *J. Photochem. Photobiol. A Chem.*, vol. 351, pp. 154–161, 2018.

# Supplementary Information

Linear sweep voltammetry measurements were preformed at 0.1V/s from 0 to 2.2$V_{RHE}$. CNT-ZnO samples show high photocurrent density in relative to Si-ZnO samples as shown in figure S1. Photocurrent density in both the configuration increases with ZnO thickness. In figure S2, we observed the steady state chronoamperometric measurement of Si-ZnO samples with varied ZnO thickness, at 1.23$V_{RHE}$ bias potential. Onset potential is defined as bias potential to reach 2µA $cm^{-2}$ current density. Onset potential shifts negative with the increase in ZnO thickness, irrespective of substrate. For thin ZnO layer, Onset potential of the CNT-ZnO is slightly negative to Si-ZnO sample. In contrast, for thick ZnO layer, onset potential becomes saturates at 0.3V, irrespective of substrate as shown in figure S2.

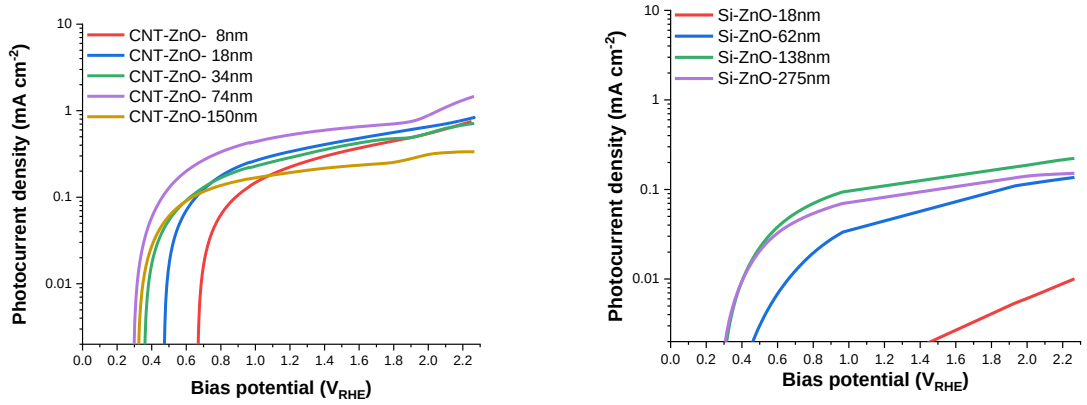


*Figure S2:Linear sweep measurement at 0.1V/s of CNT-ZnO (left), Si-ZnO (right)*

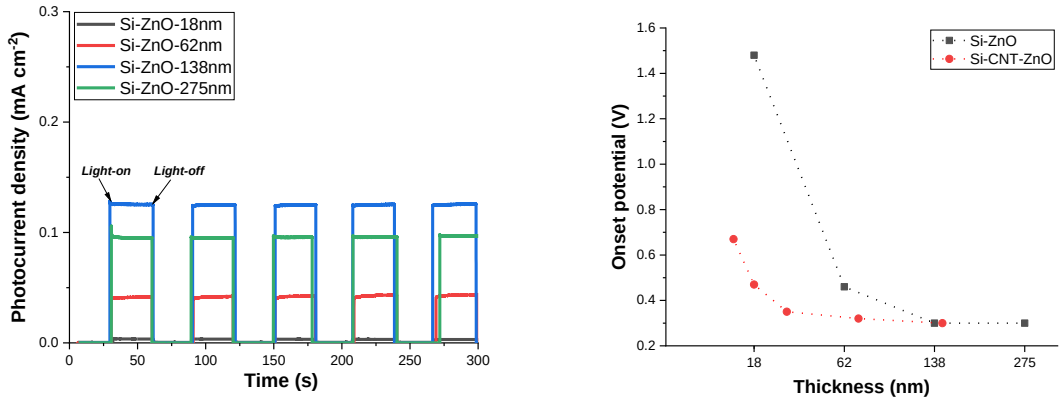


*Figure S3: chronoamperometric measurement of Si-ZnO at 1.23$V_{RHE}$ (left), Onset potential for both the configuration with varied ZnO thickness (right).*

Electrochemical impedance spectroscopy was implemented at 1.23$V_{RHE}$ in frequency range between 1Hz to 1x$10^5$ Hz to comprehend the photoanode charge carrier mechanism and the obtained results are displayed in figure S3, S4. Electrical circuit parameter such as $R_s$ is defined at contact resistance that include resistance of solution and resistance of charge flow between electrodes. $R_{ct}$ is defined as the charge transfer resistance across the electrode-electrolyte interface. C is defined as the capacitance at the electrode-electrolyte interface. Contact resistance (Rs) has shown insignificant

variation under dark and light condition, it decreased marginally with increase in ZnO thickness. However, charge transfer resistance (Rct) was higher under dark condition and with light illumination resistance decreased significantly. This reduction is intuitive, as the hole concentration increases with illumination that further induces the enhanced reaction at the electrolyte interface. Here, we assume presence of uncovered CNT sites that influence the electrode-electrolyte reaction kinetics. Therefore, with increase in ZnO thickness the CNT-electrolyte interaction is completely nullified that lead to apparent increase in charge transfer resistance.

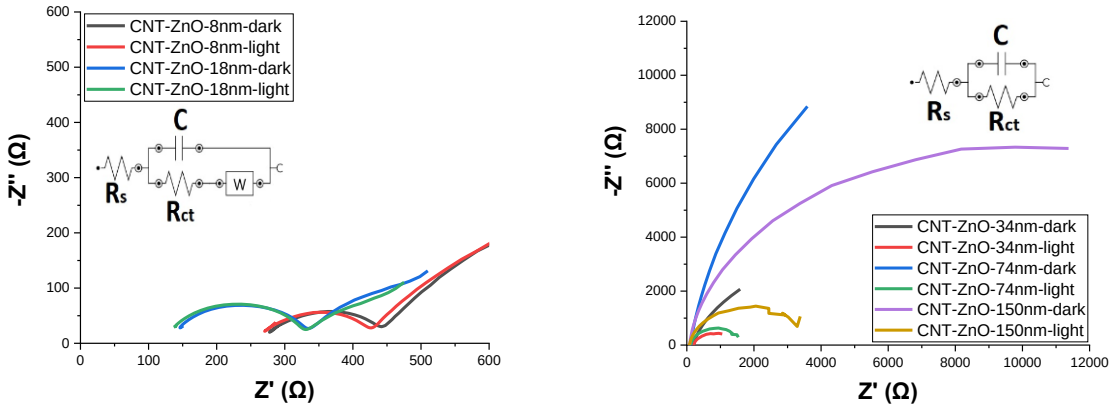


*Figure S4: Nyquist diagram of CNT-ZnO samples under dark, light at 1.23 $V_{RHE}$ (top), with a fitting electric circuit model parameter (bottom).*

| Sample | Rs- dark ($\Omega$-cm$^{-2}$) | Rs-light ($\Omega$-cm$^{-2}$) | Rct-dark ($\Omega$-cm$^{-2}$) | Rct-light ($\Omega$-cm$^{-2}$) | C-dark ($\mu$F-cm$^{-2}$) | C-light ($\mu$F-cm$^{-2}$) |
|---|---|---|---|---|---|---|
| CNT | 182 | 171 | 37 | 34 | 19.2 | 8.43 |
| CNT-ZnO-8nm | 348 | 276 | 124 | 123 | 0.449 | 0.681 |
| CNT-ZnO-18nm | 149 | 141 | 172 | 166 | 0.24 | 0.224 |
| CNT-ZnO-34nm | 200 | 196 | 3410 | 834 | 39.7 | 45.7 |
| CNT-ZnO-74nm | 110 | 110 | 19900 | 1290 | 13.4 | 14.6 |
| CNT-ZnO-150nm | 79 | 78 | 12900 | 2920 | 4.6 | 5.57 |

In case of the Si-ZnO sample, contact resistance ($R_s$) has shown similar trend as CNT-ZnO samples. However, the charge transfer resistance ($R_{ct}$) decreases with thickness, become constant after 62nm ZnO layer.

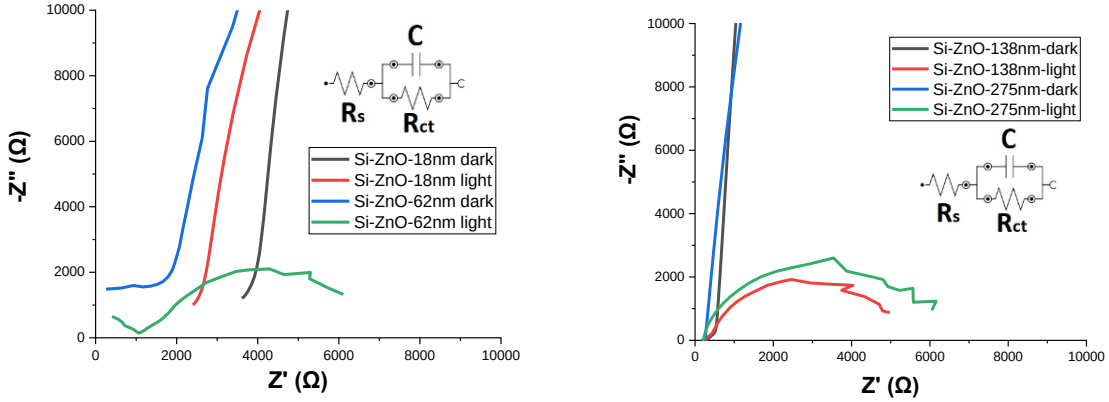

*Figure S5: Nyquist diagram of CNT-ZnO samples under dark, light at 1.23 $V_{RHE}$ (top), with a fitting electric circuit model parameter (bottom).*

| Sample | Rs- dark ($\Omega$-cm$^{-2}$) | Rs-light ($\Omega$-cm$^{-2}$) | Rct-dark ($\Omega$-cm$^{-2}$) | Rct-light ($\Omega$-cm$^{-2}$) | C-dark ($\mu$F-cm$^{-2}$) | C-light ($\mu$F-cm$^{-2}$) |
|---|---|---|---|---|---|---|
| Silicon | 5870 | 4980 | 2820000 | 197000 | 8.72e-4 | 0.02 |
| Si-ZnO-18nm | 3880 | 2600 | 239000 | 97300 | 0.00369 | 0.00381 |
| Si-ZnO-62nm | 1120 | 975 | 71973 | 4100 | 0.00637 | 4.98 |
| Si-ZnO-138nm | 365 | 294 | 370000 | 3910 | 3.04 | 4.2 |
| Si-ZnO-275nm | 245 | 211 | 355000 | 5080 | 1.47 | 2.16 |

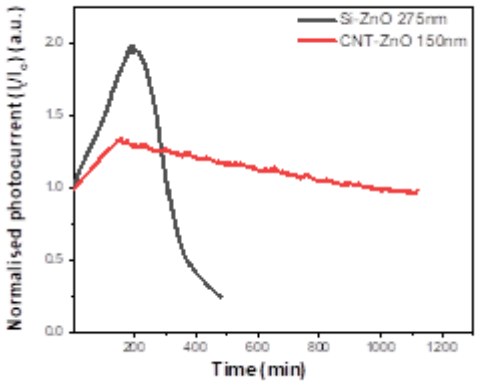


*Figure S6: Photocurrent stability measured in 0.1M NaOH solution (pH 12.7), under 1 sun illumination and a bias of 1.23 $V_{RHE}$, CNT-ZnO and Si-ZnO samples.*

### 3.2.2 MWCNT-$TiO_2$ for solar $H_2$ application

$TiO_2$ is among the most investigated oxides for water splitting. $TiO_2$ has a suitable positioning of the conduction and valence band energies to drive Hydrogen evolution (HER) and oxygen evolution reactions (OER). Furthermore, the low charge carrier mobility with short diffusion length (10-100 nm) imposes either a reduction of its thickness to match the diffusion length scale or nanostructuring. The poor electrical conduction of $TiO_2$ nanostructures and the fast recombination of photogenerated charges limit the PEC water splitting performance, and the addition of CNT is potentially beneficial as the electron transfer is energetically favourable from the $TiO_2$ conduction band to the CNT π-system.

The ALD grown $TiO_2$ films by the hydrolysis of TTIP feature an anatase phase, and conformal shell layers could be achieved around the CNTs. The experimental results show that the MWCNT-$TiO_2$ nanostructure outperforms the planar $TiO_2$, which was attributed to the hindered charge carrier recombination and enhanced electrode-electrolyte interface area.

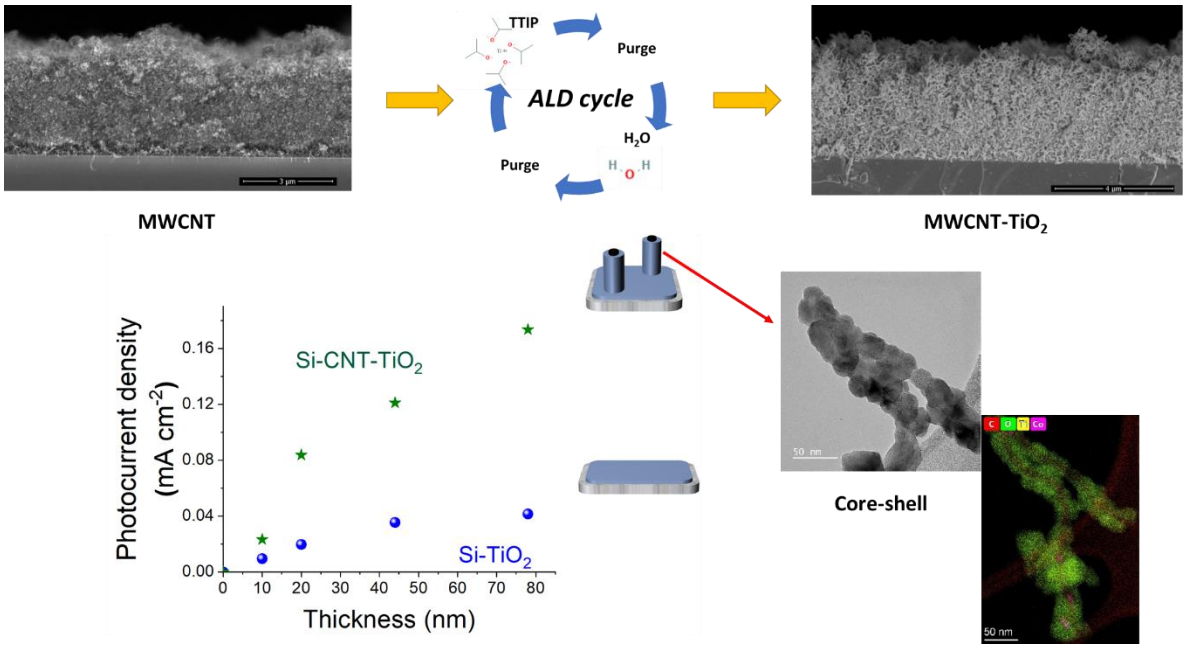

# CNT-$TiO_2$ core-shell structure: synthesis and photoelectrochemical characterization.

Vasu prasad PRASADAM, Ali Margot HUERTA FLORES, Naoufal BAHLAWANE

*Material Research and Technology Department,* Luxembourg Institute of Science and Technology, Rue du Brill, L-4422 Belvaux, Luxembourg

## ABSTRACT

Porous composite coatings, made of a CNT-$TiO_2$ core-shell structure, were synthesized by the hybrid CVD-ALD process. The resulting $TiO_2$ shell features an anatase crystalline structure that covers uniformly the surface of the CNTs. These composite coatings were investigated as photoanodes for the photo-electrochemical (PEC) water splitting reaction. The CNT-$TiO_2$ core-shell configuration outperform the bare $TiO_2$ films obtained using the same process regardless of the deposited anatase thickness. The improvement factor, exceeding 400 % in the photocurrent featured by the core-shell structure, was attributed to the enhancement of the interface area with the electrolyte and the electron fast withdrawal. The estimation of the photo-electrochemically effective surface area reveals that the strong absorption properties of CNT severely limit the light penetration depth in the CNT-$TiO_2$ system.

## Introduction

Photo-electrochemical (PEC) water splitting is an appealing approach for clean hydrogen energy generation[1]. Hereby, the process is essentially limited by the water oxidation reaction, which drives intense research for the development of high-performance anode materials. In this context, non-oxide semiconductors feature convincing performances,[2] however, they are chemically unstable in acidic and alkaline environments[3,4]. In contrast, several metal oxides exhibit better chemical stability in the dark and under illumination[5]. Furthermore, metal oxide semiconductors come with additional merits such as cost-effectiveness, non-toxicity and high abundance. In this context, $TiO_2$, ZnO, $WO_3$, $Fe_2O_3$ and $BiVO_4$ have been intensively investigated in PEC water splitting[6,7].

Among the available metal oxides, $TiO_2$ has a high abundance and high chemical stability[8]. It has eight polymorphs, among which anatase and rutile have shown a significant photocatalytic activity towards water splitting[9,10]. Anatase-rutile composite forms a heterostructure where charge carrier separation is improved, and the bandgap is decreased. As a result, the composite significantly outperform the photocatalytic property of the individual constituents[11]. $TiO_2$ has a suitable positioning of the conduction and valence band energies to drive Hydrogen evolution (HER) and oxygen evolution reactions (OER). This is associated with a band gap in the UV (3.0-3.2 eV), which limits the theoretical efficiency. Furthermore, the low charge carrier mobility with short diffusion length (10-100 nm)[12] imposes either a reduction of its thickness to match the diffusion length scale, or nano-structuring[13]. Further improvement was reported using several approaches such as, doping, forming a heterojunction with other semiconductors and by the application of a co-catalyst[14,15,16]. Nano-structured $TiO_2$ is synthesised by different processes such as hydrothermal, solvothermal, titanium-foil anodization and template-assisted process[14,15].

The poor electrical conductivity of $TiO_2$ nano-structures and the fast recombination of photogenerated charges limit the PEC water splitting performance[17], and the addition of CNT has a beneficial effect. The electron transfer is energetically favourable from the $TiO_2$ conduction band to the CNT π-system[18]. So far, CNT-$TiO_2$ structures are synthesised by sol-gel[19,20] and hydrothermal processes[21,22], which are affected by the challenging CNT dispersion in aqueous media as the unmodified CNTs are hydrophobic. Therefore, the process is difficult to control and heat treatments are needed to enhance the crystallization of $TiO_2$[23]. The electronic structure of the CNT-oxide interface is degraded due to the chemical modification of the CNT surface, a step that is necessary to enable their appropriate dispersion [20,24]. Here, $TiO_2$ is essentially present as nanoparticles decorating the CNT surface. This configuration leads to charge recombination upon interaction with the electrolyte[25]. The performance of such coatings results in a photocurrent density of 0.05 mA $cm^{-2}$ at 1.6 $V_{RHE}$[21], while the core-shell CNT-$TiO_2$ synthesised by gas phase process has shown the photocurrent density of 0.16 mA $cm^{-2}$ at 1 $V_{RHE}$ [26]. In the last case the CNTs were grown at 750 °C, detached and drawn on the PEC surface prior

to the deposition of $TiO_2$. Here we propose a simple and one-pot gas-phase process, low temperature hybrid CVD-ALD, for the synthesis of an innovative CNT-$TiO_2$ core-shell structure, for which the photo-electrochemical properties are investigated.

## Materials and Methods

The synthesis of the CNT-$TiO_2$ core-shell film architecture involves a single-pot hybrid Chemical Vapor Deposition-Atomic Layer Deposition (CVD-ALD) process. The deposition of carbon nanotube on silicon substrate was performed using thermal CVD. An equimolar ethanol solution, $0.65\times10^{-3}$ mol $L^{-1}$, of cobalt acetylacetonate ($Co(acac)_2$) and magnesium acetylacetonate ($Mg(acac)_2$) was implemented as a single precursor feedstock. This feedstock was introduced into the reactor via an evaporation cylinder at 220 °C, using a pulsed spray with a frequency of 4 Hz and using the opening time of 4 ms. The deposition was run for 2 h at 10 mbar, using a substrate temperature of 485 °C. The thickness of the film is assessed via the cross-section SEM inspection, and the density is assessed gravimetrically.

The ALD of the $TiO_2$ shell around the individual CNTs was achieved using the alternated surface exposure to titanium tetra-isopropoxide (TTIP) and water vapor. Both precursors are maintained at room temperature during the process. The deposition pressure was adjusted at 0.5 mbar, while the temperature and the exposure times were a subject of a systematic study. The thickness of the $TiO_2$ film on planar silicon was measured using a multi-wavelength Ellipsometer (Film Sense) with the Cauchy model.

X-ray diffraction (Bruker D8), with Cu-$K_\alpha$ as the X-ray source, was used to identify the present crystalline phases. Here, the data were collected in the grazing incidence mode 0.5° while scanning the detector from 0° to 90° with a step size of 0.02°. Raman scattering was performed using an InVia Raman spectrometer from Renishaw with a 633 nm laser and a power density of 87 $\mu W/cm^2$.

The CNT-$TiO_2$ structure was characterized using transmission electron microscopy (S/TEM Themis Z G3, 300kV, Thermo Fisher Scientific). The elemental mapping was performed using a combined EDX (energy dispersive X-ray spectrometer) analysis and high-angle annular dark-field scanning transmission electron microscopy (HAADF-STEM, 29.5 mrad, probe corrected). The coated CNTs were sampled, by scratching the surface, and deposited on lacey carbon grids. The morphology of the films was inspected using the FEI Helios Nanolab 650 scanning electron microscope (SEM) at a working distance of 5 mm and using an acceleration voltage of 5-10 V.

A standard three-electrode setup was used for the photoelectrochemical measurements with the CNT-$TiO_2$ as working electrode. All voltages were measured versus Ag/AgCl reference electrode and platinum (Pt) was used as the counter electrode. The electrolyte was an aqueous solution of 0.1 M

NaOH (pH 12.7). All the potentials from Ag/AgCl reference are converted to RHE based reference by given equation 1.

$$E_{RHE} = E_{Ag/AgCl} + 0.059*pH + 0.1976 \quad \text{Eq 1}$$

The electrode area, 2 $cm^2$, was front-illuminated using a Xe-lamp at 100mW/$cm^2$. Electrochemical measurements were conducted using an AUTOLAB potentiostat. Steady state current-voltage curves were used for assessing the electrochemical performance, whereas the AC impedance spectroscopy provided information on the contribution of various resistive losses (polarization and ohmic/ionic) to the performance of the photoanodes.

## Results and discussion

## CVD of CNT films:

The CNT growth is performed in a single step using a single feedstock approach. In this process ethanol vapor is thermally converted to CNTs at 485 °C under vacuum via the mediation of in situ formed catalyst and promoter. The *in situ* reaction of ethanol with transition metal acetylacetonate at moderate temperatures yields metallic nanoparticles[27,28,29], that catalyze the CNT growth; whereas, the thermal decomposition of magnesium acetylacetonate yields MgO, which the basicity promotes the CNT growth at temperatures exceeding 330 °C[30]. The resulting films are composed of randomly oriented multi-wall CNTs featuring an average diameter of 12 nm. The growth of a 4 μm thick CNT film on interdigital electrodes features an electrical resistance of 5 Ω. Such a low electrical resistance results from the strong crosslinking between the MWCNTs. The cross-section morphology of the grown film on the silicon substrate, Figure 1, displays a porous CNT structure for which the density is gravimetrically estimated at 0.4-0.6 mg/$cm^3$. This density is at least three orders of magnitude lower relative to densely packed CNTs[31]. Although the geometric thickness of the film is homogeneous throughout the substrate, the CNTs occupy a marginal volume fraction.

A close inspection at the surface of the CNT film and at the interface with the silicon substrate shows a similar morphology, which is a consequence of the simultaneous introduction of the catalyst and promoter along the deposition process. Cobalt and magnesium were found to be distributed homogeneously across the thickness of the film and their content in the CNT film was estimated using EDX at 4 at.%=Co/(C+Co+Mg), and 9 at.%=Mg/(C+Co+Mg).

The as-grown CNT films fail in the adhesion scotch test, as the CNTs are easily detached from the substrate, and they partially detach from the surface when dipped in the electrolyte under sonication. This limitation was overcome via the conformal deposition of metal oxides around the CNT to form a core/shell structure[32]. In this context, shells of aluminum oxide or silicon oxide were investigated. Here we do investigate the ALD of $TiO_2$ around the CNTs to provide them the ability to split water in a

photoelectrochemical setup. It is worth mentioning that the CVD of CNTs and their coverage with an oxide shell layer can be performed in the same reactor, and the resulting films are mechanically robust and remain unaffected when ultrasonicated or dipped in the electrolytes.

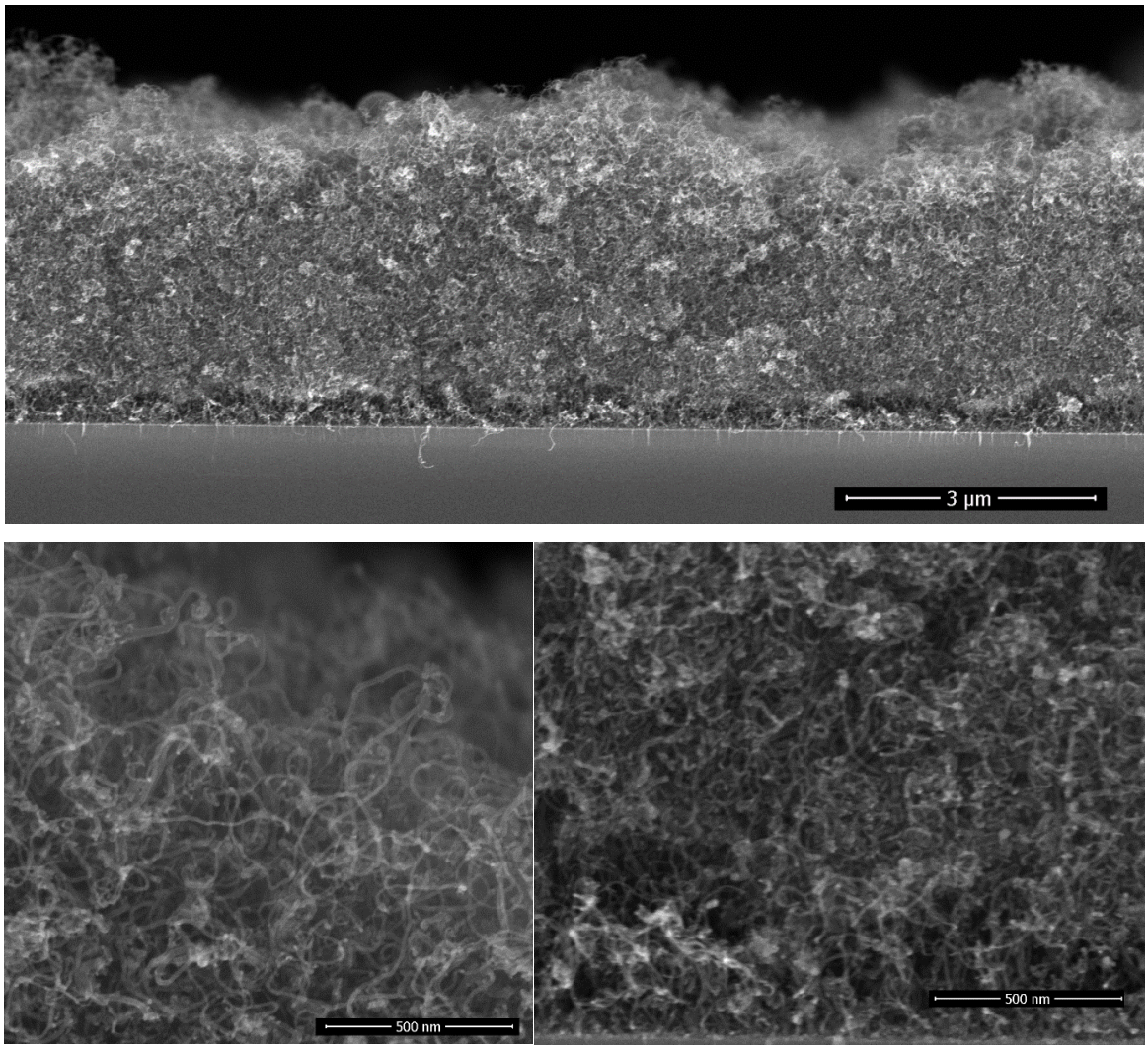


*Figure 1: The cross-section morphology of a ~4 µm thick film of randomly oriented CNT. The high magnification micrographs at the surface (bottom left) and at the interface (bottom right) illustrate the homogeneous entangled CNTs, featuring an outer diameter of 12 nm.*

## ALD of $TiO_2$:

A systematic study was performed on silicon substrates to establish conditions where the thermal ALD of $TiO_2$ can be performed using the sequential hydrolysis of titanium tetra-isopropoxide (TTIP). In this investigation, both precursors ($H_2O$ and TTIP) were evaporated at room temperature, which conveniently limits their eventual condensation in the transport lines. For the investigation of the temperature effect, Figure 2a, the deposition recipe involved a surface exposure time of 15 s to TTIP, and 8 s exposure to water vapor, both are separated by 15 s of purge using 50 sccm of Argon. Here an ALD cycle consists of 4 steps: TTIP/purge/$H_2O$/purge and the growth rate is defined by the deposited thickness of $TiO_2$ per ALD cycle (growth per cycle/GPC). The impact of the surface temperature on the growth per cycle (GPC) is marginal in the 140-195 °C temperature range. A rise of the GPC, outside

this range, is associated with the dominant thermal decomposition at high temperature and the plausible insufficient purging of water vapor at low temperature. A GPC of 0.56-0.58 Å/cycle was measured in the plateau, which agrees with the ~0.5 Å/cycle reported for the hydrolysis of TTIP at 250 °C[33]. The same ALD chemistry was implemented at 80-120 °C[34] and 160 °C[35], and GPCs of 0.33 and 0.68 Å/cycle were reported respectively. The diverging literature data regarding the GPC values might hint at the presence of competing deposition mechanisms.

Beyond the great relevance of self-limited reactions for the attainment of conformal coatings on structures with high aspect ratios, such as CNTs, studying the effect of the exposure time helps to understand the ALD process. Investigating the effect of the surface exposure to water vapor was performed at a deposition temperature of 160 °C, while maintaining the TTIP exposure time at 15 s. The displayed results in Figure 2b evidence the self-limited hydrolysis reaction step. An exposure time of 8 s is appropriate to completely hydrolyze the adsorbed TTIP, which enables a maximal GPC of ~0.6 Å/cycle. Non-complete hydrolysis at short exposures to water vapor leaves ligand moieties that poison the surface and yield a reduced GPC.

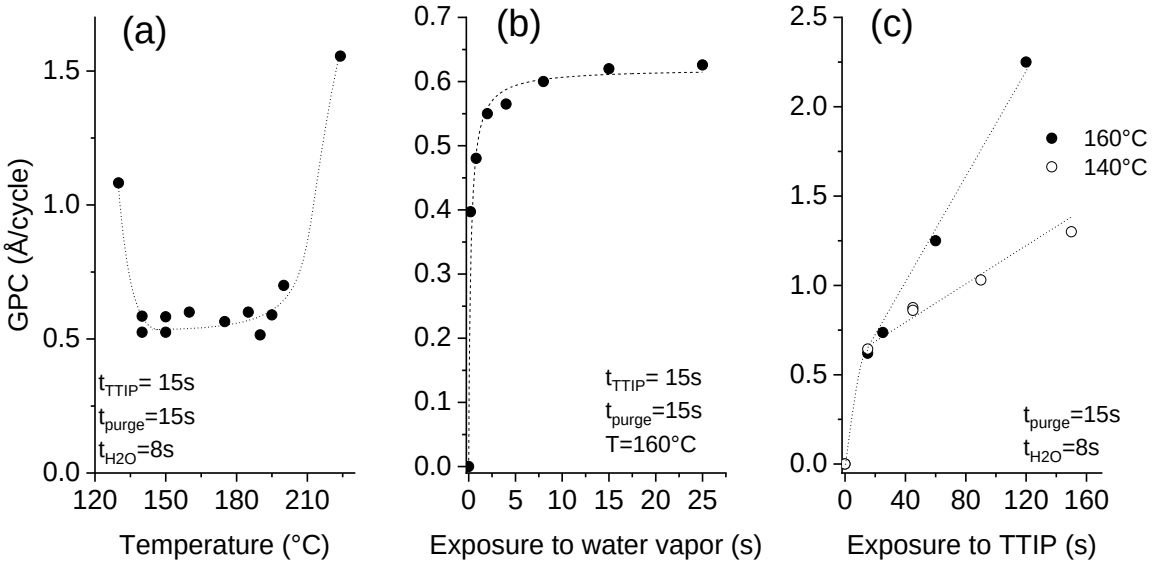


*Figure 2: Effect of the temperature (a), water (b) and TTIP (c) exposure times on the deposited thickness per cycle at a pressure of 0.5 mbar.*

Unlike the self-limited behavior observed for the hydrolysis reaction, the TTIP adsorption gives a continuous increase at 160 °C as displayed in Figure 2c. A strong rise of the GPC with the TTIP exposure time is observed, reaching 2.3 Å/cycle after 120 s. No saturation was observed, which indicates a significant CVD contribution. In this case, the thermolysis of TTIP leads to the growth of $TiO_2$ film even in the absence of water vapor.

Decreasing the deposition temperature from 160 °C to 140 °C significantly limited the rise of the GPC with the TTIP exposure; but did not suppress it. Decreasing the deposition temperature would logically

further limit the contribution of the CVD components, and likely enable the ALD-typical self-limited growth. Nevertheless, it is worth mentioning that 140 °C is at the low temperature side of the processing window featuring a constant GPC (Figure 2a). Therefore, the CVD growth contribution persists in the optimized pseudo-ALD process. The omnipresent CVD contribution might be the reason behind the diverging literature data regarding the reported values of the GPC. The occurrence of a competing CVD pathway was demonstrated below the TTIP thermolysis temperature[36,37,38]. This behavior was attributed to the catalytic effect of the under-coordinated $Ti^{+4}$, which is assumed to induce dehydration of TTIP or of the formed isopropanol[36,37]. As a result, further growth occurs instead of a surface saturation upon exposure to TTIP. Dosing isopropanol onto a surface of $TiO_2$ (110) shows that the associative dehydration reaction extends from 30 to 180 °C[39]. Therefore, only a pseudo-ALD of $TiO_2$ can be expected from the hydrolysis of TTIP; nevertheless, limiting the surface exposure to TTIP would limit the CVD contribution.

## CNT-$TiO_2$ Core-Shell structure:

The ALD of $TiO_2$ was performed on the CNT layers within the identified temperature window (140-200 °C). The SEM cross-section displayed in Figure 3 corresponds to a film grown at 160 °C. At first glance, the initial porous structure of the randomly oriented CNT is retained after deposition of $TiO_2$. The apparent diameter of the CNT is however significantly larger, 35 nm, relative to the non-coated CNTs (12 nm), and their surfaces feature faceted crystallites. The outer diameter hints at the deposition of a shell with a thickness of 11.5 nm around the CNT core after 200 cycles. This corresponds to a GPC of 0.58 Å/cycle, which is comparable to the growth on planar silicon (Figure 2). The resulting morphology was further inspected across the thickness of the CNT layer. The surface and interface regions, Figure 3, reveal an identical morphology, and the coated CNTs feature a similar diameter across the layer, which is a strong evidence about the conformality of the $TiO_2$ coating.

Raman scattering and X-ray diffraction on the ALD-grown titanium oxide over CNTs at 140, 160 and 175 °C are displayed in Figure 4. It is worth mentioning that these films have the same thickness, as the GPC in these temperature conditions is similar, but their analyses show a significant contrast. The CNT characteristic Raman bands at 1345 $cm^{-1}$ (D band) and 1589 $cm^{-1}$ (G band) are observed for all samples, whereas the anatase fingerprint is only observed for films grown at 160 °C and 175 °C. The most intense and sharp peak at ~140 $cm^{-1}$ in addition to the peaks at ~ 200 and 630 $cm^{-1}$ are attributed to the $E_g$ modes[40]. The peak at 395 $cm^{-1}$ was assigned to a $B_{1g}$ mode, whereas the peak at 513 $cm^{-1}$ involves components from $A_{1g}$ and $B_{1g}$[40]. Relative to the film grown at 175 °C, the signals are weaker for the film grown at 160 °C, while no peaks can be distinguished for the film grown at 140 °C.

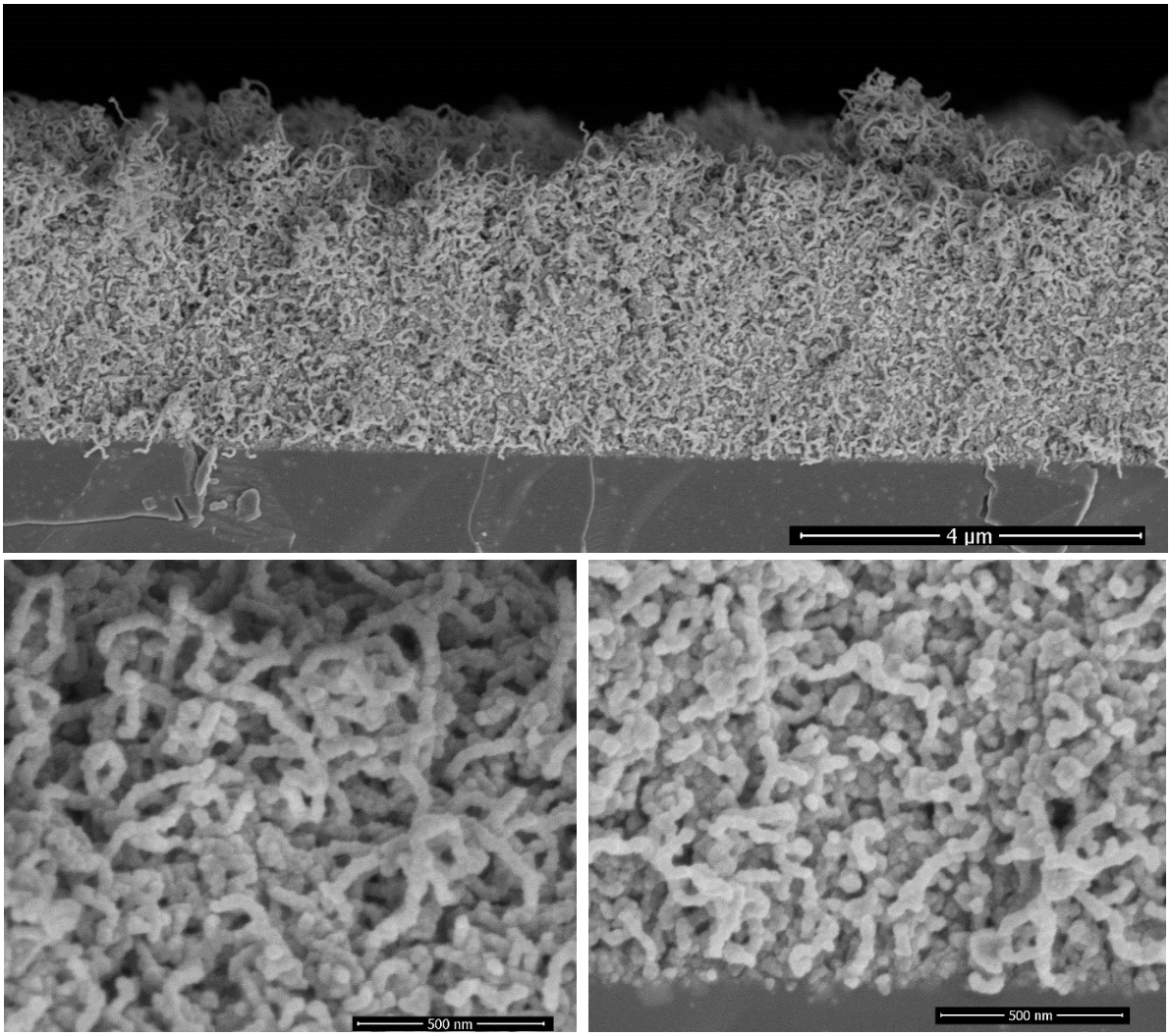


*Figure 3: The cross-section morphology of a ~4 µm thick film of randomly oriented CNT after the deposition of a $TiO_2$ shell at 160 °C. The ALD was performed using 8 s and 15 s as exposure times for water and TTIP, while the purge time was fixed at 15 s. The high magnification micrographs at the surface (bottom left) and at the Si-CNT interface (bottom right) illustrate the homogeneous entangled CNT-$TiO_2$ core-shell, featuring an outer diameter of 35 nm.*

The performed XRD analysis confirms the polycrystalline nature of the grown film at 175 °C. The recorded peaks in the XRD pattern correspond to anatase $TiO_2$ (pdf 01-075-2547). The film grown at lower temperatures show weak peaks intensities of the same phase, indicating their poor crystallinity. Weak diffraction peak corresponding to Si substrate and CNT can be identified.

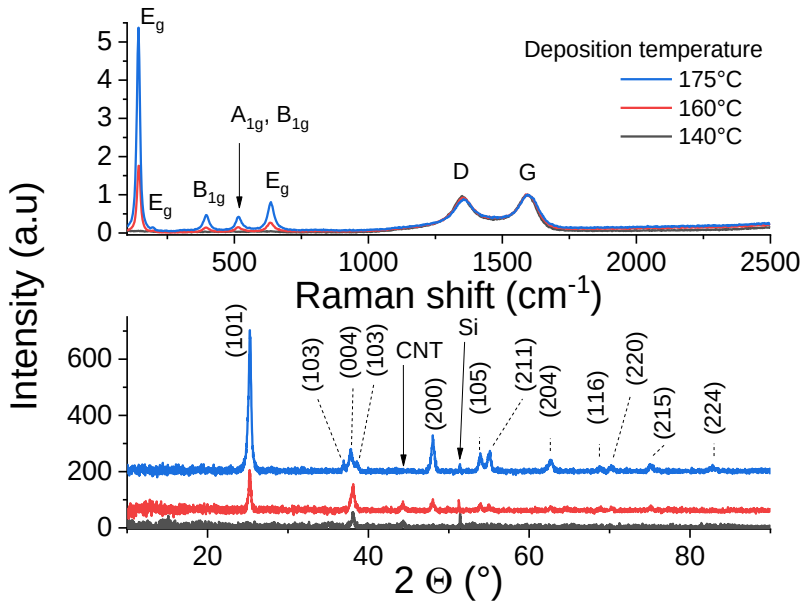


*Figure 4: Raman scattering and XRD analysis of CNT-$TiO_2$ core-shell.*

## Photoelectrochemical measurement:

$TiO_2$ deposition at 175˚C was retained for films destined to the PEC measurements. The evolution of the morphology with the thickness of $TiO_2$ is illustrated in figure 5. The preservation of the porous structure is noteworthy even after deposition of a 44 nm thick $TiO_2$ layer. High resolution TEM displayed in figure 6 shows the conformal coating of $TiO_2$ layer on CNT confirming the formation of a core-shell structure.

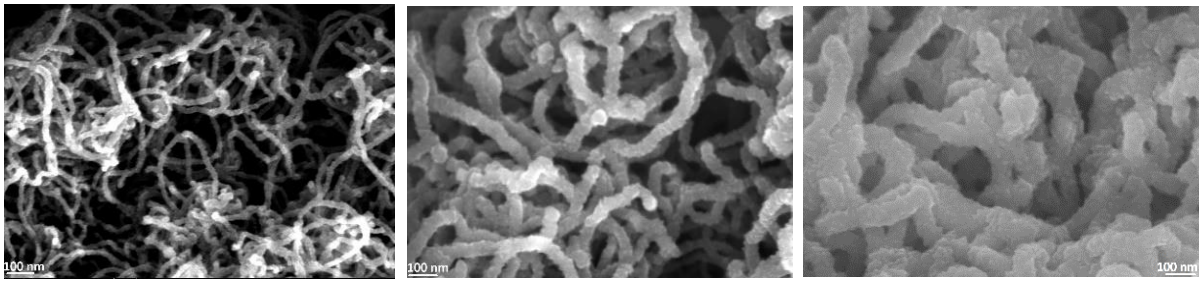


*Figure 5: SEM of CNT-$TiO_2$ structures with approximate diameters of 20 nm (left); 55 nm (middle) and 100 nm (right).*

The oxygen evolution reaction (OER) occurs at the anode involving holes, whereas the hydrogen evolution reaction (HER) occurs at the cathode involving electrons as shown in equation 2. The OER requires an overpotential of 1.23 $V_{RHE}$ that might be reduced when implementing photocatalysts such as $TiO_2$[14].

$4OH^- \rightarrow O_2 + 2H_2O + 4e^-$ (OER) Eq 2

$2H_2O + 2e^- \rightarrow H_2 + 2OH^-$ (HER)

$2H_2O \rightarrow O_2 + H_2$ (Overall reaction at 1.23 $V_{RHE}$)

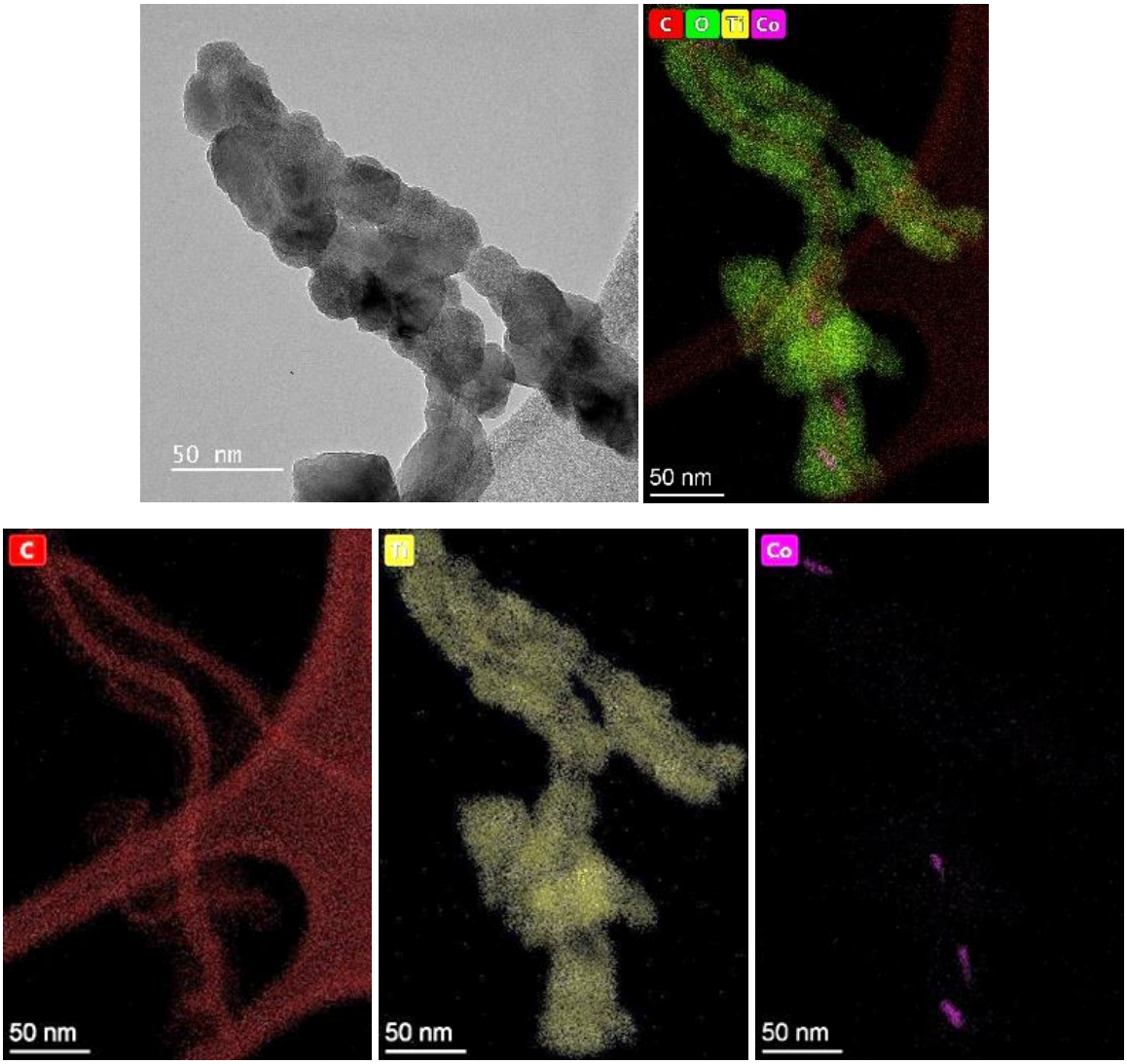


*Figure 6: HRTEM of CNT-$TiO_2$ sample confirming the core-shell structure formation.*

Due to its n-type characteristics, $TiO_2$ structures are used mostly as anode for the OER reaction. When n-type semiconductors, such as $TiO_2$, are immersed in an electrolyte, an equilibrium is reached by the transfer of electrons from the semiconductor to the electrolyte. The formed space charge at the interface features an internal electric field and inhibits the further transfer of electrons to the electrolyte. However, upon light illumination, electron-hole pairs are created and the built-in electric field contributes to their separation. The photo-generated holes are drifted to the surface of the semiconductor and participate in the oxidation of adsorbed water molecules. Whereas, electrons are drifted to the bulk under the bias effect, and are further transported to the cathode[6]. The $O_2$ evolution reaction involves 4 holes along with the formation of O-O double bond. In principle, an overpotential beyond 1.23 $V_{RHE}$ is required for the OER, while the overpotential required for $H_2$ evolution is far smaller. Hence, OER is typically considered as a rate limiting step in the water splitting reaction[41]. The extent of water oxidation is assessed by measuring the photocurrent density.

The investigated $TiO_2$ is applied either on a planar Si substrate or Si-CNTs. The surface area of CNT-$TiO_2$ is significantly higher than the planar $TiO_2$, which offers an extended interface with the

electrolyte. The surface area in this case was assessed by combining the geometric thickness around the CNTs and the weight gain as a result of $TiO_2$ deposition (Supplementary materials). The surface area assessed from the 10 nm $TiO_2$ deposition corresponds to 401 $cm^2$ per $cm^2$ of the geometric area, which reveals a specific surface area of 133 $m^2/g$ in the CNT-$TiO_2$ film. The surface area varies from 401 to 209 $cm^2/cm^2$ when the thickness of $TiO_2$ is varied from 10 to 78 nm, which is related to the partial obstruction of the channels between CNTs. If the electrochemical reactivity of CNT-$TiO_2$ might be related to the entire available $TiO_2$-electrolyte interface area, the photoelectrochemical reactivity should take into consideration the light penetration depth and the competing light absorption by the CNTs. These effects reduce substantially the effective surface area of $TiO_2$, which can be estimated using cyclic voltammetry with a varied scan rate in the negative potential range[42]. Notwithstanding the relevance of the effective surface area, the photoelectrochemical characterization in this study refers to the geometric area, as light is the factor that triggers the reactivity. The results displayed here correspond to illumination with a flux of 1 sun.

Steady state chronoamperometry measurement was performed at a bias potential of 1.23 $V_{RHE}$ to assess the photocurrent generated during intermittent illumination periods. The current is normalised to the geometric area and the results related to pristine CNTs and bare silicon substrates are depicted in the supplementary information (figure S1). The results reveal a photocurrent in the order of 1-2 $\mu A\ cm^{-2}$. Figure 7 shows the equivalent results with the application of various thicknesses of $TiO_2$. Upon illumination the current density raised quickly from 0 to reach an equilibrium plateau in the case of $TiO_2$ films on silicon substrates. However, CNT-$TiO_2$ core-shell structure features a residual dark current density that reduced gradually. Here the dark current is attributed to the presence of surface charge trapping, for which the suppression needs an extended time in the electrolyte. The current density response to light switching of thick $TiO_2$ on CNT is slow relative to the grown $TiO_2$ on silicon substrate, which is also associated with charge trapping that is emphasized by the large surface area[43]. Trapped charges might either witness a transfer across the interface or a recombination[44].

The CNT-$TiO_2$ core-shell structure features a photocurrent density of 0.17 mA $cm^{-2}$ at 1.23 $V_{RHE}$, which is 425% higher than bare $TiO_2$ with a similar thickness (i.e. 0.04 mA $cm^{-2}$). One of the primary limitations of $TiO_2$ material is the short diffusion length of minority charge carriers, ~10-100 nm[45], which is associated with the high recombination rate. This hinders holes ($h^+$) from reaching the interface with the electrolyte. In case of CNT-$TiO_2$ core-shell structure, the photogenerated electrons are likely to witness a transfer to the CNTs avoiding the bulk recombination in $TiO_2$. In both cases the photocurrent density value increased with the thickness of $TiO_2$. Photocurrent density is mostly affected by the photogenerated charge that depends on the thickness. The photocurrent density increases with the $TiO_2$ thickness on Si up to 45 nm, where a plateau above is observed in contrast to the grown $TiO_2$ on CNT.

N-type Silicon/n-type $TiO_2$ heterostructure promotes the photogenerated charge carrier recombination at the interface[46]. The electrically resistive undoped silicon substrates were used in this study, which forces a lateral 2D electron transport in $TiO_2$ resulting in enhanced recombination of the charge carriers. In the case of CNT-$TiO_2$ structures, bulk recombination is limited due to the high electron conductivity of CNTs. Here the work function of 4.95 eV[47] and 4.5 ev[48] were reported for metallic CNTs and for $TiO_2$ respectively. Therefore, the formed junction, CNT-$TiO_2$, favours the transfer of electrons towards the CNT π-system[49]. The transfer of the electron from the $TiO_2$ to CNT leads to the attainment of equilibrium by balancing the Fermi levels. A built-in electric field at this interface inhibits the further flow of electrons towards CNT, forming a Schottky barrier with negatively charged metallic multiwalled CNTs. The height of this barrier can be reduced by applying an external bias[50], enabling the flow of photogenerated electrons from $TiO_2$ to CNT as illustrated in figure 8. The $TiO_2$-electrolyte interface will also feature a built-in electric field that further enhances the photogenerated charge separation by driving the photogenerated holes towards the surface.

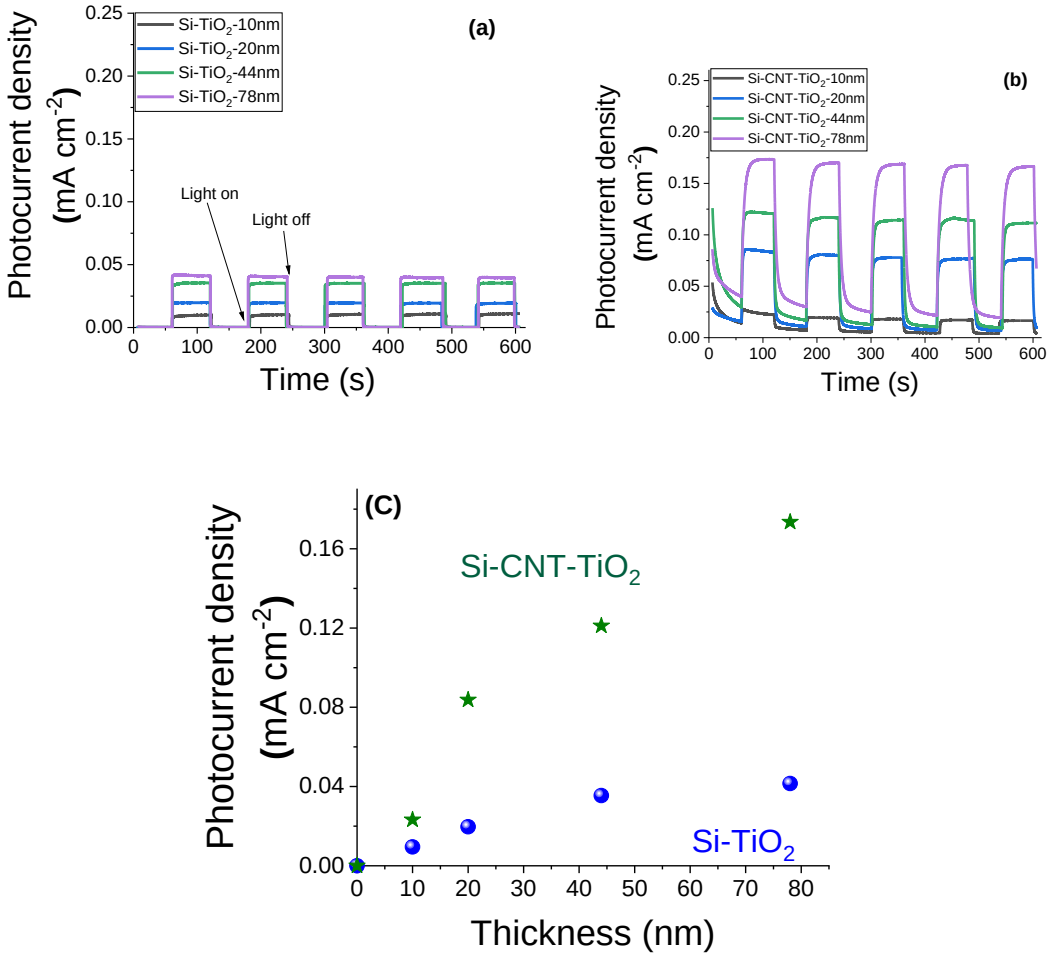


*Figure 7: Photocurrent density of bare $TiO_2$ (a) and CNT-$TiO_2$ (b), under dark and light conditions with an illustration of the effect of $TiO_2$ thickness (c).*

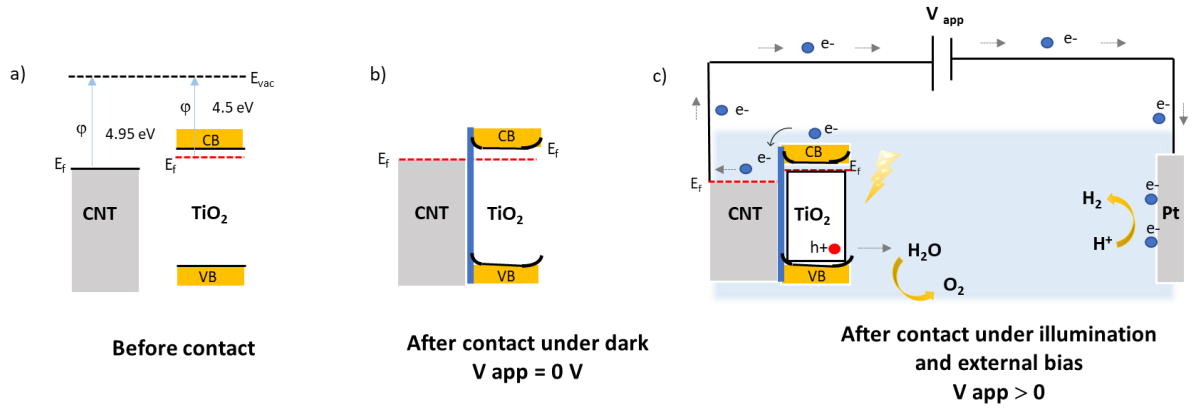


*Figure 8: Illustrative band diagram of CNT-$TiO_2$ before (a); after contact at equilibrium dark conditions (b); and under illumination with an external bias (c).*

Cyclic voltammetry (CV) measurement was performed in the 0-2.2V potential range with a 0.1 V/s scan rate and the results are displayed in figure 9. Si-$TiO_2$ samples, figure 9a, show negligible dark current densities throughout the potential range. Increasing the thickness of $TiO_2$ induces a perceptible increase of the dark current indicating the occurrence of electrocatalytic reaction. Exposing the surface to radiation brings a relatively prominent increase of the current density. The last features a significant increase with the bias potential and with the thickness of $TiO_2$. The onset potential is defined as the bias potential at which the anodic photocurrent starts to increase. This onset potential under light exposure is observed at 0.96 V for Si-10 nm $TiO_2$ sample and it shifts further negatively to reach 0.82 V with a thickness of 78 nm.

The CV measurements of CNT-$TiO_2$ samples, figure 9b-d, show significant forward & reverse dark currents that increase with the bias potential, giving rise to a hysteresis behaviour. A marginal current density increase is observed upon illumination and the hysteresis characteristics are retained. This behaviour is qualitatively like the one observed for non-coated CNTs (figure S1b). Current density obtained from the voltammetry measurement might be categorised into faradaic and non-faradaic current. The Faradaic response is due to the redox-reaction with a transfer of electrons at the electrode-electrolyte interface and the capacitive current is related to the charging of the electrochemical double layer formed at the electrode-electrolyte interface[51]. The electrochemical water oxidation occurs over pristine CNT sites at high overpotential[52,53]. The steady state current density at 1.23 V was measured with a periodic exposure to light (figure S1a). While the dark current is high for pristine CNT, the sensitivity to light exposure is relatively marginal. This variation in current density in steady state and at 0.1 V/s scan rate shows the presence of a large non-faradaic capacitive current with a marginal faradaic contribution. This behaviour was presumably attributed to the electrocatalytic reactivity over $TiO_2$, partially covered CNTs or cobalt decorated CNTs. It is worth mentioning that cobalt was implemented as a catalyst for the growth of the CNTS. The potential

contribution of electrocatalysis will be prominent as it would concern the total CNT-$TiO_2$ layer, which contrasts with the photo-electrocatalytic reaction that is limited to the penetration depth of light. The carrier charge density of $TiO_2$ was assessed as a function of the thickness using the Si-$TiO_2$ model system and the Mott-Schottky analysis (Figure S2 in the supplementary materials). A decrease from 3.8 $10^{16}$ to 2.6 $10^{15}$ $cm^{-3}$ was noticed when increasing the thickness from 10 to 78 nm, which was related to a lower density of grain boundaries. With a known density of charge carrier, the impedance spectroscopy was implemented to assess the photo-electrochemically effective surface area as a function of the thickness of $TiO_2$. The results reveal indeed that only 7 % of the available surface is photo-electrochemically effective with $TiO_2$ thickness of 10nm. This percentage rises to 36 % with thicker $TiO_2$ film (78 nm).

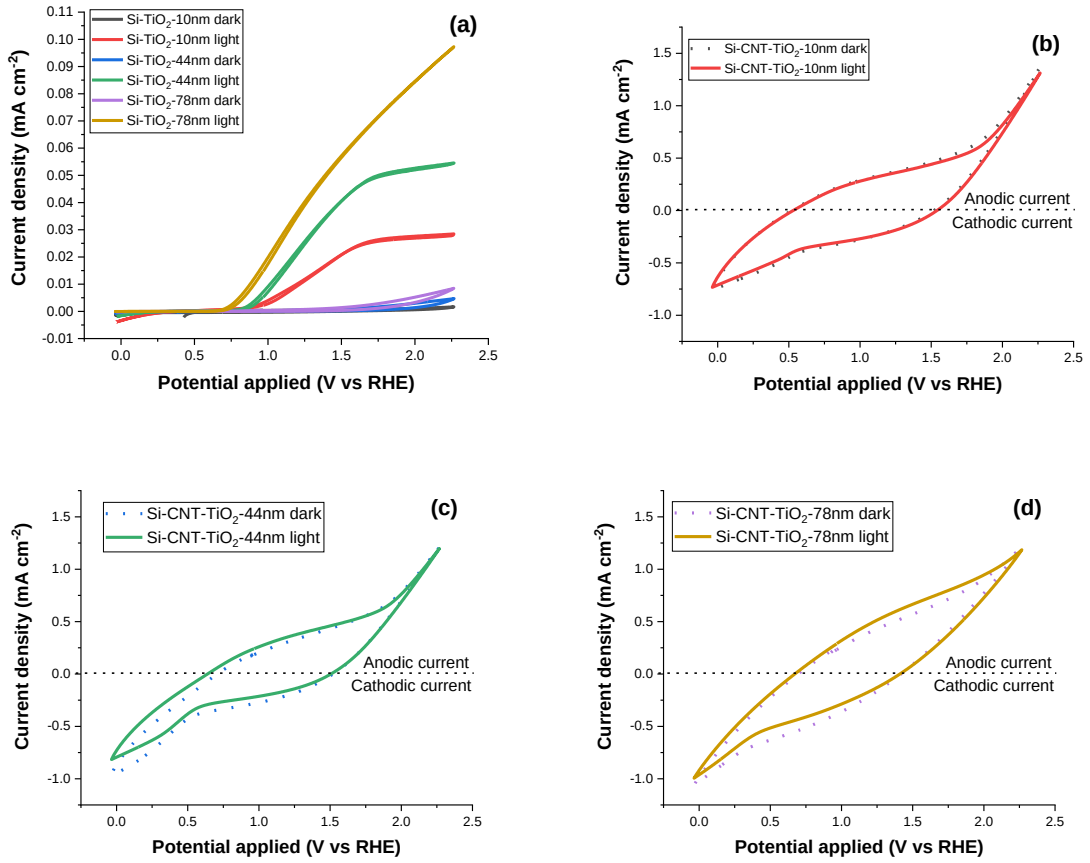


*Figure 9:Cyclic voltammetry measurement at 0.1 V/s scan rate, of Si-$TiO_2$ (a), Si-CNT-$TiO_2$ samples (b-d).*

The investigation of the CNT-$TiO_2$ system reveals advantages leading to an enhancement of the photocurrent with a factor exceeding 400 %. This includes the enhancement of the surface area and the withdrawing of electrons from $TiO_2$. The thorough analysis indicates however several limitations with further optimization potential. Among these aspects we might emphasize the band alignment between the electron collector and $TiO_2$, competing for light absorption and the contribution of parasitic capacitive current.

## Conclusion

CNT-$TiO_2$ nanocomposite coatings have been grown in this study, and their PEC characterization was performed. Single step thermal CVD process was used for the growth of CNT film, resulting in a randomly oriented CNTs, which were used for the ALD growth of the oxide layer ($TiO_2$). Anatase phase has been grown via the hydrolysis of titanium tetra-isopropoxide that exhibits a constant growth rate 0.056 nm/cycle between 140-190˚C. The crystallinity of the film improves, however, with the temperature in this range.

CNT-$TiO_2$ core-shell configuration outperforms the bare $TiO_2$ films in terms of PEC water splitting rate at a constant potential bias. The improvement in the photocurrent was attributed to the enhancement of the $TiO_2$-electrolyte interface and the electron-hole separation. Here CNTs act as nano-structuring support and as an electron transport channel. Evidences of this role are extracted from the chronoamperometry measurements and cyclic voltammetry.

## References


1 J. H. Kim, D. Hansora, P. Sharma, J. W. Jang and J. S. Lee, *Chem. Soc. Rev.*, 2019, **48**, 1908–1971.

2 W. Yang, R. R. Prabhakar, J. Tan, S. D. Tilley and J. Moon, *Chem. Soc. Rev.*, 2019, **48**, 4979–5015.

3 C. Ros, T. Andreu and J. R. Morante, *J. Mater. Chem. A*, 2020, **8**, 10625–10669.

4 J. Li and N. Wu, *Catal. Sci. Technol.*, 2015, **5**, 1360–1384.

5 S. Chen and L. W. Wang, *Chem. Mater.*, 2012, **24**, 3659–3666.

6 C. Jiang, S. J. A. Moniz, A. Wang, T. Zhang and J. Tang, *Chem. Soc. Rev.*, 2017, **46**, 4645–4660.

7 F. E. Osterloh, *Chem. Soc. Rev.*, 2013, **42**, 2294–2320.

8 K. Hashimoto, H. Irie and A. Fujishima, *Japanese J. Appl. Physics, Part 1 Regul. Pap. Short Notes Rev. Pap.*, 2005, **44**, 8269–8285.

9 J. Buckeridge, K. T. Butler, C. R. A. Catlow, A. J. Logsdail, D. O. Scanlon, S. A. Shevlin, S. M. Woodley, A. A. Sokol and A. Walsh, *Chem. Mater.*, 2015, **27**, 3844–3851.

10 E. Berardo and M. A. Zwijnenburg, *J. Phys. Chem. C*, 2015, **119**, 13384–13393.

11 D. O. Scanlon, C. W. Dunnill, J. Buckeridge, S. A. Shevlin, A. J. Logsdail, S. M. Woodley, C. R. A. Catlow, M. J. Powell, R. G. Palgrave, I. P. Parkin, G. W. Watson, T. W. Keal, P. Sherwood, A. Walsh and A. A. Sokol, *Nat. Mater.*, 2013, **12**, 798–801.

12 T. Yao, X. An, H. Han, J. Q. Chen and C. Li, *Adv. Energy Mater.*, 2018, **8**, 1–36.

13 H. M. Chen, C. K. Chen, R. S. Liu, L. Zhang, J. Zhang and D. P. Wilkinson, *Chem. Soc. Rev.*, 2012, **41**, 5654–5671.

14 M. Ge, Q. Li, C. Cao, J. Huang, S. Li, S. Zhang, Z. Chen, K. Zhang, S. S. Al-Deyab and Y. Lai, *Adv. Sci.*, 2017, 4, 1600152.

15 S. Kment, F. Riboni, S. Pausova, L. Wang, L. Wang, H. Han, Z. Hubicka, J. Krysa, P. Schmuki and R. Zboril, *Chem. Soc. Rev.*, 2017, **46**, 3716–3769.

16 K. Arifin, R. M. Yunus, L. J. Minggu and M. B. Kassim, *Int. J. Hydrogen Energy*, 2021, **46**, 4998–5024.

17 C. Xu, Y. Song, L. Lu, C. Cheng, D. Liu, X. Fang, X. Chen, X. Zhu and D. Li, *Nanoscale Res. Lett.*, 2013, **8**, 1–7.

18 M. T. Nguyen, C. K. Nguyen, T. M. P. Vu, Q. Van Duong, T. L. Pham and T. C. Nguyen, *Adv. Nat. Sci. Nanosci. Nanotechnol.*, , DOI:10.1088/2043-6262/5/4/045018.

19 H. M. Ghartavol, M. R. Mohammadi, A. Afshar and Y. Li, *Photochem. Photobiol. Sci.*, 2019, **18**, 1840–1850.

20 D. Eder and A. H. Windle, *Adv. Mater.*, 2008, **20**, 1787–1793.

21 D. Chaudhary, S. Singh, V. D. Vankar and N. Khare, *Int. J. Hydrogen Energy*, 2017, **42**, 7826–7835.

22 B. Chai, T. Peng, X. Zhang, J. Mao, K. Li and X. Zhang, *J. Chem. Soc. Dalt. Trans.*, 2013, **42**, 3402–3409.

23 K. Woan, G. Pyrgiotakis and W. Sigmund, *Adv. Mater.*, 2009, **21**, 2233–2239.

24 S. Rai, A. Ikram, S. Sahai, S. Dass, R. Shrivastav and V. R. Satsangi, *Int. J. Hydrogen Energy*, 2017, **42**, 3994–4006.

25 J. Chen, B. Li, J. Zheng, J. Zhao and Z. Zhu, *J. Phys. Chem. C*, 2012, **116**, 14848–14856.

26 J. Di, Z. Yong, Z. Yao, X. Liu, X. Shen, B. Sun, Z. Zhao, H. He and Q. Li, *Small*, 2013, **9**, 148–155.

27 P. A. Premkumar, N. Bahlawane and K. Kohse-Höinghaus, *Chem. Vap. Depos.*, 2007, **13**, 219–226.

28 P. A. Premkumar, N. Bahlawane, G. Reiss and K. Kohse-Höinghaus, *Chem. Vap. Depos.*, 2007, **13**, 227–231.

29 P. A. Premkumar, A. Turchanin and N. Bahlawane, *Chem. Mater.*, 2007, **19**, 6206–6211.

30 H. J. Basheer, C. Pachot, U. Lafont, X. Devaux and N. Bahlawane, *Adv. Mater. Interfaces*, 2017, **4**, 1–9.

31 H. J. Basheer, K. Baba and N. Bahlawane, *ACS Omega*, 2019, **4**, 10405–10410.

32 N. Bahlawane, C. Pachot and U. Lafont, in *International Conference on Space Optics — ICSO 2016,* 2017, vol. 10562, p. 156.

33 K. Cho, J. D. Park and C. Shin, *J. Semicond. Technol. Sci.*, 2016, **16**, 346–351.

34 M. Aghaee, P. S. Maydannik, P. Johansson, J. Kuusipalo, M. Creatore, T. Homola and D. C. Cameron, *J. Vac. Sci. Technol. A Vacuum, Surfaces, Film.*, 2015, **33**, 041512.

35 A. Sinha, D. W. Hess and C. L. Henderson, *J. Vac. Sci. Technol. B Microelectron. Nanom. Struct.*, 2006, **24**, 2523–2532.

36 A. M. Johnson and P. C. Stair, *J. Phys. Chem. C*, 2014, **118**, 29361–29369.

37 R. A. Hackler, G. Kang, G. C. Schatz, P. C. Stair and R. P. Van Duyne, *J. Am. Chem. Soc.*, 2019, **141**, 414–422.

38 A. R. Head, N. Johansson, Y. Niu, O. Snezhkova, S. Chaudhary, J. Schnadt, H. Bluhm, C. Chen, J. Avila and M.-C. Asensio, *J. Vac. Sci. Technol. A Vacuum, Surfaces, Film.*, 2018, **36**, 02D405.

39 O. Bondarchuk, Y. K. Kim, J. M. White, J. Kim, B. D. Kay and Z. Dohnalek, *J. Phys. Chem. C*, 2007, **111**, 11059–11067.

40 T. Ohsaka, F. Izumi and Y. Fujiki, *J. Raman Spectrosc.*, 1978, **7**, 321–324.

41 H. Narayanan, B. Viswanathan, K. R. Krishnamurthy and H. Nair, *Hydrogen from photo-electrocatalytic water splitting*, Elsevier Inc., 2019.

42 T. Berger, D. Monllor-Satoca, M. Jankulovska, T. Lana-Villarreal and R. Gómez, *ChemPhysChem*, 2012, **13**, 2824–2875.

43 I. Hwang, C. R. McNeill and N. C. Greenham, *J. Appl. Phys.*, , DOI:10.1063/1.3247547.

44 L. Bertoluzzi, P. Lopez-Varo, J. A. Jiménez Tejada and J. Bisquert, *J. Mater. Chem. A*, 2016, **4**, 2873–2879.

45 Y. J. Hwang, C. Hahn, B. Liu and P. Yang, *ACS Nano*, 2012, **6**, 5060–5069.

46 Y. J. Hwang, A. Boukai and P. Yang, *Nano Lett.*, 2009, **9**, 410–415.

47 M. Shiraishi and M. Ata, *Carbon N. Y.*, 2001, **39**, 1913–1917.

48 X. Yin, C. Battaglia, Y. Lin, K. Chen, M. Hettick, M. Zheng, C. Y. Chen, D. Kiriya and A. Javey, *ACS Photonics*, 2014, **1**, 1245–1250.

49 D. Chaudhary, V. D. Vankar and N. Khare, *Sol. Energy*, 2017, **158**, 132–139.

50 A. Di Bartolomeo, *Phys. Rep.*, 2016, **606**, 1–58.

51 N. Elgrishi, K. J. Rountree, B. D. McCarthy, E. S. Rountree, T. T. Eisenhart and J. L. Dempsey, *J. Chem. Educ.*, 2018, **95**, 197–206.

52 A. Doepke, C. Han, T. Back, W. Cho, D. D. Dionysiou, V. Shanov, H. B. Halsall and W. R. Heineman, *Electroanalysis*, 2012, **24**, 1501–1508.

53 C. Mo, J. Jian, J. Li, Z. Fang, Z. Zhao, Z. Yuan, M. Yang, Y. Zhang, L. Dai and D. Yu, *Energy Environ. Sci.*, 2018, **11**, 3334–3341.

# Supplementary information

Chrono-amperometry measurement of pristine CNT and bare silicon was performed at 1.23 $V_{RHE}$ under intermittent light illumination. Silicon shows, Figure S1a, a weak dark current (2 $10^{-5}$ mA/cm$^2$) relative to CNTs (5 $10^{-3}$ mA/cm$^2$). The dark current in the case of CNT-$TiO_2$ is attributed to the electrocatalytic activity of decorated CNTs with traces of cobalt, used as a catalyst for their growth. A photocurrent of 1 µA cm$^{-2}$ was measured for Si, while pristine CNT features a photocurrent of 2 µA cm$^{-2}$. It is worth mentioning that both photocurrent contributions are marginal in respect to that of coated samples with $TiO_2$.

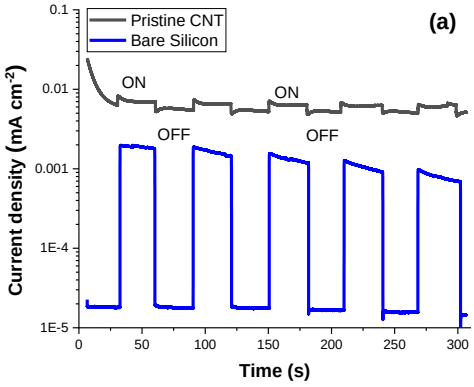

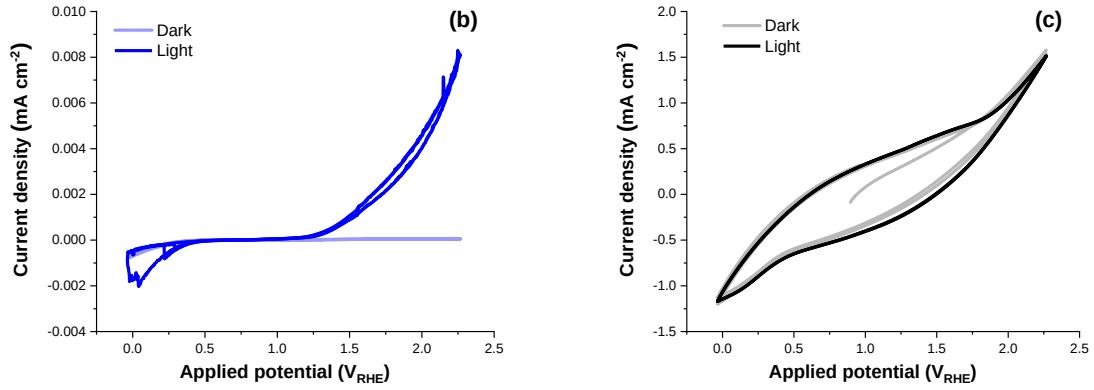


*Figure S10: Chronoamperometric measurement at 1.23 $V_{RHE}$ for pristine CNT and bare silicon (a); and the cyclic voltammetry at 0.1 V/s scan rate for bare silicon (b) and pristine CNT (c).*

Cyclic voltammetry on silicon (Figure S1b) has shown no significant sensitivity to the applied potential in the dark, however a substantial increase is observed with the applied potential under illumination to reach 8 μA/cm$^2$ at 2.25 $V_{RHE}$. This magnitude is very small relative to pristine CNT that shows a broad hysteresis with a high dark-current and a relatively weak sensitivity to illumination (Figure S1c). The non-faradaic capacitive current likely dominates the dark response, which is in line with the implementation of CNT as an electrode material for supercapacitors.

Mott-Schottky analysis was performed based on the equation 1 for the Si-$TiO_2$ configuration.

$$\frac{1}{c^2} = \left(\frac{2}{\epsilon \cdot \varepsilon_0 \cdot e \cdot N_d \cdot A^2}\right) \cdot \left(V - V_{fb} - \frac{K_B \cdot T}{e}\right) \qquad \text{Eq 1}$$

where, ε is the dielectric constant (for anatase $TiO_2$, $\varepsilon$ =48), $\varepsilon_0$ is the permittivity of vacuum, $e$ the electron charge, $N_d$ the charge carrier density, $C$ is the space charge capacitance, $V$ is the applied potential and $V_{fb}$ is the flat band potential. The charge carrier density was extracted from the slope of the Mott-Schottky plot shown in figure S2 given by equation 2.

$$N_d = \left(\frac{2}{\epsilon \cdot \varepsilon_0 \cdot e \cdot A^2}\right) \cdot \left(\frac{dV}{d\left(\frac{1}{c^2}\right)}\right) \qquad \text{Eq 2}$$

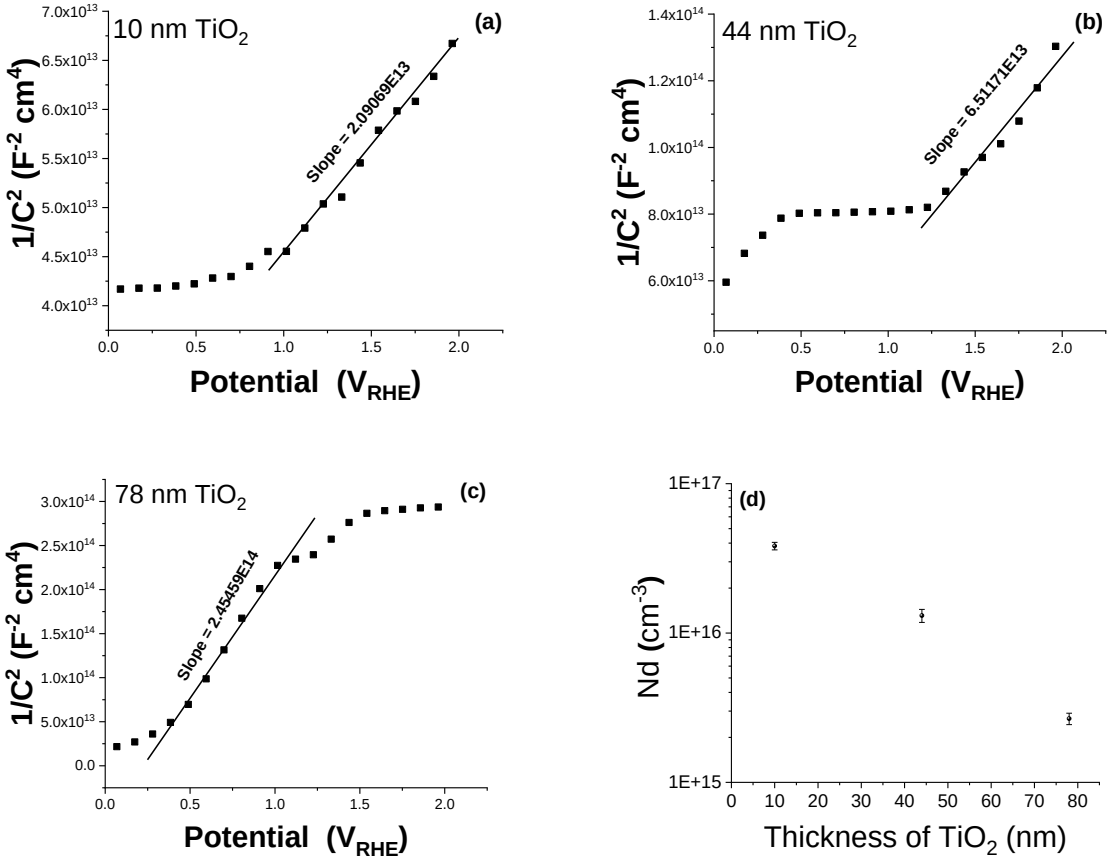


*Figure S11: Mott-Schottky curves obtained at 10Hz for Si-$TiO_2$ (a-c) samples featuring different $TiO_2$ thicknesses. Donor density extracted from the Mott Schottky analysis are displayed in the panel (d).*

The overall charge density decreases with the thickness, which might be attributed to a decrease in the concentration of the electroactive grain boundaries[1]. Thicker films allow for the growth of larger grains, which decreases the density of grain boundaries that act as donor-defective sites by the aggregation of oxygen vacancies ($V_o$) and titanium interstitials ($Ti_i$).

The open circuit potential (OCP) was measured using a three-electrode setup and the potential difference was assessed between the working electrode (Si-$TiO_2$ or Si-CNT-$TiO_2$) and the reference electrode (Ag/AgCl). The photo-potential is defined as the difference in steady state between the open circuit potential in dark and light i.e. $\left(OCP_{dark} - OCP_{light}\right)$. Here the $OCP_{light}$ shifts more to the negative potential, relative to $OCP_{dark}$, Figure S3, due to the generation and re-distribution of photo-charge carriers. The Si-$TiO_2$ samples show an increase of both $OCP_{dark}$ and $OCP_{light}$ with the increase of the $TiO_2$ thicknesses from 10 nm to 80 nm. The resulting photo-potential for $TiO_2$ shows relatively

higher values for the 10 nm and 80 nm thick films. It is worth noting that the SEM inspection shows a partial coverage and the evolution of surface roughening for these films successively (Figure S4).

The $OCP_{dark}$ in the case of CNT-$TiO_2$ samples is insensitive to the presence and to the thickness of $TiO_2$. While the Si-CNT shows a barely measurable sensitivity to illumination, Si-CNT-$TiO_2$ samples feature a clear decrease of the OCP upon illumination, however the $TiO_2$ thickness does not significantly impact the response. In fact, the Si-CNT-$TiO_2$ samples feature two contributions due to the CNT-$TiO_2$ and $TiO_2$-electrolyte junctions. Their opposing effect might explain the low photo-potential relative to the Si-$TiO_2$ samples.

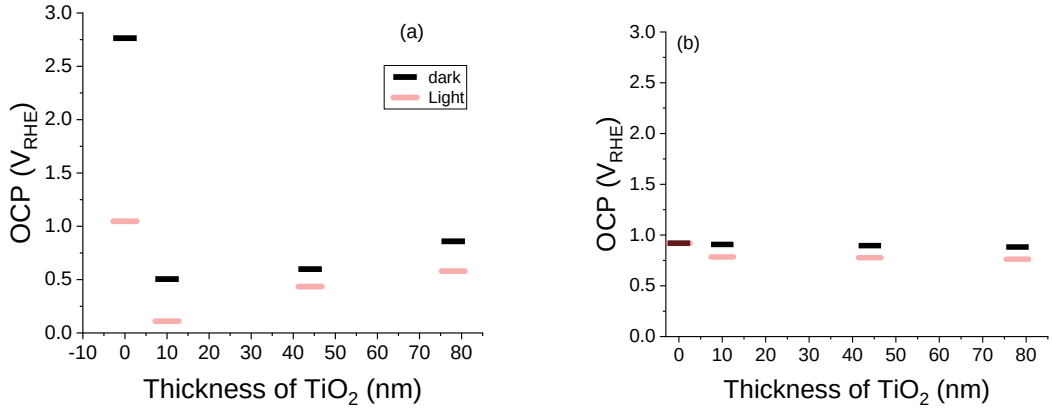


*Figure S12: Open-circuit potential under dark & light for Si-$TiO_2$ (a), Si-CNT-$TiO_2$ (b) for various $TiO_2$ thicknesses.*

The SEM inspection of planar $TiO_2$ on silicon substrates shows generally a smooth morphology composed of crystals that are far larger than the thickness of the film. The ultrathin film (10 nm) features a partial coverage, while the thickest (80 nm) features a surface roughening.

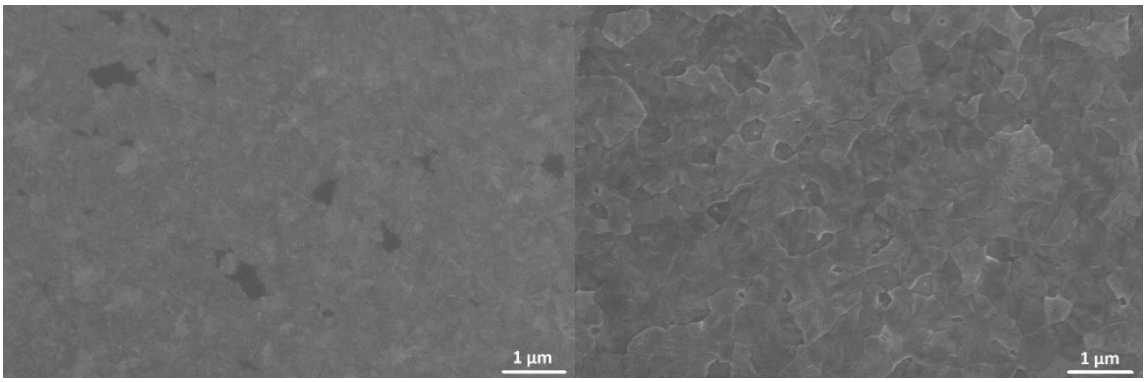


(a) (b)

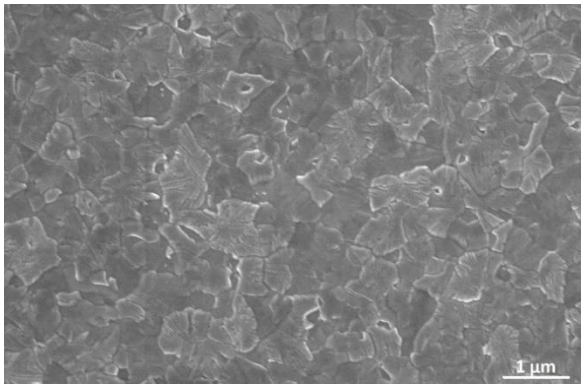


(c)

*Figure S13: SEM images of Si-$TiO_2$ with $TiO_2$ thickness of 10 nm (a), 44 nm (b), 78 nm (c)*

The mass of $TiO_2$ coating on CNTs was assessed by weighing the samples before and after the ALD process. The growth on CNTs yields a rate of 1150 ng/cm$^2$/cycle, while it is 54 ng/cm$^2$/cycle on silicon substrates. The last was calculated considering the density of the film and the thickness obtained by ellipsometry. The obtained data are depicted in figure S5.

The planar sample retains a surface area of nearly 1 cm$^2$ regardless of the $TiO_2$ thickness, whereas films grown on CNT feature a surface area evolving from 401 to 209 cm$^2$ as a function of the $TiO_2$ thickness from 10 to 78 nm. This estimation relies on the measured mass per cm$^2$ of the geometric area, and on the measured $TiO_2$ thickness around CNTs. The pristine CNTs feature a diameter of 12 nm and the assessed surface corresponds to the total $TiO_2$ surface area.

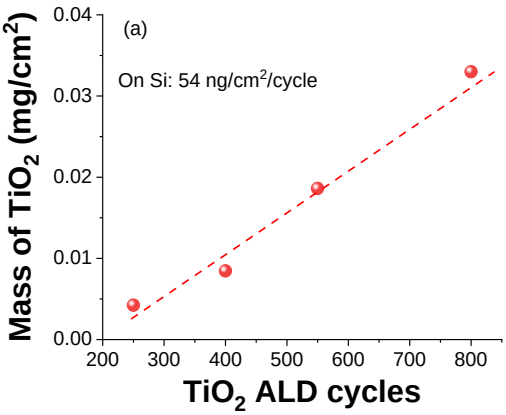


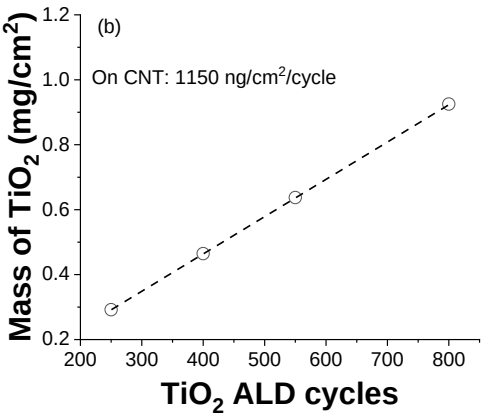

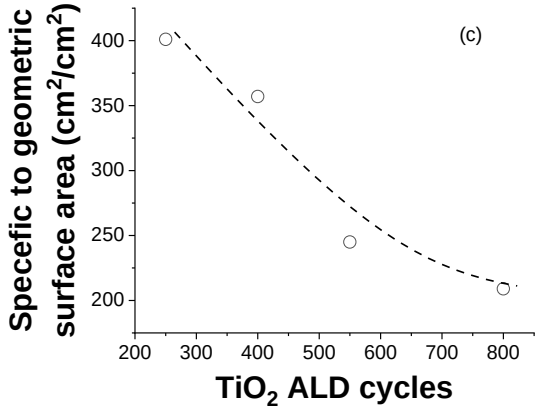


*Figure S14: The mass of $TiO_2$ on Si (a) and CNT (b) as a function of the number of ALD cycles and the extracted surface area relative to the geometric surface (c).*

The effective surface area is identified as the part participating to the photoelectrochemical reaction. The last was estimated using the impedance spectroscopy on CNT-$TiO_2$. From the equation 2, effective surface area (A) of CNT-$TiO_2$ is estimated by considering a similar carrier density value as for the grown $TiO_2$ with equivalent thickness on Si. Here we consider the charge carrier density of Si-$TiO_2$ and CNT-$TiO_2$ to be similar because the growth method and kinetics of $TiO_2$ on Si and CNT are identical. In this case the calculation leads to 29 $cm^2$ as the effective surface area for $TiO_2$ with a thickness of 10 nm. The unfavourable real/effective surface area (0.07) hints at the combined effect of limited light penetration depth and the competing absorption on CNTs. The eventual presence of a double junction in the CNT-$TiO_2$ contributes presumably to this discrepancy. This competition is lower for thicker $TiO_2$ film leading to a ratio of 0.358 for a thickness of 78 nm.

Reference

1. Sellers MCK, Seebauer EG. Manipulation of polycrystalline TiO 2 carrier concentration via electrically active native defects. *J Vac Sci Technol A Vacuum, Surfaces, Film*. 2011;29(6):061503. doi:10.1116/1.3635373

### 3.2.3 Statements

The photocurrent density of the CNT-$TiO_2$ core-shell structure surpasses the bare $TiO_2$ films irrespective of thickness, which is synthesized using the same ALD process. An enhancement of photocurrent by 400% for core-shell structure. PEC water splitting characterization was also studied for CNT-ZnO core-shell structures. Similar results as CNT-$TiO_2$ is observed but with higher photocurrent density because of better electrical properties of ZnO. We observed an increase of 458 % of the photocurrent density in relative bare ZnO. We attribute the photocurrent enhancement in both cases to the presence of CNT structures, which feature an increase in electrode-electrolyte interface area and fast electron extraction. ZnO films are prone to electrochemical corrosion with a dissolution rate of 0.8 nm/min. While the ZnO dissolution rate was estimated at 0.024 nm/min for the MWCNT-ZnO samples. The porosity of the MWCNT-ZnO core-shell structure is suspected of playing a determinant role by limiting the $Zn^{+2}$ outward diffusion in the electrolyte, which slows down the coating's degradation.

# 4 GENERAL CONCLUSIONS

We address the critical material issues of solar thermal and solar water splitting technologies through multiwalled carbon nanotubes (MWCNT)-metal oxide hybrid materials. MWCNTs are known for their high solar absorption, thermal and electrical conductivity. While metal oxides such as $VO_2$, Al-doped ZnO are known for their infrared reflecting properties with high transparency in the visible region. $TiO_2$ and ZnO have appropriate band positions for water splitting reactions. Here, combining CNTs and metal oxides at the nanoscale leads to unique properties not present in individual constituents. The most common method to synthesise CNT-metal oxide hybrids is the sol-gel, hydrothermal process. However, they have a poor electrical interface that negatively affects their performance and complicates their integration into devices. Here we fabricate the CNT-metal oxide through the chemical vapor deposition-atomic layer deposition (CVD-ALD) process, relying on the CVD to grow MWCNTs at a low temperature. The ALD process is implemented for the growth of metal oxide on high aspect ratio 3D porous MWCNT structures.

**Solar selective absorption:**

ALD process for the IR reflecting oxides such as $VO_2$ and Al-doped Zinc oxide are optimized to conformally cover MWCNT structures. MWCNTs grown by the CVD process are conformally coated with nanocrystalline $V_2O_5$ through an optimized ALD process. Post-deposition annealing has converted the oxide layer into the $VO_2$ phase. Morphology of the obtained $VO_2$ layer is determined by the thickness of the as-grown $V_2O_5$ oxide layer. Discontinuous $VO_2$ nanoparticle structure is obtained from the thin oxide layer, while the thick oxide layer resulted in the continuous $VO_2$ layer. Optical modulation across the semiconductor-metal transition is influenced by the morphology of the $VO_2$ phase. $VO_2$ nanoparticles on MWCNT feature an enhancement in the spectral emissivity across the SMT temperature, whereas a contrasting optical modulation is displayed by the continuous $VO_2$ layer on MWCNT. However, the solar absorption selectivity from the MWCNT-$VO_2$ is still insufficient, which encourages the investigation of other TCOs. In this context, aluminium doped zinc oxide (AZO) engineered by the ALD process is deposited on MWCNTs. Nanoengineered aluminium dopant concentration of 4.7 at % has improved the solar selectivity with a solar absorbance of 0.96 and thermal emittance of 0.6. The thermal stability of the engineered MWCNT-AZO is limited for the intended implementation at 1000 K under vacuum. The interface between ZnO and MWCNT is thermodynamically unstable above 670 K resulting in the carbothermal reduction of the ZnO film. However, a thin $Al_2O_3$ layer prior to the deposition of AZO stabilizes the interface with MWCNTs. A core-double shell structure, i.e., CNT-$Al_2O_3$-AZO, withstands thermal treatment at 1000 K for 72 h without degrading the solar selectivity property.

**Solar water splitting:**

ALD optimized ZnO layer is conformally coated on the MWCNT. Photoelectrochemical comparison of planar ZnO films and MWCNT-ZnO hybrid nanostructure revealed a better solar water splitting performance for hybrid nanostructures. The difference in performance between Si-ZnO and MWCNT-ZnO is associated with diminished electron-hole recombination, efficient electron collection and increased relative surface in MWCNT-ZnO core-shell structure. MWCNT-$TiO_2$ core-shell structure was developed through gas-phase synthesis and was investigated for solar water splitting. Photocurrent density of MWCNT-$TiO_2$ nanostructure outperforms the planar $TiO_2$, which was attributed to the hindered charge carrier recombination and enhanced electrode-electrolyte interface area.

# 5 PERSPECTIVES

The combination of CVD-ALD process illustrates a promising route for the synthesis for core-shell structures. Developed MWCNT-Metal oxide hybrid materials through the CVD-ALD process have displayed solar selective absorber properties with high thermal stability, and enhanced performance as photoanode for solar water splitting.

In the context of solar selective absorber, there is a broad scope in design optimization. Until now, there are not enough studies on MWCNT-metal oxide hybrid materials for the solar selective absorption application. So far, we considered only a simple design, i.e., infrared reflecting metal oxide layer over the CNT solar absorber. Nevertheless, other designs can be realized through optical simulation studies. Besides, other metal oxides such as Fluorine doped Tin oxide (FTO), Gallium doped Zinc oxide (GZO) have been identified as relevant alternatives to Aluminium doped Zinc oxide (AZO). Limited research work on gas-phase synthesis of MWCNT-$VO_2$ core-shell structure despite the large scope for vanadium oxide as electrode material in Li-ion batteries. Optical modulation of $VO_2$ across the semiconductor-metal transition (SMT) opens application for two solar thermal technologies, i.e., smart absorber in solar thermoelectric and selective absorber for concentrated solar thermal technologies. Infrared absorbance displayed by $VO_2$ nanoparticle-MWCNT can be utilized in solar thermoelectric devices for smart solar selective absorption, i.e., at low-temperature act as solar absorber and at high temperature act as thermal emitter. Obtained optical modulation across the SMT can be improved with Fabry–Perot interference using dielectric oxide layer between CNT and nanoparticle $VO_2$ layers. Continuous $VO_2$ layer over the MWCNT has illustrated solar selective characteristics across the SMT temperature. Low optical modulation displayed can be improved by altering the implemented design, i.e., thick $VO_2$ layer at the bottom and thin MWCNT structure at the top.

In the context of solar water splitting, the feasibility of gas-phase synthesis of relevant MWCNT-metal oxide core-shell structures was demonstrated Solar water splitting performance of the MWCNT-$TiO_2$/ZnO can be further improved by utilizing metal catalyst materials to achieve a faster reaction kinetics. Furthermore, this technique might be expanded to multilayer oxide with different bandgap energies. For instance, metal oxides such as $Fe_2O_3$, $Cu_2O$, $BiVO_4$, and $BiFeO_3$ have bandgaps in the visible region, indicating strong candidacy for photoelectrode application. However, these materials have poor electrical conductivity, short carrier diffusion lengths, i.e., <50nm. Introduction of 3D porous MWCNT electron collector template to the above-mentioned oxides induces increment in solar hydrogen production.

# 6 ANNEX- OPTICAL PROPERTIES OF DIFFERENT MATERIALS

Sunlight is an electromagnetic radiation with spectrum range from partial UV-visible-near infrared region, which have both wave, particle characteristic. When a light interacts with matter, basically scattering and absorption phenomena occur depending on the frequency (energy) of the light[1].

Incident light is absorbed by a compound when the incoming photon energy matches with one of its excited energy states. In general, absorption in a material is attributed to interband, intraband (free carrier) electron transitions, and phonon transition[2]. The perturbed excitation from absorption is limited for short duration of $10^{-8}$ to $10^{-9}$s. Excited atoms are relaxed to the ground states by losing the energy. Energy lost is realised as emission of light or as thermal energy by inter-atomic collisions in dense medium. The last represents the photon to thermal energy conversion process.

Scattering is basically represented as non-resonant process. Here atoms are not excited to higher energy states because the photon frequency is lower than the resonant frequency, of atoms. Electron clouds present in the atoms oscillate with respect to positive nucleus behaving like a dipole oscillator. So immediately emit the radiation at that frequency. This remission of light is termed as scattering process. In dense material where atoms are arranged periodically, each atom acts as a source of secondary emitted radiations that propagate in forward direction due to constructive interference. While in lateral and backward direction scattered radiation are nullified with destructive interference. Optical properties, such as reflection, transmission and refraction are macroscopic manifestation of scattering and interference occurring at atomic level.

Propagation of light in matter depends on the refractive index of the material. Refractive index (n) is defined as the ratio of light velocity in vacuum ($c$) to light velocity in the material ($v$). In general, light velocity is reduced while travelling any material in relative to light velocity in vacuum. This phenomenon is called as refraction, is frequency dependent. Generally refractive index increases with frequency.

$$n = \frac{c}{v}$$

Transmission can be understood as constructive scattering in forward direction. Transmission is quantified as the coefficient of transmission or transmittivity (T). It is usually defined as the ratio of the transmitted light fraction ($I_T$) to incident light ($I_O$). However, at the interfaces discontinuous arrangement of the atoms precede to constructive scattering in backward scattering. This backward scattering is considered as reflection. Reflection is quantified as coefficient of reflection or reflectivity (R). It is usually defined as the ratio of the reflected light fraction ($I_R$) to incident light ($I_O$).

Refractive index (n) determines the propagation of light in the transparent material. However, in absorbing material, propagation of light depends on the refractive index(n) and extinction coefficient(k) given by complex refractive index (N)[3].

$$N = n + ik$$

Attenuation of light while propagating through an absorbing material is given by Beer lamberts law shown in Eq.

$$I = I_O e^{-\alpha d}$$ Eq

Where α is absorption coefficient and d is the thickness of the material. Increased absorption coefficient leads to a decreased light penetration depth (dp) i.e. (dp=1/α). For opaque materials like metal, penetration depth is very small due to their high absorption coefficient. The last is weaker for transparent materials, so the light penetration depth is larger. Absorption coefficient and extinction coefficient (k) are related by equation shown below.

$$\alpha = \frac{4\pi k}{\lambda}$$

According to Fresnel equation reflectance at normal incidence can be estimated if the n, k values are known as shown in below equation.

$$R = \frac{(n-1)^2+k^2}{(n+1)^2+k^2}$$

Reflectance is high when n,k values are high. In transparent material (α=0, k=0,), then reflectance depends entirely on the refractive index value.

Solid materials are broadly categorized into metals, dielectric (semiconductor), metal-dielectric composites. We have understood in above section that propagation of light is depend on the complex refractive index of the material. However, they are determined from the dielectric polarization in the material. Dielectric polarization is a phenomenon where the electric field of the light separates the electric charges in the material. Dielectric polarization magnitude is given as permittivity or dielectric constant. Dielectric materials show large dielectric polarization because the electric charges are not free but bound by strong chemical bonds. So, upon external field application, separate regions of positive, negative charge are formed. In contrast, metals have free charge carriers that upon interaction with electric field of light leads to current flow. Therefore, dielectric polarizations are weak in metals. In dielectric (semiconducting) material, electric, atomic polarizations are commonly observed. Because of sinusoidal AC electric field of the light, the electric dipole is oscillated that leads to emission of electromagnetic radiation with similar frequency as the light. This phenomenon is referred as scattering mechanism in the above section.

There is close relation between complex refractive index and complex dielectric constant. complex dielectric constant (permittivity) given as

$$\varepsilon = \varepsilon_1 + i\varepsilon_2$$

With $\varepsilon_1$ is real permittivity and $\varepsilon_2$ is imaginary permittivity, which relates to refractive index(n) and extinction coefficient (k), as shown below

$$\varepsilon_1 = n^2 - k^2$$

$\varepsilon_2 = 2nk$

In dielectric material we observe two type of absorption i.e. inter-band transition in UV-Visible region and phonon absorption in infrared region. Therefore, a typical frequency dependent dielectric constant (dielectric function) shows Lorentz line $(\varepsilon_1)$ at each resonance frequency (absorption) with a distinct peak in the imaginary part of dielectric constant $(\varepsilon_2)$, as shown in figure 14. Constant magnitude of the real dielectric constant $(\varepsilon_1)$ in infrared region depends on the atomic and electric polarization, while the $(\varepsilon_1)$ constant in the visible region depends on the electric polarization. A constant $(\varepsilon_1)$ and negligible $(\varepsilon_2)$ in the visible region explain the transparent behaviour of most dielectric materials. Here the negative $(\varepsilon_1)$ value at slightly higher frequency than the resonance shows the polarization response is opposite to the electric field. In contrast, when frequency is slightly lower than the resonance, $(\varepsilon_1)$ is positive with enhancement shows polarization response is in phase with the electric field.

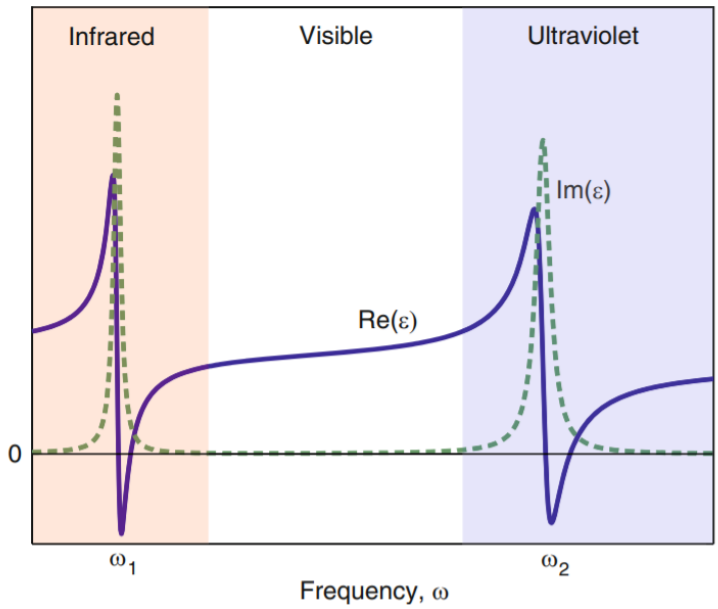


*Figure 48: The dielectric function ε(ω) for a typical dielectric material with the lattice resonance and electronic transition resonance at $\omega_1$, $\omega_2$ respectively[4].*

Dielectric function alteration in metals or doped semiconductor depends on free charge carrier absorption concurrent to inter-band transition absorption. Upon light absorption, free charge carrier oscillates at a frequency called plasma frequency $(\omega_p)$, which is given by equation.

$$\omega_p = \sqrt{\frac{ne^2}{\varepsilon_o m}}$$

Plasma frequency moves to the higher frequency region with the increase in free chare carrier concentration. Hence, we observe metal have plasma frequency in UV-Visible region while the doped semiconductors have it in infrared region. The real dielectric constant $(\varepsilon_1)$ is positive for frequency higher than the plasma frequency. For frequencies lower than the plasma frequency it becomes negative as shown in figure 15, while the dielectric constant becomes zero at the plasma frequency. Negative $(\varepsilon_1)$ value shows the free electron oscillation is out phase to incident electric field. Thus, for frequencies below the $\omega_p$, reflection is predominant. Imaginary dielectric constant $(\varepsilon_2)$ increase below the plasma frequency that is consider due to free charge carrier absorption.

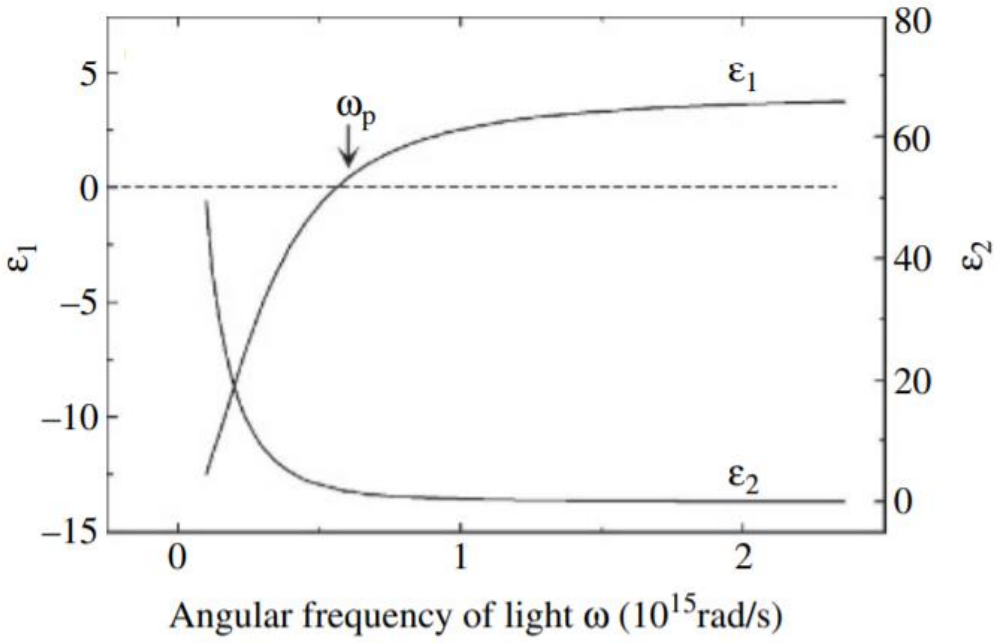


*Figure 49: Dielectric function of doped semiconductor[3].*

Drude model used for describing light propagation in metal assumes the damping parameter to be constant at a given temperature, Drude complex dielectric function is shown in below equation.

$$real\ \varepsilon_1 = \varepsilon_\infty - \frac{\omega_p^2}{\omega^2+\Gamma^2}\ ;\ imaginary\ \varepsilon_2 = \frac{\omega_p^2.\Gamma}{\omega(\omega+\Gamma^2)}$$

Where $\varepsilon_\infty$ is high frequency dielectric constant, $\omega_p$ is plasma frequency, $\Gamma$ is damping parameter. Damping parameter $(\Gamma)$ is related to electron mean free path as shown in below equation.

$$\Gamma = v_F.l$$

$v_F$ is the fermi velocity, $l$ is electron mean free path. When the geometric size of metal is comparable or smaller than the electron mean free path, then effective new mean free path is reduced to physical boundary of metal structure. New damping parameter is given as

$$\Gamma_1 = \Gamma + a.\frac{v_F}{R}$$

a is the geometric shape factor, R is the size of the metal particle. Imaginary dielectric constant $(\varepsilon_2)$ is directly proportional to the damping factor. For nanostructured metal particles, the $(\varepsilon_2)$ value increase relative to bulk metal[4]. Figure16 shows the dielectric function of silver, size effect of the imaginary dielectric constant. Hence, in nanostructure[5], absorption is predominant in relative to their counter bulk part.

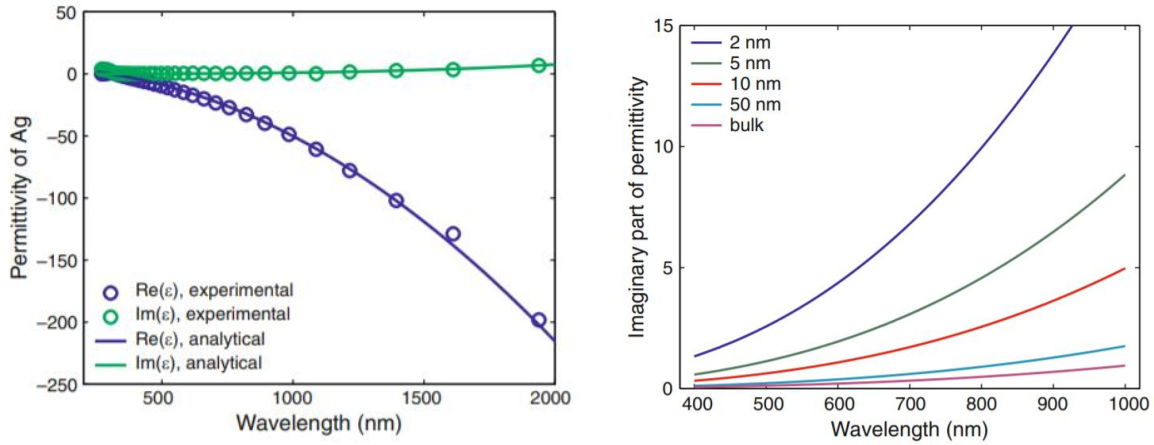


*Figure 50: Dielectric function of silver(left), size effect of the imaginary dielectric constant(right)[4].*

Light propagation in metal-dielectric composite is determined by the effective medium approach. Dielectric function of individual components, their respective volume fraction is considered to determine the effective dielectric function of the composite, given by equation

$$f_1 \frac{\varepsilon_1 - \varepsilon}{\varepsilon_1 + 2\varepsilon} + f_2 \frac{\varepsilon_2 - \varepsilon}{\varepsilon_2 + 2\varepsilon} = 0 \; ; f_1 + f_2 = 1$$

Where $f_1, f_2$ are volume fraction and $\varepsilon_1, \varepsilon_2$ are dielectric function of dielectric, metal particle respectively and $\varepsilon$ is the effective dielectric function of the composite. Figure17 displays the real, imaginary dielectric function of various metal volume fraction composites. For f=0, f=1 (metal volume fraction) the real dielectric function shows positive, negative values that characterizing typical dielectric, metal dielectric functions respectively. For metal volume fraction between 0 to 1 real dielectric function value gradually changed from positive to negative value. While the imaginary dielectric function which determines the resonance peak has shown increase in resonance peak with metal volume fraction. Nevertheless, a broad resonance band is obtained for f=0.4, which eventually disappear with increase in the metal volume fraction. Here the resonance peak is due to surface plasmon resonance at the metal-dielectric interface. An optimum metal volume fraction of f=1/3 is referred as percolation point beyond this value the metal particle forms a continuous conductivity path. Therefore, the composite shows prominent dielectric characteristic for metal fraction below percolation threshold, and metallic characteristic above them.

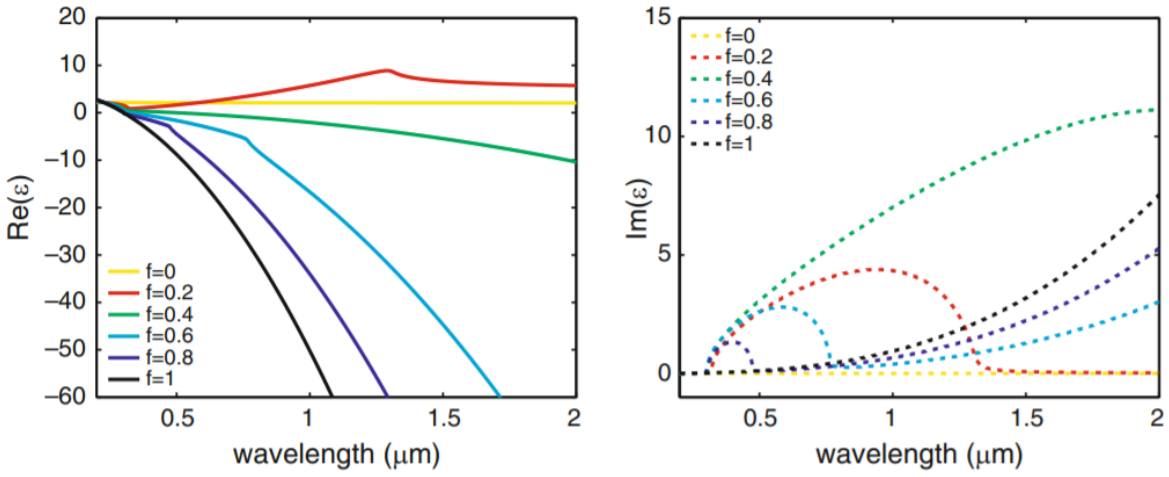


*Figure 51:The real and imaginary parts of the effective dielectric function of silver-silica composite[4].*

1. Eugene Hecht. *Optics 4th Edition*. Pearson; 2002. https://www.pearson.com/us/higher-education/product/Hecht-Optics-4th-Edition/9780805385663.html. Accessed June 16, 2021.

2. Dresselhaus M, Dresselhaus G, Cronin SB, Gomes Souza Filho A. Absorption of Light in Solids. In: *Solid State Properties*. Springer, Berlin, Heidelberg; 2018:365-389. doi:10.1007/978-3-662-55922-2_18

3. Fujiwara H. *Spectroscopic Ellipsometry: Principles and Applications*. John Wiley and Sons; 2007. doi:10.1002/9780470060193

4. Cai W, Shalaev V. *Optical Metamaterials: Fundamentals and Applications*. Springer New York; 2010. doi:10.1007/978-1-4419-1151-3

5. Agrawal A, Cho SH, Zandi O, Ghosh S, Johns RW, Milliron DJ. Localized Surface Plasmon Resonance in Semiconductor Nanocrystals. *Chem Rev*. 2018;118(6):3121-3207. doi:10.1021/acs.chemrev.7b00613